

MATER. TEHNOL.	LETNIK VOLUME	50	ŠTEV. NO.	3	STR. P.	287-466	LJUBLJANA SLOVENIJA	MAY-JUNE 2016
-------------------	------------------	----	--------------	---	------------	---------	------------------------	------------------

VSEBINA – CONTENTS

IZVIRNI ZNANSTVENI ČLANKI – ORIGINAL SCIENTIFIC ARTICLES

Experimental verifications and numerical thermal simulations of automobile lamps Eksperimentalna preverjanja in numerične toplotne simulacije avtomobilskih žarometov M. Guzej, J. Horsky	289
Tensile and compressive tests of textile composites and results analysis Natezni in tlačni preizkusi tekstilnih kompozitov in analiza rezultatov K. Kunc, T. Kroupa, R. Zemčík, J. Krystek	295
Deformation behaviour of a natural-shaped bone scaffold Obnašanje naravno oblikovanega ogrodja kosti pri deformaciji D. Kytýř, T. Doktor, O. Jiroušek, T. Fíla, P. Koudelka, P. Zlámal	301
Printed microstrip line-fed patch antenna on a high-dielectric material for C-band applications Tiskana mikrotrakasta linijsko napajana krpasta antena na visoko dielektričnem materialu za uporabo v C-pasu Md. M. Islam, M. R. I. Faruque, M. F. Mansor, M. T. Islam	307
Compressive properties of auxetic structures produced with direct 3D printing Stiskanje struktur materialov z negativnim Poissonovim razmerjem, proizvedenih z neposrednim tridimenzionalnim tiskanjem P. Koudelka, O. Jiroušek, T. Fíla, T. Doktor	311
Model of progressive failure for composite materials using the 3D Puck failure criterion Model postopnega popuščanja kompozitnega materiala z uporabo Puckovega tridimenzionalnega kriterija porušitve L. Bek, R. Zemčík	319
Physicochemical properties of a Ti67 alloy after EO and steam sterilization Fizikalno kemijske lastnosti zlitine Ti67 po EO in parni sterilizaciji W. Walke, M. Basiaga, Z. Paszenda, J. Marciniak, P. Karasinski	323
Surface properties of a laser-treated biopolymer Lastnosti površine biopolimera, obdelanega z laserjem I. Michaljaničova, P. Slepíčka, S. Rimpelova, P. Sajdl, V. Švorčík	331
Analyzing the heat-treatment effect on the mechanical properties of free-cutting steels Analiza vpliva toplotne obdelave na mehanske lastnosti avtomatnih jekel M. K. Kulekci, U. Esme, F. Kahraman, R. Ozgun, A. Akkurt	337
Analysis of the cutting temperature and surface roughness during the orthogonal machining of AISI 4140 alloy steel via the Taguchi method Analiza temperature rezanja in hrapavosti površine s Taguchi metodo pri ortogonalni strojni obdelavi legiranega jekla AISI 4140 A. R. Motorcu, Y. Isik, A. Kus, M. C. Cakir	343
Weldability of Ti6Al4V to AISI 2205 with a nickel interlayer using friction welding Preizkušanje varivosti pri varjenju s trenjem Ti6Al4V in AISI 2205 z vmesno plastjo niklja I. Kirik	353
Effect of activated flux and nitrogen addition on the bead geometry of borated stainless-steel GTA welds Vpliv aktiviranega topila in dodatka dušika na geometrijo kopeli pri GTA zvarih boriranega nerjavnega jekla G. R. Kumar, G. D. J. Ram, S. R. Koteswara Rao	357
Microstructural evolution during the transient liquid-phase bonding of dissimilar nickel-based superalloys of IN738LC and NIMONIC 75 Razvoj mikrostrukture med spajanjem s prehodno tekočo fazo neenakih superzlitin na osnovi niklja IN738LC in NIMONIC 75 M. G. Khakian, S. Nategh, S. Mirdamadi	365
Workability behaviour of Cu-TiB₂ powder-metallurgy preforms during cold upsetting Preoblikovalnost Cu-TiB ₂ predoblik izdelanih z metalurgijo prahov med hladnim kovalnim preizkusom S. Gadakary, A. Kumar Khanra, M. J. Davidson	373
Effects of extrusion shear on the microstructures and a fracture analysis of a magnesium alloy in the homogenized state Vplivi striženja med iztiskanjem homogenizirane magnezijeve zlitine na mikrostrukturo in na analizo preloma H. J. Hu, Z. Sun, D. F. Zhang	381

FSW welding of Al-Mg alloy plates with increased edge roughness using square pin tools of various shoulder geometries FSW varjenje plošč iz Al-Mg zlitine s povečano hrapavostjo robov z orodjem s kvadratno konico in različno geometrijo bokov S. Balos, L. Sidjanin, M. Dramicanin, D. Labus Zlatanovic, A. Antic	387
Improvement of selective copper extraction from a heat-treated chalcopyrite concentrate with atmospheric sulphuric-acid leaching Izboljšanje selektivne ekstrakcije bakra iz toplotno obdelanega koncentrata halkopirita z luženjem z žvepleno kislino na zraku E. Uzun, M. Zengin, İ. Atılğan	395
Homogenization of an Al-Mg alloy and alligating failure: alloy ductility and fracture Homogenizacija Al-Mg zlitine in krokodiljenje: duktilnost zlitine in prelom E. Romhanji, T. Radetić, M. Popović	403
STROKOVNI ČLANKI – PROFESSIONAL ARTICLES	
Assessment of tubular light guides with respect to building physics Ocena cevastih vodnikov svetlobe glede na gradbeno fiziko F. Vajkay, D. Bečkovský, V. Tichomirov	409
Creep behaviour of a short-fibre C/PPS composite Vedenje kratkih vlaken C/PPS kompozitov pri lezenju T. Fíla, P. Koudelka, D. Kytýř, J. Hos, J. Šleichrt	413
Increasing micro-purity and determining the effects of the production with and without vacuum refining on the qualitative parameters of forged-steel pieces with a high aluminium content Povečanje mikročistoče in določitev učinka proizvodnje, z vakuumskim rafiniranjem ali brez, na kvalitativne parametre kovanega jekla z visoko vsebnostjo aluminija V. Kurka, J. Pindor, J. Kosňovská, Z. Adolf	419
Use of the ABI technique to measure the mechanical properties of aluminium alloys: effect of heat-treatment conditions on the mechanical properties of alloys Uporaba ABI tehnike za merjenje mehanskih lastnosti aluminijevih zlitin: vpliv pogojev toplotne obdelave na mehanske lastnosti zlitin O. Trudonoshyn, M. Puchnin, O. Prach	427
Investigation of the effect of holding time and melt stirring on the grain refinement of an A206 alloy Preiskava vpliva časa zadrževanja in mešanja taline na zmanjšanje velikosti zrn zlitine A206 N. Akar, Z. Tanyel, K. Kocatepe, R. Kayikci	433
Investigating the influence of cutting speed on the tool life of a cutting insert while cutting DIN 1.4301 steel Preiskava vpliva hitrosti rezanja na zdržljivost vložka za rezanje pri rezanju jekla DIN 1.4301 R. Dubovská, J. Majerfk, R. Čep, K. Kouřil	439
NiAl intermetallic prepared with reactive sintering and subsequent powder-metallurgical plasma-sintering compaction Reakcijsko sintranje in zgoščevanje s plazemskim sintranjem NiAl intermetalne zlitine A. Michalcová, D. Vojtěch, T. F. Kubatík, P. Novák, P. Dvořák, P. Svobodová, I. Marek	447
Microscopic characterization and particle distribution in a cast steel matrix composite Mikroskopska karakterizacija in razporeditev delcev v kompozitu z matrico litega jekla A. Kračun, M. Torkar, J. Burja, B. Podgornik	451
A comparison of as-welded and simulated heat affected zone (HAZ) microstructures Primerjava mikrostrukture toplotno vplivanega področja varjenega in simuliranih vzorcev R. Celin, J. Burja, G. Kosec	455
Degradation of an AISI 304 stainless-steel tank Degradacija rezervoarja iz AISI 304 nerjavnega jekla M. Torkar, I. Paulin, B. Podgornik	461

EXPERIMENTAL VERIFICATIONS AND NUMERICAL THERMAL SIMULATIONS OF AUTOMOBILE LAMPS

EKSPERIMENTALNA PREVERJANJA IN NUMERIČNE TOPLOTNE SIMULACIJE AVTOMOBILSKIH ŽAROMETOV

Michal Guzej, Jaroslav Horský

Brno University of Technology, Faculty of Mechanical Engineering, Technická 2, 616 69 Brno, Czech Republic
guzej@lptap.fme.vutbr.cz

Prejem rokopisa – received: 2014-07-31; sprejem za objavo – accepted for publication: 2015-05-21

doi:10.17222/mit.2014.149

Over the last decade lamps became a design feature of a car body and to preserve their primary purpose they are much more complex than in the past. Today's car lamps contain powerful light sources, which utilize new technologies such as dot-concentrated light (LED chips or xenon discharge tubes). One of the unfavourable properties of these products is a high amount of thermal energy produced in a small area, causing a high thermal stress on the components. For this reason, it is important to know the temperature in critical locations to avoid damaging the lamp body or causing a defect in the light source itself. This paper presents the results of a numerical simulation of the working conditions of a lamp, the measurement inside the environmental-simulation chamber with a real lamp, providing the same conditions and the verification of the simulation results with the measurement, which confirmed the precision of the numerical simulation. The verification procedure was developed at the Heat Transfer and Fluid Flow Laboratory of the BUT in partnership with Škoda Auto a.s.

Keywords: automobile lamps, thermocouples, numerical simulation, thermal measurements, verification

Zadnje desetletje so avtomobilski žarometi postali del oblikovanja avtomobilске karoserije in za ohranitev prvotne vloge so, v primerjavi s preteklostjo, postali bolj kompleksni. Današnji avtomobilski žarometi imajo močan izvor svetlobe, ki uporablja nove tehnologije, kot je točkasto skoncentrirana svetloba (LED čip ali ksenonska razelektrivna cev). Ena od neželenih lastnosti teh proizvodov je velika količina toplotne energije, ki nastane na majhnem področju in zaradi tega pride do večje termične napetosti v komponentah. Zato je pomembno poznati temperature na kritičnih lokacijah, da se prepreči poškodba ohišja žarometu ali da nastane napaka na samem izvoru svetlobe. Članek predstavlja rezultate numerične simulacije delovnih pogojev žarometov, meritve v notranjosti numerično simuliranega okolja realnega žarometu z realno žarnico in preverjanje rezultatov simulacije z meritvami, ki so potrdile natančnost numerične simulacije. Postopek verifikacije je bil razvit v Laboratoriju za prenos toplote in tok fluidov na BUT, s sodelovanjem Škoda Auto a.s.

Ključne besede: avtomobilski žarometi, termoelementi, numerična simulacija, toplotne meritve, preverjanje

1 INTRODUCTION

Modern automobile lamps have a complex body design and contain powerful built-in sources of light. This can create problems for the materials used for their construction.¹ Manufacturers and consumers, in this case Škoda Auto a.s., need to know the temperature generated at critical locations and compare it with the temperature limit for each plastic material. Every material has a long-term temperature limit and a short-term temperature limit.² Electrical losses of dot-concentrated light are converted into thermal energy. The result of this effect is a temperature gradient, which produces significant thermal stresses within the structure.³ Solving this problem with an analytical method is a formidable task. The few solutions available cover only simple structural shapes. The only option is to use simulation software such as ANSYS, COMSOL, etc. Verifying the results of a computer simulation is always necessary when high precision is required. Experimentation under the same conditions as in the simulation determines the accuracy of the results or detects possible errors in the settings of the simulation model. Wire thermocouples built into control

points are used for the temperature measurement. Deviations between the simulation and reality are determined from the heat-settled part of the experiment.

2 EXPERIMENTAL PART

To numerically simulate an automotive lamp (**Figure 1**), the ambient temperature during the experiment must be known. A lamp placed inside an environmental simulation chamber (type: MK 720 E3.1) manufactured by Binder was used for this purpose. This device can maintain the required temperature by forced convection in a very small range.

2.1 Description of the measurement circuit

Data collection during the experiments consists of five major parts (**Figure 2**). First, data is measured through the thermocouples. Then, information in millivolts is transferred into a 7001 switch system manufactured by Keithley, an American company. This model is a half-rack, high-density, two-slot mainframe with a maximum of 80 signal channels (in this experiment, 12



Figure 1: Lamp with thermocouples, front view
Slika 1: Žaromet s termoelementi, pogled od spredaj

wire thermocouples were used). The built-in, non-volatile memory stores up to 100 complete switch patterns. Then, the signal from the switcher is transferred through a GPIB cable into a Model 2000 multimeter made by the same company. Model 2000 is a high-performance digital multimeter, which can measure DC voltage, AC voltage, DC current, AC current, two- and four-wire resistance, and temperature. A thermocouple card is placed at a built-in cold junction. The final step is to save the data as a .txt file.

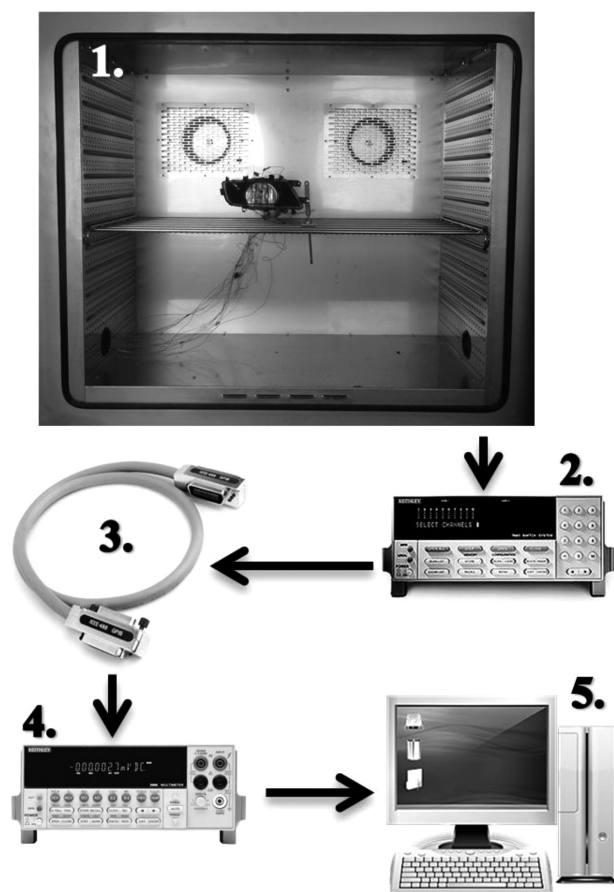


Figure 2: Data collection in the measurement circuit: 1) environmental simulation chamber with a lamp, 2) switcher, 3) GPIB cable, 4) multimeter and 5) computer

Slika 2: Zbiranje podatkov v merilnem tokokrogu: 1) simulacijska komora okolja z žarnico, 2) preklopnik, 3) GPIB-kabel, 4) multimeter in 5) računalnik

2.2 Assembly of the thermocouples

Measurement points (the locations of the thermocouples) were chosen based on the simulation results from two cross-sections, A and B (**Figure 3**). At these points, 1-mm-diameter holes were drilled to a depth of 1 mm. The junction of a wire thermocouple was embedded into to this hole and filled with a high-temperature-resistant epoxy (**Figure 4a**). The operational temperature range of this epoxy is from $-55\text{ }^{\circ}\text{C}$ to $180\text{ }^{\circ}\text{C}$, and its thermal properties are similar to PP GF30, the plastic material used for the body of the lamp. If the hole for the thermocouple is made into a transparent material (such as the glass of a lamp), an epoxy with the same optical properties must be used due to transmittance (**Figure 4b**). Using a material with different properties has a negative effect on the temperature measurement near the built-in thermocouple. A K-type thermocouple was used to record the data. This type is the most common general-purpose thermocouple, with a sensitivity of approximately $41\text{ }\mu\text{V}/^{\circ}\text{C}$.⁴ K-type thermocouples are recommended for use in oxidizing or completely inert atmospheres in a temperature range of $-200\text{ }^{\circ}\text{C}$ to $1260\text{ }^{\circ}\text{C}$. The positive wire consists of 90 % nickel and 10 % chromium, while the negative wire is consists of 95 % nickel and 5 % aluminum and silicon.⁴

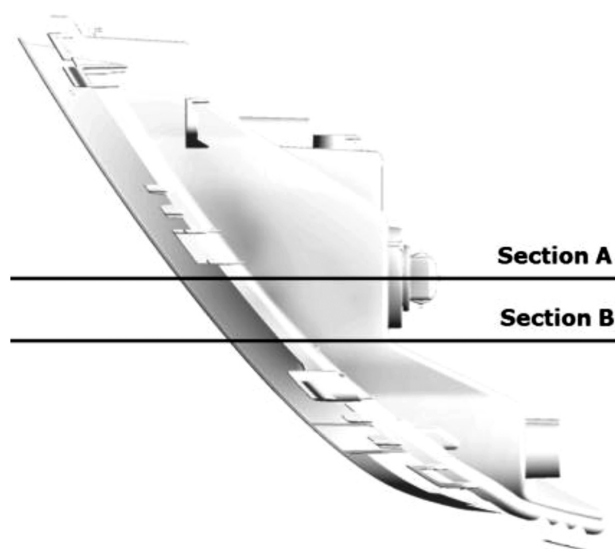


Figure 3: Top view of cross-sections A and B. Cross-section A is situated in the axis of the bulb filament, cross-section B is offset by 30 mm from section A, in the Y-axis direction.

Slika 3: Pogled od zgoraj na preseka A in B. Presek A je v osi žarilne nitke žarnice, presek B je zamaknjen za 30 mm od preseka A, v smeri Y-osi

Table 1: Thermal properties of lamp materials
Tabela 1: Toplotne lastnosti materialov žaromet

Materials	Density (kg m^{-3})	Thermal conductivity ($\text{W m}^{-1} \text{K}^{-1}$)	Specific heat ($\text{J kg}^{-1} \text{K}^{-1}$)
Body PP GF30	1066	0.3	1351
Glass PMMA	1194	0.33	1288

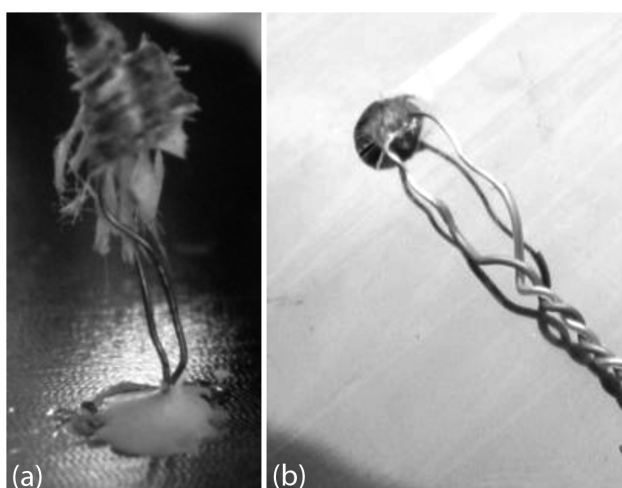


Figure 4: Thermocouple attachment: a) a normal surface and b) a transparent surface

Slika 4: Pritrditev termoelementa: a) je normalna površina, b) prozorna površina

2.3 Calibration

Each thermocouple had to be calibrated before the first measurement to obtain accurate results. This is due to the fact that thermocouples do not always have exactly the same characteristics, even if they meet fairly strict standards and tolerances. Calibration represents a deviation between the thermocouple measurement and a precise etalon. For a K-type thermocouple and a temperature range from $-40\text{ }^{\circ}\text{C}$ to $375\text{ }^{\circ}\text{C}$, the tolerance is $\pm 1.5\text{ }^{\circ}\text{C}$ (the highest class of accuracy). All the thermocouples had a deviation under the tolerance value. The tolerance of thermoelectric voltage U is determined with the following Equation (1):⁵

$$\Delta U_T = \Delta T \cdot \left(\frac{dU_T}{dT} \right) \quad (1)$$

where ΔU_T is the thermoelectric voltage tolerance, ΔT is the temperature difference ($^{\circ}\text{C}$), T is the temperature ($^{\circ}\text{C}$), and U_T is the thermoelectric voltage (V).

3 LAMP SIMULATION

Predictions of the temperatures of the lamps were computed with computational fluid dynamics (CFD). The CFD process consists of three important steps: pre-processing, solving, and post-processing.

3.1 Pre-processing

The geometry of the lamp was imported from raw CAD data. The next step was to create a computation mesh. The CutCell meshing method (**Figure 5**) in ANSYS TGrid 14.5 was used for this purpose. This method was chosen because its preparation time is shorter than the times needed for conventional

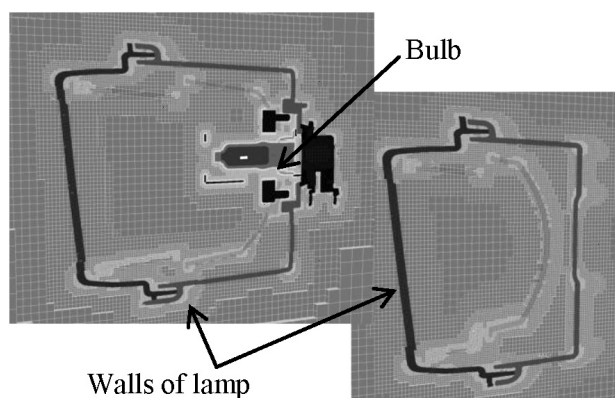


Figure 5: Example of the CutCell meshing method
Slika 5: Primer mreže pri CutCell metodi

approaches. The size of the mesh was about 13 million polyhedral cells and the average size of these cells was 1 mm.

3.2 Solving

The resulting mesh was exported into the ANSYS Fluent 14.5 solver, where appropriate boundary conditions were set up. These boundary conditions included the type of fluid flow (laminar), the material properties, the emissivity of the surfaces, the heat source, and, eventually, the forced convection around the lamp (simulating an environment as similar as possible to the climate chamber).

The distribution of temperatures inside the lamp depended mainly on natural convection (incompressible ideal gas) and radiation of the heat from the bulb. The heat absorbed by the surfaces was transported through the materials by heat conduction. The DO (discrete ordinate) model was used to model the radiation, allowing a calculation for semi-transparent walls.

The DO model uses a discretization technique, which solves the radiation-transfer equations for a finite number of angles or directions. The angular discretization is controlled by either increasing or decreasing the amount of theta-phi divisions and pixels.⁶ The number of divisions and pixels should therefore be kept at a minimum in order to keep computational costs as low as possible, but the minimum amount will also give the coarsest discretization. The settings vary between a minimum of $3 \times 3 \times 3 \times 3$, which is the coarsest, to $10 \times 10 \times 10 \times 10$, which is the maximum and gives the highest accuracy and finest discretization. Since the maximum discretization requires a lot of computational time and data storage, the angular discretization used in the radiation model was determined to be $6 \times 6 \times 6 \times 6$, which was sufficient. The effect of solar radiation could be specified but was not used for this case.

The solver solves the mass, momentum, energy and radiative-transport equations throughout the whole domain. The equations are discretized along the cells of the domain and solved until convergence is reached.

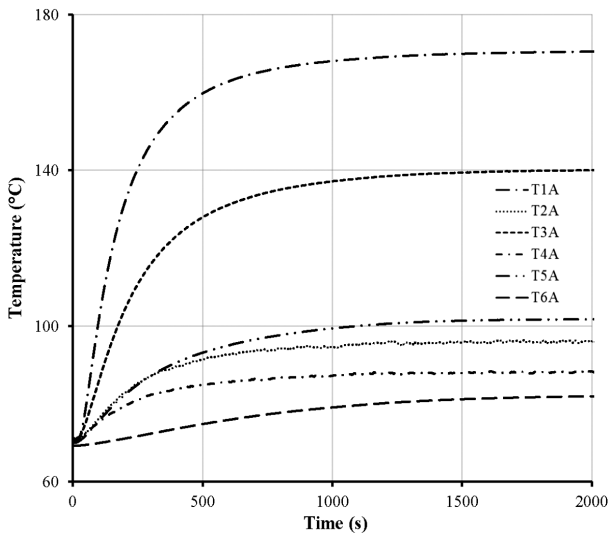


Figure 6: Results for cross-section A
Slika 6: Rezultati iz preseka A

3.3 Post-processing

The results from the solution were visualized with plotting parameters of interest for every part, in our case focusing mainly on the temperatures. Post-processing was performed in ANSYS CFD-Post.

4 MEASURED DATA

The following two diagrams (Figures 6 and 7) show recorded temperatures of the lamp during the experiment for an ambient temperature of 70 °C, a bulb supply voltage of 13.2 V and a sampling frequency of 5 s.

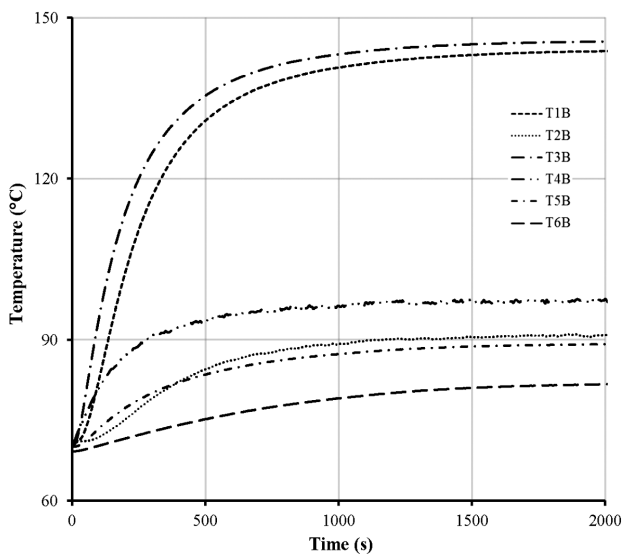


Figure 7: Results for cross-section B
Slika 7: Rezultati iz preseka B

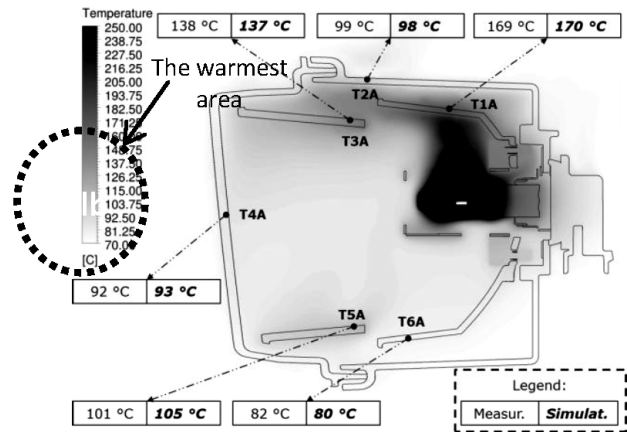


Figure 8: Temperatures for cross-section A
Slika 8: Temperature na preseku A

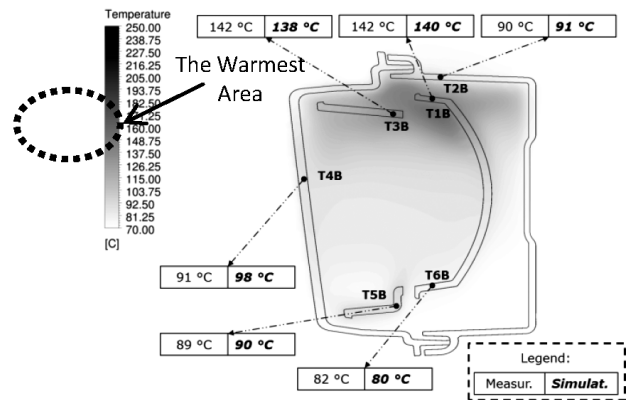


Figure 9: Temperatures for cross-section B
Slika 9: Temperature na preseku B

5 DISCUSSION

Figures 8 to 10 show a comparison between the numerical and experimental results (the temperature distributions were plotted for two cross-sectional points, A and B), including a bar graph showing the variation between the measurement and the simulation.

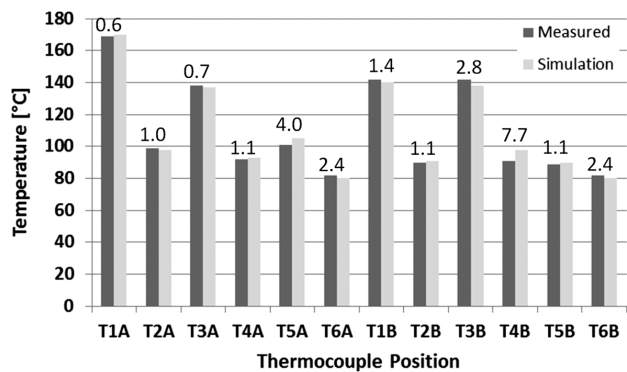


Figure 10: Comparison of the temperatures between the measurement and simulation
Slika 10: Primerjava izmerjenih in simuliranih temperatur

The numbers at the top of the columns are percent deviations between the measured and simulated values for all the positions of the thermocouples.

6 CONCLUSIONS

This paper demonstrated the importance of a comparison between an experiment and a numerical simulation due to the unknown boundary conditions at the walls of real lamps. Determining an acceptable accuracy is necessary to verify the lamp model. The greatest deviations in the data are found for the T5A thermocouples (the simulated value is 4 % above the measured value) and the T4B thermocouples (the simulated value is 7.7 % above the measured value). Possible reasons for these inaccuracies are slightly different positions of the drilled holes and the control point from the ones used in the simulation, and the air flow around the lamp during the experiment, which had a higher (or lower) speed than the value calculated with the simulation.

Acknowledgement

This work is an output of the research and scientific activities of the NETME Centre, regional R&D centre built with the financial support from the Operational Programme Research and Development for Innovations, carried out within a NETME Centre project (New

Technologies for Mechanical Engineering), Reg. No. CZ.1.05/2.1.00/01.0002 and, in the follow-up sustainability stage, supported through NETME CENTRE PLUS (LO1202) with the funds from the Ministry of Education, Youth and Sports under the National Sustainability Programme I.

7 REFERENCES

- ¹ V. A. Drebuschak, Universality of the emf of thermocouples, *Thermochimica Acta*, 496 (2009) 1–2, 50–53, doi:10.1016/j.tca.2009.06.025
- ² T. Shiozawa, Thermal air flow analysis of an automotive headlamp: the PIV measurement and the CFD calculation for a mass production model, *JSAE Review*, 22 (2001) 2, 245–252, doi:10.1016/S0389-4304(00)00111-9
- ³ K. Sokmen, K. Furkan, E. Pulat, N. Yamankaradeniz, S. Coskun, Thermal computations of temperature distribution and bulb heat transfer in an automobile headlamp, *Heat and Mass Transfer*, 50 (2014) 2, 199–210, doi:10.1007/s00231-013-1229-5
- ⁴ Thermocouples, Sponsored by ASTM Committee E-20 on Temperature Measurement and Subcommittee E20.04 on Thermocouples, Manual on the use of thermocouples in temperature measurement, 6th ed., American Society for Testing and Materials, Philadelphia 1992
- ⁵ J. H. Zhao, B. Zhou, Thermocouple Automatic Verifying Device Based on Virtual Instrument Technology, *Applied Mechanics and Materials*, 303–306 (2013), 588–596, doi:10.4028/www.scientific.net/AMM.303-306.588
- ⁶ ANSYS Fluent Theory Guide, release 14.0., ANSYS Inc., 2011

TENSILE AND COMPRESSIVE TESTS OF TEXTILE COMPOSITES AND RESULTS ANALYSIS

NATEZNI IN TLAČNI PREIZKUSI TEKSTILNIH KOMPOZITOV IN ANALIZA REZULTATOV

Kryštof Kunc, Tomáš Kroupa, Robert Zemčík, Jan Krystek

University of West Bohemia in Plzeň, NTIS, Univerzitní 22, 306 14, Plzeň, Czech Republic
ptaeck@kme.zcu.cz

Prejem rokopisa – received: 2014-08-01; sprejem za objavo – accepted for publication: 2015-05-05

doi:10.17222/mit.2014.167

The presented work is focused on an experimental investigation of the behavior of six types of textile composites subjected to pure tensile, cyclic tensile and compressive loading according to ASTM standards. Each type was loaded in directions forming angles between 0° and 90° , with a step of 15° with respect to the reference directions of the weaves. Two types of woven fabrics were tested (plain and quasi-unidirectional plain-woven fabric). Images of specimens taken during the tests were subsequently used for the calculation of the so-called locking angle of yarns (bundles) just before failure. Force-displacement dependencies were recorded during the tensile tests. Ultimate forces were obtained from the compressive tests. The second half of the article is dedicated to the analysis of the experimental data gathered with nearly 1000 experiments. Special software for automatic calculation of averaged dependencies, maximum forces and maximum displacements was created. Furthermore, the methodology for calculating the locking angle was proposed and tested. The obtained results will be used for the identification of the material parameters of the proposed material model in the following research.

Keywords: textile composites, woven fabric, tensile test, compressive test, result analysis, weave locking

Prispevek je usmerjen v eksperimentalno preiskavo obnašanja šestih vrst tekstilnih kompozitov, obremenjenih z natezno, ciklično-natezno in tlačno obremenitvijo skladno z ASTM standardi. Vsaka vrsta je bila obremenjena v smeri, ki je tvorila kot med 0° in 90° , s koraki po 15° , glede na smer tkanja. Preizkušeni sta bili dve vrsti tkanin (običajna in kvazi enosmerna običajna tkanina). Posnetki vzorcev med preizkusi so bili uporabljani za izračun zapornega kota preje (svežnjeve) tik pred poružitvijo. Odvisnosti sila-raztezek so bile posnete med nateznimi preizkusi. Končne sile so bile dobljene iz tlačnih preizkusov. Naslednji del prispevka je bil posvečen analizi eksperimentalnih podatkov iz skoraj 1000 preizkusov. Kreirana je bila posebna programska oprema za avtomatsko računanje povprečnih odvisnosti: maksimalnih sil in maksimalnih raztezkov. Poleg tega je bila predlagana in preizkušena metodologija za izračun zapornega kota. Dobljeni rezultati bodo uporabljeni pri nadaljevanju raziskav za določanje parametrov materiala v predlaganem modelu materiala.

Ključne besede: tekstilni kompoziti, tkanina, natezni preizkus, tlačni preizkus, analiza rezultatov, zaklepanje vezave

1 INTRODUCTION

Textile composites made from carbon, glass and aramid fibers are nowadays commonly used. However, to be able to simulate the behavior of these modern materials as in the case of classical metals, it is appropriate to use complex mathematical models with many more material parameters. A significantly non-linear behavior of composite materials is caused by different properties of its components and by a complicated manufacturing process. Sophisticatedly gathered data from many experimental tests are, therefore, required for identifying material parameters and designing modern tailored composite structures.¹

2 EXPERIMENTAL PART

Experimental tests were focused on three composite types – glass, carbon and aramid. Each type was tested in two woven-fabric versions: a) a plain weave with a 1:1 fiber ratio and b) a quasi-unidirectional plain weave with a 1:9 fiber ratio.²

The following markings are used to describe all the tested specimens: GP – glass plain weave, GU – glass quasi-unidirectional weave, CP – carbon plain weave, CU – carbon quasi-unidirectional weave, AP – aramid plain weave and AU – aramid quasi-unidirectional weave.

The tested specimens (coupons) were cut from six composite plates, manufactured with the RTM technology, using a water jet to get seven different groups of specimens with the principal material orientation θ of the weave (between 0° and 90° with a step of 15°) with respect to each coupon's longitudinal axis (and load direction). Average thicknesses of the coupons are shown in **Table 1**.

Table 1: Average thicknesses of composite plates

Tabela 1: Povprečne debeline kompozitnih plošč

Material	t (mm)	Material	t (mm)
GP	1.8	GU	1.8
CP	2.0	CU	1.5
AP	2.2	AU	2.0

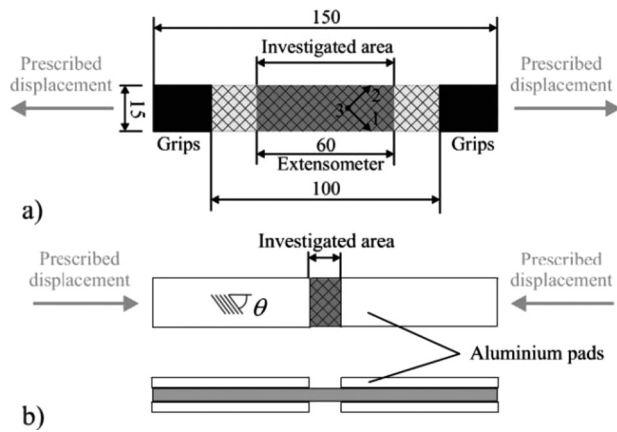


Figure 1: Dimensions of specimens for: a) tensile and b) compressive tests and the principal material orientation

Slika 1: Dimenzije vzorcev za: a) natezne in b) tlačne preizkuse in glavna orientacija materiala

To ensure the objectivity of the measurement, a minimum of seven specimens for each material, weave type and weave orientation was prepared.

Three types of tests were performed on a Zwick/Roell Z050 machine – pure tensile, cyclic tensile and compressive loading – according to ASTM standards.³ For the following experiment analysis, data from a minimum of six identical tests were accepted. The total number of specimens for one experiment (tensile/cyclic tensile/compressive) is seven coupons for seven material orientations multiplied by three different materials and two types of woven fabrics. In total, nearly 1000 specimens were tested, including the preliminary work.

Typical specimen set-ups before the tensile a) and compressive b) tests and their dimensions are shown in **Figure 1**. Cyclic tensile tests were driven by the prescribed displacement with amplitude $\Delta l = 1$ mm. In the finished cyclic tests, the number of hysteresis loops for the same specimens was not always the same. This is evident from the result graphs, where the tangents of a few last load/unload cycles are missing.

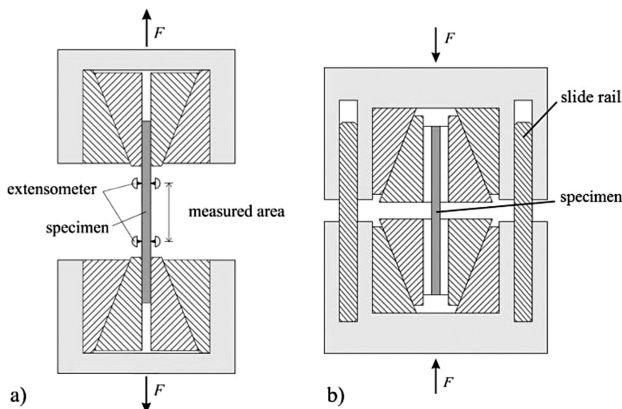


Figure 2: a) Tensile- and b) compressive-test schemes

Slika 2: Shemi: a) nateznega preizkusa in b) tlačnega preizkusa

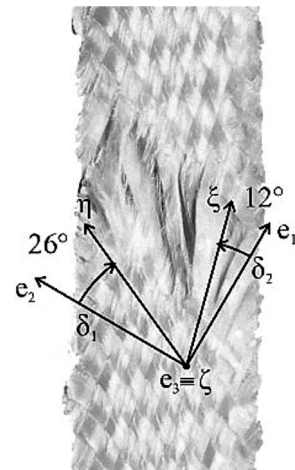


Figure 3: Aramid plain-weave specimen ($\theta = 30^\circ$) and locking-angle interpretation

Slika 3: Vzorec aramida z navadnim valom ($\theta = 30^\circ$) in predstavitev zapornega kota

The tensile tests for the plain-woven fabrics were less problematic than the ones for the quasi-unidirectional plain-woven fabrics, which had to be equipped with aluminium pads in numerous cases to avoid a premature destruction of a coupon by machine grips and to get acceptable results from the experiment. All the coupons for the compressive tests had to be prepared with aluminium pads to achieve the proper attachment to the testing machine.⁴ The schemes shown in **Figure 2** represent typical experimental set-ups for the tensile (a) and compressive tests (b).

All the specimens subjected to the tensile tests (loading) were photographed to identify the so-called locking angle.⁵

The locking angle (**Figure 3**) is defined by two angles, δ_1 and δ_2 , representing the diversions of the principal material directions, just before the rupture (axes ξ, η, ζ), from their initial states (axes e_1, e_2, e_3). This phenomenon was most notable on the specimens made of the aramid textile and least notable on the glass textile. Similarly, for the boundary material orientations

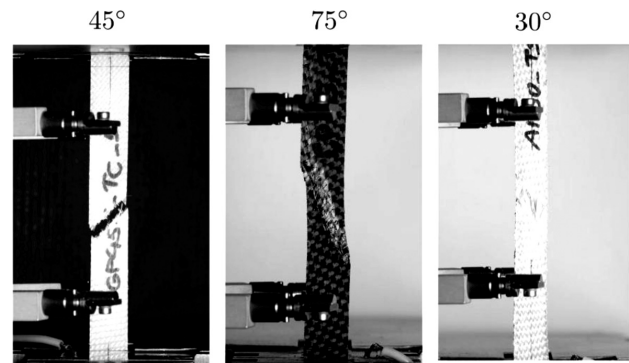


Figure 4: Photographs of selected plain-weave specimens after the tensile test (GP, CP, AP)

Slika 4: Posnetki izbranih vzorcev z navadnim valom po nateznem preizkusu (GP, CP, AP)

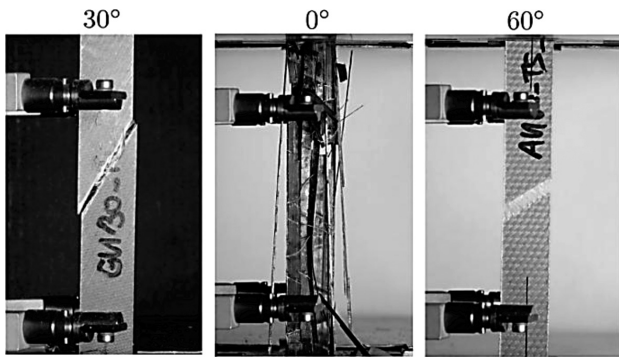


Figure 5: Photographs of selected quasi-unidirectional plain-weave specimens after the tensile test (GU, CU, AU)
Slika 5: Posnetki izbranih vzorcev s kvazi-enosmerno, običajno vezavo po nateznem preizkusu

of $\theta = 0^\circ$ and $\theta = 90^\circ$ and quasi-unidirectional plain-weave composites made of carbon and glass, no significant weave-locking phenomenon was proven. Carbon composites with plain weave showed a high strength during the tests and never ruptured completely (excluding the boundary orientations). Photographs of selected specimens taken after the tensile test are shown on **Figure 4** (with plane weave) and **Figure 5** (with quasi-unidirectional plain weave).

A further description of implementing the measured data into the identification process and the details of the material model can be found in another paper of the above co-authors.⁶

3 ANALYSIS OF THE EXPERIMENTAL DATA

Standalone application *ploTra* was written in the Python programming language for the processing of a large amount of experimental data. The application is designed to read experimental data from the Zwick/Roell

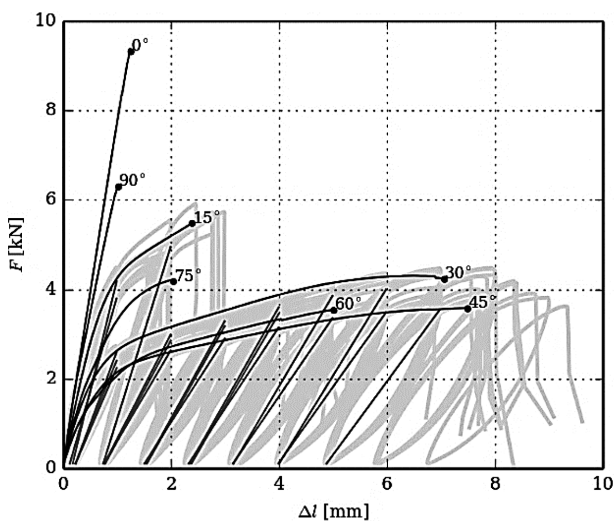


Figure 6: Averaged force-displacement dependencies and tangent of unload/load cycle for GP composite
Slika 6: Povprečna odvisnost sila-raztezeka in tangenta na neobremenjen/obremenjen cikel pri GP kompozitu

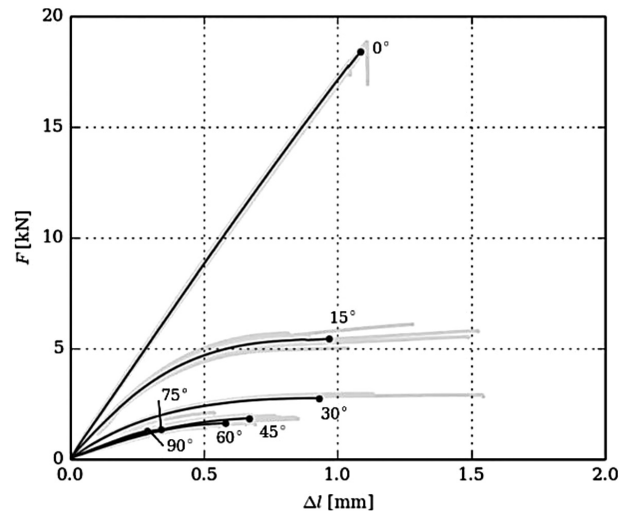


Figure 7: Averaged force-displacement dependencies for GU composite
Slika 7: Povprečna odvisnost sila-raztezeka pri GU kompozitu

software (in the TRA format) and execute multiple operations resulting in the following outputs:

Averaged force-displacement dependencies (dark curves in the presented graphs). The application accepts data from one sorted set of measurements and calculates the average using one of the various available methods, e.g., 2D averaging, averaging in a given interval, or the arc length. The results are saved as graphs (PNG/PDF) and binary files for future usage.

Averaged tangents (slopes) of unload/load cycles (straight lines in the presented graphs). All the hysteresis loops from the cyclic tensile tests are identified; their lowest and highest points are connected to form lines, the tangents of which are averaged for each experiment group including the specimens with the same orientation. It was observed that these tangents were not constant during the tests.

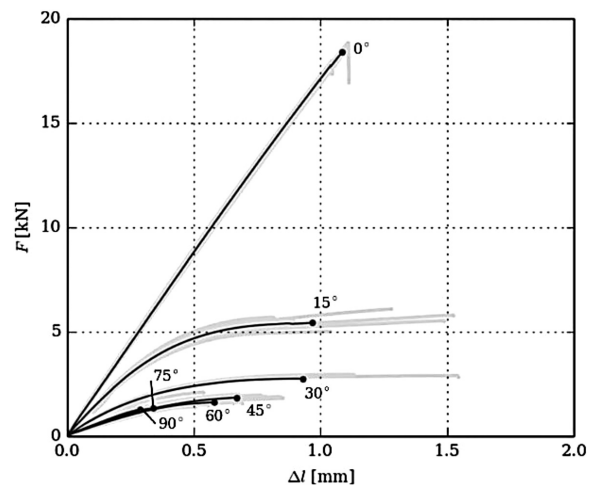


Figure 8: Averaged force-displacement dependencies and tangent of unload/load cycle for CP composite
Slika 8: Povprečne odvisnosti sila-raztezeka in tangenta cikla neobremenjeno/obremenjeno pri CP kompozitu

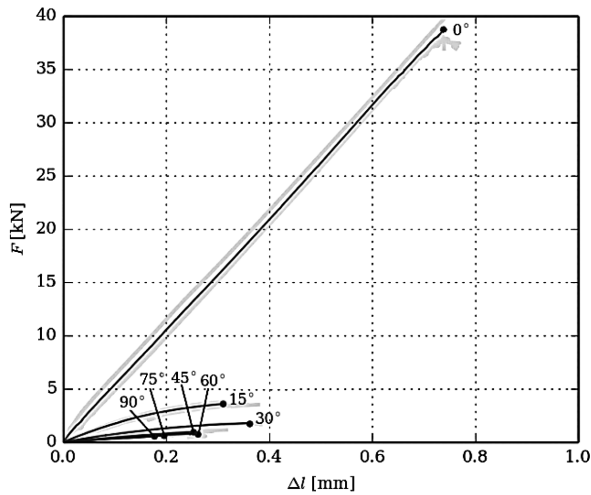


Figure 9: Averaged force-displacement dependencies for CU composite

Slika 9: Povprečne odvisnosti sila-raztezek pri CU kompozitu

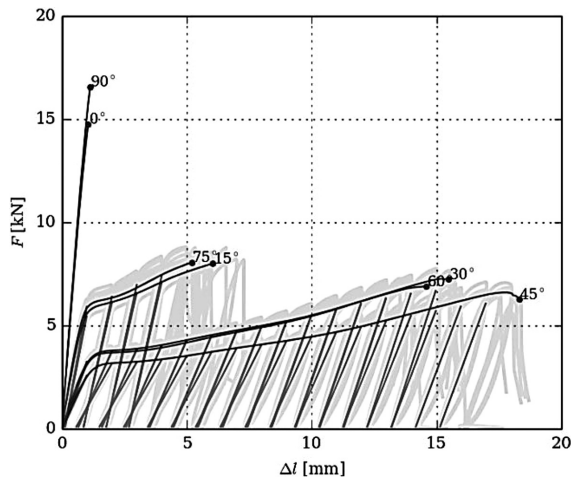


Figure 10: Averaged force-displacement dependencies and tangent of unload/load cycle for AP composite

Slika 10: Povprečne odvisnosti sila-raztezek in tangenta cikla razbremenjeno/obremenjeno pri AP kompozitu

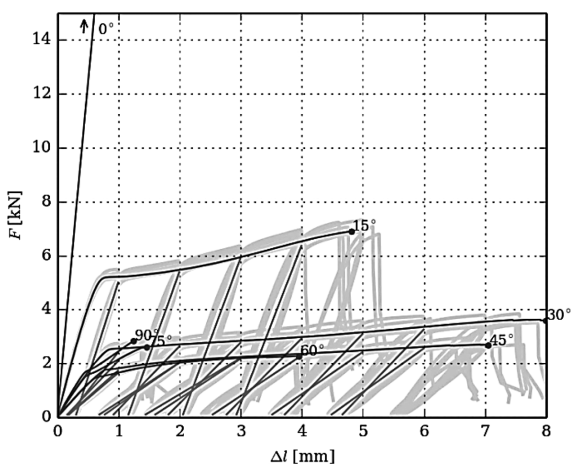


Figure 11: Averaged force-displacement dependencies and tangent of unload/load cycle for AU composite

Slika 11: Povprečne odvisnosti sila-raztezek in tangenta cikla neobremenjeno/obremenjeno pri AU kompozitu

Tables with averaged statistical data – the maximum forces and displacements including standard deviations.

4 RESULTS

The tables and graphs below represent the outputs from the *plTra* application. The maximum tensile and ultimate forces of the compressive tests are shown in **Tables 2** and **3**. Averaged force-displacement dependencies (**Figures 6 to 11**) are suitable for the use of the complex material model including damage. The weave-locking angles shown in **Tables 4** and **5** were collected using the common tools available in graphics editors.

Table 2: Tensile tests – average maximum forces in (kN)

Tabela 2: Natezni preizkusi – povprečje maksimalnih sil (kN)

θ	GP	GU	CP	CU	AP	AU
0°	9.50	18.45	20.20	39.71	16.01	29.50
15°	5.68	5.63	9.33	3.66	8.25	7.03
30°	4.33	2.78	5.96	1.80	7.33	3.66
45°	3.63	1.91	5.28	0.99	6.63	2.73
60°	3.66	1.67	5.77	0.82	7.01	2.30
75°	4.23	1.39	9.18	0.60	8.37	2.67
90°	6.40	1.36	19.09	0.57	17.37	2.87

Table 3: Compressive tests – average ultimate forces (kN)

Tabela 3: Tlačni preizkusi – povprečje končnih sil (kN)

θ	GP	GU	CP	CU	AP	AU
0°	8.32	13.21	12.01	11.70	4.89	5.36
15°	6.71	4.71	7.32	5.74	4.69	5.37
30°	4.03	4.25	4.91	3.75	3.77	3.99
45°	3.67	4.01	4.51	3.16	3.70	3.46
60°	3.96	3.96	4.75	2.81	4.01	3.37
75°	4.85	4.04	7.13	2.55	4.68	3.45
90°	4.20	4.05	11.6	2.54	4.70	3.52

Table 4: Averaged weave-locking angles δ_1 and δ_2 for plain-weave composites in (°)

Tabela 4: Povprečje kota tkanja δ_1 in δ_2 za običajno tkane kompozite v (°)

θ	GP		CP		AP	
0°	0.00	0.00	0.00	0.00	0.00	0.00
15°	2.30	2.00	8.60	1.30	17.80	2.60
30°	5.00	3.50	12.80	5.80	26.70	12.30
45°	7.50	7.10	13.30	12.50	17.30	18.00
60°	3.10	3.30	8.50	20.60	9.80	22.50
75°	1.10	3.20	1.50	11.70	1.30	17.00
90°	0.00	0.00	0.00	0.00	0.00	0.00

5 CONCLUSION

All the materials showed a complex non-linear behavior.

- Force-displacement dependencies are non-linear even for the plain-weave material orientations of $\theta = 0^\circ$ and $\theta = 90^\circ$. Hardening was noticed in the case of carbon and aramid textiles (exhibiting a convex

load-displacement curve when zoomed) and softening (a concave curve) was noticed in the case of glass textile.

- Specimens made of aramid fibers reached the highest strength during the tests; on the other hand, glass-fiber specimens reached the lowest strength.
- Weave-locking phenomenon has significant impacts on the plain-weave orientations of $\theta = 45^\circ$ – plastic behavior of the tested materials was observed.
- Unsymmetrical results for the plain-weave composites are probably caused by an imperfect technology of manufacturing the textiles or by the preparation of the specimens.

Acknowledgements

This publication was supported by the project L01506 of the Czech Ministry of Education, Youth and Sports and by the project of University of West Bohemia SGS-2016-038.

6 REFERENCES

- ¹ R. Böhm, W. Hufenbach, Experimentally based strategy for damage analysis of textile-reinforced composites under static loading, *Composites Science and Technology*, 70 (2010) 9, 1330–1337, doi:10.1016/j.compscitech.2010.04.008
- ² T. Kroupa, P. Janda, R. Zemčík, Linear two scale model for determination of mechanical properties of textile composite material, *Mater. Technol.*, 46 (2012) 2, 97–101
- ³ ASTM Standard D 3039 / D 3039M – 08, 2008, Standard Test Method for Tensile Properties of Polymer Matrix Composite Materials, ASTM International, West Conshohocken, PA 19428–2959, 2003, www.astm.org
- ⁴ ASTM Standard D 3410 / D 3410M – 03, 2008, Standard Test Method for Compressive Properties of Polymer Matrix Composite Materials, ASTM International, West Conshohocken, PA 19428–2959, 2003, www.astm.org
- ⁵ N. Hamila, P. Boisse, Locking in simulation of composite reinforcement deformations, Analysis and treatment, *Composites Part A, Applied Science and Manufacturing*, 53 (2013), 109–117 doi:10.1016/j.compositesa.2013.06.001
- ⁶ T. Kroupa, K. Kunc, R. Zemčík, T. Mandys, Non-linear finite elements simulations of the tensile tests of textile composites, *Mater. technol.*, 49 (2015) 4, 509–515, doi:10.17222/mit.2014.117

DEFORMATION BEHAVIOUR OF A NATURAL-SHAPED BONE SCAFFOLD

OBNAŠANJE NARAVNO OBLIKOVANEGA OGRODJA KOSTI PRI DEFORMACIJI

**Daniel Kytýř^{1,2}, Tomáš Doktor^{1,2}, Ondřej Jiroušek¹, Tomáš Fila^{1,2},
Petr Koudelka^{1,2}, Petr Zlámal²**

¹Czech Technical University in Prague, Faculty of Transportation Sciences, Department of Mechanics and Materials, Konviktská 20,
110 00 Prague 1, Czech Republic

²Institute of Theoretical and Applied Mechanics, v.v.i., Academy of Sciences of the Czech Republic, Prosecká 76, 190 00 Prague 9,
Czech Republic
kytyr@fd.cvut.cz

Prejem rokopisa – received: 2014-08-11; sprejem za objavo – accepted for publication: 2015-05-07

doi:10.17222/mit.2014.190

The study aims at mechanical testing of an artificial bone structure in the form of a scaffold for the application in the repairs of trabecular bones after wounds or degenerative diseases. Such artificial construct has to conform to many requirements including biocompatibility, permeability properties and bone-integration characteristics. Recently, self-degradable bone scaffolds suitable for natural-bone-tissue ingrowth optimized with respect to mechanical properties and body-fluid flow have been considered as an alternative to allografts and autografts. Here, an analysis of deformation behaviour of a scaffold with a morphology identical to the natural bone is the first step in this task. In this work, the geometry and morphology of scaffold specimens produced with direct 3D printing were based on a 3D model derived from the X-ray-computed micro-tomography measurement of a real trabecular bone. The geometrical model was upscaled four times in order to achieve the optimum ratio between its resolution and the resolution of the 3D printer. For its biocompatibility and self-degradability, polylactic acid was used as the printing material. The mechanical characteristics were obtained from a series of uniaxial compression tests, with an optical evaluation of the strain field on the surfaces of the specimens. The acquired stress-strain curves were compared with the characteristics of a real trabecular bone obtained with time-lapse microtomography measurements, evaluated with the digital volumetric correlation method. The results show good correspondence of the stiffness values for both the natural and artificial bone specimens.

Keywords: bone scaffold, polylactic acid, additive manufacturing, compression loading, microtomography

Namen študije je mehansko preizkušanje umetnega ogrodja kosti za obnovo trabekularnih kosti po poškodbah ali degenerativnih boleznih. Tako umetno ogrodje mora ustrezati mnogim zahtevam, kot so biokompatibilnost, prepustnost in možnost vraščanja kostnega tkiva. Samo razgradljivo ogrodje kosti, primerno za naravno vraščanje kostnega tkiva, optimirano glede na mehanske lastnosti in toka telesnih tekočin, je bilo proučevano kot nadomestek za presajanje tujega ali lastnega tkiva. Prvi korak pri tej nalogi je analiza obnašanja ogrodja, z morfologijo podobno naravni kosti. V tem delu je bila geometrija in morfologija vzorčnega ogrodja izdelana z neposrednim tridimenzionalnim tiskanjem, na osnovi tridimenzionalnega modela, dobljenega z meritvami s pomočjo rentgenske tomografije realne trabekularne kosti. Geometrijski model je bil povečan štirikrat, da bi dobili optimalno razmerje med njegovo resolucijo in resolucijo tridimenzionalnega tiskalnika. Za biokompatibilnost in samo razgradljivost, je bila za tiskanje uporabljena polilaktična kislina. Mehanske značilnosti so bile dobljene z vrsto enoosnih tlačnih preizkusov in z optično oceno napetostnega polja na površini vzorcev. Pridobljene krivulje napetost-raztezek so bile primerjane z značilnostmi realne trabekularne kosti, ki so bile dobljene z zaporednimi mikrotomografskimi meritvami in ocenjene z digitalno volumetrično metodo korelacije. Rezultati kažejo dobro ujemanje togosti obeh vzorcev, tako naravne kot umetne kosti.

Ključne besede: ogrodje kosti, polilaktična kislina, tridimenzionalnega tiskanje, tlačno obremenjevanje, mikrotomografija

1 INTRODUCTION

The change in the lifestyle during the past decades (the so-called modern lifestyle characteristic caused by a lack of sufficient physical activities coupled with an improper type of nutrition) coupled with an increasing life expectancy in many countries caused a significant increase in health-care costs. Globally more than 30 % of women and 20 % of men in elderly age suffer from bone disorders. The increase is expected to double by 2020,¹ partially also due to an increased occurrence of obesity. Here, bone-tissue engineering and specifically designed implants with functionally graded properties represent a modern approach to the bone-repair process² with the goal to create an implant that is anatomically and

functionally compatible with the surrounding tissue.³ In the recent orthopaedic practice, repairs of defective bones have been most commonly carried out using autografts and allografts. Although used for many years, natural grafts possess several limitations and potentials for complications due to various influences including the donor-site morbidity, a loss of bone inductive factors, resorption during healing, anatomical variations, etc.⁴ To overcome these problems, implants in the form of an artificial bone represent an attractive alternative with a significant, though not yet fully exploited potential. In order to engineer such a synthetic scaffold with optimum characteristics, several factors and parameters have to be taken into account.⁵ Among such factors, the type of the cancellous bone, mechanical properties, the geometry⁶

and the expected transport phenomena⁷ are the most important for the design of a synthetic porous bone. Thus, with respect to the selected application (i.e., the location within the skeletal microarchitecture)⁸ stiffness and permeability properties have to be properly selected to precisely match the properties of the natural cancellous bone. Identification of the trabecular microstructure and comparison of deformation behaviour of the natural bone with the synthetic replication is the first step in the artificial-bone-structure optimization. A combination of radiological imaging methods and additive manufacturing was used for preparing a natural-shaped bone scaffold. A set of uniaxial compression tests were performed to obtain the scaffold loading response represented by stress-strain diagrams. The strain calculation was based on image-registration techniques, digital image correlation (DIC) for optical data and digital volume correlation (DVC) for tomographic data.

2 MATERIALS AND METHODS

2.1 Natural bone sample

Trabecular bone tissue is a biological material consisting of basic structural elements called trabeculae. Individual trabeculae are joined into a network with a high porosity (50–90 %) naturally adapted to distribute and dissipate the energy from external loads. For the purpose of this study, original natural bone samples were prepared by drilling them from the caput femoris of 42-year and 72-year-old male donors. The samples with a diameter of 5 mm and a height of approximately 10 mm were put into an ultrasonic bath to remove the remaining bone marrow. Formaldehyde solution was used to avoid biological degradation and to ensure sample preservation. The upper and bottom parts of the samples were embedded in a 2-component epoxy resin and after the hardening, two plan-parallel baseplates were cut with a precise saw. This preparation procedure minimises the risk of a rapid collapse of the bone

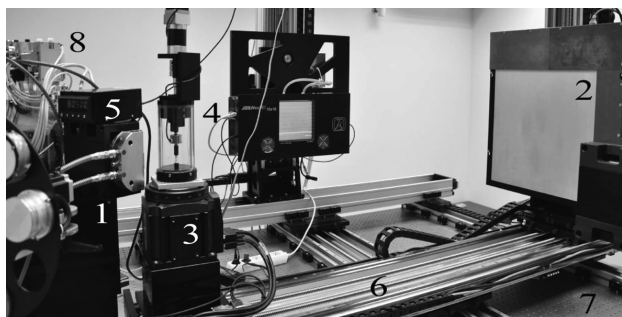


Figure 1: Microtomography set-up: 1) X-ray source, 2) detector, 3) rotary stage, 4) loading device, 5) load-cell controller, 6) linear stage, 7) anti-vibration table and 8) cooling

Slika 1: Naprava za mikrotomografijo: 1) vir rentgenskih žarkov, 2) detektor, 3) nosilec za rotiranje, 4) naprava za obremenjevanje, 5) nadzor pri obremenjevanju, 6) linearni nosilec, 7) antivibracijska mizica in 8) hlajenje

samples under loading due to a crack damage of the microstructure.

2.2 Microtomography measurement

In order to acquire a geometrically precise model of the internal trabecular structure, a custom-designed microtomography device (**Figure 1**) was employed. The irradiation of the sample was performed using a micro-focus X-ray tube with a high-resolution transmission target (XWT 160, X-Ray Worx, Germany). Radiograms were acquired using a large (410 mm × 410 mm) X-ray flat-panel scintillating detector (XRD 1622, PerkinElmer Inc., USA) with an effective resolution of 2048 pixels × 2048 pixels with a 200 μm pitch. A custom-designed loading device composed of a stiff frame with a low absorption of X-rays was designed specially for the microtomography under loading. Force was gradually applied on the specimens using the translation stage (7T173-20, Standa Ltd., Lithuania) with a 2 μm tracking accuracy and the applied force was measured using a small-scale force transducer (U9b, HBM, Germany) with a nominal capacity of 500 N. Before the loading procedure, a sample was scanned in 720 projections (acquisition 2 × 0.5 s) with an angular step of 0.5° to obtain a detailed geometrical model of the microstructure. Then a time-lapse tomography (tomography under loading) measurement was performed to obtain the information about the spatial strain distribution during the loading.⁹ The specimen was incrementally loaded with 1 % increment up to the total deformation of 6 %. After each loading step, microtomography was performed to capture the deformed microstructure. Acquisitions with 180 projections at 2° were used for this purpose to reduce the computational costs of the reconstruction procedure. The spatial strain distribution was assessed utilizing DVC, which is an extension of the image-registration techniques to three dimensions.¹⁰

Linearization of the attenuation range (a beam-hardening correction) was applied to reduce the noise and improve the contrast of individual projections.¹¹ Due to a high porosity of the samples and a small thickness of the trabeculae (approximately 200 μm), the cone-beam reconstruction algorithm¹² was used to eliminate the distortion of the reconstructed data caused by the divergent nature of the X-ray beam.

2.3 Polylactic acid

Polylactic acid ($C_3H_4O_2$)_n (PLA) is a biodegradable thermoplastic polyester derived from biomass and produced from the starch of various crop plants (e.g., corn, cereals, potatoes, etc.). The material properties of PLA are comparable with those of synthetic plastics, but they are achieved at significantly lower energetic requirements.¹³ PLA is highly biocompatible¹⁴ and suitable for the use in 3D printers making an attractive solution for endoprosthesis.

2.4 PLA bulk testing

The production of the samples was carried out using a Profi3Dmaker (Aroja, Czech Republic) 3D printing device equipped with a 200 μm printing nozzle, operated in the rapid additive-manufacturing mode with a slice resolution of 250 μm . The material properties of the PLA printer filament are not guaranteed by the producer and the influence of the printing process on the material characteristics is unknown; therefore, cylinder samples with dimensions of 20 mm \times 28 mm (diameter, height) were tested in different printing modes to choose the ideal printing set-up for the trabecular-bone replica manufacturing. The samples were produced at 100 %, 70 % and 50 % filling levels. With all the filling levels, the products consisted of a 500 μm shell and a core with a defined filling amount. In the case of a reduced filling amount, the core was created using a random-oriented fibre meshwork with a defined overall porosity. To verify the declared values of the filling level, the samples were weighed with a laboratory scale.

2.5 Bone scaffold development

The reconstructed tomographic-image data were subjected to the standard post-processing methods (including thresholding and identification of the connected components) using custom segmentation and modelling software to obtain binary spatial-image data without isolated fragments. Then the marching cube algorithm¹⁵ was used to extract the polygonal mesh of an isosurface from the three-dimensional scalar-image data (as depicted in **Figure 2**). Subsequently, this polygonal mesh was carefully smoothed and decimated in an iterative manner to obtain a surface suitable for 3D printing. Because of the technical parameters of the available 3D printer, the model was upscaled three times to ensure a proper geometry of the printed replica.

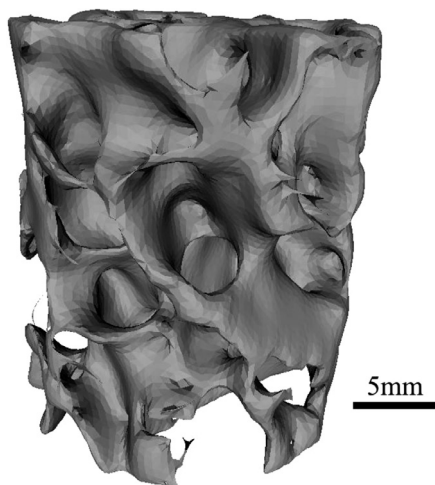


Figure 2: Model of trabecular-bone microstructure used for additive manufacturing

Slika 2: Model mikrostrukture trabekularne kosti, uporabljen pri tridimenzionalnem tiskanju

2.6 Compression tests

The compression test of both bulk and porous specimens was performed in a displacement-controlled loading mode using a custom-designed uniaxial loading device with a loading capacity of up to 2 kN. The load-bearing frame was designed as an open cylinder with expanded ends mounted on a stiff metallic plate manufactured from polyamide-imide thermoplastic. The displacement of the loading platens was controlled by stepper motor SX17-1705 (Microcon, Czech Republic) attached to a CPU 17A 100 harmonic drive (Harmonic Drive, USA) with a transmission ratio of 250 : 1 leading to an accuracy of displacement in the order of micrometers. High-accuracy load cell U9b (HBM, Germany) was connected to an OM 502T (Orbit Merret, Czech Republic) programmable indicator. The samples were loaded up to a 20 % deformation at a constant loading rate of 20 $\mu\text{m s}^{-1}$. Strains were derived from optically measured deformations, evaluated with the DIC algorithm. For this purpose, images of the loaded specimens were acquired with a high-resolution CCD camera (Manta G-504B, AVT, Germany) attached to telecentric zoom lens TCZR 072 (Opto Engineering, Italy). An in-house software based on the GNU/Linux real-time operation software and LinuxCNC open-source project was used to control the experiments. For the DIC procedure, a custom Matlab tool¹⁶ based on the Lucas-Kanade algorithm¹⁷ was used.

3 RESULTS

The material properties of bulk PLA were measured based on the compression tests of the PLA solid cylindrical samples at different levels of filling. Stress-strain curves obtained from the force record and optically measured strain are depicted in **Figure 3**. From the slope of the linear parts of the stress-strain diagrams, Young's moduli presented in **Table 1** were estimated.

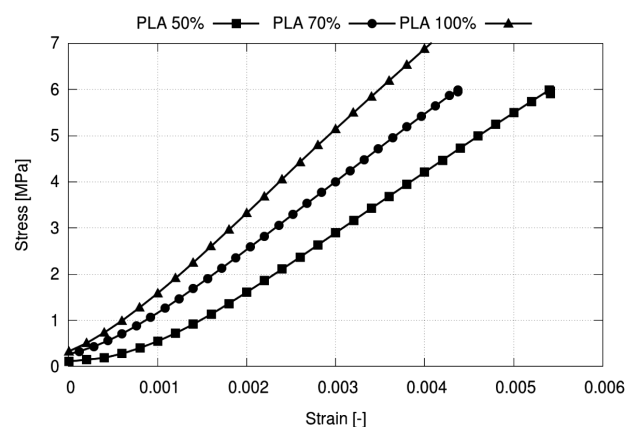


Figure 3: Stress-strain diagram of the PLA bulk material with different levels of filling

Slika 3: Obremenitveni diagram PLA materiala z različnimi stopnjami polnjenja

Table 1: Properties of PLA used for additive manufacturing**Tabela 1:** Lastnosti PLA, ki se uporabljajo pri tridimenzionalnem tiskanju

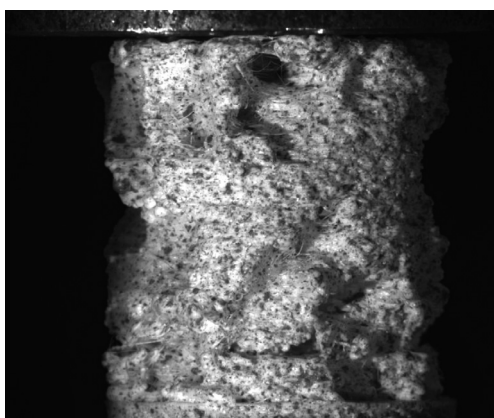
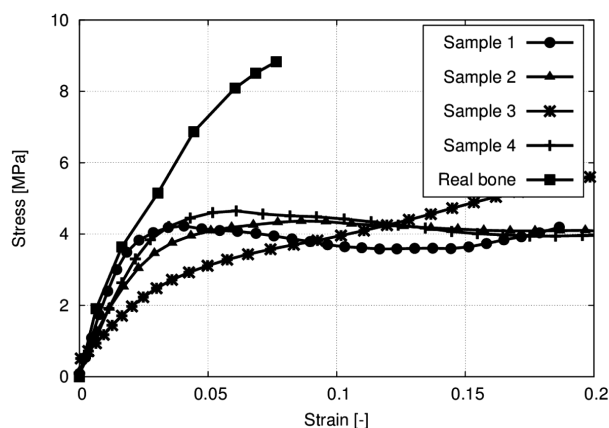
Sample	Filling (%)	Weight (g)	<i>E</i> (GPa)
1	100	15.300	2.396
2	70	11.937	1.864
3	50	9.160	1.380

Because of a low PLA elastic modulus (compared to the bone tissue) and a rod- or shell-like shape of the replicated inner structure, the PLA scaffold was manufactured only in the full filling mode. Four identical PLA specimens representing the natural-bone-shaped upscaled scaffold were used for the compression test. For the optical measurement of the deformation of the complex sample surface, the data acquired from four different loading scenes (rotated by 90°) were evaluated. A sample collapsed after the compression test is depicted in **Figure 4**.

Deformation behaviour of the PLA models of the trabecular structure in comparison with the stress-strain curves of the natural bone structure is depicted in **Figure 5**. Good agreement between the elastic parts of both materials was observed. The sample with a natural bone volume fraction (bone volume/total volume = 25 %) exhibits a stiffness similar to the real-bone structure. Therefore, PLA is suitable for other bone-scaffold developments based on regular cells.

4 CONCLUSION

Compression tests of the natural-shaped additive-manufactured PLA samples of the trabecular-bone structure were performed to assess deformation behaviour of the homogenous solid phase of the synthetic material. The results will be used for designing an artificial bone structure with effective mechanical properties, close to the ones of a real, healthy bone. A low bone volume/total volume ratio of the real-bone structure provides a sufficient reserve for increasing the strength of the scaffold

**Figure 4:** Example of a PLA scaffold collapsed after the compression test**Slika 4:** Primer porušenega PLA kostnega ogrodja po tlačnem preizkusu**Figure 5:** Stress-strain diagrams for the PLA-additive-manufactured and natural bone**Slika 5:** Diagram napetost-raztezek za 3D tiskano in naravno kost

by increasing its relative density. A higher cross-section of the basic structure elements (which would still enable the tissue ingrowth) may reduce the required resolution of manufacturing devices. Additive manufacturing of biodegradable complex structures is a promising way for the bone-scaffold development. Based on these findings, the artificial bone structure used for the replacements of trabecular bones will be optimized with respect to structural, mechanical and permeability properties.

Acknowledgements

The research was supported by the Grant Agency of the Czech Technical University in Prague (grant No. SGS15/225/OHK2/3T/16) and by institutional support RVO: 68378297.

5 REFERENCES

- 1 U.S. Department of Health and Human Services, Bone Health and Osteoporosis: A Report of the Surgeon General, Rockville 2004
- 2 H. L. M. Bao, E. Y. Teo, M. S. K. Chong, Y. Liu, M. Choolani, J. K. Y. Chan, *Advances in Bone Tissue Engineering, Regenerative Medicine and Tissue Engineering*, InTech, Rijeka 2013, doi:10.5772/55916
- 3 H. Razi, S. Checa, K. Schaser, G. N. Duda, Shaping scaffold structures in rapid manufacturing implants: A modeling approach toward mechano-biologically optimized configurations for large bone defect, *Journal of Biomedical Materials Research, Part B: Applied Biomaterials*, 100 (2012) 7, 1736–1745, doi:10.1002/jbm.b.32740
- 4 A. R. Vaccaro, K. Chiba, J. G. Heller, T. C. Patel, J. S. Thalgott, E. Truumees, J. S. Fischgrund, M. R. Craig, S. C. Berta, J. C. Wang, Bone grafting alternatives in spinal surgery, *Spine Journal*, 2 (2002) 3, 206–215, doi:10.1016/S1529-9430(02)00180-8
- 5 A. Gantar, L. P. Da Silva, J. M. Oliveira, A. P. Marques, V. M. Corrello, S. Novak, R. L. Reis, Nanoparticulate bioactive-glass-reinforced gellan-gum hydrogels for bone-tissue engineering, *Materials Science and Engineering C*, 43 (2014), 27–36, doi:10.1016/j.msec.2014.06.045
- 6 V. P. W. Shim, L. M. Yang, J. F. Liu, V. S. Lee, Characterisation of the dynamic compressive mechanical properties of cancellous bone from the human cervical spine, *International Journal of Impact Engineering*, 32 (2005) 1–4, 525–540, doi:10.1016/j.ijimpeng.2005.03.006

- ⁷ S. S. Kohles, J. B. Roberts, M. L. Upton, C. G. Wilson, L. J. Bonassar, A. L. Schlichting, Direct perfusion measurements of cancellous bone anisotropic permeability, *Journal of Biomechanics*, 34 (2001) 9, 1197–1202, doi:10.1016/S0021-9290(01)00082-3
- ⁸ E. F. Morgan, H. H. Bayraktar, T. M. Keavenyemail, Trabecular bone modulus-density relationships depend on anatomic site, *Journal of Biomechanics*, 36 (2003) 7, 897–904, doi:10.1016/S0021-9290(03)00071-X
- ⁹ O. Jirousek, P. Zlamal, D. Kytýř, M. Kroupa, Strain analysis of trabecular bone using time-resolved X-ray microtomography, *Nuclear Instruments and Methods in Physics Research, Section A: Accelerators, Spectrometers, Detectors and Associated Equipment*, 633 (2011) 1, 148–151, doi:10.1016/j.nima.2010.06.151
- ¹⁰ O. Jirousek, I. Jandjsek, D. Vavřík, Evaluation of strain field in microstructures using micro-CT and digital volume correlation, *Journal of Instrumentation*, 6 (2011) 1, C01039, doi:10.1088/1748-0221/6/01/C01039
- ¹¹ D. Vavřík, J. Jakubek, Radiogram enhancement and linearization using the beam hardening correction method, *Nuclear Instruments and Methods in Physics Research Section A: Accelerators, Spectrometers, Detectors and Associated Equipment*, 607 (2009) 1, 212–214, doi:10.1016/j.nima.2009.03.156
- ¹² L. A. Feldkamp, L. C. Davis, J. W. Kress, Practical cone-beam algorithm, *Journal of the Optical Society of America A*, 1 (1984) 6, 612–619
- ¹³ A. P. Mathew, K. Oksman, M. Sain, Mechanical properties of biodegradable composites from poly lactic acid (PLA) and microcrystalline cellulose (MCC), *Journal of Applied Polymer Science*, 97 (2005) 5, 2014–2025, doi:10.1002/app.21779
- ¹⁴ J. M. Anderson, M. S. Shive, Biodegradation and biocompatibility of PLA and PLGA microspheres, *Advanced Drug Delivery Reviews*, 28 (1997) 1, 5–24, doi:10.1016/S0169-409X(97)00048-3
- ¹⁵ W. E. Lorensen, H. E. Cline, Marching cubes: A high resolution 3D surface construction algorithm, *ACM SIGGRAPH Computer Graphics*, 21 (1987) 1, 163–169
- ¹⁶ I. Jandjsek, J. Valach, D. Vavřík, Optimization and Calibration of Digital Image Correlation method, *Proc. of Experimental Stress Analysis, Olomouc 2010*, 121–126
- ¹⁷ B. D. Lucas, T. Kanade, An iterative image registration technique with an application to stereo vision, *Proc. of the 7th International Joint Conference on Artificial Intelligence – Volume 2, San Francisco 1981*, 674–679

PRINTED MICROSTRIP LINE-FED PATCH ANTENNA ON A HIGH-DIELECTRIC MATERIAL FOR C-BAND APPLICATIONS

TISKANA MIKROTRAKASTA LINIJSKO NAPAJANA KRPASTA ANTENA NA VISOKO DIELEKTRIČNEM MATERIALU ZA UPORABO V C-PASU

**Md. Moinul Islam¹, Mohammad Rashed Iqbal Faruque¹, Mohd Fais Mansor²,
Mohammad Tariqul Islam²**

¹Universiti Kebangsaan Malaysia, Complex Penyelidikan Building, Centre for Space Science Angkasa, 43600 UKM, Bangi, Selangor D. E., Malaysia

²Universiti Kebangsaan Malaysia, Department of Electrical, Electronic & Systems Engineering, 43600 UKM, Bangi, Selangor D. E., Malaysia
mmoislam@yahoo.com

Prejem rokopisa – received: 2014-08-15; sprejem za objavo – accepted for publication: 2015-03-11

doi:10.17222/mit.2014.199

A printed microstrip line-fed patch antenna for C-band applications is presented, using a high-dielectric material. The proposed antenna dimensions are $0.53 \lambda \times 0.53 \lambda \times 0.02 \lambda$ and it is fed by a microstrip line. The antenna outline and electromagnetic analysis were done with the help of a commercially available computer-aided EM simulator. This antenna initiates three resonances at 4.64 GHz, 5.52 GHz, and 6.34 GHz with the average gains of 2.68 dBi, 6.02 dBi and 4.83 dBi, respectively, covering the entire frequency bands. The overall performance analysis and a nearly omnidirectional radiation pattern prove that the proposed antenna is promising for C-band applications.

Keywords: C-band, dielectric material, microstrip line feeding

Predstavljena je tiskana mikrotrakasta, linijsko napajana, krpasta antena za uporabo v C-pasu, z uporabo visoko dielektričnega materiala. Predlagana dimenzija antene je $0,53 \lambda \times 0,53 \lambda \times 0,02 \lambda$, ki je napajana z linijo mikrotraku. Oris antene in elektromagnetska analiza sta bili izvršeni s pomočjo komercialno razpoložljivega in računalniško podprtega EM simulatorja. Ta antena sproži tri resonance pri 4,64 GHz, 5,52 GHz in 6,34 GHz, s povprečno sposobnostjo 2,68 dBi, 6,02 dBi in 4,83 dBi pri pokrivanju vseh frekvenčnih pasov. Analiza zmogljivosti in skoraj vsesmerna slika sevanja kažeta, da predlagana antena obeta dobro uporabo v C-pasu.

Ključne besede: C-pas, dielektrični material, linijsko napajanje z mikrotrakom

1 INTRODUCTION

Currently, the microstrip patch antenna is a milestone in the wireless communication system and it continues to fulfill the changing requirements of the new-generation antenna technology. Microstrip patch antennas are widely utilized in the present wireless communication system because of their low profile, light weight, conformal design, low cost, and because they are easy to fabricate and integrate. Advances in wireless communications have initiated remarkable demands. Antennas are used for a wide range of cellular mobile phones in the current society, causing concerns about their harmful radiation.¹⁻⁵ Many researches were done, covering the entire C-band and many techniques and methods are stated in the reference literature.

A hexagonal scrimp-horn antenna with different aperture sizes was proposed for operating in C-band applications.⁶ A modified dual-band CPW-fed antenna was proposed for a WLAN-band application on a thin substrate.⁷ A broadband planar monopulse antenna was presented to increase the impedance bandwidth for C-band applications, where a monopulse comparator was

used as the sum-difference feed network.⁸ A rectangular slot antenna with a U-shaped strip was proposed for a dual broadband operation in WLAN applications.⁹ A compact broadband slot antenna with a circular polarization was proposed for C-band applications, where two rectangular stubs are embedded to excite two orthogonal E vectors in the feedline structure.¹⁰

In this paper, a printed microstrip line-fed patch antenna with a high-dielectric material that attains a compact triple-resonant profile due to a nearly omnidirectional radiation, high gain and a reasonable current distribution is proposed. This line-fed antenna is made of circular radiating patches with a partial ground plane generating three resonances for C-band applications. The antenna is smooth, with a simple design and comfortable fabrication. The proposed line-fed antenna generates three resonances to cover C-band applications. The results are impedance bandwidth values of (160, 100 and 160) MHz at three resonances on the C-band. Due to a double Ω -shaped radiating patch with a partial ground, nearly omnidirectional radiation properties are realized over the entire operating bands with a reasonable gain.

This line-fed antenna with a high-dielectric material is very effective for C-band applications.

2 ANTENNA STRUCTURES

The design of the proposed antenna is indicated in **Figure 1**. The antenna comprises of a double Ω -shaped patch and a partial ground. The design procedure begins with a radiating patch with a substrate, a ground plane and a feed line. It is printed on a ceramic-filled bioplastic substrate with a relative permittivity of 15 and a relative permeability of 1. The overall antenna dimensions are 40 mm \times 40 mm \times 1.2 mm. An SMA (Sub-Miniature version A) connector is used for providing a 50 Ω impedance and it is attached at the end of the antenna feeding.

Figure 2 exhibits the structure of the substrate material. This sandwich-structured substrate material was generated using ceramic powder and bioplastic. The selected ceramic powder was sintered with a polymeric binder using the polymeric sponge method. A 9.8 ml (0.25) bioplastic sheet was included. This bioplastic sheet was obtained from organic biomass sources, such as cornstarch, vegetable oil and palm oil, and used as the ceramic cover. The three-layer bioplastic-ceramic-bioplastic sandwich structure was laminated using 35 μ m of copper foil. The characteristics of this substrate material are low cost, ease of fabrication, design flexibility and availability. For this reason, a high-dielectric material is preferred for the antenna design.

Two Ω -shaped circular slots were cut from the copper patch with a partial ground. In this way, the proposed line-fed patch antenna was achieved. Three resonant frequencies of (4.64, 5.52 and 6.34) GHz were obtained, continuously adjusting the length, the width and the slots of the proposed antenna. Here, the

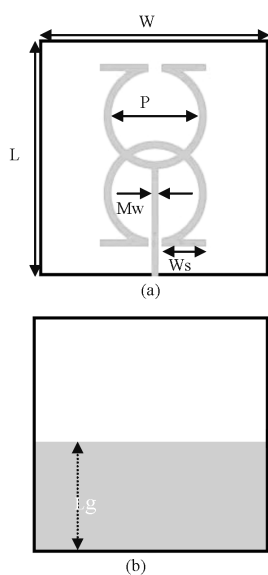


Figure 1: Proposed C-band antenna: a) front view, b) back view

Slika 1: Predlagana antena za C-pas: a) pogled spredaj, b) pogled zadaj

microstrip line is used to provide the feeding to the proposed antenna. The length and width of the patch antenna can be calculated from Equations (1) and (2).¹¹ L and W are the length and width of the patch, c is the velocity of light, ϵ_r is the dielectric constant of the substrate, f_0 is the target center frequency, and ϵ_e is the effective dielectric constant:

$$W = \frac{c}{2f_0} \sqrt{\frac{\epsilon_r + 1}{2}} \quad (1)$$

$$L = \frac{c}{2f_0 \sqrt{\epsilon_r}} - 2\Delta l \quad (2)$$

Finally, the optimum dimensions were determined as follows: $L = 40$ mm, $W = 40$ mm, $P = 20$ mm, $M_w = 2.5$ mm, $W_s = 8$ mm, and $L_g = 19$ mm.

3 RESULTS AND DISCUSSION

The simulated return loss of the proposed antenna is illustrated in **Figure 3**. Return losses of -20.21 dB, -19.58 dB and -16.70 dB were acquired at three resonant frequencies of (4.64, 5.52 and 6.34) GHz, respectively.

We obtained the 160 MHz bandwidth with the 1st resonant frequency, 100 GHz with the 2nd and 1.60 MHz with the 3rd frequency. The mutual coupling effect was increased with the lower frequency; as a result, the bandwidth was small with the 1st and 2nd resonances. On the other hand, the bandwidth was broadened due to the suppressed mutual coupling effect. These bandwidths

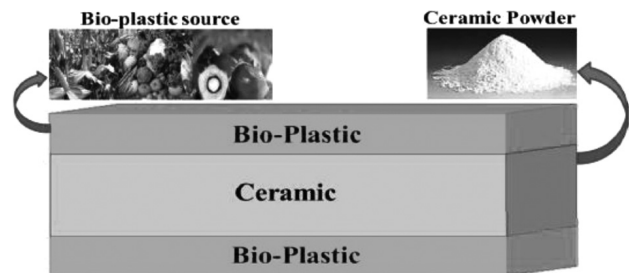


Figure 2: Structure of the substrate material¹²

Slika 2: Struktura materiala podlage¹²

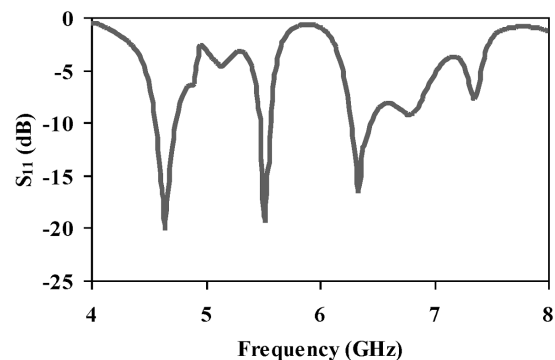


Figure 3: Proposed C-band antenna return loss

Slika 3: Povratne izgube, predlagane antene za C-pas

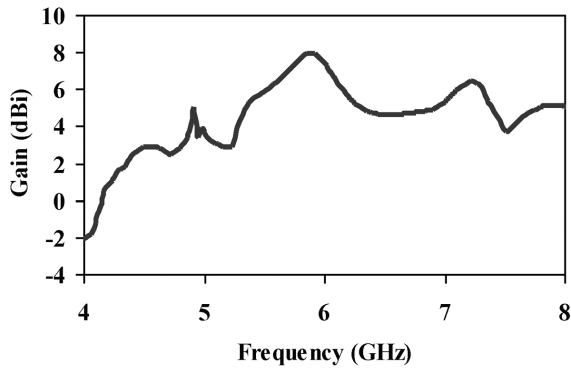


Figure 4: Proposed C-band antenna gain
Slika 4: Sposobnost predlagane antene za C-pas

were generated at the operating frequencies throughout the entire C-band application.

The average gain of the proposed antenna is shown in **Figure 4**. The average gains of (2.68, 6.02 and 4.83) dBi are achieved in the operating frequency bands of (4.64, 5.52 and 6.34) GHz, respectively. The used dielectric substrate material controls the mutual coupling effect and, as a result, the antenna gain is widened. It can be observed that the antenna gain was considerably increased with the incorporation of this high-dielectric material in the lower and upper bands, compared to the existing antennas.

The voltage standing wave ratio (*VSWR*) of the proposed antenna is plotted in **Figure 5**. The value of the *VSWR* is less than 2, as clearly seen on the graph. It is the desired value.

Figure 6 exhibits the result of the radiation efficiency of the proposed patch antenna. The radiation efficiency is 94 % with the 1st resonance, 90.06 % with the 2nd resonance and 94.08% with the 3rd resonance. This efficiency is broadly appropriate for C-band applications. It is considerable in comparison with the existing ones. It is obtained using a high-dielectric material for the proposed antenna and this antenna is perfect for C-band applications.

The surface-current distribution of the proposed patch antenna is demonstrated in **Figure 7**. The arrow sign is applied to denote the flow of the current distribution. From the graph, it can be easily observed that the

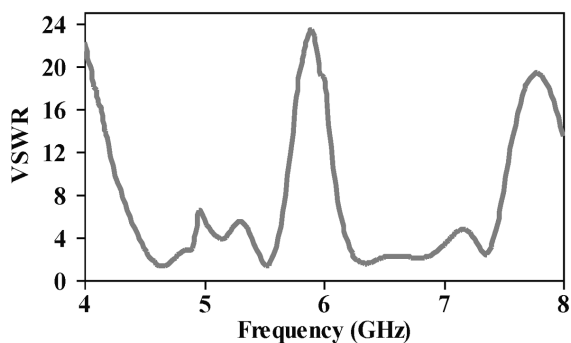


Figure 5: Proposed C-band antenna *VSWR*
Slika 5: *VSWR* predlagane antene za C-pas

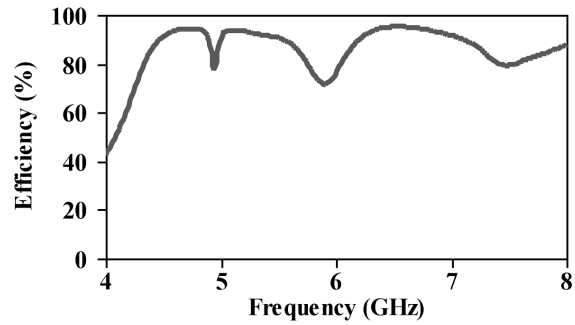


Figure 6: Proposed C-band antenna efficiency
Slika 6: Učinkovitost predlagane antene za C-pas

current flow is maximum at the microstrip line and the lower Ω -shaped slot, at 4.64 GHz. At 5.52 GHz, the upper Ω -shaped slot and the microstrip line show the maximum current. At 6.34 GHz, the parts of the intersection between double Ω -shaped slots control the maximum current flow. Due to the high-dielectric substrate material, the overall surface-current distribution is smooth and sharp. As a result, the mutual coupling effect is under consideration and it is controlled in the case of the proposed patch antenna.

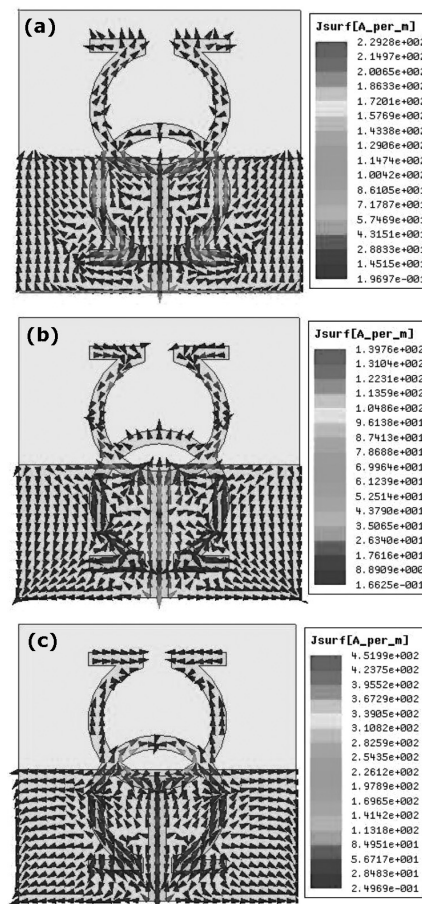


Figure 7: Surface current of the proposed C-band antenna at: a) 4.64 GHz, b) 5.52 GHz and c) 6.34 GHz

Slika 7: Tok na površini predlagane antene za C-pas pri: a) 4,64 GHz, b) 5,52 GHz in c) 6,34 GHz

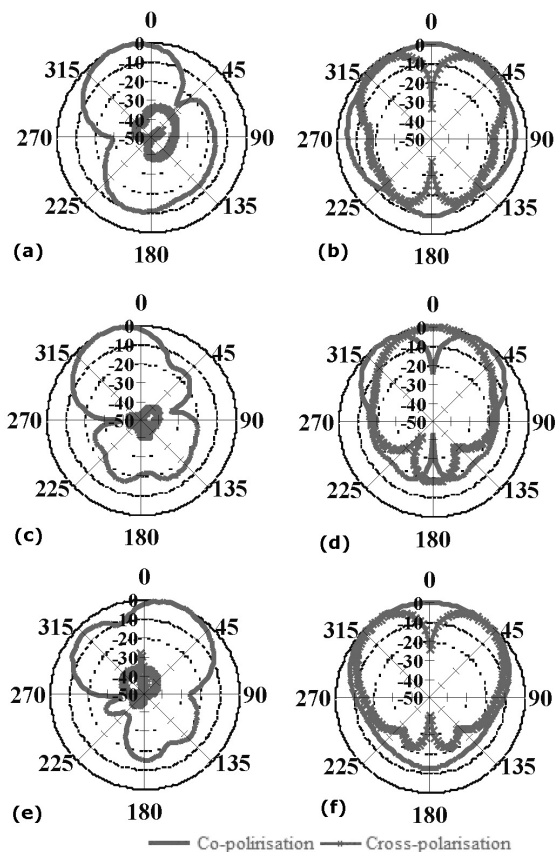


Figure 8: Radiation patterns: a) E-plane at 4.64 GHz, b) H-plane at 4.64 GHz, c) E-plane at 5.52 GHz, d) H-plane at 5.52 GHz, e) E-plane at 6.34 GHz and f) H-plane at 6.34 GHz

Slika 8: Sevalni diagrami: a) E-ravnina pri 4,64 GHz, b) H-ravnina pri 4,64 GHz, c) E-ravnina pri 5,52 GHz, d) H-ravnina pri 5,52 GHz, e) E-ravnina pri 6,34 GHz in f) H-ravnina pri 6,34 GHz

The radiation patterns of the proposed antenna on the E-plane and H-plane, at resonant frequencies of (4.64, 5.52 and 6.34) GHz are shown in **Figure 8**. It is shown from the results that significant, nearly omnidirectional radiation patterns are acquired along the H-plane and E-plane, respectively. The cross-polarization is low on the E-plane at all the resonances; on the other hand, the cross-polarization is high on the H-plane. The cross-polarization is lower than the co-polarization at all the resonances, leading to omnidirectional or nearly omnidirectional radiation characteristics. As a result, the radiation pattern of the proposed patch antenna is almost durable for C-band applications.

4 CONCLUSION

The article presents a printed line-fed patch antenna with a high-dielectric material appropriate for C-band applications. It uses a double Ω -shaped patch instead of a conventional patch with a view to obtaining a triple band operation. The microstrip line-fed antenna with a high-dielectric material was designed and simulated using the HFSS software, while the current-distribution

plots were made to verify the proposed track. The simulation results indicate good characteristics. Consequently, the proposed microstrip line-fed antenna with a high-dielectric material can be appropriate for C-band applications.

Acknowledgement

This work was supported by the Ministry of Education (MOE) under Fundamental Research Grant Scheme Top Down, Code: FRGS TOP DOWN/2014/TK03/UKM/01/1.

5 REFERENCES

- ¹ M. R. I. Faruque, M. T. Islam, N. Misran, Evaluation of specific absorption rate (SAR) reduction for PIFA antenna using metamaterials, *Frequenz*, 64 (2010) 7–8, 144–149, doi:10.1515/FREQ.2010.64.7-8.144
- ² M. M. Islam, M. R. I. Faruque, W. Hueyshin, J. S. Mandeep, T. Islam, A double inverted F-shape patch antenna for dual-band operation, *International Journal of Antennas and Propagation*, 8 (2014), doi:10.1155/2014/791521
- ³ M. M. Islam, M. T. Islam, M. Samsuzzaman, M. R. I. Faruque, N. Misran, M. F. Mansor, A Miniaturized Antenna with Negative Index Metamaterial Based on Modified SRR and CLS Unit Cell for UWB Microwave Imaging Applications, *Materials*, 8 (2015) 2, 392–407, doi:10.3390/ma8020392
- ⁴ M. R. I. Faruque, M. T. Islam, B. Yatim, M. A. M. Ali, Analysis of the effects of metamaterials on the radio-frequency electromagnetic fields in the human head and hand, *Mater. Tehnol.*, 47 (2013) 1, 129–133
- ⁵ M. M. Islam, M. R. I. Faruque, M. T. Islam, A Compact 5.5 GHz Band-Rejected UWB Antenna Using Complementary Split Ring Resonators, *The Scientific World Journal*, 2014 (2014) 10, doi:10.1155/2014/528489
- ⁶ S. A. Muhammad, A. Rolland, H. D. Samsul, R. Sauleau, H. Legay, Hexagonal-shaped broadband compact scrimp horn antenna for operation in C-band, *IEEE Antennas and Wireless Propagation Letters*, 11 (2012), 842–845, doi:10.1109/LAWP.2012.2208259
- ⁷ C. Yoon, W. J. Lee, S. P. Kang, S. Y. Kang, H. C. Lee, H. D. Park, A planar CPW-fed slot antenna on thin substrate for dual-band operation of WLAN applications, *Microwave and Optical Technology Letters*, 51 (2009), 2799–2802, doi:10.1002/mop.24742
- ⁸ Z. W. Yu, G. M. Wang, C. X. Zhang, A broadband planar monopulse antenna array of C-band, *IEEE Antennas and Wireless Propagation Letters*, 8 (2009), 1325–1328, doi:10.1109/LAWP.2009.2038077
- ⁹ J. W. Wu, H. M. Hsiao, J. H. Lu, S. H. Chang, Dual broadband design of rectangular slot antenna for 2.4 and 5 GHz wireless communication, *Electronics Letters*, 40 (2004) 23, 1461–1463, doi:10.1049/el:20046873
- ¹⁰ S. Mohammadi, J. Nourinia, J. Pourahmadazar, M. Shokri, Compact broadband circularly polarized slot antenna using two linked elliptical slots for C-band applications, *IEEE Antennas and Wireless Propagation Letters*, 12 (2013), 1094–1097, doi:10.1109/LAWP.2013.2280457
- ¹¹ M. M. Islam, M. T. Islam, M. R. I. Faruque, Dual-band operation of a microstrip patch antenna on a duroid 5870 substrate for Ku- and K-bands, *The Scientific World Journal*, 2013 (2013) 10, doi:10.1155/2013/378420
- ¹² M. T. Islam, M. H. Ullah, M. J. Singh, M. R. I. Faruque, A new metasurface superstrate structure for antenna performance enhancement, *Materials*, 6 (2013) 8, 3226–3240, doi:10.3390/ma6083226

COMPRESSIVE PROPERTIES OF AUXETIC STRUCTURES PRODUCED WITH DIRECT 3D PRINTING

STISKANJE STRUKTUR MATERIALOV Z NEGATIVNIM POISSONOVIM RAZMERJEM, PROIZVEDENIH Z NEPOSREDNIM TRIDIMENZIONALNIM TISKANJEM

Petr Koudelka^{1,2}, Ondřej Jiroušek², Tomáš Fíla^{1,2}, Tomáš Doktor^{1,2}

¹Institute of Theoretical and Applied Mechanics, Academy of Sciences of the Czech Republic, Prosecká 76, 190 00 Prague, Czech Republic

²Czech Technical University in Prague, Faculty of Transportation Sciences, Konviktská 20, 110 00 Prague 1, Czech Republic
jirousek@fd.cvut.cz

Prejem rokopisa – received: 2014-08-19; sprejem za objavo – accepted for publication: 2015-04-24

doi:10.17222/mit.2014.204

In the presented paper, three types of auxetic structures were produced with direct 3D printing and their compressive mechanical properties were tested. Samples were prepared from acrylic material suitable for high-resolution direct printing. Three different structures exhibiting in-plane and volumetric negative strain-dependent Poisson's ratio were selected for the analysis: two-dimensional missing-rib cut, two-dimensional inverted (re-entrant) honeycomb and three-dimensional inverted (re-entrant) honeycomb. The samples were subjected to quasi-static compression, from which stress-strain relationships were established. For a proper strain evaluation, digital-image correlation was applied to measure full-field displacements on the sample surfaces. From the displacement fields, true strain/true stress curves were derived for each sample. Furthermore, for each structure a three-dimensional FE model was developed using beam elements and subjected to identical loading conditions. Then, experimentally obtained stress-strain relationships were compared with numerically obtained results. For all the tested auxetic structures, the compressive behaviour was predicted well by the FE models. This demonstrates that parametric FE models can be used to tune the design parameters of the structures with a negative Poisson's ratio to optimize their overall properties.

Keywords: auxetics, cellular materials, quasi-static testing, finite-element method

V prispevku so predstavljene tri vrste struktur materialov z negativnim Poissonovim razmerjem, ki so proizvedene z neposrednim tridimenzionalnim tiskanjem. Preizkušene so bile njihove mehanske lastnosti pri stiskanju. Vzorci so bili pripravljene iz akrilnih materialov, ki so primerni za visoko resolucijsko neposredno tiskanje. Za analizo so bile izbrane tri različne strukture, ki prikazujejo negativno odvisno Poissonovo razmerje v ravnini in v prostoru: dvodimenzionalni prerez z manjkajočim rebrom, dvodimenzionalni obrnjeni (navznoter usmerjeni) vzorec satovja in tridimenzionalni obrnjeni (navznoter usmerjeni) vzorec satovja. Vzorci so bili izpostavljeni kvazi-statičnem stiskanju pri katerem smo ugotavljali razmerja sile – raztezek. Za primerno oceno sile obremenitve je bila uporabljena metoda korelacije digitalne slike in s tem izmerjeni odmiki na površini vzorcev. Glede na te odmike so bile za vsak vzorec izpeljane dejanske obremenitvene krivulje. Nadalje je bil za vsako strukturo izdelan tridimenzionalni FE model, z uporabo matematičnega modela podpornih struktur in izpostavljen identičnim pogojem obremenitve. Nato smo primerjali eksperimentalno pridobljena razmerja med silo in obremenitvijo, z računsko pridobljenimi rezultati. S pomočjo primerjalnih diagramov sile in raztezka lahko ugotovimo, da FE modeli dobro napovedujejo obnašanje pri stiskanju vseh preizkušenih struktur z negativnim Poissonovim razmerjem. To prikazuje možnost uporabe parametričnih FE modelov za prilagoditev zasnovnih parametrov struktur z negativnim Poissonovim razmerjem za optimiziranje njihovih splošnih lastnosti.

Ključne besede: materiali z negativnim Poissonovim razmerjem, celični materiali, kvazi-statično preizkušanje, metoda končnih elementov

1 INTRODUCTION

Porous solids (i.e., open- or closed-cell foams) are materials suitable for applications requiring a significant mass reduction and a simultaneous high-impact energy absorption. This is provided by the foams' low specific weight and thus high specific stiffness. However, for certain applications (including blast protection), it may be necessary to use materials with a relatively high compressive strength, which disqualifies the usage of most foam types including metallic foams.¹ To improve the strength and energy absorption capacity without increasing the mass of constructional elements, a new type of material had to be found. One of the possible approaches to dealing with the absorption of enormous

amounts of deformation energy during blast and impact loading of structures is to produce a highly optimized porous structure, taking advantage of the negative Poisson's ratio of its skeleton.²

Historically, a structure with a negative Poisson's ratio was first reported for single crystals of iron pyrites and was attributed to crystal twinning.³ This initial finding was followed only by isolated reports in the 1970s and 1980s showing that negative Poisson's ratio is a rather unique phenomenon among natural constructs. First artificially prepared auxetic polymeric foam was reported in 1987 by Lakes⁴ when commercially available foam was modified in a process involving 30 % volumetric compression and heating of the samples to the polymer's softening temperature followed by cooling

whilst remaining under compression. Although research of the microstructures prepared with various similar techniques from the existing materials continued, the investigation of the auxetic-based materials capable of deformation-energy absorption closely followed the advances in additive manufacturing (i.e., selective laser sintering, direct 3D printing, etc.).

The reported auxetic topologies are mostly based on re-entrant, chiral, double-arrow-head and rotating-rigid unit cells.⁵⁻⁸ Deformation behaviour (both elastic and plastic) of such a porous construct is determined by concurrent effects of intrinsic behaviour of the material used for the scaffold production, cell topology and connectivity. To optimize its microstructure to suit the intended application and to achieve a stable negative Poisson's ratio up to high strains, a control over the pore structure is required. Here, the usage of additive manufacturing is favourable as all the intended geometrical characteristics can be attained deterministically, satisfying the need for a high mechanical integrity of the construct during deformation and the need for precise tuning of the overall stiffness and plastic properties.

Several unit-cell models having a well-defined Poisson's function (strain-dependent Poisson's ratio) described analytically have already been proposed.⁹⁻¹² In this study, samples of three microstructures utilizing both the in-plane and volumetric negative Poisson's ratio were produced with direct 3D printing to evaluate their compressive-deformation behaviour in both elastic and plastic regime up to the densification. Deformation of the microstructures during quasi-static uni-axial compression tests was optically observed using a CCD camera and the digital-image-correlation (DIC) method was used for the strain evaluation. Moreover, mechanical behaviour of the structures was investigated numerically with virtual experiments (i.e., simulations of the compression tests) using finite element (FE) method. The simulations were carried out using identical loading and boundary conditions and the numerically obtained stress-strain curves were compared to the experimental ones to test the proposed material model for the base material.

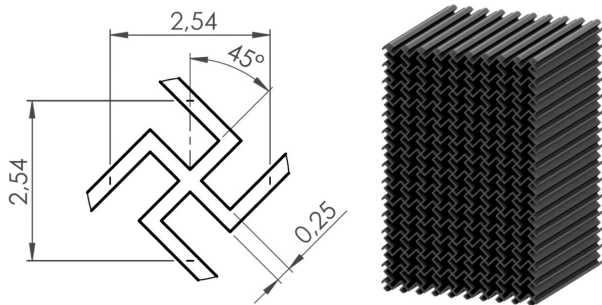


Figure 1: Missing-rib-cut structure: a) unit cell geometry and b) visualisation of the whole sample

Slika 1: Struktura prereza z manjkajočim rebrom: a) geometrija celice in b) vizualizacija celotnega vzorca

2 EXPERIMENTAL PART

2.1 Specimen geometry

In this study, three different types of unit-cell geometry were used: a) two-dimensional missing-rib cut, b) two-dimensional inverted (re-entrant) honeycomb and c) three-dimensional inverted honeycomb. These unit cells were arranged so that predictable (determinate) in-plane or volumetric negative strain-dependent Poisson's ratio was achieved in the cases of two-dimensional and three-dimensional geometries, respectively. Constructs of two-dimensional geometries were generated by extruding a planar (single-layer) arrangement of the unit cells whereas a three-dimensional construct was created by copying a fully three-dimensional unit cell along all the spatial directions.

The missing-rib-cut model was formed by removing selected ribs (the elements forming a unit cell) from the periodical arrangement of squares and by rotating the construct by 45° to the direction of loading.¹³ Auxetic behaviour of such a construct depends on the unit-cell dimensions and the angles between individual ribs. The geometry of a unit cell with the dimensions used in this work and a visualisation of the specimen are depicted in **Figure 1**. The dimensions of the produced construct were 25.05 mm × 25.40 mm × 37.75 mm (width, depth, height), the overall porosity was 72.8 % and the construct consisted of 10 × 15 cells.

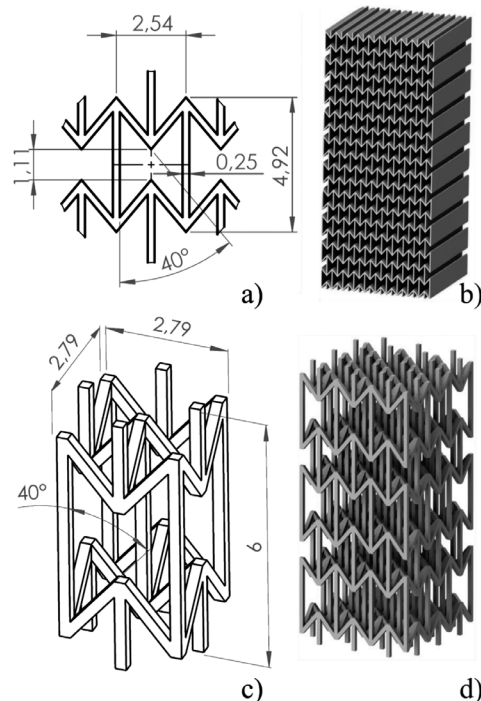


Figure 2: a) 2D re-entrant structure – unit cell geometry, b) visualisation of the whole sample, c) 3D re-entrant structure – unit cell geometry and d) visualisation of the whole sample

Slika 2: a) dvodimenzionalna navznoter usmerjena struktura – geometrija celice, b) vizualizacija celotnega vzorca, c) tridimenzionalna navznoter usmerjena struktura – geometrija celice in d) vizualizacija celotnega vzorca

The re-entrant mesh is generated by changing the four side angles between the ribs in a six-sided honeycomb.¹⁴ The magnitude of Poisson's ratio at a given strain is here primarily given with the length ratio of individual ribs forming the unit cell. Both two-dimensional and three-dimensional arrangements of the re-entrant unit cells together with visualisations of the specimens are shown in **Figure 2**. Dimensions of the produced two-dimensional construct were 25.65 mm × 25.40 mm × 58.89 mm (width, depth, height), the overall porosity was 73.2 % and the construct consisted of 10 × 15 cells; dimensions of the produced three-dimensional construct were 7.87 mm × 7.87 mm × 18 mm (width, depth, height), the overall porosity was 91.7 % and the construct consisted of three cells in every spatial direction.

2.2 Specimen preparation

The specimens were manufactured from VisiJet EX200 (3D Systems, USA) UV curable acrylic material suitable for high-resolution 3D printing. The physical properties of the material are summarised in **Table 1**.

For the specimen production, a Pro Jet HD3000 (3D Systems, USA) 3D printer in the high-definition mode was used. The manufacturing principle is based on a multi-jet modelling technology where a special printing head covers the whole working area of 198 mm × 185 mm × 203 mm and builds up the model by adding individual layers of the produced geometry. Simultaneously, while modelling the material, a supporting wax material is automatically added to the construct to enable a production of very complex geometries.

Thanks to its low melting point (approximately 55–65 °C) all the supporting material can be simply removed from the products by heating it in a water bath to approximately 80 °C without a potential mechanical damage to the products. A SolidWorks (Dassault Systèmes SolidWorks Corp., France) parametric modeller was used to design the sample geometry that was exported to the STL format for the 3D printing. The final samples were produced with a resolution of (328 × 328 × 606) DPI (*x*, *y*, *z* direction) with a layer thickness of 0.036 mm. In this mode, the accuracy of printing was approximately 0.025–0.05 mm and the production process took approximately 11 h.

Table 1: Properties of the VisiJet EX200 material

Tabela 1: Lastnosti materiala VisiJet EX200

Mass density	1.02	g/cm ³
Tensile modulus	1.283	GPa
Tensile strength	42.4	MPa
Flexural modulus	1.159	GPa
Glass transition temp.	52.5	°C

2.3 Experimental set-up

The experiments were carried out using an in-house designed loading set-up based on a novel modular

compression/tension loading device suitable for both optical and X-ray observation of deformation processes¹⁵ equipped with a U9b force transducer (HBM, Germany) with a nominal force capacity of 2 kN. The signal from the load cell was read out using an OM502T (Orbit Merret, CZ) load-cell indicator at a sampling rate of 50 Hz.

Imaging was performed using a Manta G504B monochromatic GigE vision camera (AVT, Germany). The camera was equipped with an ICX655 CCD sensor and its maximum frame rate was 9 fps, achieved at a resolution of 2452 px × 2056 px. In order to guarantee a high reliability of the correlation procedure and an accuracy of the computed strains, the camera was equipped with a TCZR 072 bi-telecentric zoom lens (Opto Engineering, Italy). The lens used a stepper-motor-controlled zoom revolver to set four different magnifications of the scene in the range of 0.125–1.000, with a very high image-centre stability, parfocality and no need for a re-calibration after the zooming. The specimens were illuminated using a KL2500 high-power white-light LED source (Schott, Germany).

A detailed description of the loading set-up is shown in **Figure 3**.

2.4 Loading procedure and strain measurement

The loading of the samples was performed as a displacement-driven uniaxial compression. The maximum displacement was set to 8 mm with a loading rate of 20 μm s⁻¹. The positioning of the camera as well as the loading were carried out using in-house developed control software based on the GNU/Linux real-time operating software and LinuxCNC open-source project.

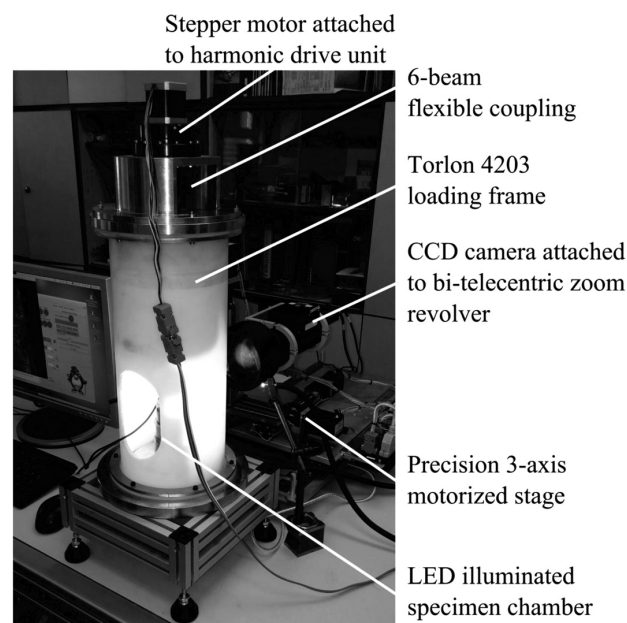


Figure 3: Loading set-up used in the experiments

Slika 3: Postavitev obremenjevanja, ki je bilo uporabljeno pri preizkusih

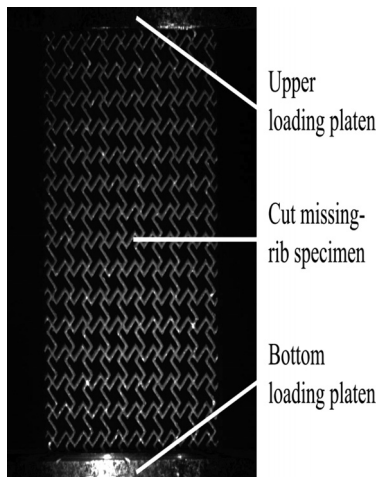


Figure 4: Loading scene captured using a CCD camera during the experiment. Missing-rib specimen with sprayed surface for a DIC strain evaluation.

Slika 4: Trenutek obremenitve, ki je prikazan na CCD kameri med preizkusom. Vzorec z manjkajočim rebrom z napršeno površino za oceno DIC sile obremenitve.

The strains were derived from optically measured displacements using a sequence of the images capturing a deforming sample. Depending on the sample height, 0.125 or 0.25 magnifications were used and the images were captured with the maximum resolution of 2452 px × 2056 px at 2 fps, enabling the identification of a sufficient number of points on the stress-strain curve. The acquisition of the projections was controlled with custom-developed software based on the OpenCV library and Python programming language. The observed faces of the specimens were sprayed using granite paint to generate a random pattern for a high reliability of the optical deformation tracking. A selected loading scene is depicted in **Figure 4**.

2.5 Stress-strain diagram evaluation

Displacements were determined from the image sequences using a custom-developed DIC software tool¹⁶ based on the Lucas-Kanade tracking algorithm¹⁷ implemented in MATLAB. Two rows of correlation points (markers) perpendicular to the loading direction were selected near the upper and lower edges of the observed surfaces of the specimens. Each marker was in a series of projections tracked by searching for the highest correlation coefficient between two consequent projections.

Engineering-stress (σ_{eng}) and strain (ϵ_{eng}) values were determined from the geometrical properties of the tested specimens and optically measured displacements of the markers. Then, true stress (σ_{true}) and true strain (ϵ_{true}) were calculated according to Equations (1) and (2):

$$\sigma_{true} = \sigma_{eng} (1 + \epsilon_{eng}) \quad (1)$$

$$\epsilon_{true} = \ln(1 + \epsilon_{eng}) \quad (2)$$

3 NUMERICAL PART

Apart from the experimental methods, analytical and FE models can be used for a description of deformation behaviour of auxetic constructs, allowing a prediction and optimization of the effective mechanical characteristics that facilitate the material design for a specific application.

Most of the analytical models assume small deflections, neglecting the axial deformation of the struts.¹⁹ Thus, analytical approach can be used to prove the concept of negative Poisson's ratio, optimize the parameters of a structure (e.g., the re-entrant angle, relative density, strut thickness) and maximize parameters of the resulting constructs (i.e., deformation energy per unit volume, yield strength of the structure, compressive strength) according to specific requirements. For instance, using these analytical models, it is possible to express Poisson's ratio μ of the re-entrant honeycomb structure (**Figure 2a**) with Equation (3):

$$\mu = \frac{\sin(90-\theta)(L_2 / L_1 + \sin(90-\theta))}{\cos^2(90-\theta)} \quad (3)$$

where L_1 and L_2 are the strut lengths and θ is the strut angle (measured in degrees). The value of resulting Poisson's ratio is negative and its dependency on the magnitude of the angle θ and the strut length ratio L_2/L_1 corresponds to the observed experimental results. Using the Timoshenko beam theory and the elastic-behaviour assumption, it is possible to express the overall elastic modulus E and critical-yield compressive force F_m based on the yield strength σ_y of the bulk solid material. From the yield compressive force the compressive strength of the structure can be then expressed.

However, these analytical models are effective only when simplifying the assumptions such as the small-deflection theory and linear elastic-material properties are used. Consequently, these models only give satisfactory results for small deformations and are limited to the calculation of the overall elastic properties or to the estimation of the yield point of a structure.

When large strains with non-linear material properties are to be considered, FE models have to be used instead. Thus, FE models of the tested auxetic structures were developed and subjected to the same loading conditions as during the compression tests. Deformation behaviour of the tested samples under large strains (up to 10 % or 20 % strain) was then compared with the predictions obtained from the numerical models to verify their suitability for a representation of such microarchitectures.

Stress-strain curves were inversely assessed from the FE simulations, i.e., from the reaction forces calculated at the restrained side of a sample. Using such inverse FE simulations, it is relatively easy not only to obtain the stress-strain curves for each considered sample, but also to establish the stresses and strains arising at individual

struts from the deformation of the structure. Hence, these strains can be easily compared to the values experimentally obtained from the digital-image correlation at the same positions (i.e., individual markers).

For all the considered auxetic constructs, the FE model was created using 3D beam elements with 6° of freedom (three translational and three rotational ones) defined at two nodal points. The element is based on Timoshenko beam theory, which includes shear-deformation effects. The material model set in the simulations was elasto-plastic, combining von Mises yield criteria and bilinear isotropic work hardening. The material properties are summarised in **Table 2**.

Table 2: Material properties used in the FE simulations

Tabela 2: Lastnosti materiala uporabljenega pri FE simulaciji

Young's modulus	1.159	GPa
Poisson's ratio	0.2	–
Yield stress	42.4	MPa
Hardening tangent modulus	12.8	MPa

The loading was prescribed to be done in 100 loading steps, i.e., in each step a 0.1 % or 0.2 % deformation was applied.

In the case of such a large-strain analysis, a highly deformed geometry has an important effect on the strain and, therefore, geometric nonlinearities must be considered. To consider the post-buckling behaviour of the thin beams subjected to a large compression, strain measures have to account for higher-order terms. Thus, in our analyses, material stress-strain properties were input in terms of true stress versus logarithmic strain. In every loading step, reaction forces originating from the

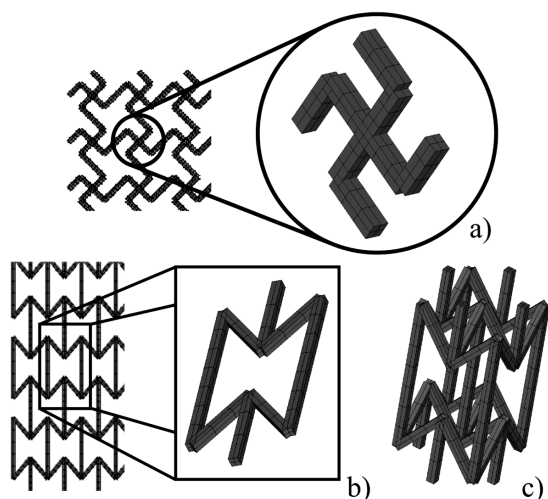


Figure 5: Visualization of FE-model elements used in the numerical simulations: a) missing-rib-structure cut with a detail of the unit cell, b) 2D re-entrant structure with a detail of the unit cell and c) detail of 3D re-entrant unit cell

Slika 5: Vizualizacija elementov FE modela, ki je bil uporabljen v številčnih simulacijah: a) struktura prereza z manjkajočim rebrom s podrobnostmi enote celice, b) dvodimenzionalna navznoter usmerjena struktura s podrobnostmi enote celice in c) podrobnosti tridimenzionalna navznoter usmerjene enote celice

supports were calculated and the true stresses and strains were established using Equations (1) and (2). Visualizations of the FE models for individual constructs can be seen in **Figure 5**.

4 RESULTS AND DISCUSSION

From both the numerical and experimental quasi-static compression tests true stress/true strain diagrams for all three considered auxetic microarchitectures were plotted.

A comparison of the experimental and numerical stress-strain diagrams of the missing-rib-structure cut is depicted in **Figure 6**.

It can be seen that this type of microstructure exhibits a similar initial compressive behaviour as a typical closed-cell porous solid. The initial linear elastic part is followed by an apparent yield point and a compaction region with a constant stress plateau. These parts are then, at an approximately 17.5 % strain, followed by a region of localized densification due to negative Poisson's ratio of the unit cell and repeated decreases of the stress that can be attributed to the ruptures of beams due to excessive bending. Good correlation of the numerical and experimental results was obtained in terms of stiffness, yield point and plateau stress up to a 20 % strain.

In **Figure 7**, a comparison of the experimentally and numerically acquired stress-strain diagrams of the two-dimensional inverted honeycomb structure is presented.

It is clearly apparent that the microstructure of such a construct exhibits a significantly different deformation behavior than the missing-rib-structure cut. After the initial linear elastic region, a 30 % drop in the stress is followed by cyclic increases and decreases in the stress levels in the specimens with an apparent progressive trend. After a visual inspection of individual projections during the deformation, the occurrence of the cycles can

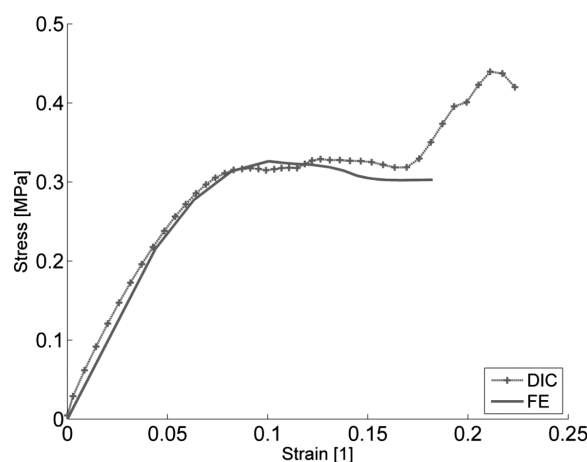


Figure 6: Comparison of experimentally and numerically obtained stress-strain diagrams of the missing-rib-cut structure

Slika 6: Primerjava eksperimentalno in številčno pridobljenih diagramov sile in razteška za strukturo prereza z manjkajočim rebrom

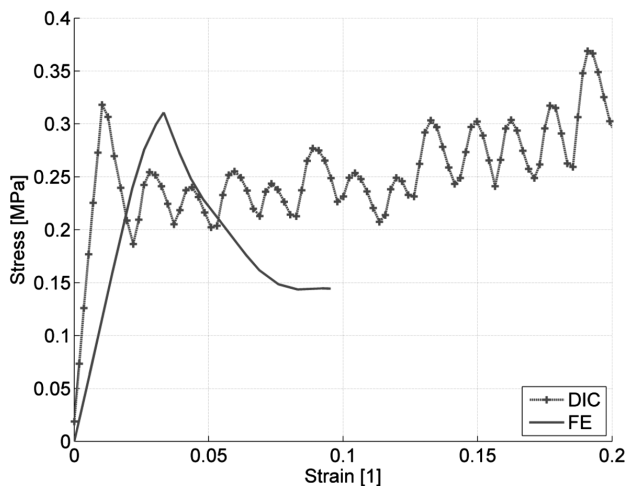


Figure 7: Comparison of experimentally and numerically obtained stress-strain diagrams of the 2D inverted honeycomb structure
Slika 7: Primerjava eksperimentalno in številčno pridobljenih diagramov sile in raztezka za dvodimenzionalno obrnjeno strukturo satovja

be attributed to the collapse of individual layers of the unit cells in the microstructure. For this type of microstructure, FE simulations give a good prediction of the yield point and strain-softening behaviour up to the densification of the individual layers in the microstructure.

A stress-strain diagram showing the experimentally and numerically assessed behavior of the three-dimensional inverted honeycomb structure is shown in **Figure 8**.

The mechanical response is similar to that of the two-dimensional structure but with a more significant stress drop after the linear elastic region and a lower number of the stress cycles, caused by a 20 % lower overall porosity and a lower number of the cells in the structure. The performance of the FE model is, in this

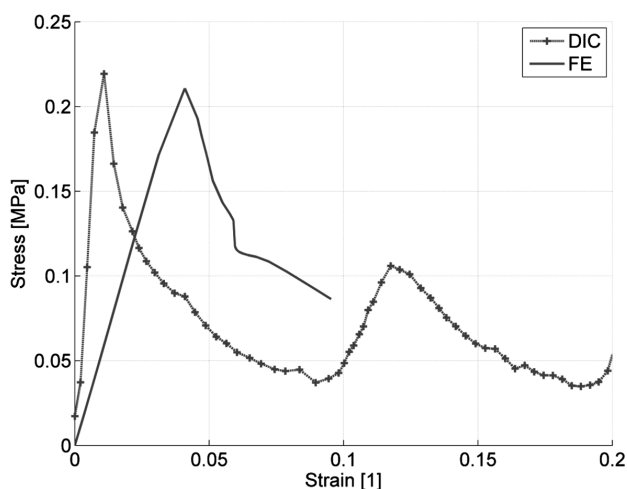


Figure 8: Comparison of experimentally and numerically obtained stress-strain diagrams for the 3D inverted honeycomb structure
Slika 8: Primerjava eksperimentalno in številčno pridobljenih diagramov sile in raztezka za tridimenzionalno obrnjeno strukturo satovja

case, similar to the two-dimensional re-entrant structure with a numerically well-determined yield point and strain-softening characteristics.

Only for the missing-rib cut of the auxetic structure, it was possible to perform the FE analysis up to a 20 % strain. Larger strain values could not be calculated as the elements became extremely distorted, yielding instability and convergence issues of the simulations. Furthermore, to capture the stiffening during the compaction, it would have been necessary to include self-contact between individual struts, which would have significantly increased the complexity and computational costs of the simulations.

The FE simulations of the re-entrant structures predict a smaller overall stiffness, which is apparent from the comparison between the experimental stress-strain curves and the numerically obtained responses. For this reason, a set of three-point-bending experiments was carried out using prismatic beams with rectangular cross-sections that were carefully cut from the printed specimens. Based on the DIC strain evaluation, a bending modulus of approximately 1.5 GPa was calculated. This value is close to the nominal flexural modulus of 1.2 GPa provided by the manufacturer that was also used in the FE simulations. Thus, the discrepancies between the numerically and experimentally evaluated stiffness might have been caused by properties that were different from the predicted properties of the joints between individual struts, influencing the bending characteristics of individual layers, which formed the principal mode of deformation of the re-entrant structures. Here, a combination of a precise inspection of the geometry and possibly a nanoindentation measurement of the joints should be applied to obtain an accurate material model for the FE simulations.

5 CONCLUSIONS

Mechanical behaviour of three different porous microarchitectures exhibiting in-plane and volumetric negative Poisson's ratios was studied both experimentally and numerically. The specimens prepared with high-resolution direct 3D printing were compressively loaded up to the densification regions of their mechanical responses. The true stress/true strain diagrams for the compression were derived from a high-precision force measurement and an optical DIC evaluation of the strain field. Based on the experimental results, numerical FE models of all the considered microarchitectures were developed and their ability to predict mechanical responses of the studied constructs was assessed by comparing the numerically and experimentally obtained stress-strain diagrams. It was found that the deformation response of the missing-rib-cut structure was well captured by the FE model up to a 20 % strain. Simulations of the re-entrant honeycomb structures showed good correlation of the yield point and strain-softening charac-

teristics up to a 10 % strain, while the calculated stiffness of the models was lower than the stiffness of the measured specimens. Still, the acquired results demonstrate that parametric FE models can be used to tune the design parameters of the structures with negative Poisson's ratio and numerically optimize their overall properties. Therefore, we can conclude that such FE models can be successfully used in material engineering to design highly optimized structures for a given range of strain rates, with maximized strain-deformation energy.

Acknowledgements

The research was supported by the Czech Science Foundation (research project Nos. P105/12/0824 and 15-15480S) and by RVO: 68378297.

6 REFERENCES

- ¹ Y. Sugimura, J. Meyer, M. Y. He, H. Bart-Smith, J. Grenestedt, A. G. Evans, On the mechanical performance of closed cell foams, *Acta Materialia*, 45 (1997), 5245–5259
- ² M. Grujicic, J. Galgalikar, J. S. Snipes, R. Yavari, S. Ramaswami, Multi-physics modeling of the fabrication and dynamic performance of all-metal auxetic-hexagonal sandwich-structures, *Materials & Design*, 51 (2013), 113–130, doi:10.1016/j.matdes.2013.04.004
- ³ W. Voigt, *Lehrbuch der Kristallphysik*, Teubner, Leipzig 1928
- ⁴ R. Lakes, Foam Structures with a Negative Poisson's Ratio, *Science*, 235 (1987), 1038–1040, doi:10.1126/science.235.4792.1038
- ⁵ C. Lira, P. Innocenti, F. Scarpa, Transverse elastic shear of auxetic multi re-entrant honeycombs, *Composite Structures*, 90 (2009) 3, 314–322, doi:10.1016/j.compstruct.2009.03.009
- ⁶ J. Grima, A. Alderson, K. Evans, Auxetic behaviour from rotating rigid units, *Physica Status Solidi (b)*, 242 (2005) 3, 561–575, doi:10.1002/pssb.200460376
- ⁷ D. Prall, R. Lakes, Properties of a chiral honeycomb with a Poisson's ratio of -1, *International Journal of Mechanical Sciences*, 39 (1997) 3, 305–314
- ⁸ U. D. Larsen, O. Sigmund, S. Bouwstra, Design and fabrication of compliant micromechanisms and structures with negative Poisson's ratio, *Journal of Microelectromechanical Systems*, 6 (1997) 2, 99–106
- ⁹ S. Burns, Negative Poisson's Ratio Materials, *Science*, 238 (1987), 551, doi:10.1126/science.238.4826.551
- ¹⁰ R. H. Baughman, S. Stafstrom, C. Cui, S. O. Dantas, *Science*, 279 (1998), 1522–1524, doi:10.1126/science.279.5356.1522
- ¹¹ K. E. Evans, M. A. Nkansah, I. J. Hutchinson, S. C. Rogers, Molecular network design, *Nature*, 353 (1991), 124, doi:10.1038/353124a0
- ¹² L. Rothenburg, A. A. Berlin, R. J. Bathurst, Materials with Negative Poisson's Ratio, *Nature*, 354 (1991), 470–472
- ¹³ C. W. Smith, J. N. Grima, K. E. Evans, A novel mechanism for generating auxetic behaviour in reticulated foams: missing rib foam mode, *Acta Materialia*, 48 (2000) 17, 4349–4356, doi:10.1016/S1359-6454(00)00269-X
- ¹⁴ I. G. Masters, K. E. Evans, Models for the elastic deformation of honeycombs, *Composite Structures*, 35 (1996), 403–422, doi:10.1016/S0263-8223(96)00054-2
- ¹⁵ P. Zlámal, O. Jiroušek, D. Vavřík, A Novel Compression/Tension Device for Investigation of Trabecular Bone Failure Using Real-Time Micro-CT Imaging, 7th Youth Symposium on Experimental Solid Mechanics, 2008, Wrocław, Poland, 91
- ¹⁶ I. Jandejsek, J. Valach, D. Vavřík, Optimization and Calibration of Digital Image Correlation Method, *Proceedings of Experimental Stress Analysis 2010*, edited by P. Smid, (2010), Olomouc, Czech Republic, 121–126
- ¹⁷ B. D. Lucas, T. Kanade, An Iterative Image Registration Technique with an Application to Stereo Vision, *Proceedings of Imaging Understanding Workshop*, 1981, Vancouver, Canada, 121–130
- ¹⁸ T. L. Warren, Negative Poisson's ratio in a transversely isotropic foam structure, *Journal of Applied Physics*, 67 (1990), 7591–7594, doi:10.1063/1.345826
- ¹⁹ L. Yang, O. Harrysson, H. West, D. Cormier, Compressive properties of Ti-6Al-4V auxetic mesh structures made by electron beam melting, *Acta Materialia*, 60 (2012) 8, 3370–3379, doi:10.1016/j.actamat.2012.03.015

MODEL OF PROGRESSIVE FAILURE FOR COMPOSITE MATERIALS USING THE 3D PUCK FAILURE CRITERION

MODEL POSTOPNEGA POPUŠČANJA KOMPOZITNEGA MATERIALA Z UPORABO PUCKOVEGA TRIDIMENZIONALNEGA KRITERIJA PORUŠITVE

Lukáš Bek, Robert Zemčík

University of West Bohemia, European Centre of Excellence, Faculty of Applied Sciences, NTIS – New Technologies for the Information Society, Univerzitní 22, 306 14 Pilsen, Czech Republic
lukasbek@kme.zcu.cz

Prejem rokopisa – received: 2014-09-16; sprejem za objavo – accepted for publication: 2015-05-07

doi:10.17222/mit.2014.233

A model for the progressive failure of composite materials that considers the materials' non-linearity was developed and implemented with the Abaqus FE software. An extended Puck failure criterion for the 3D stress state was used for the failure prediction. Furthermore, a simplified approach for the simulation of the delamination was considered. For the progressive failure simulation, the stiffness matrix degradation was used and the degradation parameters were a function of the fracture angle. The model was tested on problems of a pin-loaded composite plate and of a composite tube subjected to compressive loading perpendicular to the tube axis.

Keywords: progressive failure, composite, Puck criterion, finite-element analysis

Razvit je bil model postopnega popuščanja kompozitnega materiala z upoštevanjem nelinearnosti materiala, ki je bil uporabljen v Abaqus FE programski opremi. Razširjeni Puckov kriterij porušitve za tridimenzionalno napetostno stanje je bil uporabljen za napoved porušitve. Poleg tega je bil uporabljen tudi poenostavljen približek za simulacijo delaminacije. Za simulacijo napredovanja popuščanja je bila uporabljena degradacija togosti matrice. Degradacijski parametri pa so bili funkcija kota porušitve. Model je bil preizkušen na problemu obremenjevanja kompozitne plošče s konico in kompozitne cevi, izpostavljene tlačni obremenitvi pravokotno na os cevi.

Ključne besede: postopno popuščanje, kompozit, Puckov kriterij, analiza končnih elementov

1 INTRODUCTION

Composite materials are frequently used in the aerospace, automotive and marine industries, where extremely strong components and structures are necessary. Due to the complex loading, finite-element (FE) analyses are frequently used for the investigation of the stress state and the failure of structures.¹ Commercial FE software systems are usually able to predict only the first failure, which can occur at 20 % of the total strength of composite structures. Some new releases of FE systems are able to perform progressive failure analyses. However, the analyses are often not sufficiently precise or have problems with numerical stability. Therefore, new models of progressive failure are developed and implemented into the FE systems using a user-defined material subroutine.²

The development, implementation and testing of the progressive failure model for the 3D stress state based on the Puck failure criterion and considering the material's non-linearity in the Abaqus FE software using the UMAT material subroutine was the aim of this investigation.

2 NON-LINEAR MATERIAL BEHAVIOUR

For the simulation of the non-linear material behaviour of composite materials, a non-linear function with a constant asymptote was used for the calculation of the shear modulus G_{12} and G_{13} :³

$$G_{12}(\gamma_{12}) = \frac{G_{12}^0}{\left[1 + \left(\frac{G_{12}^0 \cdot \gamma_{12}}{\tau_{12}^0}\right)^{n_{12}}\right]^{1 + \frac{1}{n_{12}}}} \quad (1)$$

$$G_{13}(\gamma_{13}) = \frac{G_{12}^0}{\left[1 + \left(\frac{G_{12}^0 \cdot \gamma_{13}}{\tau_{12}^0}\right)^{n_{12}}\right]^{1 + \frac{1}{n_{12}}}} \quad (2)$$

where G_{12}^0 is the initial shear modulus, γ_{12} and γ_{13} are the shear strains, τ_{12}^0 is the asymptote value of the shear stress and n_{12} is the shape parameter.

3 FAILURE CRITERION

The failure criterion determines the occurrence of failure and indicates the failure's propagation. The Puck

criterion for the 3D stress state, described in ^{2,4}, was selected for this model because it provides the fracture angle θ_{fr} , later used for the stiffness degradation. Furthermore, the influence of the fibre parallel-stress extension and the influence of the non-fracture plane extension were used with this criterion.⁴

4 PROGRESSIVE FAILURE IN THE CASE OF INTER-FIBRE FAILURE

The stiffness-matrix degradation method was used to simulate the progressive failure. In order to simplify the determination of the degradation parameters, the stiffness matrix C , in UMAT, called *DDSDDE*, was transformed from the material coordinate system (1, 2, 3) to the crack coordinate system (x, y, z) described in **Figure 1**.

The transformation of the C matrix in the (1, 2, 3) system to the C' in the (x, y, z) system was carried out using the Equation (3):

$$C'(\theta_{fr}) = T_{\sigma}^{-1} \cdot C \cdot T_{\sigma} \quad (3)$$

where

$$T_{\sigma} = \begin{bmatrix} 1 & 0 & 0 & 0 & 0 & 0 \\ 0 & c^2 & s^2 & 0 & 0 & 2sc \\ 0 & s^2 & c^2 & 0 & 0 & -2sc \\ 0 & 0 & 0 & c & s & 0 \\ 0 & 0 & 0 & -s & c & 0 \\ 0 & -sc & sc & 0 & 0 & c^2 - s^2 \end{bmatrix} \quad (4)$$

is the transformation matrix for the stress vector and T_{ϵ}^{-1} is the inverted transformation matrix

$$T_{\epsilon} = \begin{bmatrix} 1 & 0 & 0 & 0 & 0 & 0 \\ 0 & c^2 & s^2 & 0 & 0 & sc \\ 0 & s^2 & c^2 & 0 & 0 & -sc \\ 0 & 0 & 0 & c & s & 0 \\ 0 & 0 & 0 & -s & c & 0 \\ 0 & -2sc & 2sc & 0 & 0 & c^2 - s^2 \end{bmatrix} \quad (5)$$

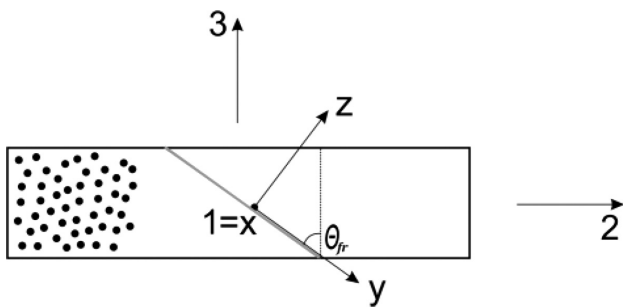


Figure 1: Description of the material coordinate system (1, 2, 3) and the crack coordinate system (x, y, z)

Slika 1: Opis koordinatnega sistema materiala (1, 2, 3) in koordinatnega sistema razpoke (x, y, z)

for the strain vector. In Equations (4) and (5), c represents $\cos \theta_{fr}$ and s represents $\sin \theta_{fr}$.

The non-zero components of the C' matrix C'_{ij} are multiplied by $(1 - d_{ij})$ terms. The degradation parameters $d_{ij} \in \langle 0,1 \rangle$ are constant values and differ for tensile and compressive failure.

Afterwards, the C' matrix is transformed back from the (x, y, z) system to the (1, 2, 3) system using the transformation matrices:

$$C''(d_{ij}) = T_{\sigma}^{-1} \cdot C'(\theta_{fr}, d_{ij}) \cdot T_{\epsilon} \quad (6)$$

5 PROGRESSIVE FAILURE IN THE CASE OF FIBRE FAILURE

The transformation of the C matrix is not necessary. Therefore, the non-zero components of the C matrix C_{ij} are only multiplied by $(1 - d_{ij})$ terms, as in the case of inter-fibre failure.

6 DELAMINATION

During the testing it was observed that delamination must be considered because after the initial fibre or inter-fibre failure, the crack often propagates in the form of a delamination. Therefore, an approach for the simulation of the delamination was also implemented.

A thin isotropic layer of brittle matrix was inserted between each of the orthotropic layers in the FE model. For the prediction of the matrix failure, the maximum stress criterion, originally used for orthotropic materials, was considered because it provides information about which stress component suffered failure. The normal stress components were compared to the compressive and tensile strengths of the matrix, while the shear components were compared to the shear strength of the matrix.

In the case of the failure, the non-zero components of the C matrix C_{ij} are again multiplied by $(1 - d_{ij})$ terms as in the case of inter-fibre failure.

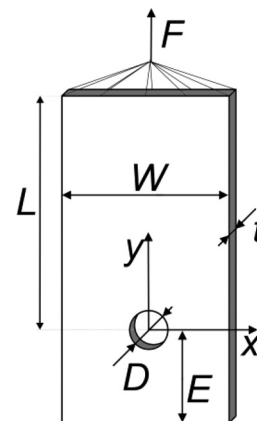


Figure 2: Geometric properties of the pin-loaded plate
Slika 2: Geometrijske lastnosti s konico obremenjene plošče

7 CASE STUDY 1 – PIN JOINT

First, in order to test the model, the failure simulations of pin-loaded carbon composite plates were compared with the experiments. Two types of specimens with different failure modes (shear-out and net-tension⁵) were selected for the failure simulation. The geometric properties of the specimens are described in **Figure 2**, where the 0° layup orientation is parallel to the y axis and the pin diameter $D = 8$ mm.

The failure simulation for the first type of specimens with the shear-out failure mode, a composite layup $[0^\circ|45^\circ|-45^\circ|90^\circ]$ s, ratios $E/D = 1$ and $W/D = 3$, and a thickness $t = 2.32$ mm, is illustrated in **Figure 3**. The black colour indicates the elements with a degraded

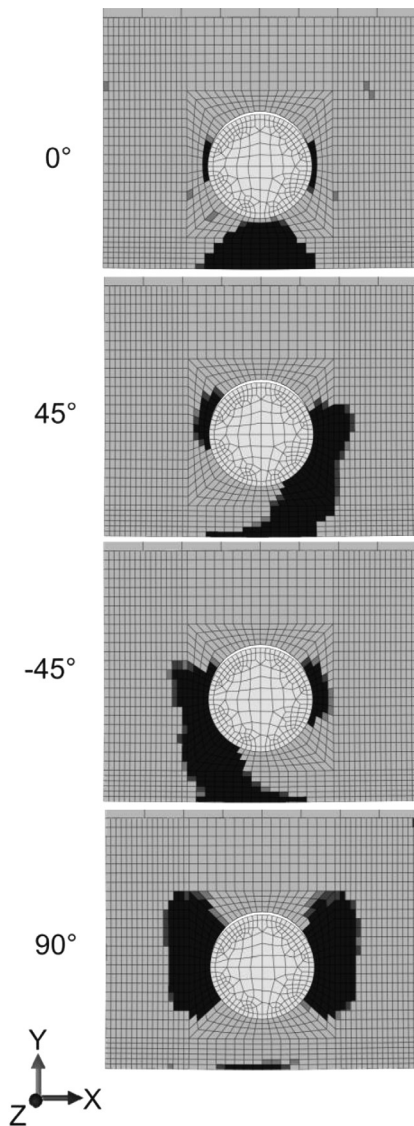


Figure 3: Numerical simulation of the final shape of failure in the case of specimens with a shear-out failure mode; different layers displayed

Slika 3: Numerična simulacija končne oblike porušitve v primeru vzorca s porušitvijo z izstriženjem; prikazane so različne plasti

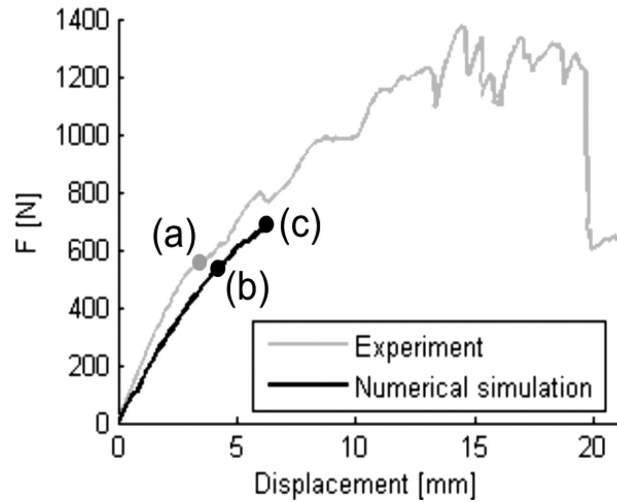


Figure 4: Load-displacement diagrams of the experiment and the numerical simulation: a) first failure investigated using experiment, b) first failure investigated using numerical simulation and c) loss of numerical stability

Slika 4: Diagram obremenitev-raztezek eksperimenta in numerične simulacije: a) prva preiskovana porušitev pri eksperimentu, b) prva preiskovana porušitev pri numerični simulaciji in c) izguba numerične stabilnosti

stiffness matrix and represents the failure of the material. All the layers representing the isotropic matrix were also degraded. The error for the ultimate load F was 6.8 % (compared to the average value from the experiments).

The error for the ultimate load F investigated using the failure simulation of the second type of specimens with a net-tension failure mode, a composite layup $[90^\circ|45^\circ|-45^\circ|0^\circ]$ s, ratios $E/D = 4$ and $W/D = 2$, and a thickness $t = 2.32$ mm was 10.9 % (compared to the average value from the experiments as well).

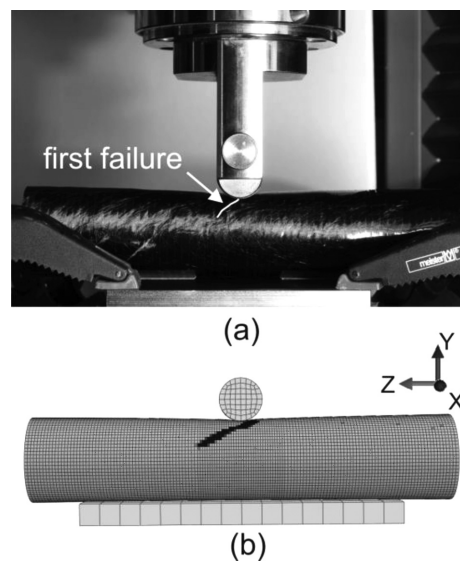


Figure 5: Comparison of the position and shape of the first failure investigated using the experiment and the numerical simulation

Slika 5: Primerjava položaja in oblike prve porušitve pri preizkusu in pri numerični simulaciji

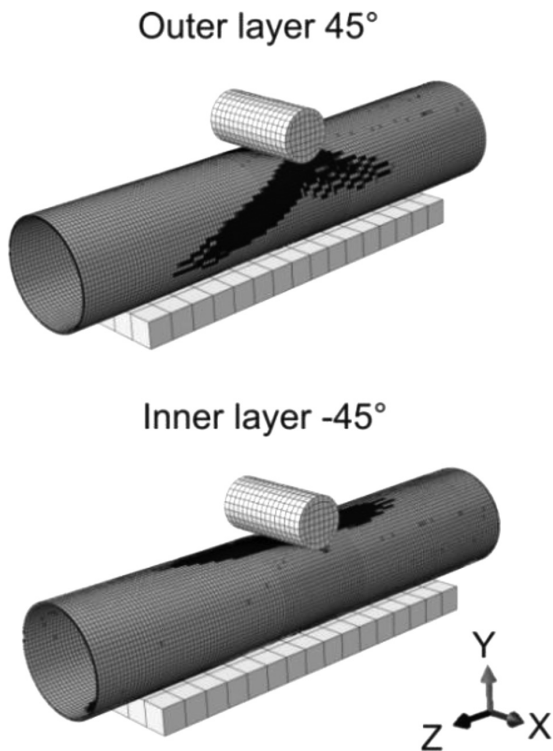


Figure 6: Numerical simulation of the shape and the position of failure just before the loss of numerical stability

Slika 6: Numerična simulacija oblike in položaja poškodbe tik pred izgubo numerične stabilnosti

8 CASE STUDY 2 – COMPOSITE TUBE

In addition, the testing was carried out on a thin-walled composite tube subjected to compressive loading perpendicular to the tube's axis. The tube consisted of carbon fibres with a composite layup $[45^{\circ}|_{-45^{\circ}}$, a wall-thickness of 1 mm and an outer diameter of 42 mm. The length of the tested tube was 200 mm.

A stiffness comparison of the experiment and the numerical simulation is illustrated in **Figure 4**. A comparison of the position and the shape of the first failure investigated using the experiment (**Figure 4a**) and the numerical simulation (**Figure 4b**) is illustrated in **Figure 5**. Unfortunately, the numerical model was not able to

simulate the whole specimen failure due to a loss of numerical stability. In **Figure 6**, the failure just before the loss of numerical stability in both layers is illustrated. The error of the simulation at this point (**Figure 4c**) is 13.8 %.

9 CONCLUSION

Our model of progressive failure using the extended Puck failure criterion for the 3D stress state and considering the simplified approach for the simulation of delamination and the material's non-linearity showed very good agreement between the numerical simulation and the experiments. The error for all the simulations was below 14 %. In future work, the problem of numerical stability will be further investigated.

Acknowledgements

This work was supported by the European Regional Development Fund (ERDF), project "NTIS – New Technologies for Information Society", European Centre of Excellence, CZ.1.05/1.1.00/02.0090, by the research project GACR_P101/11/0288 and by the grant project SGS-2013-036.

10 REFERENCES

- ¹ V. Lašová, P. Bernardin, Numerical modelling of glued joints between metal and fibre composites using cohesive elements, *Applied Mechanics and Materials*, 611 (2014), 156–161, doi:10.4028/www.scientific.net/AMM.611.156
- ² H. M. Deuschle, 3D Failure Analysis of UD Fibre Reinforced Composites: Puck's Theory within FEA, Institut für Statik und Dynamik der Luft- und Raumfahrtkonstruktionen, Universität Stuttgart, Stuttgart 2010
- ³ J. Krystek, T. Kroupa, R. Kottner, Identification of mechanical properties from tensile and compression tests of unidirectional carbon composite, 48th International Scientific Conference proceedings: Experimental Stress Analysis 2010, Palacky University, 2010, 193–200
- ⁴ A. Puck, *Festigkeitsanalyse von Faser-Matrix-Laminaten: Modelle für die Praxis*, Carl Hanser Verlag, München, Wien 1996
- ⁵ H. Schürmann, *Konstruieren mit Faser-Kunststoff Verbunden*, Springer Verlag, Berlin, Heidelberg 2007, doi:10.1007/978-3-540-72190-1

PHYSICO-CHEMICAL PROPERTIES OF A Ti67 ALLOY AFTER EO AND STEAM STERILIZATION

FIZIKALNO KEMIJSKE LASTNOSTI ZLITINE Ti67 PO EO IN PARNI STERILIZACIJI

Witold Walke¹, Marcin Basiaga¹, Zbigniew Paszenda¹, Jan Marciniak,
Paweł Karasinski²

¹Silesian University of Technology, Faculty of Biomedical Engineering, Roosevelta 40, 41-800 Zabrze, Poland

²Silesian University of Technology, Faculty of Electrical Engineering, Bolesława Krzywoustego 2, 44-100 Gliwice, Poland
witold.walke@polsl.pl

Prejem rokopisa – received: 2014-09-23; sprejem za objavo – accepted for publication: 2015-05-15

doi:10.17222/mit.2014.242

The techniques of surface modification play a significant role in forming the physical and chemical properties of titanium and its alloys. Among many techniques for the layers' application, chemical and electrochemical methods are particularly interesting, as they make it possible to control the process of depositing thin layers of the material and modifying their properties through a change of reagents and the parameters of the deposition process. A special advantage the methods bring is the possibility to obtain layers that offer a perfect coating for geometrically complex surfaces. Apart from improved haemocompatibility, a significant issue related to the creation of the layers is also a proper set of physicochemical properties. Therefore, the study comprised tests of the physicochemical properties of oxide layers deposited on the surface of samples taken from a Ti-6Al-7Nb alloy. The samples were subject to various surface modifications, i.e., grinding, electrolytic polishing, a SiO₂ layer was applied using the sol-gel method and TiO₂ by means of an anodic oxide and medical sterilisation methods (EO and steam). The corrosion-resistance tests were performed on the basis of registered anodic polarisation curves and the Stern method. Electrochemical Impedance Spectroscopy (EIS) was also used in order to evaluate the phenomena taking place on the surface of the tested alloys. As a part of the evaluation of the mechanical properties of surface layers created in such a way, hardness tests and tests of the adhesion of those layers to a metallic substrate were made. Measurements of the instrumental hardness were made with the Oliver & Pharr method, whereas the adhesion of the layers to the substrate was measured by means of a scratch test. The suggestion of proper surface treatment variants has perspective significance and will help to develop the technological conditions with specified parameters of the oxide coating's creation on the surface of metallic implants.

Keywords: Ti-6Al-7Nb (Ti67) alloy, sol-gel, anodic oxide, scratch-test, nanohardness, EIS, potentiodynamic method

Tehnike modifikacije površine igrajo pomembno vlogo pri doseganju fizikalnih in kemijskih lastnosti titana in njegovih zlitin. Med mnogimi tehnikami uporabe tankih plasti so še posebej zanimive kemijske in elektrokemijske metode, ker omogočajo kontrolo postopka depozicije tanke plasti materiala in spreminjanje njihovih lastnosti, z zamenjavo reagentov in parametrov procesa depozicije. Posebna prednost, ki jo omogočajo metode, je možnost izdelave plasti, ki omogočajo popolno prevleko pri geometrijsko kompleksnih površinah. Poleg izboljšane hemokompatibilnosti je pomembno vprašanje povezano z nastankom plasti in tudi z doseganjem ustreznih fizikalno kemijskih lastnosti. Zato je študija obsegala preizkuse fizikalno kemijskih lastnosti oksidnih plasti, po depoziciji na površini vzorcev iz Ti-6Al-7Nb zlitine. Na vzorcih so bile opravljene različne modifikacije površine: brušenje, elektrolitsko poliranje, SiO₂ plast, izdelana po sol-gel postopku in TiO₂ plast, izdelana z anodno oksidacijo in metodo medicinske sterilizacije (EO in para). Preizkusi korozijske odpornosti so bili izvršeni na osnovi zabeleženih polarizacijskih krivulj in metode Oliver & Pharr. Za oceno pojavov na površini preizkušanih zlitin je bila uporabljena tudi elektrokemijska impedančna spektroskopija. Kot del ocene mehanskih lastnosti nastalih plasti na površini, so bile izvršene tudi meritve trdote in preizkusi oprijemljivosti plasti na kovinski podlagi. Meritve trdote so bile izvršene z metodo Oliver & Pharr, medtem ko je bila oprijemljivost izmerjena s preizkusom razenja. Predlog primernih načinov obdelave površine je pomemben, ker bo v prihodnje pomagal pri razvoju tehnoloških pogojev za določene parametre oksidne plasti, nastale na površini kovinskih vsadkov.

Ključne besede: Ti-6Al-7Nb (Ti67) zlitina, sol-gel, anodni oksid, preizkus razenja, nanotrdoča, EIS, potenciodinamična metoda

1 INTRODUCTION

The haemocompatibility of titanium alloys, including the Ti-6Al-7Nb alloy, is increased by, e.g., modification of the surface layer of cardiovascular implants with surface-engineering methods. The methods used to modify the surface layers must ensure the repeatability and uniformity of their physical and chemical properties.¹ The structure and chemical composition of the titanium and titanium-alloy implant layer may be modified with the use of various methods, among which the main ones are mechanical, chemical, electrochemical and thermal

methods. Mechanical treatment techniques are used to modify the surface topography. The properties of the oxide layer after the application of these techniques are difficult to control.² Chemical methods include primarily etching and passivation, which result in the formation of a thin (<10 nm) oxide layer composed mostly of TiO₂ and oxides of the alloying elements, as well as impurities from chemical reagents.³⁻⁶ Repeatable layers with a fully controlled thickness, microstructure and chemical composition are obtained with high-temperature treatments, immersion in H₂O₂, alkaline etching, electropolishing, anodic oxidation and vacuum treatments. However, the

method for increasing the haemocompatibility of titanium and titanium-alloy surfaces, which is increasingly often applied, involves using the sol-gel technique to produce thin oxide coatings based on Si. The advantage of this method is the low temperature at which the coating is produced, which guarantees unchanged mechanical properties of the metal base. Moreover, this method ensures the sol's homogeneity, the possibility to regulate polycondensate molecules, a large number of metalorganic and inorganic metal salt compounds, used as precursors, as well as the possibility to obtain multi-ingredient coatings of high purity on different bases.^{7,8} Another important factor affecting the final quality of the products that come into contact with blood is the proper resistance of the modified surface to medical sterilisation. Presently, cardiovascular implants are usually sterilised with ethylene oxide (EO) and with pressurised-water steam in an autoclave. The positive results of already-published papers by the authors regarding the assessment of the usefulness of the surface-layer modification processes involving anodic oxidation, as well as the creation of a SiO₂ layer with the sol-gel method, enabled the selection of the most beneficial parameters for the process.^{1,9-11} An analysis of the literature data indicates that reducing the number of failed blood-system disease treatments depends to a large extent on the electrochemical stability of the surface layer under the medical sterilisation conditions. Therefore, this article evaluates the effects of steam and ethylene oxide sterilisation processes on the physical and chemical properties of the surface layer of the Ti-6Al-7Nb (Ti67) alloy.

2 MATERIALS AND METHODS

The tested material was a titanium alloy Ti-6Al-7Nb (Ti67) in the form of discs of diameter $d = 14$ mm and thickness $g = 2$ mm. A number of surface-treatment methods were applied to the samples, including the following processes: grinding with the use of 1000- and 1200-grit sand paper, electrolytic polishing, the application of layers with the sol-gel technique, and anodic oxidation. The electrolytic polishing was conducted in a solution based on chromic acid z (E-395 by POLIGRAT GmbH), with a current density $i = 10-30$ A/cm². The final stage of the surface treatment consisted of applying layers with two different techniques: sol-gel and anodic oxidation. In the case of the sol-gel method, a layer of SiO₂ was applied with the following process parameters: $v = 2.5$ cm/min, $T = 430^\circ\text{C}$, $t = 60$ min. The silica precursor used in the test was tetraethoxysilane Si(OC₂H₅)₄, TEOS, and tetramethoxysilane Si(OCH₃)₄, TMOS. The remaining starting ingredients contained ethyl alcohol (EtOH) and water.^{1,9} In the case of anodic oxidation a layer of TiO₂ was applied in an electrolyte based on phosphoric acid and sulphuric acid (TitanColor by POLIGRAT GmbH) at a potential of 90 V. Previous

studies conducted by the authors made it possible to select the most favourable parameters, both for the sol-gel technique and for the anodic oxidation.^{10,11}

Next, the prepared samples were sterilised with ethylene oxide and steam. The sterilisation with ethylene oxide was conducted in a 12-h cycle of exposure to ethylene oxide at 30 °C. After the process was completed, the samples were ventilated for 2 h with the use of an EOGas series steriliser from the Andersen Products company. The sterility assurance level (SAL) obtained during the cycle was 10⁻⁶. The process was controlled with a chemical and biological indicator, as well as an indicator of exposure to the ethylene oxide control. The steam sterilisation was conducted in a Basic Plus autoclave at $T = 134$ °C, under a pressure of $p = 2.1$ bar for $t = 12$ min.

To evaluate the effect of ethylene oxide sterilisation and steam sterilisation on the mechanical and electrochemical properties of the proposed Ti67 surface modification, the authors suggested the following tests of the mechanical properties: measurements of the adhesion of the analysed layers to the base and their hardness. Electrochemical tests included potentiodynamic and impedance measurements.

First, as part of the mechanical properties' tests, the measurement of a layer's adhesion to the base was performed using the scratching method, with the use of an open platform equipped with a Micro-Combi-Tester from the CSM company, in accordance with the standard.¹² The test consisted of making a scratch using a penetrator – a Rockwell diamond cone – with a gradually increasing normal force weighting the penetrator. To assess the value of the critical force L_c , records of variations in the acoustic emission signals, the friction force and the friction coefficient were used, as well as a microscopic observation with the use of an optical microscope, and an integral component of the platform. The tests were performed with an increasing weighting force of 0.03–20 N, and with the following parameters: weighting speed 10N/min, table movement speed 1.5 mm/min, and length of the scratch ~3 mm.

Later, measurements of the nanohardness of the layers applied with the sol-gel method, and with the anodic oxidation method, were conducted. The instrumental hardness measurement was performed with the Oliver and Pharr method, using a Berkovich penetrator. The speed of the increasing weighting and relieving force was 0.40 mN/min. The measurement of the layer's nanohardness was made with the Micro-Combi-Tester open platform from the CSM Instruments company, where the weighting force of the penetrator was 0.20 mN.¹³

Subsequently, as part of the electrochemical properties testing, the resistance to pitting erosion was tested with the potentiodynamic method, recording the polarisation curves. They were used as a base to determine the values of specific parameters: the corrosion potential

E_{corr} (V) and the polarisation potential R_p (Ωcm^2). At the beginning of the testing, the value of the opening potential E_{OCP} was determined without any electric current. Then, the anode polarisation curves were recorded. The measurements started for the potential of $E_{start} = E_{OCP} - 100$ mV, and the change of potential in the anodic direction was at a speed of 0.16 mV/s, until the anodic current density reached a value of $i = 1$ mA/cm², or the measurement range of 4V was reached.¹⁴

As part of the EIS testing, the impedance spectra of the analysed corrosive systems were determined, and then the obtained measurement data were adjusted to the corresponding substitute systems. The impedance spectra of the systems tested are presented on Nyquist diagrams for the different frequencies as well as on Bode diagrams. Also, the numerical values of the resistance R were established, as well as the capacities C of the analysed corrosive systems. The resulting spectra were interpreted after being adjusted with the least-squares

method to the substitute electric systems. Based on the results obtained, it was possible to characterise the impedance of the phase boundaries, i.e., Ti-6Al-7Nb (Ti67) – surface layer – blood plasma, with an approximation of the impedance data using an electric model of a substitute circuit. The testing environment was an artificial blood-plasma solution of $T = 37 \pm 1$ °C. The measurements were performed using the AutoLab PGSTAT 302N measurement system, equipped with a FRA2 (Frequency Response Analyser) module. The reference electrode was a saturated calomel electrode SCE, type KP-113, whereas the supporting electrode was a platinum electrode type PtP-201. The system used made it possible to conduct tests within the frequency range 10^4 to 10^{-3} Hz. The voltage amplitude of the sinusoid stimulating signal was 10 mV.^{15, 16}

Table 1: The results of the adhesion of the layer on the Ti67 substrate
Tabela 1: Orijemljivost plasti na podlagi iz Ti67

	Failure of the layer	The value of registered indenter load F_n , N					
		Ti67+SiO ₂			Ti67+TiO ₂		
		initial state	steam	EO	initial state	steam	EO
Measurement 1	Delamination Lc_1	2.01	1.57	1.54	6.64	2.98	3.14
	Complete break Lc_2	3.57	2.24	3.21	8.01	6.54	5.03
Measurement 2	Delamination Lc_1	2.48	1.33	1.89	3.06	3.14	2.36
	Complete break Lc_2	3.89	2.45	3.22	6.88	6.18	4.27
Measurement 3	Delamination Lc_1	3.55	1.41	2.41	4.33	3.52	2.86
	Complete break Lc_2	5.02	2.12	4.31	7.37	6.88	4.81
Average	Delamination Lc_1	2.68	1.43	1.94	4.67	3.21	2.78
	Complete break Lc_2	4.16	2.27	3.58	7.42	6.53	4.70
Standard deviation	Delamination Lc_1	± 0.78	± 0.12	± 0.43	± 1.81	± 0.59	± 0.39
	Complete break Lc_2	± 0.76	± 0.16	± 0.63	± 0.56	± 0.35	± 0.39

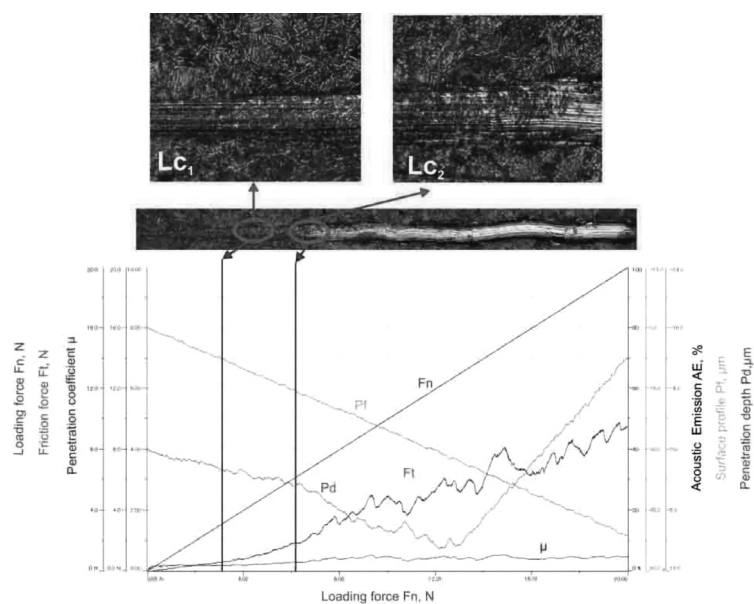


Figure 1: Results of the adhesion tests of the sample Ti67+TiO₂ (steam)
Slika 1: Rezultati preizkusov oprijemljivosti vzorca Ti67+TiO₂ (para)

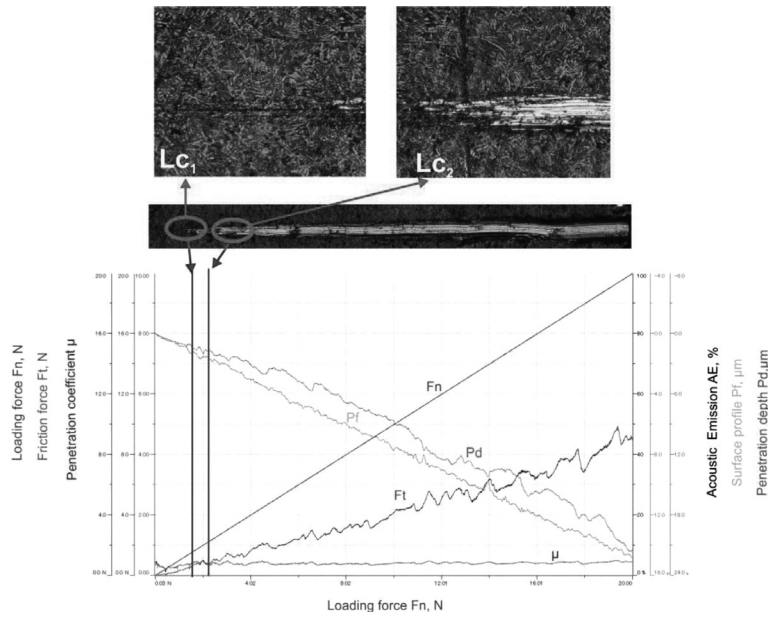


Figure 2: Results of the adhesion tests of the sample Ti67+SiO₂ (steam)
Slika 2: Rezultati preizkusov oprijemljivosti vzorca Ti67+SiO₂ (para)

3 RESULTS AND DISCUSSION

The test results for the adhesion of the analysed layers to the base made of Ti-6Al-7Nb (Ti67) alloy are presented in **Table 1**, **Figures 1** and **2**. It was found that in the case of samples in the initial state the critical value that caused the layer delamination, the external and the internal delamination, was $Lc_2 = 4.16\text{ N} - \text{Ti67+SiO}_2$ and $Lc_2 = 7.42\text{ N} - \text{Ti67+TiO}_2$. While using both steam and ethylene oxide sterilisation, the critical force value was reduced and for Ti67+SiO₂ it was $Lc_2 = 2.27\text{ N}$ (steam), $Lc_2 = 3.58\text{ N}$ (EO), whereas for Ti67+TiO₂ it was $Lc_2 = 6.53\text{ N}$ (steam), $Lc_2 = 4.70\text{ N}$ (EO). Regardless of the analysed sample type, an acoustic emission signal did not occur during the test, which indicates that the binding energy between the coating and the base was too low. Moreover, no significant differences between using

steam sterilisation or ethylene oxide sterilisation were found.

Furthermore, the hardness of the analysed layers was tested. The test results are presented in **Figures 3** and **4**. On the basis of the results obtained, an increase in the hardness value following the steam sterilisation, as well as the ethylene oxide sterilisation, compared to the initial state was observed. The polarisation curves determined for the samples with a Ti67(TiO₂) layer are presented in **Figure 5**, and for the samples with a Ti67(SiO₂) layer in **Figure 6**.

Regardless of the surface-preparation method or the sterilisation technique, a hysteresis loop was not present in the anodic range up to 4 V, which is a positive phenomenon, indicating the absence of pitting erosion. The determined values of the corrosive potential E_{corr} and the polarisation resistance R_p for the individual variant of the samples tested were as follows: Ti67+TiO₂ – $E_{\text{corr}} = -112\text{ mV}$,

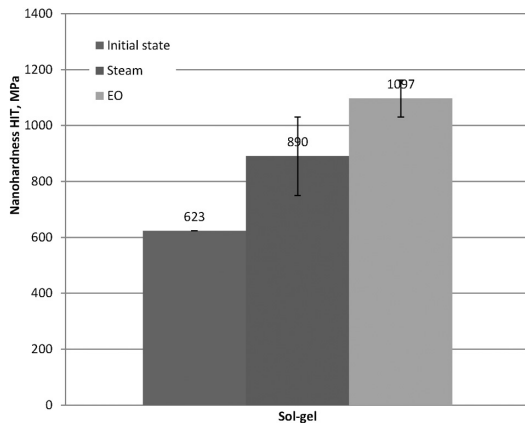


Figure 3: Results of the nanohardness tests of the sample Ti67+SiO₂
Slika 3: Nanotrđota vzorca Ti67+SiO₂

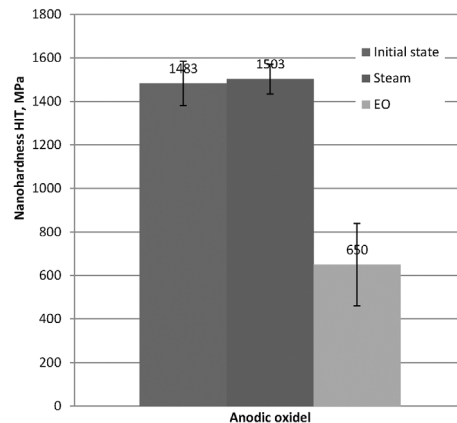


Figure 4: Results of the nanohardness tests of the sample Ti67+TiO₂
Slika 4: Nanotrđota vzorca Ti67+TiO₂

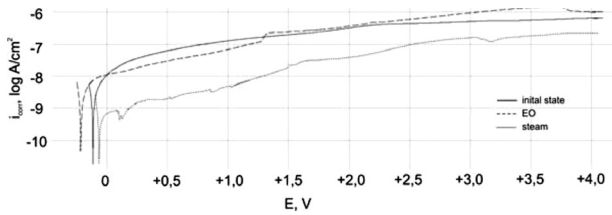


Figure 5: Anodic polarisation curves of Ti67+TiO₂
Slika 5: Krivulje anodne polarizacije Ti67+TiO₂

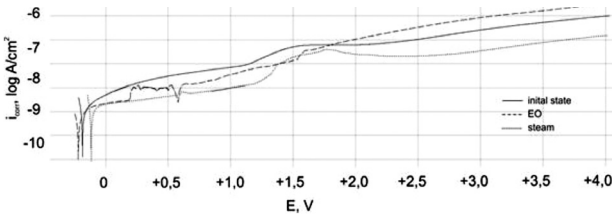


Figure 6: Anodic polarisation curves of Ti67+SiO₂
Slika 6: Krivulje anodne polarizacije Ti67+SiO₂

$R_p = 7480 \text{ k}\Omega \text{ cm}^2$; Ti67+TiO₂ (steam) – $E_{\text{corr}} = -67 \text{ mV}$, $R_p = 3340 \text{ k}\Omega \text{ cm}^2$; Ti67+TiO₂ (EO) – $E_{\text{corr}} = -217 \text{ mV}$, $R_p = 8340 \text{ k}\Omega \text{ cm}^2$; Ti67+SiO₂ – $E_{\text{corr}} = -108 \text{ mV}$, $R_p = 1460 \text{ k}\Omega \text{ cm}^2$; Ti67+SiO₂ (steam) – $E_{\text{corr}} = -118 \text{ mV}$, $R_p = 1850 \text{ k}\Omega \text{ cm}^2$; Ti67+SiO₂ (EO) – $E_{\text{corr}} = -219 \text{ mV}$, $R_p = 4290 \text{ k}\Omega \text{ cm}^2$, respectively. Figures 7 and 8 present the impedance spectra recorded for the samples before and after the sterilisation process for different variants of the surface preparation. To analyse the experimentally determined impedance spectra for the corrosive system of Ti67+SiO₂, Ti67+SiO₂ (steam), Ti67+SiO₂ (EO), a substitute electric system was used, which indicates the presence of a double layer (two time invariables visible in the diagram), where R_s signifies the electrolyte resistance, R_p is the electrolyte resistance in pores, and CPE_p is the capacity of the double layer (porous layer, surface layer), while R_{ct} and CPE_{dl} are the resistance and capacity of the oxide layer. Using two constant phase elements in the electric substitute circuit had an advantageous effect on the quality of the adjustment of the experimentally determined curves (Figure 9a and Table 2).

Table 2: EIS analysis results
Tabela 2: Rezultati EIS-analize

Surface	R_s , $\Omega \text{ cm}^2$	R_{pore} , $\Omega \text{ cm}^2$	CPE_{pore}		R_p $\text{k}\Omega \text{ cm}^2$	CPE_p		R_{ct} $\text{M}\Omega \text{ cm}^2$	CPE_{dl}		W $\mu\Omega \text{ cm}^2$	
			Y_0 , $\Omega^{-1} \text{ cm}^{-2} \text{ s}^{-n}$	n		Y_0 , $\Omega^{-1} \text{ cm}^{-2} \text{ s}^{-n}$	n		Y_0 , $\Omega^{-1} \text{ cm}^{-2} \text{ s}^{-n}$	n		
Ti67(TiO ₂)												
initial state	17	–	–	–	68	0,3580E-4	0,92	25,00	0,2306E-4	0,90	3	
EO	18	54	0,5407E-6	0,93	1830	0,6381E-6	0,83	20,88	0,1455E-5	0,81	–	
steam	17	–	–	–	42	0,2534E-6	0,96	0,96	0,2504E-6	0,90	35	
Ti67(SiO ₂)												
initial state	17	–	–	–	53	0,9823E-5	0,98	9,44	0,5294E-5	0,93	–	
EO	18	–	–	–	52	0,7975E-5	0,92	11,87	0,1068E-4	0,87	–	
steam	18	–	–	–	87	0,1213E-4	0,89	4,84	0,1524E-6	0,96	–	

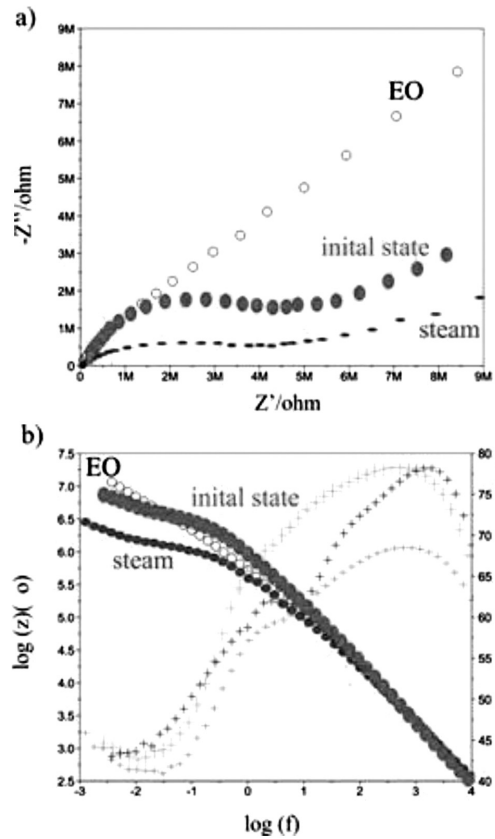


Figure 7: Impedance spectra for the sample Ti67+SiO₂: a) Nyquist plot, b) Bode diagram
Slika 7: Impedančni spekter vzorca Ti67+SiO₂: a) diagram Nyquist, b) diagram Bode

The impedance spectra obtained for the Ti67+TiO₂ and Ti67+TiO₂ (steam) samples were interpreted by comparing them to the substitute electric system, which indicates the presence of an anodic layer composed of two sublayers:⁹⁻¹¹ a compact internal layer and a porous external one, composed primarily of titanium oxide TiO₂ (Figure 9b). It is indicated by the presence of the Warburg impedance, which in this case represents probable oxygen transport to the alloy surface. In addition, the CPE_p element models the capacity of the surface material sphere with a significant surface extension, while R_p

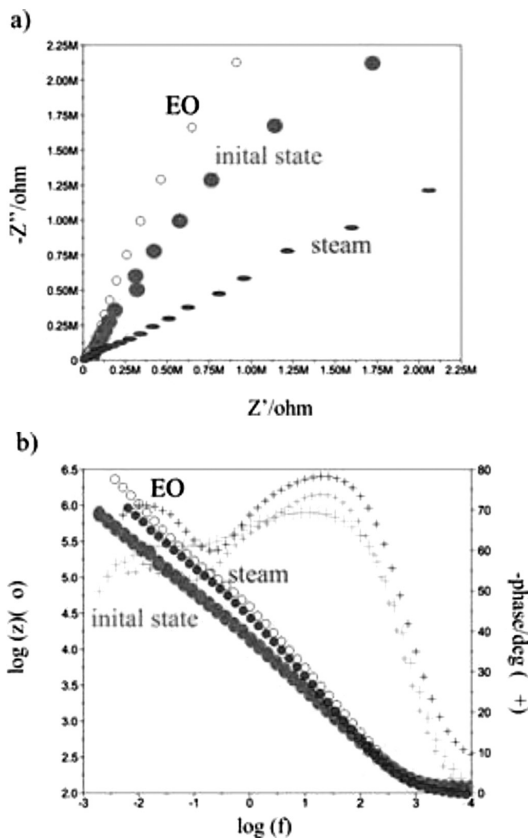


Figure 8: Impedance spectra for the sample Ti67+TiO₂: a) Nyquist plot, b) Bode diagram

Slika 8: Impedančni spekter vzorca Ti67+TiO₂: a) diagram Nyquist, b) diagram Bode

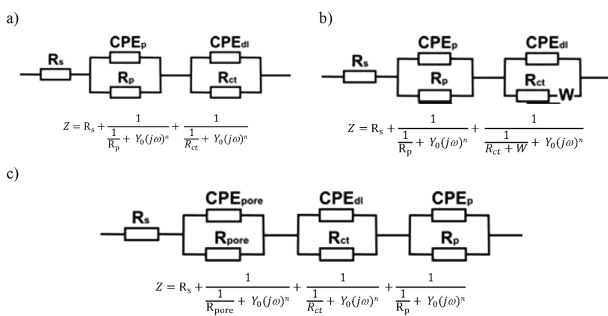


Figure 9: Physical models of an electrical equivalent system of the corrosion system metal – solution⁹⁻¹¹

Slika 9: Fizikalni model električnega ekvivalentnega sistema korozijskega sistema kovina-raztopina⁹⁻¹¹

reflects the electrolyte resistance in this sphere of the material (Table 2).

The impedance spectra obtained for the Ti67+TiO₂ (EO) sample were adjusted to the substitute system, which indicates the presence of three time invariables (Figure 9c). The symbols in Figure 9c signify the following: *CPE_{pore}* – capacity of the surface sphere of the material with a high level of surface extension (porous), *R_{pore}* – electrolyte resistance in pores, *CPE_{dl}* – capacity of the double layer, *R_{ct}* – charge-transfer resistance at the phase boundary (it characterises the speed of the corro-

sive process), *C_{dl}* – capacity of the double layer, *CPE_p* – capacity of the passive layer (oxide), *R_p* – passive (oxide) layer resistance (Table 2).⁹⁻¹¹

4 CONCLUSIONS

An important problem in the process of modelling the performance properties of the implants used in cardiology is the proper selection of the physical and chemical characteristics of their surface. The physico-chemical properties of the implant surface should be adjusted to the characteristics of the human tissue environment – in this case, to the blood environment. The safety of the device’s use is also associated with the need to follow the proper procedures preventing the transfer of pathogenic microorganisms into the human organism. The aim of these procedures is to remove and effectively destroy the microorganisms, i.e., to obtain sterile devices that meet the quality requirements defined in the standards. For medical devices that come into contact with blood, sterilisation with ethylene oxide or pressurised-water steam are the most frequently used. Therefore, accounting for the effect of these sterilisation processes on the properties of the analysed surface layer will enable their complete characterisation.¹⁷

The conducted impedance tests revealed that on the surface of the Ti-6Al-7Nb alloy, modified through anodic oxidation, a porous layer (TiO₂) is found, in which parallel channels with an ionic conduction are formed. These processes intensify during the activity of pressurised-water steam in the sterilisation process. As a consequence, it leads to the partial dissolution of TiO₂, as indicated by the lower value of the ionic transfer resistance *R_{ct}*. Sterilisation with ethylene oxide positively increases the *R_{ct}* value. This phenomenon may be caused by the increased oxygen concentration near the surface during the process, and the formation of an additional oxide layer. Diffusion processes associated with the partial dissolution of oxide in the solution were not observed in the samples with an applied SiO₂ layer. This layer appears to be more compact than the TiO₂. Regardless of the sterilisation method used, no changes in the properties of the layer were found. Only, as was the case with the samples undergoing anodic oxidation, a reduction in the ion-transfer resistance *R_{ct}* was observed. The conducted tests for layer adhesion to the base revealed a slight reduction in the adhesive force of the sterilised layers versus the samples in the initial state. The tests demonstrated the better adhesion of TiO₂ than SiO₂ to the Ti-6Al-7Nb alloy base. The hardness testing conducted in the study revealed that pressurised steam does not cause significant changes to the hardness of the TiO₂ or SiO₂, whereas sterilisation with ethylene oxide results in an increased hardness of the SiO₂ and a significant reduction in the hardness of the TiO₂. This phenomenon

may cause increased porosity of the TiO₂ layer, resulting from the effect of ethylene oxide, as demonstrated in the EIS tests. The SiO₂ layer also reacts when in contact with ethylene oxide. Its hardness significantly increases, which may be the cause of the formation on its surface of an additional oxide layer, based on Ti and Si, revealing better mechanical properties. To sum up, the conducted study of the modified surfaces of the Ti-6Al-7Nb alloy samples with the TiO₂ and SiO₂ layers demonstrated that the medical sterilisation process affects the physical and chemical properties of these layers. The selection of the proper surface layers should also depend on the manner and the method of sterilisation.

Acknowledgements

The project was funded by the National Science Centre, allocated on the basis of decision No. 2011/03/B/ST8/06499.

5 REFERENCES

- ¹ W. Walke, Z. Paszenda, M. Basiaga, P. Karasiński, M. Kaczmarek, EIS study of SiO₂ oxide film on 316L stainless steel for cardiac implants. *Information Technologies in Biomedicine*, 4, *Advances in Intelligent Systems and Computing*, 284 (2014), 403–410 doi:10.1007/978-3-319-06596-0_38
- ² N. Ibris, J. C. M. Rosca, EIS study of Ti and its alloys in biological media, *Journal of Electroanalytical Chemistry*, 526 (2002), 53–62, doi:10.1016/S0022-0728(02)00814-8
- ³ J. Y. Park, J. E. Davies, Red blood cell and platelet interactions with titanium implant surfaces, *Clinical Oral Implants Research*, 11 (2000) 6, 530–539, doi:10.1034/j.1600-0501.2000.011006530.x
- ⁴ J. E. Ellingsen, Pre-treatment of titanium implants with fluoride improves their retention in bone, *Biomaterials*, 12 (1991) 6, 593–596, doi:10.1016/0142-9612(91)90057-H
- ⁵ M. Basiaga, Z. Paszenda, A. Kajzer, The effect of EO and steam sterilization on mechanical and electrochemical properties of titanium Grade 4, *Mater. Tehnol.*, 50 (2016) 1, 153–158 doi:10.17222/mit.2014.241
- ⁶ C. Sitting, G. Hahner, A. Marti, M. Textor, N. D. Spencer, R. Hauert, Mechano-electrochemical synthesis of porous Ti-based nanocomposite biomaterials, *Journal of Materials Science: Materials in Medicine*, 10 (1999), 191–198
- ⁷ S. Shibli, S. Mathai, The role of calcium gluconate in electrochemical activation of titanium for biomimetic coating of calcium phosphate, *J. Mat. Sci.*, 19 (2008), 2971–2981
- ⁸ P. Karasiński, J. Jaglarz, M. Reben, E. Skoczek, J. Mazur, Porous silica xerogel films as antireflective coatings. Fabrication and characterization, *Optical Materials*, 33 (2011), 1989–1994
- ⁹ M. Basiaga, Z. Paszenda, W. Walke, P. Karasiński, J. Marciniak, Electrochemical impedance spectroscopy and corrosion resistance of SiO₂ coated cpTi and Ti-6Al-7Nb alloy, *Information Technologies in Biomedicine*, 284 (2014), 411–420, doi:10.1007/978-3-319-06596-0_39
- ¹⁰ W. Walke, M. Basiaga, Z. Paszenda, Tests of mechanical properties of SiO₂ layers for implants used in vascular system, *Engineering of Biomaterials*, 124 (2014), 36–41
- ¹¹ A. Kajzer, W. Kajzer, J. Dzielicki, D. Matejczyk, The study of physicochemical properties of stabilizing plates removed from the body after treatment of pectus excavatum. *Acta of Bioengineering and Biomechanics*, 2 (2015), 35–44 doi:10.5277/ABB-00140-2014-02
- ¹² J. von Stebut, Multi-mode scratch testing – a European standards, measurements and testing study, *Surface and Coatings Technology*, 200 (2005), 346–350, doi:10.1016/j.surfcoat.2005.02.055
- ¹³ EN ISO 14577-1 Metallic materials-Instrumented indentation test for hardness and materials parameters-Part1: Test method
- ¹⁴ ASTM F2129-08 Standard Test Method for Conducting Cyclic Potentiodynamic Polarization Measurements to Determine the Corrosion Susceptibility of Small Implant Devices
- ¹⁵ M. Kaczmarek, W. Walke, Z. Paszenda, Application of electrochemical impedance spectroscopy in evaluation of corrosion resistance of Ni-Ti alloy, *Electrical Review*, 12b (2011), 74–78
- ¹⁶ M. Kiel-Jamrozik, J. Szewczenko, W. Walke, J. Marciniak, Zastosowanie EIS do oceny własności fizykochemicznych modyfikowanego powierzchniowo stopu Ti-6Al-4V ELI, *Electrical Review*, 12b (2012), 232–235
- ¹⁷ W. Walke, J. Przędziona, J. Szade, Electrochemical and XPS studies of AISI 316L after Development of warm forging method for magnesium alloy *European Cells and Materials*, 26 (2013) 6, 117

SURFACE PROPERTIES OF A LASER-TREATED BIOPOLYMER

LASTNOSTI POVRŠINE BIOPOLIMERA, OBDELANEGA Z LASERJEM

Iva Michaljaničová¹, Petr Slepíčka¹, Silvie Rimpelová², Petr Sajdl³, Václav Švorčík¹

¹University of Chemistry and Technology, Department of Solid State Engineering, Technická 5, 166 28 Prague, Czech Republic

²University of Chemistry and Technology, Department of Biochemistry and Microbiology, Technická 5, 166 28 Prague, Czech Republic

³Institute of Chemical Technology, Department of Power Engineering, Technická 5, 166 28 Prague, Czech Republic
iva.michaljanicova@vscht.cz

Prejem rokopisa – received: 2014-10-14; sprejem za objavo – accepted for publication: 2015-05-04

doi:10.17222/mit.2014.260

Structured surfaces allow the application of commonly used polymers to be extended into specialized fields. This paper describes the construction of surface structures on biopolymer poly(L-lactide) (PLLA), with a method combining krypton fluoride laser (KrF), excimer laser exposure and thermal annealing. PLLA is a commonly used substrate for medical purposes, such as implants and tissue matrices, but it still has a number of limitations, which can be eliminated with its modification. This work is focused on morphological studies and roughness measurements of a structured PLLA substrate using atomic-force microscopy (AFM) and chemical changes investigated with UV-Vis spectroscopy and X-ray photoelectron spectroscopy (XPS). Finally, the biocompatibility of the material was tested using a model cell line of mouse embryonic fibroblasts (NIH 3T3). Using the laser treatment in combination with thermal annealing, we prepared surface layers with various patterns dependent on the chosen input parameters.

Keywords: biopolymer, excimer laser, nanostructuring, thermal annealing, characterization

Strukturirane površine omogočajo razširitev uporabe običajnih polimerov tudi na posebna področja. Članek opisuje pripravo površinske zgradbe biopolimera poly(L-lactide) (PLLA), s kombinirano metodo, z izpostavitvijo excimer laserju (KrF) in toplotno obdelavo. PLLA je običajno uporabljena osnova za medicinske namene kot so vsadki in osnove tkiv, vendar so še številne omejitve, ki se jih da odpraviti z njihovim modificiranjem. Članek je osredotočen na študij morfologije in meritve hrapavosti strukturirane PLLA podlage, z mikroskopijo na atomsko silo (AFM) in preiskave kemijskih sprememb z UV-Vis spektroskopijo in rentgensko fotoelektronsko spektroskopijo (XPS). Preizkušena je bila tudi biokompatibilnost materiala z uporabo modelne celične linije embrionskih fibroblastov miši (NIH 3T3). Z lasersko obdelavo, v kombinaciji s toplotno obdelavo, so bile pripravljene plasti na površini z različnimi vzorci odvisno od izbranih vhodnih parametrov.

Ključne besede: biopolimer, ekscimer laser, nanostrukturiranje, postopek žarjenja, karakterizacija

1 INTRODUCTION

Poly(L-lactic acid) or poly(lactide) is a biodegradable and bioabsorbable thermoplastic polyester, produced from renewable sources.¹ In medical applications, it is used in the matrices for tissue engineering, stents, sutures or in drug delivery systems, but it still has a lot of limitations, which can be eliminated with its appropriate modification.

Polymer structuring allows a utilization of ordinary materials in highly specialized fields. Nanostructured materials find different applications, e.g., in DNA and protein sequencing², in the creation of a suitable synthetic environment for cell growth³ or in the solar-cell technology.⁴ Self-organized structures are prepared with a bottom-up method. A typical example of nanostructuring is a ripple or dot formation caused by laser irradiation. The ripples arise due to the interference pattern formation at a surface and the subsequent response of the surface.⁵

Another example of a self-organizing mechanism is wrinkling instability, which exhibits a variety of surface patterns. Wrinkles are produced by the residual stress,

which exceeds the critical value.⁶ Wrinkle patterns are included, e.g., in tunable optical devices⁷ or flexible electronics.⁶⁻⁸

This paper deals with the surface modification of poly(L-lactic acid) using laser treatment in combination with thermal annealing. Treated samples were studied with atomic-force microscopy (AFM), UV-Vis spectroscopy, and ARXPS (angle-resolved photoelectron spectroscopy). Tests of biocompatibility were carried out with mouse embryonic fibroblasts (NIH 3T3). With this modification, we prepared various surface patterns with a wrinkle-like structure.

2 MATERIALS AND METHODS

2.1 Materials and modification

We used biopolymer poly(L-lactic acid) (PLLA, a density of 1.25 g cm⁻³, $T_g = 60$ °C, a crystallinity of 60–70 %, 50- μ m-thick foils, supplied by Goodfellow Ltd., Cambridge, Great Britain).

For the irradiation of PLLA we used a KrF excimer laser (Coherent Compex Pro 50, a wavelength of 248 nm, a pulse duration of 20–40 ns, a repetition rate of 10

Hz). The beam of the KrF laser was polarized linearly with a cube of UV-grade fused silica 25 mm × 25 mm × 25 mm with an active polarization layer. For a homogeneous illumination of the samples, we used only the central part of the beam profile by means of an aperture 0.5 cm × 1.0 cm. The samples were mounted onto a translation stage, being perpendicular to the laser beam. The chosen pulses were in a range of 100–6000, having laser fluences in an interval of 6–30 mJ cm⁻².

The thermal treatment of the polymers was accomplished with a BINDER thermostat. The samples were heated to 60 °C (the glass-transition temperature of PLLA) immediately after the laser treatment. After 30 min of thermal annealing, the samples were cooled down to room temperature (RT).

2.2 Measurement techniques

The surface morphology and roughness of the pristine and modified polymer samples were examined with the atomic-force-microscopy (AFM) technique using a VEECO CP II device in the tapping mode. The tapping mode was chosen to minimize the damage to the sample surface. A RTESPA-CP Si probe with a spring constant of 20–80 N m⁻¹ was used. The mean roughness value (R_a) represents the arithmetic average of the deviations from the center plane of a sample.

The presence of oxygen and carbon in the PLLA surface layer was determined with X-ray photoelectron spectroscopy (XPS). An Omicron Nanotechnology ESCAProbeP spectrometer was used. The exposed and analyzed area had a dimension of 2 mm × 3 mm. The X-ray source was monochromated at 1486.7 eV. Characteristic O(1s) and C(1s) peaks were searched for. Atomic concentrations of the elements were determined with the CASA XPS program using an integrated area of spectrum lines and relative sensitivity factors, quoted in the database of CASA XPS.

UV-Vis spectra were measured using a Perkin Elmer Lambda 25 spectrometer in a spectral range of 190–1100 nm with a bandwidth of 1 nm (fixed).

2.3 Cytocompatibility tests

For cell-culture experiments, we used an adherent model cell line of mouse embryonic fibroblasts (NIH 3T3) (ATCC, USA). NIH 3T3 cells were cultivated on a regular basis in high-glucose Dulbecco's modified Eagle medium (DMEM, Sigma, USA) supplemented with stable 2 mM L-glutamine, 10 % fetal bovine serum and 1 % MEM vitamin solution (Invitrogen, USA). The cells were maintained at standard conditions (37 °C, a 95 % humidified atmosphere, 5 % CO₂). The cells were maintained in exponential growth.

The bio-response of individual PLLA samples was tested. The polymers were first sterilized in 70 % ethanol for 1 h, air dried, inserted into 12-well plates for cell cultures (VWR, Ø 2.14 cm) and weighted with poly(methyl

methacrylate) cavus cylinders. The samples were seeded with the NIH 3T3 cells, with a density of 14,000 cells per cm⁻² in 800 µL of a complete DMEM. An identical batch of cells growing on a polystyrene Petri dish (PS) was used as a control. The experiments were done in triplicates.

The cells intended for a fluorescence-microscopy analysis were fixed and stained. They were washed twice with phosphate-buffered saline (PBS, pH = 7.4) and fixed with 1 mL of a 4 % formaldehyde (Thermo Scientific, USA) solution in PBS at 37 °C for 20 min. A phalloidin-tetramethylrhodamine B isothiocyanate (Sigma, USA) solution in PBS (0.5 µg·mL⁻¹, 10 min) was used to visualize F-actin; cellular nuclei were stained with a solution of 4',6-diaminido-2-phenylindole dihydrochloride (DAPI, Sigma, USA) in PBS (0.5 µg·mL⁻¹, 5 min). During and after the staining, the cells were rinsed twice with PBS to remove the excess of unbound dyes.

3 RESULTS

Because the laser itself has just a small effect on the surface morphology and the roughness of PLLA, we investigated the influence of the laser treatment in a combination with thermal annealing. We used excimer radiation followed by thermal annealing, which was proven to significantly influence the morphology. For the reverse order of the applied methods, we observed just insignificant morphological deviations on the samples in comparison to the samples treated only by a laser beam. On the contrary, for those samples where the thermal annealing was the second step of the treatment, the sample surfaces were rapidly changed. Moreover, for a low laser fluence and a high number of pulses (6–15 mJ cm⁻² and 6000 pulses) the surface roughness was also significantly increased.

Figure 1 shows the influence of the applied methods on the sample morphology. The modification of the samples at the top of **Figure 1** shows a structure practically identical with the pristine PLLA and the roughness is also similar to the R_a value of the pristine PLLA, which was determined as 6.9 nm. By applying different laser parameters, we prepared different patterns with various roughness values. An important parameter affecting the sample roughness is the combination of the laser fluence and the number of pulses. If the laser energy is too high, the surface is flattened (30 mJ cm⁻², 6000 pulses, R_a = 0.7 nm), but with a lower energy, the surface prepared can be extremely rough, with a spongy structure (15 mJ cm⁻², 3000 pulses, R_a = 44.7 nm).

The concentration of the surface oxygen was determined with XPS and the results for the selected samples are listed in **Table 1**. According to these results, it is not possible to conclude that the oxygen concentration decreases or increases after the modification because the differences in the concentration were within the stati-

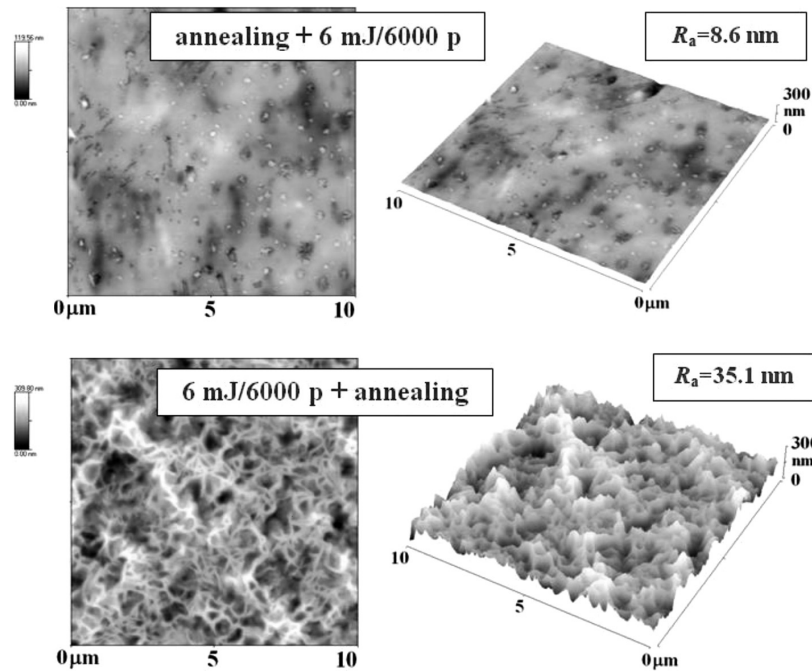


Figure 1: Surface morphology of the samples treated with a combination of an excimer laser (6 mJ cm^{-2} , 6,000 pulses) and thermal annealing ($60 \text{ }^\circ\text{C}$, 30 min). The samples at the top were first annealed and then modified with the laser; the samples at the bottom were treated in the reverse order. R_a represents the arithmetic mean surface roughness in nm.

Slika 1: Morfologija površine vzorcev obdelanih s kombinacijo ekscimer laserja in žarjenja. Morfologija površine vzorcev, obdelanih s kombinacijo ekscimer laserja (6 mJ cm^{-2} , 6,000 pulzov) in žarjenjem ($60 \text{ }^\circ\text{C}$, 30 min). Vzorci zgoraj so bili najprej žarjeni in nato modificirani z laserjem, vzorci spodaj so bili obdelani v obratnem vrstnem redu. R_a predstavlja aritmetično sredino hrapavosti površine v nm.

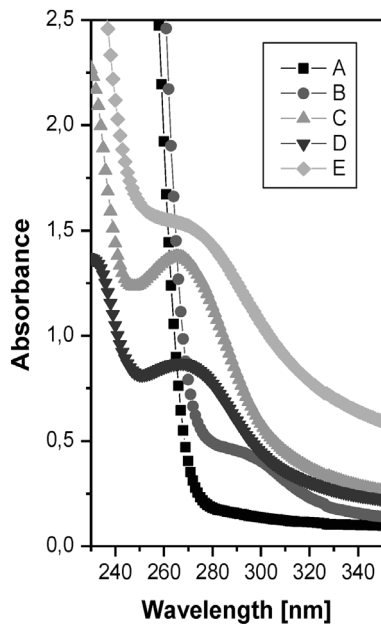


Figure 2: UV-Vis spectra of PLLA. UV-Vis spectra of: A) pristine PLLA and samples exposed to laser fluence 9 mJ cm^{-2} and 30 mJ cm^{-2} (1000 and 6000 pulses) and subsequently treated by thermal annealing ($60 \text{ }^\circ\text{C}$, 30 min), B) 9 mJ cm^{-2} , 1000 pulses + annealing, C) 9 mJ cm^{-2} , 6000 pulses + annealing, D) 30 mJ cm^{-2} , 1,000 pulses + annealing and E) 30 mJ cm^{-2} , 6,000 pulses + annealing.

Slika 2: UV-Vis spekter PLLA. UV-Vis spekter: A) prvoten PLLA in vzorci izpostavljeni laserju pri 9 mJ cm^{-2} in 30 mJ cm^{-2} (1000 in 6000 pulzov) in nato obdelani z žarjenjem ($60 \text{ }^\circ\text{C}$, 30 min), B) 9 mJ cm^{-2} , 1000 pulzov + žarjenje, C) 9 mJ cm^{-2} , 6000 pulzov + žarjenje, D) 30 mJ cm^{-2} , 1000 pulzov + žarjenje in E) 30 mJ cm^{-2} , 6000 pulzov + žarjenje.

stical error (about 2 %), which could have taken place during the measurement. It is possible to conclude that the oxygen concentration decreases towards the surface of the spongy structure (the plane-surface oxygen concentration is higher in comparison with the pattern at the very top). This decrease can be contributed to the reorientation of dipoles (oxygen-containing groups) toward the polymer surface.

Table 1: Element concentration of the PLLA surface. The values were determined, with XPS method, for pristine and laser-treated (9 mJ cm^{-2} , 6000 pulses) samples, further for samples treated with laser followed by thermal annealing (9 mJ cm^{-2} , 6000 pulses, $60 \text{ }^\circ\text{C}$, 30 min). The samples were measured at angles of 0° and 80° .

Tabela 1: Koncentracija elementov na površini PLLA. Vrednosti so bile določene z metodo XPS na originalnih in z laserjem obdelanih (9 mJ cm^{-2} , 6000 pulzov) vzorcih, nato na vzorcih obdelanih z laserjem, ki mu je sledilo žarjenje (9 mJ cm^{-2} , 6000 pulzov, $60 \text{ }^\circ\text{C}$, 30 min). Vzorci so bili merjeni pri kotih 0° in 80° .

Sample	Angle ($^\circ$)	C (amount fractions, x/%)	O (amount fractions, x/%)
Pristine	0	64.4	35.6
	80	67.7	32.3
Laser treatment	0	63.2	36.8
	80	65.4	34.6
Laser treatment + annealing	0	62.6	37.4
	80	67.7	32.3

The UV-Vis absorption spectra of the samples exposed to laser fluences of 9 and 30 mJ cm^{-2} with 1000 and 6000 pulses and subsequently treated with thermal

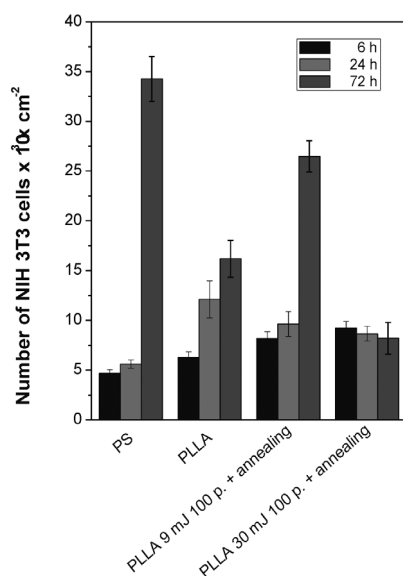


Figure 3: Tests of surface cytocompatibility. Dependence of the number of adhered and proliferated NIH 3T3 cells (6, 24, and 72) h after seeding on pristine PLLA (PLLA) and PLLA modified by laser beam (9 mJ cm^{-2} or 30 mJ cm^{-2} , 100 pulses) and subsequent thermal annealing ($60 \text{ }^\circ\text{C}$, 30 min). The values for tissue polystyrene (PS) are also shown for comparison.

Slika 3: Preizkus citokompatibilnosti površine. Odvisnost števila oprijetih in razmnoženih NIH 3T3 celic, (6, 24, 72) h po sejanju na prvotni PLLA (PLLA) in na PLLA obdelan z laserskim žarkom (9 mJ cm^{-2} ali 30 mJ cm^{-2} , 100 pulzov), ki mu je sledilo žarjenje ($60 \text{ }^\circ\text{C}$, 30 min). Za primerjavo so prikazane tudi vrednosti za tkivni polistiren (PS).

annealing ($60 \text{ }^\circ\text{C}$, 30 min) are shown in **Figure 2**. In the case of the spectra of the modified samples, there are significant peaks at a position of approximately 275 nm. The curve with the most significant peak represents the treatment with a laser fluence of 9 mJ cm^{-2} and 6000 pulses, belonging to a sample with an interesting spongy morphology. The other modified samples also show at least a "small" peak. After the combination of the laser

treatment and thermal annealing, a diagonal shift of the absorbance curve was observed.

The cell adhesion represents the first stage of the cell-substrate interaction, thus the quality of adhesion influences cell ability to proliferate and differentiate in the contact with a substrate. After successful adhesion, the adaptation of the cells to the new environment (the lag phase) occurs. For adhesion and proliferation studies NIH 3T3 cells were chosen. The selected samples of the modified PLLA substrate (9 or 30 mJ cm^{-2} , 100 pulses, annealing) were tested and compared with PLLA pristine and control samples of polystyrene used for tissue cultures (PS). Samples with 100 pulses were chosen, because with the increasing number of pulses the material became brittle. From the **Figure 3**, it is apparent that the best results were obtained on PS, which is commonly considered as a model substrate. The PLLA pristine is a material which biocompatibility can be improved by plasma modification. It was shown that modified material with 30 mJ cm^{-2} was slightly less cytocompatible, but with 9 mJ cm^{-2} moderately improved its cytocompatibility. Immediately after seeding cell adhesion was found unaffected. In the **Figure 4**, there are introduced selected pictures of cells growing on treated and pristine PLLA samples.

4 DISCUSSION

By the combination of excimer laser and thermal annealing, it is possible to prepare different surfaces of PLLA with a wide range of surface roughness. The most interesting part of this work is a wrinkle pattern creation. Wrinkles could appear on polymer after annealing as a thin bi-layer film (prepared by treatment and by annealing). In this case, the surface laser treatment and following thermal annealing has created the wrinkle pattern. We suggest that the structure is influenced also during cooling. With less counts of pulses, the staminate

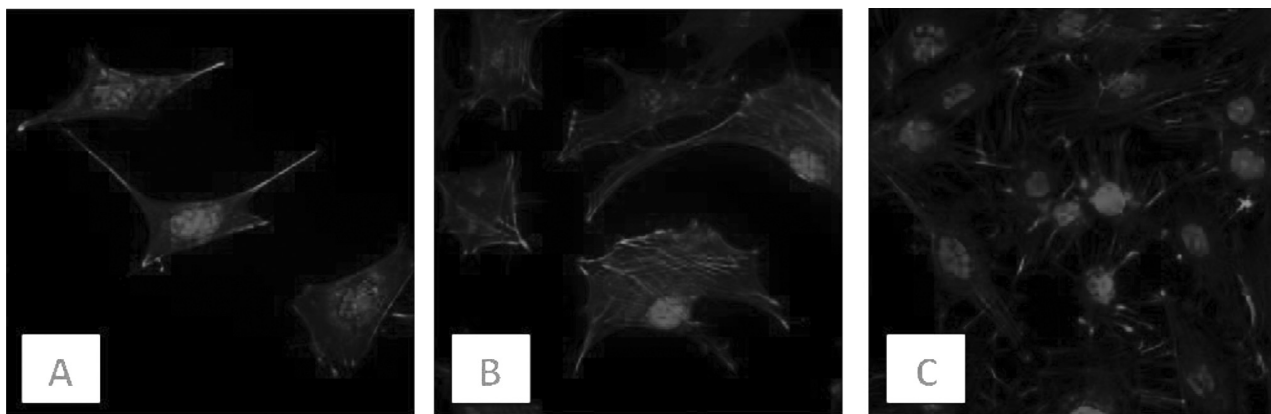


Figure 4: Mouse embryonic fibroblasts (NIH 3T3) growing on different substrates. Proliferated NIH 3T3 cells 72 h after seeding on various substrates: A) modified PLLA (30 mJ cm^{-2} , 100 pulses and subsequent thermal annealing ($60 \text{ }^\circ\text{C}$, 30 min)); B) pristine PLLA, and C) tissue polystyrene for comparison.

Slika 4: Mišji embrionski fibroblasti (NIH 3T3), ki so zrasli na različnih podlagah. Razmnožene NIH 3T3 celice po 72 h po sejanju na različne podlage: A) modificiran PLLA (30 mJ cm^{-2} , 100 pulzov in nato toplotna obdelava ($60 \text{ }^\circ\text{C}$, 30 min), B) prvotni PLLA in C) tkivni polistiren za primerjavo.

patterns were built up. We propose that difference in the structure was caused by the thickness of laser treated layer, which was insufficient to create wrinkles. Instead of that surface cracking occurred. We suggest that “rods” on the PLLA surface were produced by crystallization of the newly formed material from chopped polymer strings. By reverse order of treatment, when the samples were exposed to annealing and subsequently treated by laser beam, the samples showed the same structure as the samples treated just by laser without annealing. This supports the theory, how the structure was formed.

The peak around area of 275 nm is typical for transitions of n electrons to the π^* excited state, and represents the presence of C=O group. This type of transition needs an unsaturated group in the molecule to provide the π electrons. The diagonal shift could be explained by increasing concentration of double bonds.

Cytocompatibility tests show slight decrease of ability to support cell proliferation for the PLLA treated by high laser fluence, the biocompatibility increases for lower laser fluence. The application of lower energy has therefore similar effect as plasma treatment which we studied in our previous experiments.

5 CONCLUSIONS

Various types of surface structures on modified samples of PLLA were produced by exposure of KrF excimer laser beam and subsequent thermal annealing:

- by UV-Vis spectroscopy we observed new C=O groups and creation of double bonds;
- by choosing optimal input parameters, it is possible to prepare structures from porous and spongeous to flat biopolymer surface with staminate structures;
- the roughness is significantly dependent on laser treatment and annealing input values;

- low laser fluence has a positive effect on cytocompatibility, but high laser fluence loses this effect.

Acknowledgements

This work was supported by the GACR under project 13-06609S.

6 REFERENCES

- ¹ R. M. Rasal, A. V. Janorkar, D. E. Hirt, *Progress in Polymer Science*, 3 (2010) 35, 38–356, doi:10.1016/j.progpolymsci.2009.12.003
- ² B. L. Hancock-Hanser, A. Frey, M. S. Leslie, P. H. Dutton, F. I. Archer, P. A. Morin, Targeted multiplex next-generation sequencing: advances in techniques of mitochondrial and nuclear DNA sequencing for population genomics, *Molecular Ecology Resources*, 2 (2013) 13, 254–268, doi:10.1111/1755-0998.12059
- ³ E.-K. Yeong, S.-H. Chen, Y.-B. Tang, The Treatment of Bone Exposure in Burns by Using Artificial Dermis, *Annals of Plastic Surgery*, 6 (2012) 69, 607–610, doi:10.1097/SAP.0b013e318273f845
- ⁴ R. Lecover, N. Williams, N. Markovic, D. H. Reich, D. Q. Naiman, H. E. Katz, Next-Generation Polymer Solar Cell Materials: Designed Control of Interfacial Variables *ACS Nano*, 4 (2012) 6, 2865–2870, doi:10.1021/nn301140w
- ⁵ M. Bolle, S. Lazare, Large scale excimer laser production of sub-micron periodic structures on polymer surfaces, *Applied Surface Science*, 1–4 (1993) 69, 31–37, doi:10.1016/0169-4332(93)90478-T
- ⁶ C.-M. Chen, S. Yang, Wrinkling instabilities in polymer films and their applications, *Polymer International*, 7 (2012) 61, 1041–1047, doi:10.1002/pi.4223
- ⁷ H. S. Kim, A. J. Crosby, Solvent-Responsive Surface via Wrinkling Instability, *Advanced Materials*, 36 (2011) 23, 4188–4192, doi:10.1002/adma.201101477
- ⁸ D. Y. Khang, H. Q. Jiang, Y. Huang, J. A. Rogers, A Stretchable Form of Single-Crystal Silicon for High-Performance Electronics on Rubber Substrates, *Science*, 5758 (2006) 311, 208–212, doi:10.1126/science.1121401

ANALYZING THE HEAT-TREATMENT EFFECT ON THE MECHANICAL PROPERTIES OF FREE-CUTTING STEELS

ANALIZA VPLIVA TOPLLOTNE OBDELAVE NA MEHANSKE LASTNOSTI AVTOMATNIH JEKEL

Mustafa Kemal Kulekci^{1,2}, Ugur Esme^{1,2}, Funda Kahraman^{1,2}, Rahim Ozgun³, Adnan Akkurt⁴

¹Mersin University, Institute of Applied and Natural Sciences, Manufacturing Engineering Department, 33480 Tarsus, Mersin, Turkey

²Mersin University, Faculty of Tarsus Technology, 33480 Tarsus, Mersin, Turkey

³Mersin University, Faculty of Tarsus Technical Education, 33480 Tarsus, Mersin, Turkey

⁴Gazi University, Faculty of Technology, 06500 Ankara, Turkey
mkkulekci@yahoo.com

Prejem rokopisa – received: 2015-01-14; sprejem za objavo – accepted for publication: 2015-06-02

doi:10.17222/mit.2015.011

In this research, the heat-treatment effect on the mechanical properties of free-cutting steels was investigated. Free-cutting steels (FCSs) are used where high degrees of machining are required as they increase the machining speed and reduce the tool wear. The effect of heat treatment on mechanical properties was identified using tensile and fatigue tests, and microstructure images taken with a scanning electron microscope (SEM). The studied material included commercially available AISI 12L14 cylindrical bars of free-cutting steel. FCS was heated to 900 °C and held at this temperature for different time spans. The degradation of the mechanical properties of free-cutting steel due to the elevated temperature was assessed. At a microscopic level, more mechanical damage was observed between the steel matrix and the second phase of the heat-affected specimens.

Keywords: fatigue, tensile strength, free-cutting steel, heat treatment

V prispevku je bil raziskan vpliv toplotne obdelave na mehanske lastnosti avtomatnih jekel. Avtomatna jekla (FCS) se uporabljajo v primerih, ko so zahtevane velike stopnje obdelave, saj dopuščajo večje hitrosti rezanja ob manjši obrabi orodja. Vpliv toplotne obdelave na mehanske lastnosti je bil določen z rezultati nateznega preizkusa in preizkusa utrujenosti. Z vrstičnim elektronskim mikroskopom (SEM) so bili narejeni posnetki mikrostrukture. Preiskovane so bile komercialno dosegljive palice iz avtomatnega jekla AISI 12L14. FCS je bil segret na 900 °C in različno dolgo zadržan na tej temperaturi. Določeno je bilo zmanjšanje mehanskih lastnosti avtomatnega jekla zaradi povišane temperature. V toplotno obdelanih vzorcih je bilo z mikroskopom opaženih več mehanskih poškodb.

Ključne besede: utrujenost, nateg, avtomatna jekla, toplotna obdelava

1 INTRODUCTION

A significant increase in mechanical-machining costs has led to a reappraisal of the importance of steel machinability.¹ In order to achieve higher automation and cost competitiveness, a series of steels commonly known as free-cutting steels (an S minimum of 0.10 %) are being increasingly used. Special lead-containing steels differ from the normal structural, quenched-and-tempered and case-hardened steels because of the presence of Pb (approximately 0.15–0.35 %) in order to improve their machinability. These steels allow an excellent chip removal and they are particularly suitable for large productions.^{2,3} Lead has a very good lubricating effect and, combined with the heating produced by the tools, breaks the chips, thus allowing for a higher productivity resulting in more advantageous production runs. It also guarantees a lower tool wear.

Free-cutting steels are used where high degrees of machining are required as they increase the machining speed and reduce the tool wear. These steels contain manganese, lead, sulphur and phosphorous, which improve the machining performance. The additives reduce

the coefficient of friction between the tool and chip, thereby reducing the cutting force, the temperature and the built-up edge formation, allowing higher feeds and/or speeds.⁴⁻⁶ Free-cutting steels are preferred in manufacturing mechanical components for their improved machinability.⁶⁻⁸

AISI 12L14 is a Pb-added low-carbon resulphurised free-cutting steel containing 0.3 % Pb and 0.3 % S. It is used in large quantities in automotive applications such as transmission oil hydraulic control valves and oil hydraulic hose connectors, in printer shafts and other parts of office automation equipment. Lead is insoluble in free-cutting steel and during the cutting process lead particles are sheared and smeared over the tool-chip interface.^{9,10} Lead improves the machinability with little effect on mechanical properties. Due to its low shear strength, lead acts as a solid lubricant. Manganese and sulphides assist the chip formation and reduce the friction and wear of a cutting tool. Free-cutting steels are used where high degrees of machining are required as they increase the machining speed and reduce the tool wear.

Table 1: Chemical composition of free-cutting steel (AISI 12L14) in mass fractions, (w%)**Tabela 1:** Kemijska sestava avtomatnega jekla (AISI 12L14) v masnih deležih, (w%)

C	Si	Mn	P	S	Cr	Mo	Ni	Cu	Pb	Fe
0.074	0.005	1.203	0.045	0.294	0.04	0.02	0.08	0.12	0.30	balance

In this study, the heat-treatment effect on the mechanical properties of FCS was investigated. FCS was heated to 900 °C and held at this temperature for different time spans. Degradation of the mechanical properties of the free-cutting steel due to the elevated temperature was assessed. The effect of heat treatment on mechanical properties was investigated using tensile and fatigue test results, and microstructure images taken with a scanning electron microscope (SEM).

2 EXPERIMENTAL PROCEDURE

The studied material included commercially available AISI 12L14 cylindrical bars of free-cutting steel with a diameter of 12 mm. The bars were machined into tensile and fatigue specimens with dimensions as shown in **Figure 1**. After the machining, the specimens were grinded with 4000 emery paper. Two samples were used for each stress level and the results were averaged for the as-received specimens and the specimens exposed to 900 °C for (3, 6, 9, 12 and 15) h. The percent chemical composition (% of mass fractions) and mechanical properties of the FCS are given in **Tables 1** and **2**, respectively. Tensile-test specimens were machined according to EN ISO 6892-1 standard. Fatigue tests were conducted on an R. R. Moore type rotating-beam fatigue-testing machine with a frequency of 25 Hz. Microstructural changes in the FCS exposed to high temperature were investigated using SEM images. Tensile tests were conducted to investigate the heat-treatment effect on the ultimate tensile strength (R_m), the yield strength (R_e), the ductility and the toughness. FCS specimens were heated to 900 °C and held at this temperature for different time spans. Degrada-

tion of the mechanical properties of free-cutting steel due to elevated temperature was investigated. More mechanical damage was observed between the steel matrix and the phase in the heat-affected specimens at a microscopic level. The effect of heat treatment on the mechanical properties was investigated using tensile and fatigue tests, and microstructure images taken with SEM. The R_m and R_e values of the FCS decreased as the toughness and ductility increased due to the effect of elevated heat.

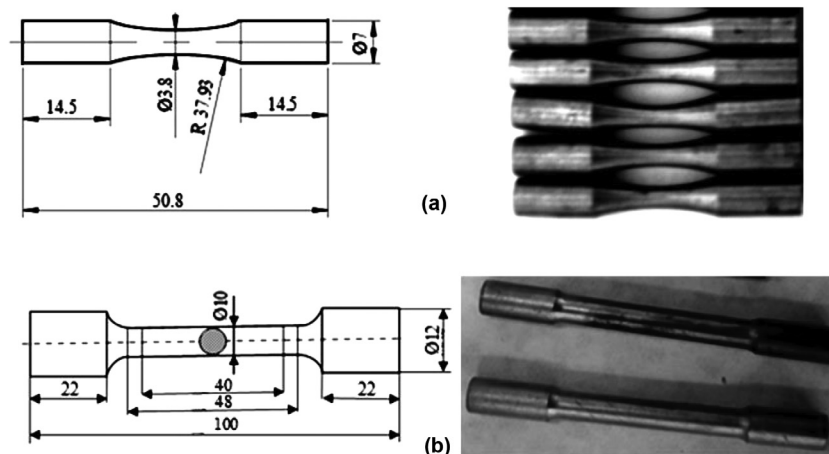
Table 2: Mechanical properties of free-cutting steel (AISI 12L14)**Tabela 2:** Mehanske lastnosti avtomatnega jekla (AISI 12L14)

Yield strength (MPa)	Tensile strength (MPa)	Elongation (%)	Brinell hardness (HB) (10 mm steel ball and 500 kg load)
465	587	12	150

3 RESULTS AND DISCUSSION

Fatigue test results for the FCS specimens with different dwell times and the as-received specimens are given in **Figure 2**. From this figure, it is seen that the fatigue strength of the FCS exposed to elevated temperature decreased. There was a limited effect of the time span affecting the fatigue strength of the tested specimens. Under the cyclic load of 300 MPa, the heat-affected and as-received specimens fractured at 50,000 and 300,000 cycles, respectively. The fatigue strength of the FCS reduced in the ratio of 83 % because of the effect of high temperature. The regression lines of the fatigue strength given in **Figure 2** are expressed as:

$$y = -a \ln(x) + b \quad (1)$$

**Figure 1:** Dimensions and images of test specimens: a) fatigue, b) tensile test**Slika 1:** Mere in posnetki preizkušancev: a) utrujanje, b) natezni preizkus

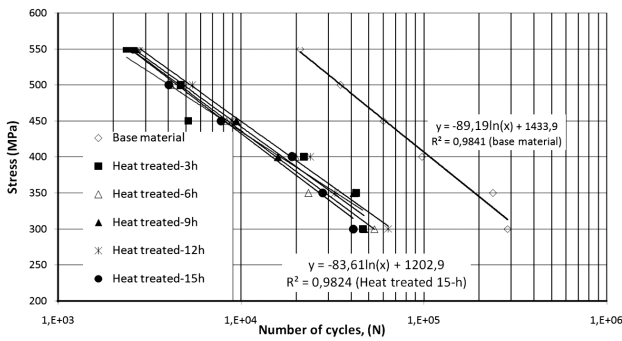


Figure 2: Effect of the heat exposure and time on the fatigue test results for FCS

Slika 2: Vpliv časa ogrevanja na rezultate utrujenostnega preizkusa FCS

where y is the loaded stress range, x is the number of cycles to failure, a and b are the fitting constants. The constants of the equations of regression lines, the R -square, which indicates how well data points fit a statistical model (the coefficient of determination: R^2) and the residual variance (R_v), which is a measure of the variation of the y values about the regression line ($R_v = 1 - R^2$) of the fatigue tests are given in **Table 3**.

Table 3: R-square, residual variance and fitting constants of the tests

Tabela 3: R-kvadrat, preostale variance in ustrezne konstante preizkusov

Experimental variables	Fitting constants of regression lines		R -square (R^2)	Residual variance ($R_v = 1 - R^2$)
	a	b		
Base material	-89.19	1433.9	0.9841	0.0159
Heat treated: 15h	-83.61	1202.9	0.9824	0.0176
Heat treated: 12h	-78.819	1176.1	0.9885	0.0115
Heat treated: 9h	-79.957	1178.6	0.9805	0.0195
Heat treated: 6h	-81.643	1188.4	0.9816	0.0184
Heat treated: 3h	-71.404	1093.6	0.9367	0.0633

The reduction in the fatigue strength of the specimens exposed to high temperature can be explained with microstructural changes. The grain size of the base material and the heat-affected specimens were measured as $10\ \mu\text{m}$ and $25\ \mu\text{m}$, respectively, as seen from **Figure 3**. From this figure, it is seen that the grain size of the FCS increased by 250 % with the heat effect and 3–15 h time spans. The grain growth reduced the load-carrying capacity of the specimens. At the elevated temperature of $900\ \text{°C}$ and under a long dwell time, the precipitated phase coalesced and grew in the microstructure as seen in **Figure 3**. Kalpakjian states that the grain growth reduces the grain boundaries per volume unit of a grain.^{11,12} Smaller grains have a higher strength and a higher contact surface area.

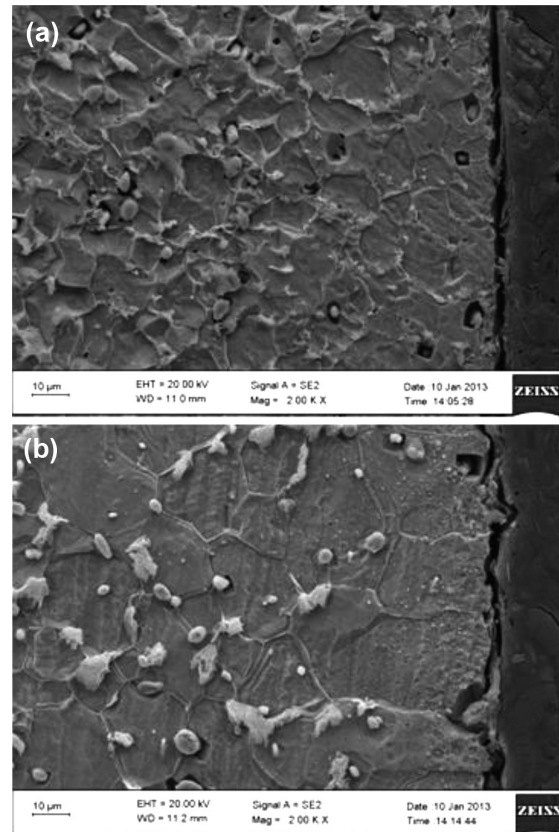


Figure 3: SEM images of grains: a) as received and b) heat treated at $900\ \text{°C}$ for 15 h

Slika 3: SEM-posnetek zrn: a) stanje ob dobavi in b) žarjena 15 h na $900\ \text{°C}$

The increase in the size of the grains reduced the fatigue strength of the FCS. The ultimate tensile strength (R_m) and the yield strength (R_e) of the heat-affected FCS were reduced as seen in **Figure 4**. The toughness of the heat-affected FCS specimens was calculated with the following Equation (2):

$$\text{Toughness} = \frac{R_e + R_m}{2} \cdot e \quad (2)$$

where R_e and R_m are the yield and tensile strengths, respectively, and e is the engineering strain. The R_e and R_m values of the initial FCS specimens were $616\ \text{MPa}$ and $512\ \text{MPa}$, respectively. For the specimens heat-treated at $900\ \text{°C}$ for 3 h, these values were reduced to $441\ \text{MPa}$ and $318\ \text{MPa}$. The reduction in R_m and R_e was 28.4 and 37.8 %, respectively. The amounts of energy per volume (toughness) that the FCS absorbed before rupturing were $100.51\ \text{MPa}$ and $143.67\ \text{MPa}$ for the specimens in the as-received state and heat treated at $900\ \text{°C}$ for 15 h, respectively, as seen in **Figure 4**. The toughness of the FCS increased in the ratio of 42.94 % due to the effects of heat and time. This increase in the toughness of FCS can be explained with the disposal of the residual stress induced during manufacturing stages. The ductility of the FCS specimens was determined

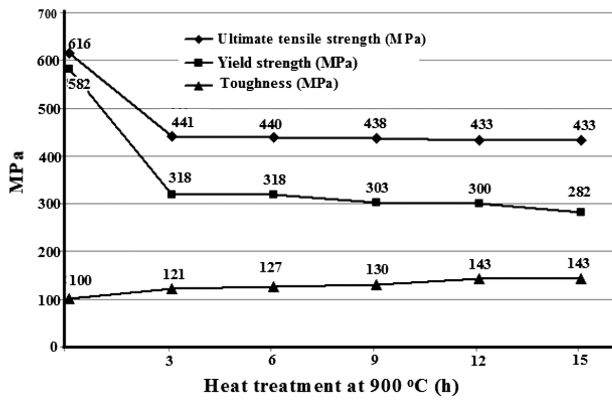


Figure 4: Effect of heat treatment on ultimate tensile strength (R_m), yield strength (R_e) and toughness of FCS

Slika 4: Vpliv žarjenja na natezno trdnost (R_m), mejo plastičnosti (R_e) in žilavost FCS

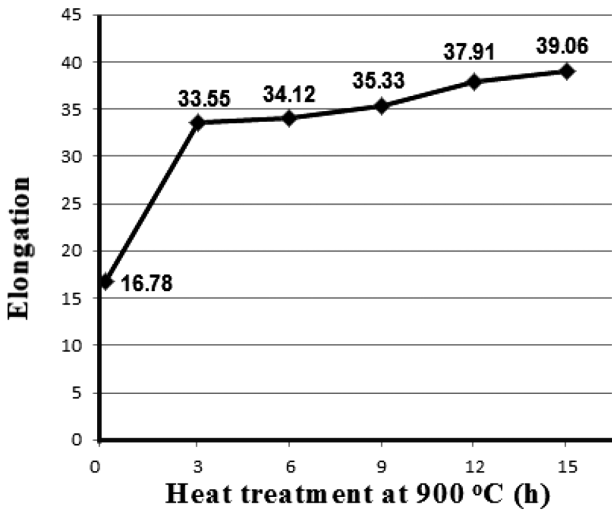


Figure 5: Heat-treatment effect on the elongation of free-cutting steel

Slika 5: Vpliv žarjenja na raztezek avtomatnega jekla

with the elongation calculated with the following Equation (3):

$$\text{Elongation} = \frac{l_f + l_0}{l_0} \cdot 100 \quad (3)$$

where l_0 and l_f are the gage lengths of the original and fractured sample, respectively. The ductility of the FCS changed with the effect of heat treatment, as shown in Figure 5. The ductility was 16.78 % and 39.06 % for the as-received specimens and the specimens heat-treated at 900 °C for 15 h, respectively. SEM images of the fatigue-fractured surfaces of the as-received and heat-affected specimens are given in Figure 6. The heat effect increased the voids between the matrix and the second phase of the FCS under cyclic load during the fatigue test, as seen in Figure 6. From this figure, it is clearly seen that the voids between the matrix and the

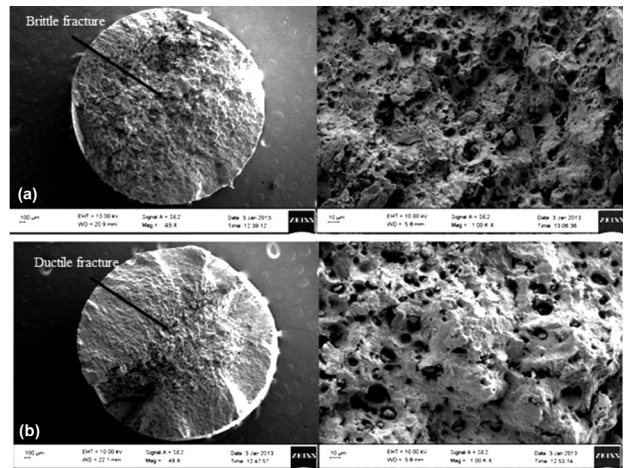


Figure 7: Macrostructures (49X) and microstructures (1000X) of fractured specimens: a) as received and b) heat treated at 900 °C for 15 h

Slika 7: Makrostruktura in mikrostruktura prelomljenega vzorca: a) dobavljeno in b) žarjeno 15 ur na 900 °C

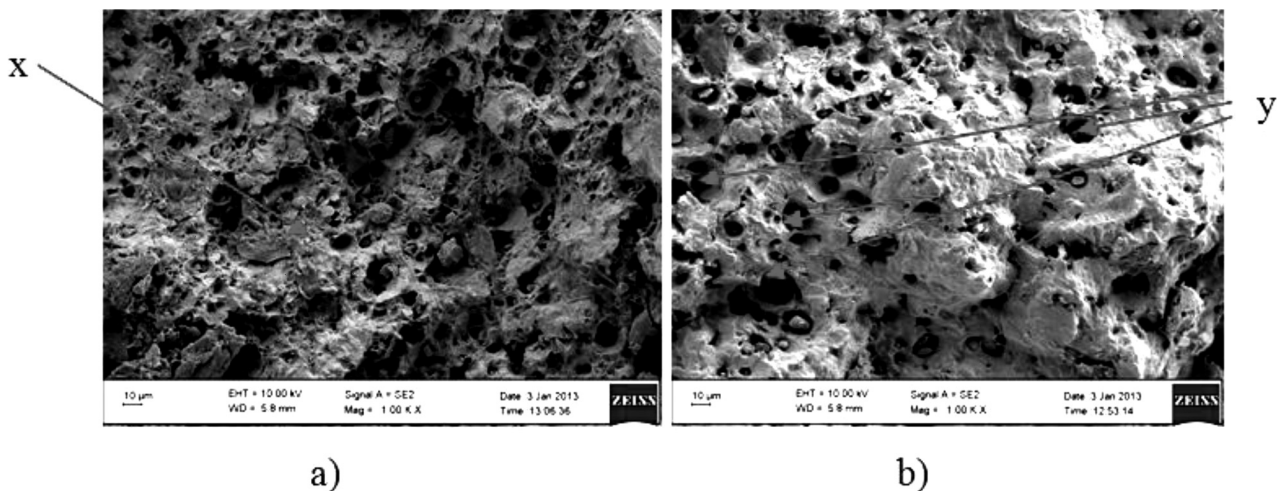


Figure 6: SEM images of fatigue-fractured surfaces of FCS: a) as received, b) heat treated at 900 °C for 15 h (x and y are voids)

Slika 6: SEM-posnetek površine utrujenostnega loma FCS: a) stanje ob dobavi, b) žarjeno 15 h na temperaturi 900 °C (x in y so praznine)

second phase are larger in the structure of the heat-affected specimens (**Figure 6b**). The heat-treatment effect made the material more ductile and, as a result, the bonding between the matrix and the second phase was weakened, while the fatigue and tensile strengths of the FCS decreased as well.

Macro- and microstructure images of the fractured specimens in the as-received and heat-affected states are given in **Figures 7a** and **7b**, respectively. The base material exhibited brittle fracture, while the heat-treated specimens exhibited ductile fracture. The fatigue values, R_m and R_e , of the base material were higher than those of the heat-treated FCS, as seen in **Figures 2** and **4**. This situation can be explained with the residual stress included in the as-received specimens. The grain growth due to the heat treatment of the FCS material also reduced these values.

4 CONCLUSION

From the above results, the following conclusions can be drawn:

- The heat effect made the material more ductile and weakened the bonding between the matrix and the second phase.
- The microstructure of the FCS changed at 900 °C. The elevated temperature and a long dwell time resulted in the grain growth and precipitation, which caused a decrease in the fatigue and tensile strengths.
- The grain size of the FCS increased by up to 250 % with the heat treatment at 900 °C and a dwell time of 15 h. The grain growth reduced the load-carrying capacity of the specimens.
- The fatigue strength of the FCS was reduced in the ratio of 83 % due to the effect of the high temperature and long dwell time.
- The heat treatment at 900 °C, for a period of less than 3 h reduced R_m and R_e in the ratio of 28.4 and 37.8 %, respectively, when compared to the base material.
- The toughness of the FCS increased in the ratio of 42.94 % due to the effect of heat treatment and dwell time.
- The heat effect led to increased ductility and larger voids between the matrix and the second phase of the FCS under a cyclic load. At a microscopic level, more mechanical damage was observed between the steel matrix and the second phase of the heat-affected specimens.
- The effect of time on the fatigue strength of the tested specimens is less significant.

Acknowledgement

This work was financially supported by the Scientific Research Foundation of the Mersin University under contract MAE-1-2010. This support is gratefully acknowledged.

5 REFERENCES

- ¹ M. Toshiyuki, T. Kunikazu, S. Tetsuo, Development of free cutting steel without lead addition to replace AISI12L14, JFE Technical Report, 15 (2010), 10–16
- ² L. D. Chiffre, of metal cutting and cutting fluid action, International Journal of Machine Tool Design and Research, 17 (1977) 4, 225–234, doi:10.1016/0020-7357(77)90016-6
- ³ A. J. Deardo, C. I. Garcia, U. S. Patent Nr. 6200395, 2001
- ⁴ P. L. B. Oxley, Mechanics of Machining: An Analytical Approach to Assessing Machinability, John Wiley & Sons, New York 1989
- ⁵ P. S. Sreejith, B. K. A. Ngoi, Dry machining: Machining of the future, Journal of Materials Processing Technology, 101 (2000) 1–3, 287–291, doi:10.1016/S0924-0136(00) 00445-3
- ⁶ H. Roelofs, A. M. G. Boeira, R. Margot, J. T. Gomes, M. Eglin, Machinability of Inclusion Engineered Free Cutting Steel Under Built Up Edge Conditions, 8th Int. Conf. on Advanced Manufacturing Systems and Technology, Udine 2008, 12–13
- ⁷ Z. Li, D. Wu, Effect of Free-cutting Additives on Machining Characteristics of Austenitic Stainless Steels, Journal of Materials Science & Technology, 26 (2010) 9, 839–844, doi:10.1016/S1005-0302(10) 60134-X
- ⁸ Y. Y. Wei, Z. Q. Liu, Q. L. An, M. Chen, Study on the Machinability of Free-Cutting Steels 1214 and 12L15 with Coated Tool, Advanced Materials Research, 426 (2012), 151–154, doi:10.4028/www.scientific.net/AMR.426.151
- ⁹ A. D. Foster, J. Lin, D. C. J. Farrugia, T. A. Dean, An Investigation into Damage Nucleation and Growth for a Free-Cutting Steel at Hot Rolling Conditions, The Journal of Strain Analysis for Engineering Design, 42 (2007) 4, 227–235, doi:10.1243/03093247JSA230
- ¹⁰ J. Polak, M. Petrevec, J. Man, Cyclic plasticity, cyclic creep and fatigue life of duplex stainless steel in cyclic loading with positive mean stress, Metallic Materials, 49 (2011) 5, 347–354, doi:10.4149/km_2011_5_347
- ¹¹ R. Özgün, Investigation of the Effect of High Temperature and Boric Acid Environment on the Mechanical Properties of Free Cutting Steels, University of Mersin, 2014
- ¹² S. Kalpakjian, S. Schmid, Manufacturing Engineering and Technology, 6th Ed., Pearson Hall, New York 2010

ANALYSIS OF THE CUTTING TEMPERATURE AND SURFACE ROUGHNESS DURING THE ORTHOGONAL MACHINING OF AISI 4140 ALLOY STEEL VIA THE TAGUCHI METHOD

ANALIZA TEMPERATURE REZANJA IN HRAPAVOSTI POVRŠINE S TAGUCHI METODO PRI ORTOGONALNI STROJNI OBDELAVI LEGIRANEGA JEKLA AISI 4140

Ali Riza Motorcu¹, Yahya Isik², Abdil Kus², Mustafa Cemal Cakir³

¹Çanakkale Onsekiz Mart University, Engineering Faculty, Department of Industrial Engineering, 17100 Çanakkale, Turkey

²Uludağ University, Vocational School of Technical Science Machinery Program, 16059 Bursa, Turkey

³Uludağ University, Engineering Faculty, Department of Mechanical Engineering, 16059 Bursa, Turkey
armotorcu@comu.edu.tr

Prejem rokopisa – received: 2015-01-22; sprejem za objavo – accepted for publication: 2015-06-08

doi:10.17222/mit.2015.021

In this research, the tool-chip interface temperature (T_{CTI}), the tool temperature (T_T) and the average surface roughness (R_a) were measured experimentally during the turning of AISI 4140 alloy steel with TiAlN-TiN, PVD-coated, WNVG 080404-IC907 tungsten carbide inserts using an IR pyrometer technique, a K-type thermocouple and a portable surface-roughness measurement device, respectively. The workpiece material was heat treated by an induction-hardening process and hardened up to a value of 50 HRC. The Taguchi method L18 (21×37) was used for the determination of the optimum control factors. The depth of cut, the cutting speed and the feed rate were taken as control factors. The analysis of variance was applied in order to determine the effects of the control factors on the tool-chip interface temperature, the tool temperature and the surface roughness. The optimum combinations of the control factors for T_{CTI} , T_T and R_a were determined as $a_2v_1f_3$, $a_1v_3f_2$ and $a_2v_3f_1$, respectively. Second-order predictive models were developed with a linear-regression analysis, and the coefficients of correlation for T_{CTI} , T_T and R_a were calculated as $R^2 = 92.8$, $R^2 = 68.1$ and $R^2 = 82.6$, respectively.

Keywords: tool temperature, thermocouple, pyrometer, machining, Taguchi method

V raziskavi so bile eksperimentalno izmerjene temperature na stiku orodje-ostružek (T_{CTI}), temperatura orodja (T_T) in povprečna hrapavost površine (R_a) pri struženju legiranega jekla AISI 4140, z volfram karbidnimi vložki WNVG 080404-IC907 s PVD prevleko iz TiAlN-TiN, z uporabo IR pirometra, termoelementi vrste K in s prenosnim merilnikom hrapavosti. Obdelovanec je bil toplotno obdelan z indukcijskim ogrevanjem in hlajenjem na trdoto 50 HRC. Za določanje optimalnih kontrolnih faktorjev je bila uporabljena Taguchi metoda L18 (21×37). Globina rezanja, hitrost rezanja in hitrost podajanja so bile vzete kot kontrolni faktorji. Analiza variance je bila uporabljena za določanje vpliva kontrolnih faktorjev na temperaturo prehoda orodje-ostružek, temperaturo orodja in hrapavost površine. Določene so bile optimalne kombinacije kontrolnih faktorjev za T_{CTI} , T_T in R_a , kot $a_2v_1f_3$, $a_1v_3f_2$ and $a_2v_3f_1$. Z linearno regresijsko analizo so bili razviti modeli drugega reda za napovedovanje in izračunani so bili koeficienti korelacije za T_{CTI} , T_T in R_a kot $R^2 = 92,8$, $R^2 = 68,1$ in $R^2 = 82,6$.

Gljučne besede: temperatura orodja, termočlen, pirometer, strojna obdelava, Taguchi metoda

1 INTRODUCTION

In order to overcome the difficulties in terms of efficiency and the quality of production encountered in the metal-cutting industries, all the stages of the machining process need to be monitored. During the metal-cutting processes, one of the key factors is the cutting temperature, which directly affects the surface quality, the tool wear, the tool life, and the cost of production. The amount of heat generated varies with the type of material being machined and the cutting parameters (especially the cutting speed, which had the biggest influence on the temperature).¹

Temperature monitoring is one of the most difficult and complicated procedures in metal-cutting operations. It is extremely complex to develop a model for measuring the temperature due to the complexity of the different events at the point of contact between the tool

and the workpiece. Therefore, an accurate and repeatable temperature prediction still remains as a challenge due to this complexity of the contact phenomenon.² It is quite difficult to measure the temperature since the heat in the region is very close to the cutting edge. Due to a lack of sufficient experimental data, it is not possible to verify a mathematical model. Numerous attempts have been made to measure the temperature during machining operations.³

Amongst the many experimental methods to measure the temperature directly, only a few systems have used the temperature as an indicator of machine performance and for industrial applications.⁴ Therefore, the temperature can be controlled using the appropriate cutting parameters to design and develop the system and it will be beneficial to increase the efficiency in production.

In recent years, experimental studies related to metal-cutting processes have made use of the Taguchi

method. This method has been used successfully for a determination of the appropriate cutting parameters and in the optimization of parameters related to tool wear, tool life, and the surface quality. The Taguchi method and Analysis of Variance (ANOVA) can conveniently optimize the cutting parameters with several experimental runs that are well designed. Taguchi parameter design can optimize the performance characteristics through the settings of the design parameters and reduce the sensitivity of the system's performance to the source of variation.⁵ On the other hand, ANOVA is used to identify the most significant variables and interaction effects.^{6,7}

In the Taguchi method, quality is measured by the deviation of a quality characteristic from its target value. Therefore, the objective is to create a design that is insensitive to all possible combinations of uncontrollable factors and is at the same time effective and cost efficient as a result of setting the key controllable factors at their optimum levels.⁸ Taguchi's parameter design offers a simple and systematic approach that can reduce the number of experiments to optimize the design for performance, quality and cost. The signal-to-noise (S/N) ratio and the orthogonal array (OA) are two major tools used in robust design.⁹

A lot of research has been conducted for determining the optimal cutting parameters. W. H. Yang and Y. S. Tarn¹⁰ employed the Taguchi method, and the optimal cutting parameters for the turning of S45C steel bars were successfully obtained. B. M. Gopalsamy et al.¹¹ applied the Taguchi method to find the optimum machining parameters while machining hard steel and used the L18 orthogonal array. The S/N ratio and ANOVA were used to study the performance characteristics of the machining parameters. F. Ficici et al.¹² used the Taguchi method to study the wear behaviour of boronized AISI 1040 steel. They used the S/N ratio to investigate the optimum setting parameters.

M. Adinarayana et al.¹³ presented the multi-response optimization of the turning parameters for the turning of AISI 4340 alloy steel. The experiments were designed and conducted based on Taguchi's L27 orthogonal array design. They discussed an investigation into the use of Taguchi parameter design to predict and optimize the surface roughness, the metal removal rate and the power consumption during turning operations. E. D. Kirby¹⁴ discussed an investigation into the use of Taguchi parameter design for optimizing the surface roughness generated by a CNC turning operation. He used a standard orthogonal array for determining the optimum turning parameters with an applied noise factor. The controlled factors include the spindle speed, the feed rate, and the depth of cut.

In this paper, the measurement of temperature during the turning of AISI 4140 alloy steel was performed using various cutting parameters. The tool-chip interface temperature T_{CTI} was measured by infrared thermometer, the tool temperature T_T was measured with a K-type

thermocouple in the cutting zone, and the average surface roughness R_a was measured using a portable surface-roughness measurement device. The Taguchi design was selected to find the relationships between the control factors. The depth of cut (a_p), the cutting speed (v_c), and the feed rate (f) were taken as the control factors.

2 TEMPERATURES DURING METAL CUTTING

In the cutting process, nearly all of the energy dissipated during plastic deformation is converted into heat, which in turn raises the temperature in the cutting zone. Since the heat generation is closely related to the plastic deformation and friction, we can specify three main sources of heat when cutting:

- plastic deformation by shearing in the primary shear zone;
- friction on the cutting face and friction between the chips;
- tool on the tool flank.

Temperature results in dimensional errors on the machined surface. The cutting tool elongates as a result of the increased temperature, and the position of the cutting tool edge shifts towards the machined surface, resulting in a dimensional error of about 0.01–0.02 mm. Since the processes of thermal generation, dissipation, and solid-body thermal deformation are all transient, some time is required to achieve the steady-state condition.

Heat is mostly dissipated by: the discarded chip that carries away about 60–80 % of the total heat, the workpiece acts as a heat sink drawing away 10–20 % of heat, while the cutting tool draws away ~10 % of the heat. The balance between heat generation and heat dissipation during metal cutting is shown in **Figure 1**.

3 MATERIALS AND METHOD

3.1 Workpiece and cutting tool

The workpiece material is AISI 4140 alloy steel. The chemical composition of the workpiece material (in volume fractions) is shown in **Table 1**. The machining process was performed using a NR 2020K-08 tool holder

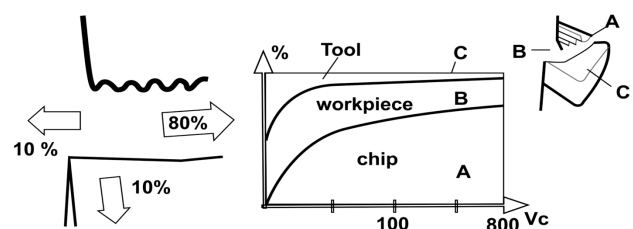


Figure 1: The balance of heat generation and heat dissipation during metal cutting

Slika 1: Izravnava med sproščeno in odvedeno toploto pri rezanju kovin

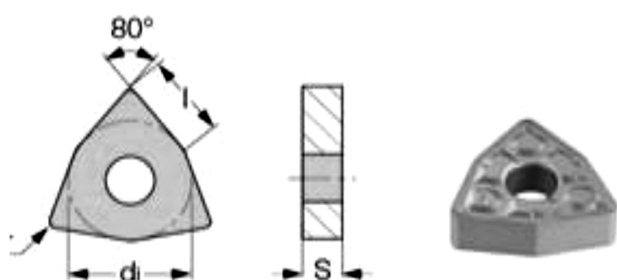


Figure 2: Schematic of tip geometry

Slika 2: Shema geometrije rezilne konice

and a TiAlN-TiN, PVD-coated, WNVG 080404-IC907 solid carbide insert. Figure 2 and Table 2 show a schematic of the tip geometry and the specifications of the insert.

Table 1: Chemical composition of AISI 4140 alloy steel (in volume fractions, $x/\%$)

Tabela 1: Kemijska sestava legiranega jekla AISI 4140 (v volumenskih odstotkih, $x/\%$)

C	Cr	Ni	Mn	P	S	Si	Mo
0.38	0.80	9.58	0.75	0.035	0.04	0.15	0.15

Table 2: The specifications of the insert

Tabela 2: Specifikacije vložka za rezanje

TiAlN-TiN PVD-coated WNVG 080404-IC907						
d_1	S	I	r	HRA	TRS	d
12.70	4.83	8.70	0.40	92.80	560	4.70
Property			Value			
ISO Range – P/M/K			(P10-P30)(M05-M20)			
ISO Range – H/S/N			(H05-H15)(S05-S20)			
Grade or coating type			PVD			
Coating layers			TiAlN-TiN			

3.2 Experimental conditions, temperature and surface-roughness measurements

In this study, two methods of tool-temperature evaluation are presented:

- the placement of the K-type thermocouple on the tool,
- the infrared pyrometer.

A schematic view of the experimental setup is shown in Figure 3. Cylindrical workpieces ($\varnothing 45 \times 300$ mm) were fixed between the chuck and the tailstock and were pre-machined using a separate insert. The workpiece samples were heat treated by induction hardening and a hardness of 50 HRC was maintained. The samples were then solution heat treated and oil quenched in order to achieve the proper hardness.

In this study, an Optris CF4 infrared thermometer was used to measure T_{CTI} . The maximum temperature (which was about 525 °C) was recorded around the cutting zone. A total of 18 trials were conducted throughout these experiments and brand new inserts were used for each temperature measurement. Hence, the cutting temperature increased with the cutting speed, the

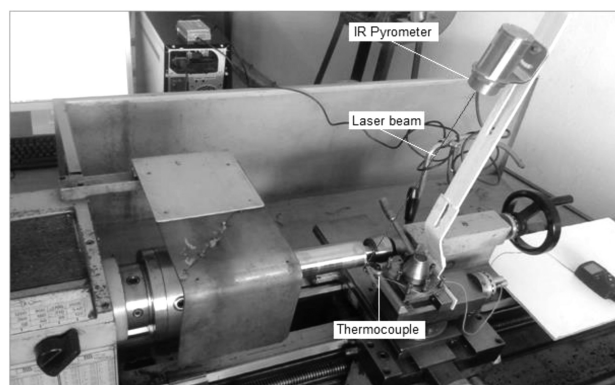


Figure 3: Thermocouple and IR pyrometer connections to the lathe
Slika 3: Povezava termočlena in IR-pirometra na stružnici

feed rate and the depth of cut. The experiments were repeated three times for the same cutting conditions and the measured values were averaged. T_T was measured using a K-type thermocouple. The thermocouple measurements were recorded every five seconds.

The R_a surface roughness was measured to characterize the surface quality. The R_a measurements were carried out using a Time TR 200 device by obtaining values from different points that were parallel to the workpiece axis at a cut-off length of 5.6 mm. According to the experimental design, three measurements were made on the surfaces at the specified values of the control factors, and the R_a values were determined by taking the average of the measurement results.

3.3 Experimental design using the Taguchi method

The Taguchi design was selected to find the relationships between the control factors and the quality characteristics. The cutting speed (v_c), feed rate (f) and depth of cut (a_p), whose levels are given Table 3, were selected as the control factors. The quality characteristics were the tool-chip interface temperature (T_{CTI}), the tool temperature (T_T) and the average surface roughness (R_a). As the total degree of freedom of the factor group was 5, a standard Taguchi experimental plan with the notation L18 ($2_1 \times 3_7$) was chosen as the orthogonal array. The rows in the L18 orthogonal array used in the experiment corresponded to each trial and the columns contained the factors to be studied. The first column consists of the depth of cut; the second and the third columns contain the cutting speed and the feed rate, respectively. In the Taguchi method, the experimental results are transformed into a S/N ratio. The S/N ratio is used while approaching or moving away from the desired value and measuring the quality characteristics.¹⁵⁻¹⁸ The smaller-is-better (SB), the nominal-best (NB) and the larger-is-better (LB) approaches are found according to the results of the S/N ratio.¹⁵⁻¹⁸ As the tool-chip interface temperature (T_{CTI}), the tool temperature (T_T) and the surface roughness (R_a) values were required to be the lowest, the S/N ratios of these quality characteristics were calculated in dB using Equation (1) according to the SB option in the study.¹⁵⁻¹⁸

$$S/N_{SB} = -10 \cdot \lg \left(\frac{1}{2} \sum_{i=1}^n y_i^2 \right) \quad (1)$$

In the Equation (1), n is the number of the experiment and y_i is the i th data point obtained.¹⁵⁻¹⁸ ANOVA was applied in order to determine the percentage effects of the control factors on T_{CTI} , T_T and R_a .

Table 3: Control factors and their levels

Tabela 3: Kontrolni faktorji in njihovi nivoji

Symbol	Control factors	Unit	Level 1	Level 2	Level 3	Degree of freedom (DoF)
a_p	Depth of cut	mm	0.40	0.60	–	1
v_c	Cutting speed	m/min	76	114	170	2
f	Feed rate	mm/rev	0.05	0.08	0.12	2

3.4 Predictive models for temperature and surface roughness with multiple regression analysis

Equations were developed for the prediction of T_{CTI} , T_T and R_a using the experimental results in a multiple regression analysis. The second-order linear models containing the main effects of the control factors and their interactions are signified with the Equation (2):

$$Y_1 = y - \varepsilon = b_0 x_0 + b_1 x_1 + b_2 x_2 + b_3 x_3 + b_4 x_{12} + b_5 x_{13} + b_6 x_{23} \quad (2)$$

where Y_1 is the estimated answer of the second-order equation and y is the tool-chip interface temperature (T_{CTI}), tool temperature (T_T) or surface roughness (R_a) measured on a the logarithmic scale, $x_0 = 1$ is the fixed variable, the x_1 , x_2 and x_3 control factors are the logarithmic transformations of the depth of cut, the cutting speed and the feed rate and, the x_{12} , x_{13} and x_{23} interactions of the control factors are the logarithmic transformations of the depth of cut–cutting speed, the depth of cut–feed rate and cutting speed–feed rate. The coefficient of the experimental error is ε , and the b values (b_0 , b_1 , b_2 , b_3 , b_4 , b_5 and b_6) are the coefficients of related factors.

4 ANALYSIS OF THE RESEARCH RESULTS

The present study was performed to understand and evaluate the infrared- and thermocouple-based temperature measurements during metal cutting and to consider the practical difficulties. T_{CTI} , T_T and R_a were used as the quality characteristics. The experimental results are shown in **Table 4**.

The T_{CTI} , T_T and R_a measurement results from the turning of the quenched and tempered AISI 4140 steel with coated carbide tools were resolved and analyzed by means of the Minitab 16.0 package software. From **Table 4** it is clear that the overall means for T_{CTI} , T_T and R_a were calculated as 446.11 °C, 70.78 °C and 0.578 μm, respectively.

Table 4: The experimental results for the quality characteristics and S/N ratios

Tabela 4: Rezultati preizkusov za opis kvalitete in S/N razmerja

Exp. no	Control factors			Measured values			S/N Ratios (dB)		
	a_p	v_c	f	Tool-chip interface temperature, T_{CTI} (°C) (IR Pyrometer)	Tool temperature, T_T (°C) (Thermocouple)	Surface roughness, R_a (μm)	$S/N_{T_{CTI}}$	S/N_{T_T}	S/N_{R_a}
1	0.4	76	0.05	410	57	0.295	-52.26	-35.12	10.60
2	0.4	76	0.08	405	66	0.483	-52.15	-36.39	6.32
3	0.4	76	0.12	410	72	0.958	-52.26	-37.15	0.37
4	0.4	114	0.05	460	65	0.484	-53.26	-36.26	6.30
5	0.4	114	0.08	465	61	0.579	-53.35	-35.71	4.75
6	0.4	114	0.12	425	67	0.988	-52.57	-36.52	0.10
7	0.4	170	0.05	520	65	0.410	-54.32	-36.26	7.74
8	0.4	170	0.08	500	67	0.492	-53.98	-36.52	6.16
9	0.4	170	0.12	475	71	0.872	-53.53	-37.03	1.19
10	0.6	76	0.05	400	72	0.489	-52.04	-37.15	6.21
11	0.6	76	0.08	390	80	0.530	-51.82	-38.06	5.51
12	0.6	76	0.12	395	76	0.720	-51.93	-37.62	2.85
13	0.6	114	0.05	430	80	0.429	-52.67	-38.06	7.35
14	0.6	114	0.08	435	75	0.547	-52.77	-37.50	5.24
15	0.6	114	0.12	420	83	0.722	-52.46	-38.38	2.83
16	0.6	170	0.05	485	81	0.354	-53.71	-38.17	9.02
17	0.6	170	0.08	525	67	0.406	-54.40	-36.52	7.83
18	0.6	170	0.12	480	69	0.643	-53.62	-36.78	3.84

Overall mean of T_{CTI} = 446.11 °C, S/N ratio of T_{CTI} = -52.95 dB

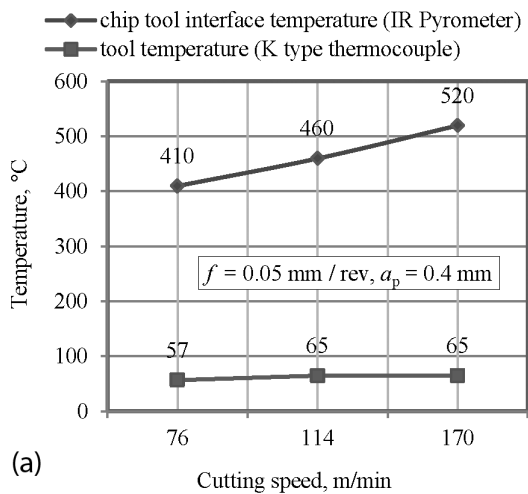
Overall mean of T_T = 70.78 °C, S/N ratio of T_T = -36.95 dB

Overall mean of R_a = 0.578 μm, S/N ratio of R_a = 5.24 dB

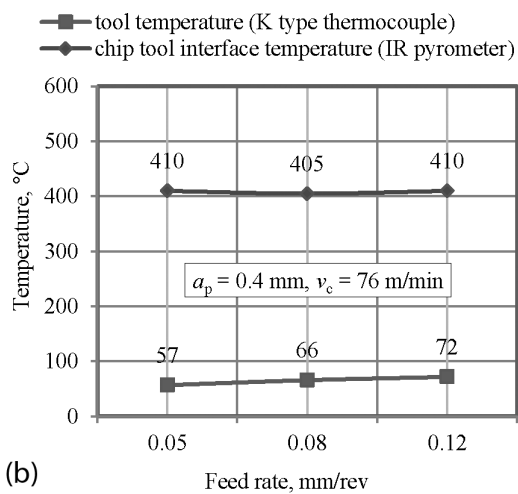
The variation of the tool temperature and the tool-chip interface temperature with the cutting parameters are shown in **Figures 4a** and **4b**. Obviously, it is clear that the tool-chip interface temperature and the tool temperature increase with an increase in the cutting speed (**Figure 4a**). The influence of the tool temperature and the feed rate on the surface roughness is shown in **Figure 5a**. It was observed that the lowest feed rate produced a better surface quality. The experiments showed that the cutting speed and the feed rate are the main factors affecting the surface roughness (**Figure 5b**).

4.1 Analysis of the control factors for the temperature and surface roughness

The responses for the S/N ratios (smaller is better) of T_{CTI} , T_T and R_a are presented in **Table 5** and the responses for the means in **Table 6**. While the signal value represents the real desired value that the system gives and which is to be measured, the noise factor represents the portion of the undesired factors in the measured value. The S/N ratio analysis provided significant information about the nature of the process of turning hardened AISI 4140 steel with coated carbide cutting tools under selected conditions. The fact that the differences between the highest and the lowest S/N ratio values of each control factor calculated at different levels



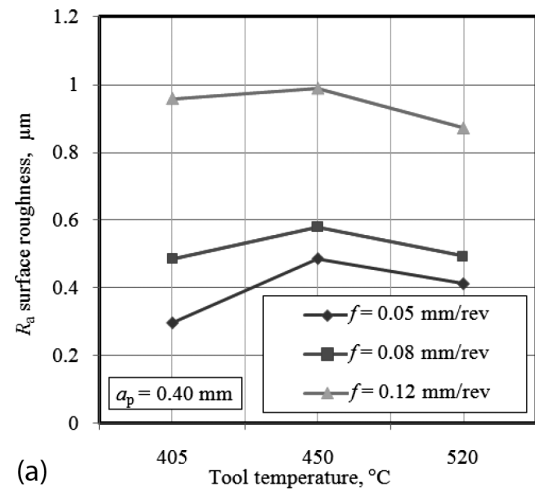
(a)



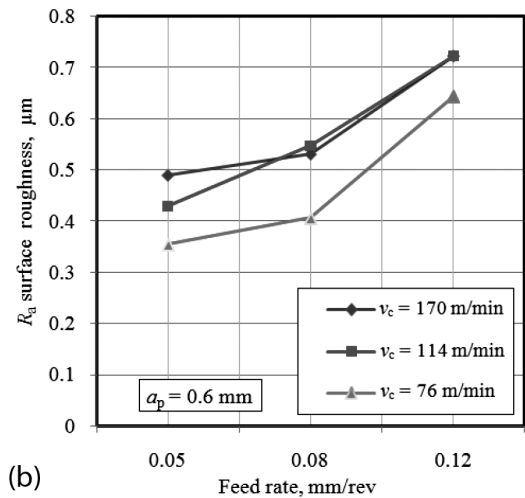
(b)

Figure 4: The influence of cutting speed and feed rate on the temperature: a) cutting speed, b) feed rate

Slika 4: Vpliv hitrosti rezanja in hitrosti podajanja na temperaturah: a) hitrost rezanja, b) hitrost podajanja



(a)



(b)

Figure 5: Influence of tool temperature and feed rate on surface roughness: a) tool temperature, b) feed rate

Slika 5: Vpliv temperature orodja in hitrosti podajanja na hrapavost površine: a) temperatura orodja, b) hitrost podajanja

Table 5: Response table for S/N ratios (smaller is better) of T_{CTI} , T_T and R_a

Tabela 5: Razpredelnica odgovorov za S/N razmerja (manjše je boljše) za T_{CTI} , T_T in R_a

Level	Tool-chip interface temperature, T_{CTI} (dB)			Tool temperature, T_T (dB)			Surface roughness, R_a (dB)		
	a_p	v_c	f	a_p	v_c	f	a_p	v_c	f
1	-53.07	-52.08	-53.04	-36.33	-36.91	-36.84	4.838	5.313	7.873
2	-52.83	-52.85	-53.08	-37.58	-37.07	-36.78	5.632	4.429	5.969
3	-	-53.93	-52.73	-	-36.88	-37.24	-	5.963	1.864
Δ	0.25	1.85	0.35	1.25	0.19	0.46	0.793	1.534	6.008
Rank	3	1	2	1	3	2	3	2	1

Table 6: Response table for means of T_{CTI} , T_T and R_a

Tabela 6: Tabela odgovorov za pomen T_{CTI} , T_T in R_a

Level	Tool-chip interface temperature, T_{CTI} (°C)			Tool temperature, T_T (°C)			Surface roughness, R_a (μm)		
	a_p	v_c	f	a_p	v_c	f	a_p	v_c	f
1	452.2	401.7	450.8	65.67	70.50	70.00	0.6179	0.5792	0.4102
2	440.09	439.2	453.3	75.89	71.83	69.33	0.5378	0.6248	0.5062
3	-	497.5	434.2	-	70.00	73.00	-	0.5295	0.8172
Δ	12.2	95.8	19.2	10.22	1.83	3.67	0.0801	0.0953	0.4070
Rank	3	1	2	1	3	2	3	2	1

are higher or lower was used in the determination of the factors effective on T_{CTI} , T_T and R_a . The most effective parameters on T_{CTI} were the cutting speed, the feed rate and the depth of cut because there were (1.85, 0.35 and 0.25) dB differences between their levels (Table 5). The most effective parameters on T_T were determined to be the depth of cut, the feed rate and the cutting speed, with differences of (1.25, 0.46 and 0.19) dB, respectively (Table 5). The most effective parameters on R_a were determined to be the feed rate, the cutting speed and the depth of cut, with differences of (6.008, 1.534 and 0.793) dB, respectively (Table 5). The optimum values for the surface roughness and the dimensional accuracy were reported to be $a_2v_1f_3$, $a_1v_3f_2$ and $a_2v_3f_1$, respectively (Table 6).

The main effects of the control factors on the performance characteristics during the turning of the quenched and tempered AISI 4140 steel with coated carbide cutting tools were demonstrated using the "Graphical Representation of Factor Effects" and evaluated.⁸⁻¹¹ The main effect graphs showing the effects of the control factors on T_{CTI} , T_T and R_a are given in Figures 6 and 7, respectively.

In Figure 6, the optimum levels of the control factors for the tool-chip interface temperature are a_2 ($a_p = 0.6$

mm), v_1 ($v_c = 76$ m/min) and f_3 ($f = 0.12$ mm/rev), respectively. T_{CTI} increases depending on the increase of the cutting speed and the decrease of the depth of cut and the feed rate. From the same graphic it is clear that the most effective control factor on T_{CTI} is the cutting speed. In Figure 7, the optimum levels of the control factors for the tool temperature are a_1 ($a_p = 0.4$ mm), v_2 ($v_c = 114$ m/min) and f_2 ($f = 0.08$ mm/rev), respectively.

In Figure 7, when the effects of the control factors on tool temperature were examined, a significant increase was observed on T_T , depending on the increase in the depth of cut. With an increase of the cutting speed from 76 m/min to 114 m/min and an increase of the feed rate from 0.08 mm/rev to 0.12 mm/rev the tool temperature was increased (Figure 7). Similarly, the optimum levels for the minimum R_a surface roughness were observed to be a_2 ($a_p = 0.6$ mm), v_3 ($v_c = 170$ m/min) and f_1 ($f = 0.05$ mm/rev), respectively (Figure 5). The most effective parameter on R_a was the feed rate (Figure 7). With a further increase in the feed rate value the R_a surface roughness value increased.

ANOVA is a statistically based, objective, decision-making tool used for determining any difference in the average performance of a group of items being tested.¹⁵⁻¹⁸ In the case when the F value of a process parameter is greater than the tabulated F ratio, it shows that the control factor has a significant effect on the performance characteristic. An analysis of variance (ANOVA) with a 95 % confidence interval was carried out for each experiment using the L_{18} orthogonal array in order to determine the effects of the control factors and their interactions on selected performance/quality characteristics. The results of the ANOVA carried out for T_{CTI} , T_T and R_a are presented in Tables 7, 8 and 9. The cutting speed became the most effective factor for the tool-chip interface temperature, with a contribution of 86.57 % followed by the feed rate with 4.03 % (Table 7). The effects of other control factors and their interactions on T_{CTI} became insignificant with a smaller 5 % contribution (Table 7). The results of the ANOVA for the tool

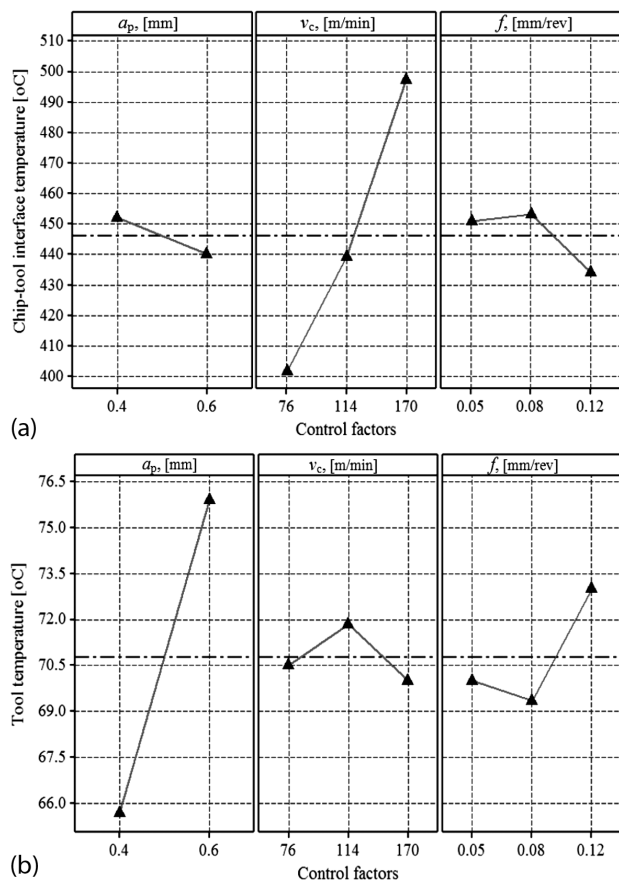


Figure 6: Mean effect plots for temperatures: a) tool-chip interface temperature, b) tool temperature

Slika 6: Diagram srednjega vpliva na temperature: a) temperatura stika orodje-ostružek, b) temperatura orodja

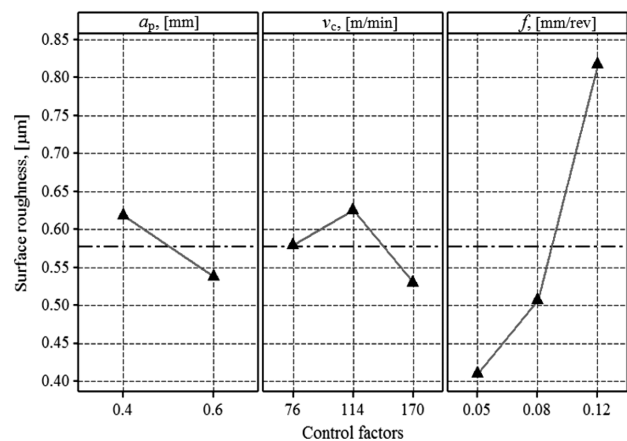


Figure 7: Mean effect plots for R_a surface roughness

Slika 7: Diagrami srednjega vpliva na hrapavost površine R_a

temperature (T_T) indicate that the depth of cut (a_p) has more influence on the tool temperature, with a contribution of 52.65 % and a cutting speed–feed rate (vx_f) 16.75 %, depth of cut–cutting speed (ax_v) 9.12 %, depth of cut–feed rate (ax_f) 7.51 %, feed rate (f) 5.13 % and cutting speed (v_c) 1.21 % followed by a contribution %, respectively (Table 8). Finally, from Table 9, it is concluded that the feed rate with a contribution of 76.63 % has more influence on the surface roughness (R_a) followed by the depth of cut–feed rate (ax_f), the depth of cut (a_p) and the cutting speed (v_c) to obtain the minimum surface roughness (Table 9).

Table 7: Results of ANOVA for tool-chip interface temperature (T_{CTI})

Tabela 7: Rezultati ANOVA za temperaturo stika orodje-ostružek (T_{CTI})

Source	DoF	SS	V	F-Ratio	Prob.>F	Contr. (%)
a_p	1	672.3	672.2	3.44	0.137	2.08
v_c	2	27986.1	13993.1	71.71	0.001	86.57
f	2	1302.8	651.4	3.34	0.140	4.03
ax_v	2	302.8	151.4	0.78	0.519	0.94
ax_f	2	369.4	184.7	0.95	0.461	1.14
vx_f	4	913.9	228.5	1.17	0.441	2.83
Res.Err.	4	780.6	195.1			2.41
Total	17	32327.8				100.00

$R^2 = 97.6$, R^2 (adj) = 89.7 (significant at 95 % confidence level)

Table 8: Results of ANOVA for tool temperature (T_t)

Tabela 8: Rezultati ANOVA za temperaturo orodja (T_t)

Source	DoF	SS	V	F-Ratio	Prob.>F	Contr. (%)
a_p	1	470.22	470.22	27.57	0.006	52.65
v_c	2	10.78	5.389	0.32	0.746	1.21
f	2	45.78	22.889	1.34	0.358	5.13
ax_v	2	81.44	40.722	2.39	0.208	9.12
ax_f	2	67.11	33.556	1.97	0.254	7.51
vx_f	4	149.56	37.389	2.19	0.233	16.75
Res.Err.	4	68.22	17.056			7.64
Total	17	893.11				100.00

$R^2 = 92.4$, R^2 (adj) = 67.5 (significant at 95 % confidence level)

Table 9: Results of ANOVA for surface roughness (R_a)

Tabela 9: Rezultati ANOVA za hrapavost površine (R_a)

Source	DoF	SS	V	F-Ratio	Prob.>F	Contr. (%)
a_p	1	0.028880	0.028880	10.73	0.031	4.18
v_c	2	0.027281	0.013641	5.07	0.080	3.95
f	2	0.543172	0.271586	100.89	0.000	78.63
ax_v	2	0.014830	0.007415	2.75	0.177	2.15
ax_f	2	0.062656	0.031328	11.64	0.022	9.07
Vx_f	4	0.003192	0.000798	0.30	0.867	0.46
Res.Err.	4	0.010767	0.002692	–	–	1.56
Total	17	0.690779	–	–	–	100.00

$R^2 = 98.4$, R^2 (adj) = 93.4 (significant at 95 % confidence level)

4.2 Developed second-order predictive equations for the temperature and surface roughness

The equations that were developed with multiple linear regression analysis to predict T_{CTI} , T_T and R_a in the turning of quenched and tempered AISI 4140 steel with coated carbide cutting tools and the equations that contain the main effects of the control factors and their interaction effects are presented in Equations (3) to (5), respectively.

$$T_{CTI} = 382 - 146a + 0.966v + 179f + 0.708av - 358vf \quad (4)$$

$$T_T = 2.0 - 96.8a + 0.328v + 255f - 0.381av - 1.74vf \quad (5)$$

$$R_a = -0.114 - 0.34a + 0.00332v + 7.15f - 0.00617av - 0.0102vf \quad (6)$$

These equations were developed according to the un-coded values of the control factors (i.e., 0.4, 0.6 mm, etc. for a_p ; i.e., 76, 114, 170 m/min, etc. for v_c ; i.e., 0.05, 0.08, 0.012 mm/rev, etc. for f). af is highly correlated with other variables, so af has been removed from all of the equations. The correlation coefficients (R^2) and the adjusted correlation coefficients (R^2 (adj)) of the second-order equations developed for the predictive tool-chip interface temperature (T_{CTI}) measured with an IR pyrometer, the tool temperature (T_T) measured with a thermocouple and the surface roughness (R_a) were calculated as $R^2 = 92.8$ %, R^2 (adj) = 89.8 %, $R^2 = 68.1$ %, R^2 (adj) = 54.8 % and $R^2 = 82.6$ % R^2 (adj) = 75.3 %, respectively. R^2 (adj) determines the amount of deviation about the mean that is described by the model. The predicted R^2 value and the R^2 (adj) value were found to be in good agreement. These values show that the equations developed are sufficient to determine all the response values at a confidence interval of 95 %. The regression models can be successfully adopted for estimating T_{CTI} , T_T and R_a . Moreover, as seen in these equations, v_c and f have additive effects, while a_p has a negative effect on T_{CTI} , T_T and R_a .

The comparisons of the results of T_{CTI} , T_T and R_a measured experimentally (Table 4) with the fits for T_{CTI} , T_T and R_a estimated via the Taguchi method and fits for T_{CTI} , T_T and R_a estimated via the Regression model (Equation (3) to (5)) are given in Table 8. As can be seen from this table, the T_{CTI} results obtained from the Taguchi method and the linear regression analysis were found to be very close. The mean of the % error ratios of the estimated results obtained by the Taguchi method and the predictive equations were less than 14 %. This reflects the reliability of the statistical analyses (Tables 10 and 11).

5 CONCLUSIONS

In this study, the Taguchi design was selected to determine the effects of the control factors. The effects of the depth of cut, the cutting speed and the feed rate on the tool-chip interface temperature (T_{CTI}), the tool

Table 10: The comparisons of measured of T_{CTI} , and T_t experimentally with fits estimated via the Taguchi method and regression models

Tabela 10: Primerjava izmerjenih T_{CTI} in eksperimentalnih T_t , z ujemANJI, določENIMI po Taguchi metodi in z regresijskimi modeli

Exp. no	Tool-chip interface temperature, T_{CTI} (°C)					Tool temperature, T_t (°C)				
	Measured T_{CTI}	Fits for T_{CTI} estimated via Taguchi method	Error %	Fits for T_{CTI} estimated via Regression model	Error %	Measured T_t	Fits for T_t estimated via Taguchi method	Error %	Fits for T_t estimated via Regression model	Error %
1	410	418	2.0	414	0.9	57	56	1.0	60	5.7
2	405	401	0.9	411	1.4	66	68	2.9	64	3.2
3	410	406	1.1	407	0.7	72	71	1.9	69	4.5
4	460	462	0.5	454	1.3	65	62	3.9	64	2.1
5	465	458	1.5	447	3.8	61	61	0.1	65	7.0
6	425	430	1.1	438	3.1	67	70	3.9	68	0.8
7	520	510	2.0	514	1.1	65	68	4.8	69	5.5
8	500	511	2.1	501	0.2	67	65	2.8	67	0.5
9	475	475	0.1	484	1.9	71	70	1.7	66	7.5
10	400	392	2.0	395	1.2	72	73	0.8	74	2.5
11	390	394	0.9	392	0.6	80	78	2.4	77	3.1
12	395	399	1.1	389	1.6	76	77	1.8	82	8.4
13	430	428	0.5	441	2.6	80	83	3.2	74	7.1
14	435	442	1.6	434	0.2	75	75	0.1	76	1.3
15	420	415	1.1	425	1.2	83	80	3.1	78	5.8
16	485	495	2.1	509	4.9	81	78	3.8	75	7.4
17	525	514	2.0	496	5.5	67	69	2.8	74	10.1
18	480	480	0.1	479	0.2	69	70	1.8	72	4.5
Min	390	392	0.1	389	0.2	57	56	0.1	60	0.5
Max	525	514	2.1	514	5.5	83	83	4.8	82	10.1
Mean	446	–	1.3	–	1.8	71	–	2.4	–	4.8

Table 11: The comparisons of the measured R_a with fits estimated via the Taguchi method and the regression models

Tabela 11: Primerjava izmerjene R_a z ujemANJI, določENIMI po Taguchi metodi in z regresijskimi modeli

Exp.no	Measured R_a	Fits for R_a estimated via Taguchi method	Error %	Fits for R_a estimated via Regression model	Error %
1	0.295	0.338	14.4	0.406	37.5
2	0.483	0.478	1.1	0.597	23.5
3	0.958	0.921	3.9	0.851	11.1
4	0.484	0.461	4.7	0.418	13.5
5	0.579	0.594	2.5	0.598	3.3
6	0.988	0.996	0.8	0.837	15.3
7	0.410	0.390	4.9	0.438	6.7
8	0.492	0.483	1.9	0.600	21.9
9	0.872	0.901	3.4	0.816	6.4
10	0.489	0.446	8.7	0.380	22.3
11	0.530	0.535	1.0	0.571	7.7
12	0.720	0.757	5.2	0.826	14.7
13	0.429	0.452	5.3	0.346	19.4
14	0.547	0.532	2.7	0.525	4.0
15	0.722	0.714	1.1	0.765	5.9
16	0.354	0.374	5.7	0.296	16.5
17	0.406	0.415	2.3	0.458	12.8
18	0.643	0.614	4.6	0.674	4.9
Min	0.295	0.338	0.8	0.296	3.3
Max	0.988	0.996	14.4	0.851	37.5
Mean	0.578	–	4.1	–	13.7

temperature (T_T) and the surface roughness (R_a) were investigated in the turning of the quenched and normalized AISI 4140 steel workpieces that were machined using TiAlN-TiN, PVD-coated, carbide tools and the obtained results are as follows:

The most effective parameter on the tool-chip interface temperature was the cutting speed with a contribution ratio of 86.57 %. The effective parameters for tool temperature were the depth of cut, the cutting speed-feed rate, the depth of cut-cutting speed, the depth of cut-feed rate, the feed rate and the cutting speed with contributions of 52.65 %, 16.75 %, 9.12 %, 7.51 %, 5.13 % and 1.21 %.

The feed rate with a contribution of 76.63 % has more influence on the surface roughness (R_a) followed by the depth of cut-feed rate (axf), the depth of cut (a_p) and the cutting speed (v_c) to obtain the minimum surface roughness.

The optimum levels of the control factors were $a_p = 0.6$ mm, $v_c = 76$ m/min and $f = 0.12$ mm/rev for the minimum tool-chip interface temperature; $a_p = 0.4$ mm, $v_c = 114$ m/min and $f = 0.08$ mm/rev for the minimum tool temperature, and $a_p = 0.6$ mm, $v_c = 170$ m/min and $f = 0.05$ mm/rev for the minimum R_a surface roughness.

The tool-chip interface temperature increased significantly depending on the increase of the cutting speed. The depths of cut and feed rate do not have a significant effect on the tool-chip interface temperature.

The tool temperature increased significantly depending on the increase of the depth of cut.

The surface roughness increased depending on the increase of the feed rate, while the same tendency was not observed for the depth of cut and the cutting speed.

The correlation coefficients of the predictive equations developed for the estimation of the minimum tool-chip interface temperature, the tool temperature and the surface roughness by multiple linear regression analysis were calculated as 0.928, 0.681 and 0.826, respectively. Higher correlation coefficients reflect the reliability of the developed equations.

The mean of the % error ratios of the estimated results obtained by Taguchi method and the predictive equations were less than 14 %. This reflects the reliability of the statistical analyses.

6 REFERENCES

- ¹X. L. Liu, D. H. Wen, Z. J. Li, L. Xiao, F. G. Yan, Cutting temperature and tool wear of hard turning hardened bearing steel, *Journal of Materials Processing Technology*, 129 (2002), 200–206, doi:10.1016/S0924-0136(02)00651-9
- ²N. A. Abukhshim, P. T. Mativenga, M. A. Sheikh, Investigation of heat partition in high speed turning of high strength alloy steel, *International Journal of Machine Tools and Manufacture*, 45 (2005), 1687–1695, doi:10.1016/j.ijmactools.2005.03.008
- ³N. A. Abukhshim, P. T. Mativenga, M. A. Sheikh, Heat generation and temperature prediction in metal cutting: a review and implications for high speed machining, *International Journal of Machine Tools and Manufacture*, 46 (2006) 7–8, 782–800, doi:10.1016/j.ijmactools.2005.07.024
- ⁴A. H. Suhail, N. Ismail, S. V. Wong, N. A. Abdul Jalil, Optimization of cutting parameters based on surface roughness and assistance of workpiece surface temperature in turning process, *American Journal of Engineering and Applied Sciences*, 3 (2010) 1, 102–108, doi:10.3844/ajeassp.2010.102.108
- ⁵P. D. Berger, R. E. Maurer, *Experimental design with applications in management, Engineering and The Sciences*, 1th ed., Duxbury Press, USA 2001
- ⁶G. R. Henderson, *Six sigma: Quality improvement with MINITAB*, 2nd ed., John Wiley and Sons, England 2006, 452–460
- ⁷T. P. Ryan, *Statistical methods for quality improvement*, 2nd ed., John Wiley and Sons, USA 2000
- ⁸A. Mishra, A. Gangele, Application of Taguchi method in optimization of tool flank wear width in turning operation of AISI 1045 steel, *Industrial Engineering Letters*, 2 (2012) 8, 11–18
- ⁹M. S. Phadke, *Quality engineering using design of experiment, quality control, Robust design and Taguchi method*, 1st ed., Warsworth and Books, California 1998
- ¹⁰W. H. Yang, Y. S. Targ, Design optimization of cutting parameters for turning operations based on Taguchi method, *Journal of Materials Processing Technology*, 84 (1998), 122–129, doi:10.1016/S0924-0136(98)00079-X
- ¹¹B. M. Gopalsamy, B. Mondal, S. Ghosh, Taguchi method and ANOVA: An approach for process parameters optimization of hard machining while machining hardened steel, *Journal of Scientific and Industrial Research*, 68 (2009) 8, 686–695
- ¹²F. Fici, M. Kapsiz, M. Durat, Applications of Taguchi design method to study wear behaviour of boronized AISI 1040 steel, *International Journal of Physical Sciences*, 6 (2011) 2, 237–243
- ¹³M. Adinarayana, G. Prasanthi, G. Krishnaiah, Parametric analysis and multi objective optimization of cutting parameters in turning operation of AISI 4340 alloy steel with CVD cutting tool, *International Journal of Research in Engineering and Technology*, 3 (2014) 2, 449–456
- ¹⁴E. D. Kirby, A parameter design study in a turning operation using the Taguchi method, *The Technology Interface*, (2006), 1–14
- ¹⁵P. J. Ross, *Taguchi techniques for quality engineering: Loss function, orthogonal experiments, parameter and tolerance design*, McGraw-Hill, New York 1988
- ¹⁶D. C. Montgomery, *Taguchi's contributions to experimental design and quality engineering, design and analysis of experiment*, Wiley, Canada 1991
- ¹⁷E. Canyılmaz, F. Kutay, An alternative approach to analysis of variance in Taguchi method, *Journal of the Faculty of Engineering & Architecture of Gazi University*, 18 (2003) 3, 51–63
- ¹⁸R. K. Roy, *A primer on the Taguchi method*, Van Nostrand Reinhold, New York 1990

WELDABILITY OF Ti6Al4V TO AISI 2205 WITH A NICKEL INTERLAYER USING FRICTION WELDING

PREIZKUŠANJE VARIVOSTI PRI VARJENJU S TRENJEM Ti6Al4V IN AISI 2205 Z VMESNO PLASTJO NIKLJA

Ihsan Kirik

Batman University, Faculty of Engineering and Architecture, Department of Metallurgical and Materials Engineering, 72060 Batman, Turkey
alihsankirik@gmail.com

Prejem rokopisa – received: 2015-02-12; sprejem za objavo – accepted for publication: 2015-05-04

doi:10.17222/mit.2015.039

The aim of this study was to friction weld dissimilar metals, i.e., Ti6Al4V to duplex stainless steel, with and without a nickel interlayer using a new method. The metallographic examinations of the weld were carried out and the strength of the joints was determined with tensile tests. The experimental results indicate that the Ti6Al4V and duplex stainless steel could be joined with a nickel interlayer. The highest tensile strength (605 MPa) was obtained and the tensile strength of the joint was significantly increased with an increase of the rotation speed and the friction pressure.

Keywords: friction welding, titanium alloy, duplex stainless steel, nickel interlayer

Namen te študije je varjenje s trenjem različnih materialov Ti6Al4V in dupleks nerjavnega jekla, z in brez vmesne plasti niklja, z uporabo nove metode. Izvršeni so bili metalografski preizkusi zvara. Rezultati preizkusov kažejo, da je z vmesnim slojem niklja mogoče spajati Ti6Al4V in dupleks nerjavno jeklo. Z naraščanjem hitrosti vrtenja in pritiska pri trenju je mogoče doseči najvišjo natezno trdnost (605 MPa), hkrati pa narašča tudi natezna trdnost spoja.

Ključne besede: varjenje s trenjem, titanova zlitina, dupleks nerjavno jeklo, vmesni sloj niklja

1 INTRODUCTION

Materials such as low-carbon steels, ceramics and composites that are problematic and difficult to join using traditional welding methods can be joined by friction welding (FW). One of the biggest advantages of FW is the production of a new material from pairs of dissimilar materials.¹⁻² FW is an important manufacturing technique used in the machine construction and hydraulic industry, the automotive industry, and the industry for cutting and drilling tools. This technique has an important application area in welding technology, as it can join materials with different compositions if their sizes and shapes are appropriate, it does not have a limited melting event and it has a very low welding failure.³⁻⁵

The joinability of Ti and its alloys to steels is extremely important because more and more of these metals are used together.⁶ When Ti alloys and stainless steels join mechanically, many intermetallic phases and different tension concentration areas occur at the intermediate of the joint, which then causes embrittlement and cracking.⁷ When Ti directly welds to the stainless steel, intermetallic compounds such as FeTi and Fe₂Ti can occur at the joining area due to Ti and Fe having very little fusion capabilities. Besides, TiC may form since Ti is a strong carbide-forming element and also occurrences of these compounds cause a crispiness in the joining area. On the other hand, cracks may occur in the

welding area due to the difference in the thermal conductivity between the Ti alloy and the steel. To avoid these negatives, the Ni interlayer diffusion welding method was used to combine the TiC₄, the Ti alloy and the stainless steel, and sound joints were obtained, which had high strengths.⁸ The Ti-6Al-4V alloy and a micro-duplex stainless steel (AVESTA 2205) were joined using the diffusion-welding technique, and good results were obtained at temperatures as low as 800 °C in 30 min.⁹ Aleman et al.¹⁰ studied pure Ti and 316L stainless steel using the diffusion-welding technique and they stated that the σ -phase was observed on the stainless-steel side, Fe₂Ti and FeTi in the inner side, and Fe₂Ti₄O oxide on the Ti side. Muralimohan et al.¹¹ welded Ti and 304L stainless steel by FW and through a nickel interlayer, which is deposited by electroplating on stainless-steel substrates with a range of 100±3 μm. The joining of dissimilar materials such as aluminium, titanium, magnesium and their alloys to stainless steels was reported in¹⁻¹⁴, but very limited studies are reported for titanium and its alloy to stainless steel using FW. Moreover, using an interlayer in FW is very limited, because it is difficult to keep the intermediate layer in the intermediate zone. TiAl and AISI 4140 steel were joined through FW with a copper insert layer and two-step joining of the FW was carried out to complete the joints by W. B. Lee et al.¹² Madhusudhan and Venkata¹³ investigated the role of the nickel insert layer in the FW of maraging steel to low-alloy steel. To incorporate nickel as an interlayer, maraging

Table 1: Chemical compositions of the test materials, in mass fractions (w%)**Tabela 1:** Kemijska sestava preiskovanih materialov, v masnih deležih (w%)

Materials	Alloying elements, in mass fractions (w%)										
	Ti	C	Mn	P	Si	Cr	Al	Ni	Cu	V	Fe
Ti6Al4V	Bal	= 0.08	–	–	0.15	–	5–6.50	–	–	3.5–4.5	= 0.40
AISI 2205	–	0.01–0.03	1.68–2.00	0.026	–	21–23	–	3.37	–	–	Bal
Nickel	–	–	0.007	–	–	–	–	Bal	0.01	–	–

Table 2: The process parameters, used in the FW and the tensile test results according to these parameters**Tabela 2:** Procesni parametri, uporabljeni pri FW in rezultati nateznega preizkusa pri teh parametrih

Sample No.	Welding parameters						
	Rotation speed (m ⁻¹)	Fric. time (s)	Fric. press. (MPa)	Forging pressure (MPa)	Forging time (s)	Without Interlayer	With Interlayer Ten. Stren. (MPa)
N1	1500	6	150	200	4	Failed	380
N2	1500	6	125	200	4	Failed	326
N3	1500	6	100	200	4	Failed	–
N4	1800	6	150	200	4	Failed	420
N5	1800	6	125	200	4	Failed	605
N6	1800	6	100	200	4	Failed	180
Nickel	–	–	–	–	–	–	450
AISI 2205	–	–	–	–	–	–	956
Ti6Al4V	–	–	–	–	–	–	870

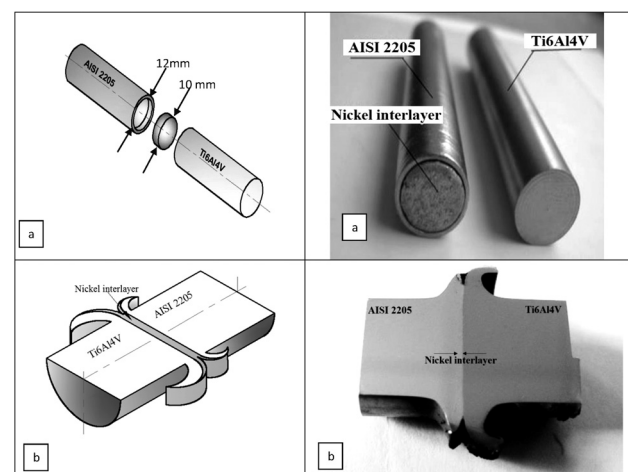
ing steel and nickel were welded first. To maintain the 5-mm length of interlayer the nickel was cut. Subsequently, low-alloy steel was welded on the nickel side of the joint.

The literature examined for using an insert layer in FW joining revealed two stages or the interlayer is kept at the interface using a different method. For this reason, the goal of this study is the successful joining of the Ti6Al4V titanium alloy and the AISI 2250 duplex stainless using FW single stage and with a nickel interlayer using a new technique. The strengths of the joints were determined by tensile tests and compared with those of base materials. Then, the microstructures in the welding zone were obtained and investigated using macro- and micro-photographs.

2 EXPERIMENTAL PROCEDURES

In this study, three materials with different properties were used in order to be joined using friction welding. The analysed chemical compositions of the materials are illustrated in **Table 1**. The duplex stainless steel and the Ti6Al4V alloy bars were provided commercially with a 12-mm diameter and were processed on a turning lathe machine according to the sizes shown in **Figure 1a**. Firstly, during the FW the most difficult stage while using the insert layer is to keep it at the interface. Thus, to avoid the escape of the interlayer, the surface of the duplex stainless steel is processed with a 10 mm diameter and a 3 mm depth, as shown in **Figure 1a**. Later, the nickel interlayer was placed on the forehead of the duplex stainless steel with the help of a press and then the welding was performed in a continuously driven FW machine using the parameters given in **Table 2**. After the

FW, in order to determine the microstructural changes to the samples that were friction welded, the axial cross-section of the joint was achieved by abrasive cutting and attached for polishing, and then the samples were etched in a chemical solution for the metallographic examination. The microstructure analyses of the joints were carried out with an optical microscope, and the scanning electron microscopy (SEM) and quantitative chemical analyses were performed with an energy-dispersive spectrometer (EDS). The friction-welded joints, with and without an interlayer, were tested for their tensile strength.

**Figure 1:** Schematic illustration of friction welded Ti6Al4V and AISI 2205 using: a) nickel interlayer, b) macrograph of cross-section of friction welded N5 sample

Slika 1: Shematski prikaz zvara pri trenju Ti6Al4V in AISI 2205: a) z uporabo vmesnega sloja niklja, b) makroposnetek preseka vzorca N5, zvarjenega s trenjem

3 RESULTS AND DISCUSSION

3.1 Examinations of microstructure

A macro image of the FW joint N5 sample is shown in **Figure 1b**. It is evident that the joint is unsymmetrical and the flash dimensions of the Ti alloy are much larger than the stainless steel due to the decrease of the tensile yield strength of the Ti alloy with temperature being much more significant than that of duplex stainless steel, although at room temperature the situation is exactly reversed.¹⁵

The optical photographs taken from the FW joint N5 sample shows that the Ti6Al4V/AISI 2205 materials were successfully friction welded using a nickel interlayer (**Figure 2**). It is clear that there is a structural disorder and differently directed grains on the Ti6Al4V side near the nickel interlayer. Moreover, the FW of dissimilar metals, Ti6Al4V to duplex stainless steel, without an interlayer were tried so many times with different parameters, but the joints were not achieved due to brittle phase reaction and volume expansion.

The SEM micrograph for the N4 sample joined at a rotation of 1800 min⁻¹, a 6-s friction time, a 150 MPa friction pressure, a 200 MPa forging pressure and a 4-s forging time is illustrated in **Figure 3**. From the micrograph it is clear that at the nickel and Ti6Al4V interface there were three different zones: (α -Ti + β -Ti) of Ti6Al4V, β -phase and intermetallic phase in interface zone, nickel zone and invisible stainless steel zone. From¹⁴, when Ti alloys and the stainless-steel joint FeTi and Fe₂Ti intermetallic phase occurred. Also, these phases adversely affect the quality of the joint. To eliminate the effects of this occurrence a nickel interlayer was used and the results confirmed that this is necessary. The concentrations of the elements across the interface zone are shown in **Table 3** and the EDS graph is presented in **Figure 3**. From the EDS results of the N4 sample different amounts of Al, Si, Ti, V, Ni and Mo were obtained, but in the nickel some oxygen is obtained. As shown in **Table 3**, Ti and Ni have a high degree of diffusion in the

approximately 15- μ m region. Also, Ti diffused from Ti6Al4V to the nickel interlayer, the nickel diffused into the Ti alloy over the same distance. The FW of dissimilar materials with a nickel interlayer exhibits a wider plasticized zone in the middle of the welding interface. The variation of the alloying elements at the mutual interference is on account of the thermo-plastic stirring and the diffusion mechanism.

Table 3: Elementary variation rates from EDS analyses across the welding interface of the N4 sample

Tabela 3: Spreminjanje vsebnosti elementov določena z EDS analizo preko zvara vzorca N4

Alloying elements (wt%)	EDS points		
	1	2	3
O	–	–	12.47
Al	6.799	5.755	–
Si	–	0.799	–
Ti	88.087	60.583	0.181
V	4.025	1.950	–
Ni	0.910	30.705	87.160
Mo	0.189	0.208	0.188

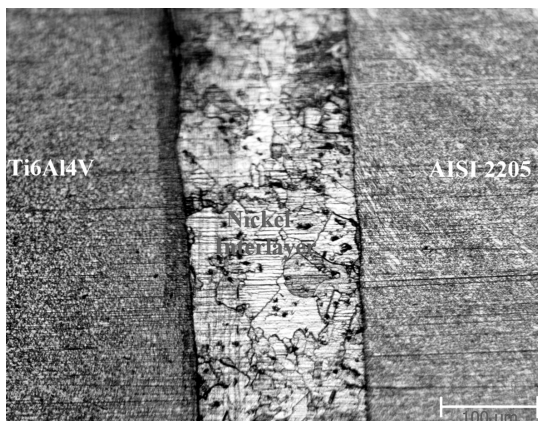


Figure 2: Optical microstructure of the interface of the N5 sample
Slika 2: Mikrostruktura vmesnega sloja pri vzorcu N5

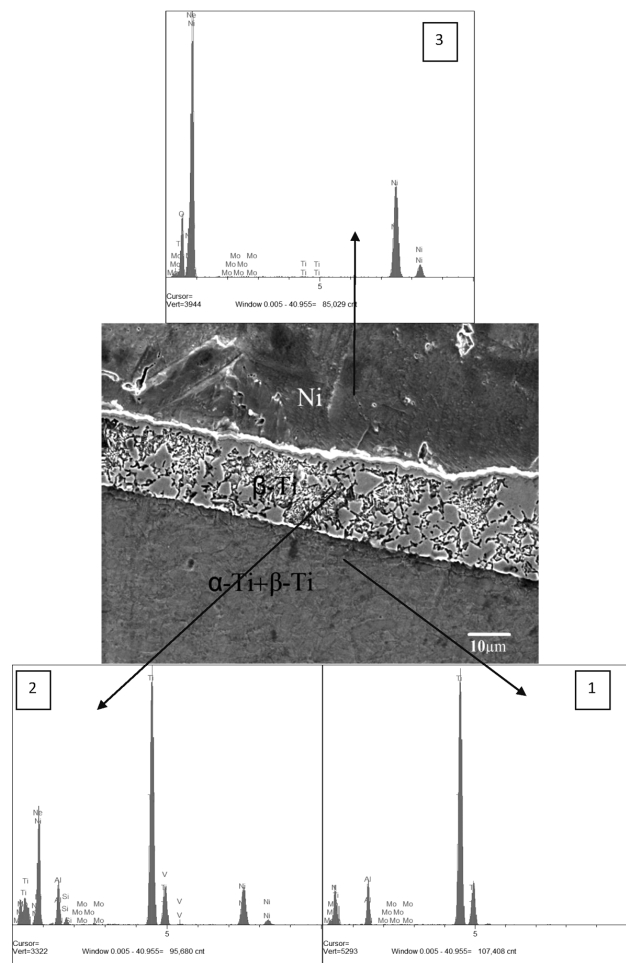


Figure 3: SEM photograph of the interface of the N4 sample and the EDS analysis

Slika 3: SEM-posnetek vmesnega sloja pri vzorcu N4 in EDS-analiza

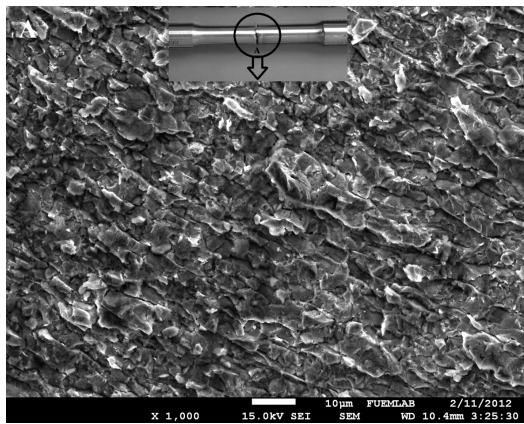


Figure 4: SEM photograph of fractured surface of N5 sample
Slika 4: SEM-posnetek površine preloma vzorca N5

3.2 Tensile testing

The tensile strength of the joints was determined, as seen in **Table 2**, based on two different rotation speeds (1500 min^{-1} and 1800 min^{-1}), three different friction pressures (100, 125 and 150) MPa, a constant friction time (6 s), a forging time (4 s) and a forging pressure (200 MPa). The highest tensile strength (605 MPa) was obtained for the N5 sample. The tensile strength was increased by increasing the rotation speed with a constant friction time and pressure, and increasing the tensile strength results in heat input and a high plastic deformation. The fracture surface of the tensile test sample N5 is characterized with SEM to understand the failure mechanism. **Figure 4** illustrates the fracture-surface morphologies taken from the centre of N5. It is clear that the fracture surface of the joint indicates a brittle cleavage fracture for Ti6Al4V/AISI 2205 stainless steel for different materials welding by FW using a nickel interlayer.

4 CONCLUSION

The effects of a nickel interlayer and the process parameters on the microstructure and tensile strength of friction welds between a Ti6Al4V alloy and AISI 2205 duplex stainless steel with and without an interlayer were studied. The following results were achieved:

Ti6Al4V and AISI 2205 were successfully joined by FW using a nickel interlayer.

In the event of FW between the Ti6Al4V and AISI 2205 the soundness of the joints was increased with a nickel interlayer and the rotation speed; but without an interlayer cracks occurred and it was not joined due to a brittle phase reaction and the volume expansion.

The highest tensile strength (605 MPa) was obtained for the N5 sample joined at 1800 min^{-1} , a 6-s friction

time, 125 MPa of friction pressure, 200 MPa of forging pressure and a 4-s forging time. The tensile strength was increased when the rotation speed and the friction pressure increased.

5 REFERENCES

- ¹ N. Özdemir, Investigation of the mechanical properties of friction-welded joints between AISI 304L and AISI 4340 steel as a function rotational speed, *Materials Letters*, 59 (2005), 2504–2509, doi:10.1016/j.matlet.2005.03.034
- ² I. Krik, N. Özdemir, Weldability and joining characteristics of AISI 420/AISI 1020 steels using friction welding, *Int. J. of Mat. Research*, 8 (2013), 769–776, doi:10.3139/146.110917
- ³ M. Sahin, Characterization of properties in plastically deformed austenitic-stainless steels joined by friction welding, *Materials and Design*, 30 (2009), 135–144, doi:10.1016/j.matdes.2008.04.033
- ⁴ V. V. Satyanarayana, G. M. Reddy, T. Mohandas, Dissimilar metal friction welding of austenitic-ferritic stainless steels, *J. of Mat. Proc. Tech.*, 160 (2005) 2, 128–137, doi:10.1016/j.jmatprotec.2004.05.017
- ⁵ H. Ates, M. Turker, A. Kurt, Effect of friction pressure on the properties of friction welded MA956 iron-based superalloy, *Materials and Design*, 28 (2007) 3, 948–953, doi:10.1016/j.matdes.2005.09.015
- ⁶ M. Ghosh, S. Chatterjee, Effect of interface microstructure on the bond strength of the diffusion welded joints between titanium and stainless steel, *Materials Characterization*, 54 (2005) 4–5, 327–337, doi:10.1016/j.matchar.2004.12.007
- ⁷ M. Ghosh, S. Chatterjee, Characterization of transition joints of commercially pure titanium to 304 stainless steel, *Materials Characterization*, 48 (2002) 5, 393–399, doi:10.1016/S1044-5803(02)00306-6
- ⁸ P. He, J. C. Feng, B. G. Zhang, Y. Y. Qian, A new technology for diffusion bonding intermetallic TiAl to steel with composite barrier layers, *Materials Characterization*, 50 (2003) 1, 87–92, doi:10.1016/S1044-5803(03)00122-0
- ⁹ N. Orhan, T. I. Khan, M. Eroğlu, Diffusion bonding of a microduplex stainless steel to Ti–6Al–4V, *Scripta Materialia*, 45 (2001) 4, 441–446, doi:10.1016/S1359-6462(01)01041-7
- ¹⁰ B. Aleman, I. Gutiérrez, J. J. Urcola, The use of kirkendall effect for calculating intrinsic diffusion coefficients in a 316L/Ti6242 diffusion bonded couple, *Scripta Materialia*, 36 (1997) 5, 509–515, doi:10.1016/S1359-6462(96)00414-9
- ¹¹ C. H. Muralimohan, V. Muthupandi, K. Sivaprasad, Properties of friction welding titanium-stainless steel joints with nickel interlayer, *Procedia Materials Science*, 5 (2014), 1120–1126, doi:10.1016/j.mspro.2014.07.406
- ¹² W. B. Lee, Y. J. Kim, S. B. Jung, Effects of copper insert layer on the properties of friction welded joints between TiAl and AISI 4140 structural steel, *Intermetallics*, 12 (2004) 6, 671–678, doi:10.1016/j.intermet.2004.02.004
- ¹³ G. Madhusudhan Reddy, P. Venkata Ramana, Role of nickel as an interlayer in dissimilar metal friction welding of maraging steel to low alloy steel, *J. of Mat. Process. Tech.*, 212 (2012), 66–77, doi:10.1016/j.jmatprotec.2011.08.005
- ¹⁴ B. Kurt, N. Orhan, E. Evin, A. Çalik, Diffusion bonding between Ti–6Al–4V alloy and ferritic stainless steel, *Materials Letters*, 61 (2007) 8–9, 1747–1750, doi:10.1016/j.matlet.2006.07.123
- ¹⁵ P. Li, J. Li, M. Salman, L. Liang, J. Xioeng, F. Shang, Effect of friction time on mechanical and metallurgical properties of continuous drive friction welded Ti6Al4V/SUS321 joints, *Materials and Design*, 56 (2014), 649–656, doi:10.1016/j.matdes.2013.11.065

EFFECT OF ACTIVATED FLUX AND NITROGEN ADDITION ON THE BEAD GEOMETRY OF BORATED STAINLESS-STEEL GTA WELDS

VPLIV AKTIVIRANEGA TOPILA IN DODATKA DUŠIKA NA GEOMETRIJO KOPELI PRI GTA ZVARIH BORIRANEGA NERJAVNEGA JEKLA

Guttikonda Raja Kumar¹, Gabbita Durga Janaki Ram², Sajja Rama Koteswara Rao³

¹Swarna Barathi Institute of Science and technology, Khammam, T. S., 507002, India

²IIT Madras, Department of Metallurgical & Materials Engineering, Chennai 600036, India

³S.S.N. College of Engineering, Department of Mechanical Engineering, Chennai 603110, India
rajkumardotcom@yahoo.com

Prejem rokopisa – received: 2015-03-05; sprejem za objavo – accepted for publication: 2015-05-14

doi:10.17222/mit.2015.052

Borated stainless steels (304B) are used in nuclear power plants as control rods, shielding material, spent-fuel storage racks and transportation casks as they have a high capacity to absorb thermal neutrons. In this study, bead-on-plate welds were made on 10-mm-thick 304B plates using gas tungsten arc welding with Ar and Ar+2% nitrogen as the shielding gases, activated-flux GTA and electron-beam welding processes. The effects of the activated flux and nitrogen addition to the weld metal through the shielding gas, on the microstructure, bead geometry and mechanical properties were investigated. Activated-flux GTA welding and electron-beam welding substantially enhanced the depth of penetration and the aspect ratio compared to the other processes. Full-penetration welds were obtained in a single pass using activated-flux GTA and EB welding. The fusion-zone (FZ) microstructure of an activated GTA weld exhibits a columnar dendritic structure with eutectic borides in interdendritic regions, while a fine equiaxed dendritic structure was noticed in EB welds. GTA, nitrogen-added GTA and activated-flux GTA welds exhibited a partially melted zone adjacent to the fusion zone, with the activated-flux GTAW process resulting in a significantly thinner partially melted zone (PMZ). No PMZ was noticed in the EB welds. All the welds exhibited a high joint efficiency and impact toughness equal to those of the base material. It is concluded that the activated-flux GTA and EB welding processes are advantageous due to the use of a low heat input and failure location.

Keywords: borated stainless steels, bead geometry, activated flux, GTAW, partially melted zone, nitrogen

Borirana nerjavna jekla (304B) se uporabljajo v nuklearnih elektrarnah kot kontrolne palice, zaščitni material, nosilci shranjeval za izrabljene palice in za transportne sode, saj imajo sposobnost velike absorpcije termičnih nevtronov. V tej študiji so bili izdelani okrogli in ploščati zvari na 10 mm debelih ploščah iz 304B, z uporabo TIG varjenja v zaščitni atmosferi iz Ar + 2 % dušika, z aktiviranim talilom GTA in varjenjem z elektronskim curkom. Preiskovan je bil vpliv aktiviranega talila in dodatka dušika v zvar s pomočjo zaščitnega plina, na mikrostrukturo, geometrijo kopeli in mehanske lastnosti. Varjenje z aktiviranim talilom GTA in varjenje z elektronskim curkom, občutno povečata globino penetracije in razmerje, v primerjavi z drugimi procesi. Z uporabo aktiviranega talila GTA in z varjenjem z elektronskim curkom je bila dosežena popolna penetracija zvarov. Mikrostruktura cone zlivanja (FZ) pri zvaru z aktiviranim talilom GTA, kaže stebrasto dendritno strukturo z evtektičnimi boridi v meddendritnih področjih, medtem ko je bila pri zvarih z elektronskim curkom opažena struktura z drobnimi enakoosnimi dendriti. Zvari GTA, GTA z dodanim dušikom in GTA z aktiviranim talilom, so kazali delno raztaljena področja okrog področja zlivanja ter z močno stanjšano delno staljeno področje (PMZ) pri postopku z aktiviranim talilom GTA. V zvarih z elektronskim curkom ni bilo opaziti PMZ. Vsi zvari so pokazali veliko učinkovitost spoja in udarno žilavost, ki je enaka kot pri osnovnem materialu. Ugotovljeno je, da imata varjenje z aktiviranim talilom GTA in varjenje z elektronskim snopom, prednost zaradi uporabe majhnega vnosa toplote in zaradi možnosti lokacije napak.

Ključne besede: borirano nerjavno jeklo, geometrija kopeli, aktivirano talilo, GTAW, delno staljeno področje, dušik

1 INTRODUCTION

Borated stainless steel 304B is an austenitic-type stainless steel containing 0.2 % to 2.25 % boron; it is widely used in nuclear industries for various applications. These applications involve storage of spent nuclear fuel in the forms of long-term storage tanks or caskets, transportation baskets and control rods.^{1,2} The objective of developing these steels is to absorb radiation from the spent fuel. Due to the presence of the ¹⁰B isotope, these stainless steels have superior neutron-absorption capabilities.³ Spent fuel rods are stored in dry casks, made up of borated stainless steel for long-term thermal neutron

irradiation. Despite the fact that boron allows an adequate neutron absorption, it has an adverse influence on mechanical properties, particularly on the fracture toughness. Very low solubility of boron in an austenitic matrix results in the formation of hard, brittle (Cr, Fe)₂B precipitating phases, which are low-melting eutectics.⁴ The size, shape and distribution of these borides also deteriorate the mechanical properties.⁵ Park et al.⁶ conducted post-weld heat treatments and reported that spheroidized accicular eutectic phases were found to enhance the ductility.

Earlier, borated SSs were typically used as bolts on additions to a structural framework. However, due to the

slow and non-automatic riveting process, welding was adopted. The solidification cracking susceptibility is high at 0.2 % of mass fractions of boron due to a wider solidification range.⁷ In later studies, it was found that a boron content of 0.5 % of mass fractions or more, i.e., above its solid-solubility limit causes a reduction in the coefficient of thermal expansion and constricts the solidification range, which, in turn, causes the crack-healing phenomenon and decreases the cracking susceptibility.^{8,9} The lower solidification-cracking susceptibility of high-boron steels is mainly due to the healing of cracks by the abundant amounts of the low-melting eutectic liquid of (Cr,Fe)₂B.¹⁰

ASTM A887-89 covers eight different types of borated stainless steels, and each type has two grades, i.e., A and B with different boron contents.¹¹ Specification designates Grade A for the materials produced with powder metallurgy containing finer and more uniformly distributed borides compared to Grade B made with ingot metallurgy. The borated SSs fabricated with the hot-rolling technique, employing the powder-sintering method have sufficient ductility and other properties.¹²

The GTAW is the welding process normally used in the fabrication of borated stainless steels. However, its disadvantage is a relatively shallow penetration during a single-pass welding operation on thicker plates. The thickness of the austenitic stainless steels that can be welded in a single pass with argon as the shielding gas is normally restricted to 3 mm. In this connection, a novel variant of the GTA welding process called the activated-flux GTA welding process was initially developed for the welding of titanium at the Paton Institute of Electric Welding.^{13,14} Several investigations were carried out by various researchers to develop suitable flux components to extend this technique to other alloys. In the activated-flux GTA welding process, a thin coating of the activated flux is applied onto the surface of a joint and the electrons outside the arc are captured by the flux when it is vaporized during welding. Thus, the arc gets constricted which, in turn, leads to an increase in the penetration. Sun and Pan reported that the penetration capability can be increased by as much as 300 % due to the activated-flux GTA welding when compared with the conventional GTA welding.^{15,16}

The main reasons for the significant improvement in the penetration in the steels are reported to be the arc constriction and the reversed Marangoni convection.¹⁷ However, several researchers stated that the increase in the penetration is due to the positive surface-tension gradient in a molten-weld pool, which causes the fluid to flow towards the bottom of the weld.^{18,19} Thus, based on the productivity, the activated GTA welding process is more viable than the conventional GTA welding process. The activated GTA welding of austenitic stainless steels was investigated by various authors to understand the effect of the flux on the depth of penetration, the aspect

ratio, the microstructure and the mechanical behavior.²⁰⁻²⁶

Furthermore, the effect of the activated flux on the GTA welding of austenitic stainless steel 316L was studied by Kuang Hung et al.²⁷ It was reported that the activated TIG welding increases the joint penetration and the aspect ratio, which, in turn, reduce the angular distortion of the weldments. A great deal of research was carried out to develop various flux combinations and understand their beneficial influence on the GTA welding of austenitic stainless steels. Several investigations showed that an addition of nitrogen to the shielding gas influences the weld-bead shape, the depth of penetration and the weld metal microstructure.^{28,29}

However, not much information pertaining to the effect of the activated flux and nitrogen addition on the GTA welding of borated SS has been reported so far. Therefore, this work presents the microstructure and mechanical behavior of GTAW, activated-flux GTAW, nitrogen-added GTAW and electron-beam welding (EBW) of 10-mm-thick borated stainless steel.

2 EXPERIMENTAL WORK

The base material used in this study was borated stainless steel (BSS) 304B4 and its chemical composition is given in **Table 1**. As-received rolled plates of 40 mm were cut, using an electrical discharge machine to prepare plates of 300 mm × 110 mm × 10 mm. The plates were cleaned using acetone to remove surface contamination before the welding.

Table 1: Chemical composition of the base material

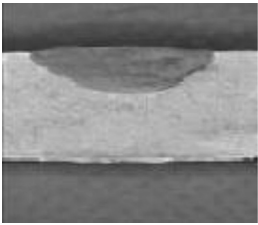
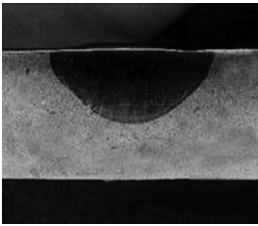
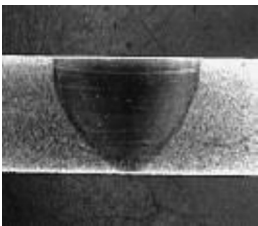
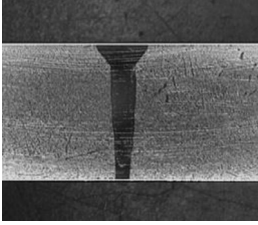
Tabela 1: Kemijska sestava osnovnega materiala

Material	Cr	Ni	Mn	B	Si	P	C
304B4	19.3	13.4	2.0	1.05	0.74	0.045	0.08

Bead-on-plate welds were produced using the automatic GTAW process. A tungsten electrode (AWS classification EWTh-2) with a diameter of 3.2 mm and the shielding gas of pure argon were used in the conventional GTAW process with direct-current electrode negative (DCEN) polarity. In addition to argon-shielded bead-on-plate welds, welds were produced using a shielding-gas mixture containing 2 % (volume) nitrogen along with argon. Also, autogenous full-penetration electron-beam welds were also made.

For the activated GTA welding, the activated flux was prepared, with its constituents in the required proportions, and then mixed with ethanol and the resulting mixture was stirred until it turned into paste. The flux used in this process is commercially available and its composition was reported in the patent by M.Vasudevan.³⁰ A thin layer of this paste was applied manually on the surface to be welded and dry powder remained there after the evaporation of ethanol. Using this activated flux, several bead-on-plate experiments were

Table 2: Common used welding parameters**Tabela 2:** Uporabljeni splošni parametri varjenja

Cross-sections of the welds	Depth of penetration (mm)	Aspect ratio (d/w)	Weld area (mm^2)	Welding parameters	Heat input (KJ/mm)
 GTAW	3.8	0.27	51.45	Weld current: 235 A Arc voltage: 17 V Travel speed: 120 mm/min Gas flow rate: $25,3 \text{ Pa m}^3 \text{ s}^{-1}$	2
 Nitrogen-added GTAW	5.77	0.4	57.54	Weld current: 235 A Arc voltage: 17 V Travel speed: 120 mm/min Gas flow rate: $25,3 \text{ Pa m}^3 \text{ s}^{-1}$	2
 Activated GTAW	10	0.8	92.01	Weld current: 235 A Arc voltage: 17 V Travel speed: 120 mm/min Gas flow rate: $25,3 \text{ Pa m}^3 \text{ s}^{-1}$	2
 EBW	10	2.82	17.02	Acceleration voltage: 60KV Beam current: 70 mA Travel speed: 700 mm/min	0.36

carried out in order to achieve a single-pass full-penetration weld in the activated GTAW process.

The parameters used in various welding processes are presented in **Table 2**. Using standard metallographic procedures, specimens were prepared for a microstructural investigation. After polishing, the specimens were etched with Kalling's 1 solution containing 5 g of cupric chloride, 100 mL of hydrochloric acid and 100 mL of ethanol. The welds were initially examined with a stereo microscope and then bead-geometry measurements were taken using image-analysis software. The microstructures of different zones of interest such as FZ, PMZ and the base metal (BM) were observed with a light microscope. Micro-hardness tests were carried out using a Vickers digital micro-hardness tester along the weld joint. A load of 500 g was applied for a duration of 10 s.

In accordance with ASTM E8, tensile specimens were machined with an EDM-wire-cutting machine so that the weld metal was located in the center of gauge length. The tensile properties of weldments, i.e., the ultimate tensile strength, the proof strength and the percent elongation were evaluated on the basis of the results of the tensile tests conducted at room temperature. The tensile-test results are listed in **Table 3** and all the values presented are average values of at least three specimens. Charpy-impact test specimens were prepared in accordance with ASTM standard E23. Identical V-notches were machined on three specimens, at the weld center, using a broaching machine. Impact testing was conducted at room temperature using a pendulum-type machine with the maximum capacity of 300 J.

3 RESULTS

Cross-sections of the welds made using different welding processes are presented in **Table 2**, along with the bead-profile parameters and corresponding welding parameters. The microstructure of the base metal is presented in **Figure 1**. The microstructures of FZ and PMZ for the welds made using various welding processes are shown in **Figures 2a to 2d** and **Figures 3a to 3d**, respectively. The microhardness surveys carried out along the various weld zones such as FZ, PMZ and BM of different welds are shown in **Figures 4a to 4d**. The tensile properties for the different welds considered in the

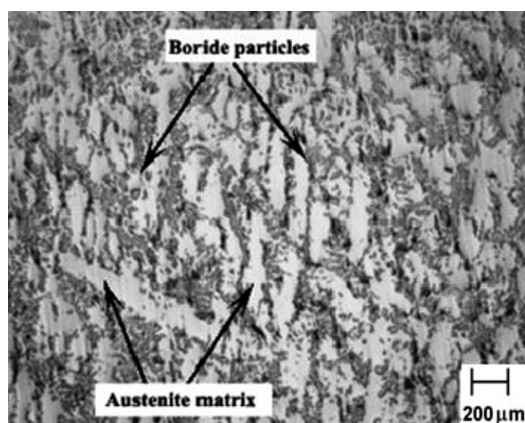


Figure 1: Microstructure of the base metal showing a boride network in an austenitic matrix

Slika 1: Mikrostruktura osnovnega materiala, ki kaže mrežo boridov v avstenitni osnovi

present study are presented in **Table 3**. The results of the Charpy-impact test conducted at room temperature for the welds produced using various welding processes are presented in **Table 3**.

4 DISCUSSION

4.1 Weld bead geometry

From **Table 2**, it can be seen that the three variants of the GTA process use the same welding parameters and heat input, i.e., 2 kJ/mm. The use of Ar+2%N shielding gas in place of Ar significantly increases the depth of penetration, from 3.8 mm to 5.7 mm; and the aspect ratio of the weld bead also increases. This was observed by earlier researchers for other materials.^{28,29} For the same heat input, the effect of the activated flux on the bead geometry is much more significant and a full penetration of 10 mm is observed. It can also be seen from the macrograph presented in **Table 2** that the activated flux causes the aspect ratio of the weld bead to reach 0.8, which is a significant change. Electron-beam welds exhibit the keyhole type of the bead geometry and a full penetration can be achieved using a much smaller heat input of 0.36 kJ/mm, showing the process to be greatly enhanced.

It was observed in this study that the bead shape becomes relatively wider and shallower with an increase in the welding current for both GTA and nitrogen-added GTA welding. Generally, the surface tension (σ) on the pool surface, formed by the cohesive forces of liquid metal, decreases with an increase in the temperature. Thus,

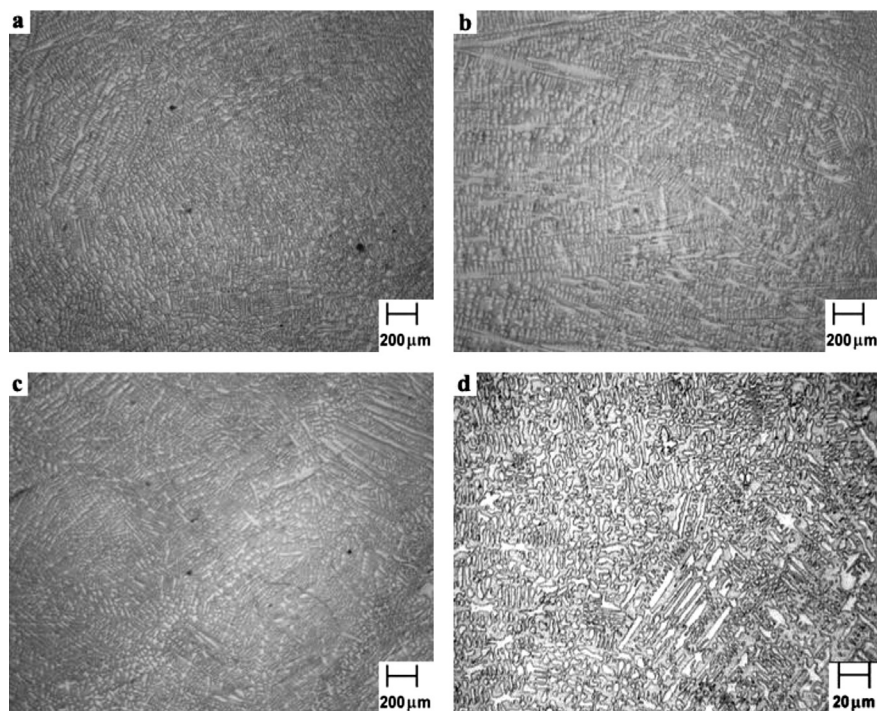
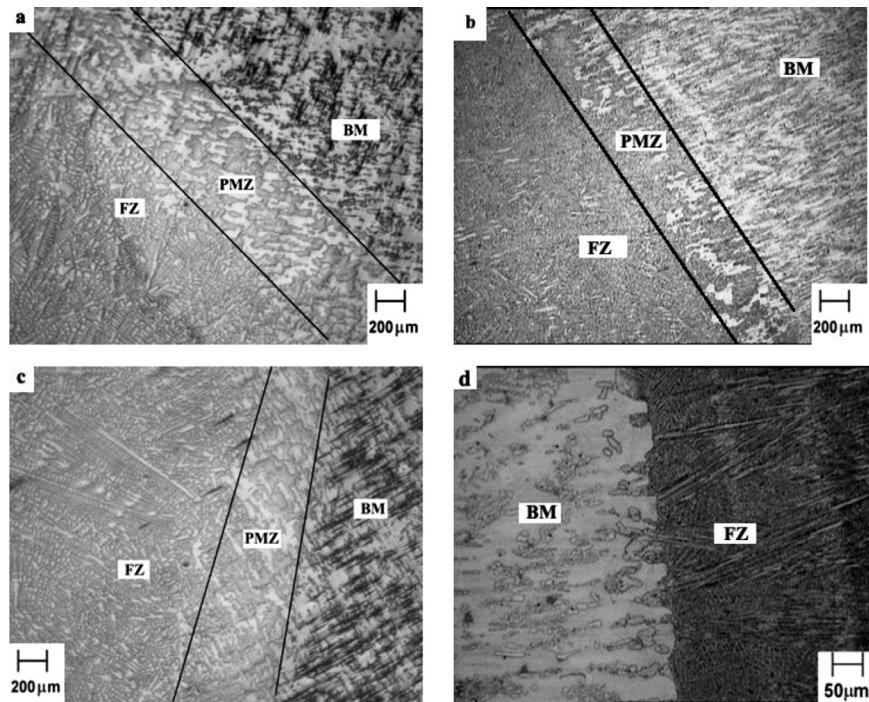


Figure 2: Microstructures of the FZs after various welding processes: a) GTA, b) activated GTA, c) nitrogen-added GTA, d) EBW

Slika 2: Mikrostrukture FZ pri različnih postopkih varjenja: a) GTA, b) aktiviran GTA, c) dušik dodan GTA, d) EBW

Table 3: Mechanical properties of 304B stainless-steel welds made with various GTA welding processes**Tabela 3:** Mehanske lastnosti zvarov nerjavnega jekla 304B, izdelanih po različnih GTA varilnih postopkih

Process	Proof strength	Ultimate tensile strength	% Elongation	Joint efficiency in terms of tensile strength	Failure location	Impact toughness
Base metal	384	576	12	–	–	7
GTAW	379	545	10	94.62	PMZ	7
Nitrogen added GTAW	390	550	11	96.32	PMZ	8
Activated GTAW	400	569	14	98.78	BM	7
EBW	415	570	12	98.95	BM	10

**Figure 3:** Microstructures of the weldments after various welding processes: a) GTAW, b) activated GTAW, c) nitrogen-added GTAW, d) EBW
Slika 3: Mikrostrukture zvarov pri različnih procesih varjenja: a) GTAW, b) aktiviran GTAW, c) GTAW z dodanim dušikom, d) EBW

the temperature gradient becomes negative, i.e., $d\sigma/dT < 0$ which, in turn, generates centrifugal Marangoni convection in the molten pool. This constitutes one of the main reasons for the shallow penetration and lower aspect ratio in the conventional GTA welding. However, in the case of activated GTA welds, the presence of the activated flux changes the temperature gradient to a positive value, i.e., $d\sigma/dT > 0$. This positive temperature gradient causes centripetal Marangoni convection, which, in turn, directs the flow toward the pool center resulting in a deeper and narrower weld pool. By and large, it was noticed that the activated flux beneficially influenced the Marangoni convection mode by changing the temperature gradient. Furthermore, the aspect ratio was increased due to the variation in the temperature gradient.^{21,22}

4.2 Microstructure

As it can be noticed, irregular boride particles $(Fe,Cr)_2B$, seen as a dark phase, are dispersed in the

austenitic matrix. Boron is insoluble in austenite virtually at all temperatures. The insolubility is more significant in the case of steels with high boron levels, which, in turn, results in a continuous network of boride eutectics such as Fe_2B and Cr_2B in an austenitic matrix. The boride eutectics strengthen the austenitic matrix but adversely affect the toughness and ductility of these steels. Furthermore, the shape of these eutectic phases is also one of the factors affecting the mechanical behavior of a weld.⁶

In order to have full-penetration welds for microstructural studies and an evaluation of mechanical properties, the welds were made using two passes in the case of the GTA and nitrogen-added GTA processes and a single pass in the case of the activated-flux and EB processes. The fusion zone of the activated-flux-GTA weld was characterized by a columnar, austenite dendritic structure with eutectic borides solidified in the interdendritic regions (**Figure 2b**). However, the GTA and nitrogen-added-GTA welds exhibited both equiaxed

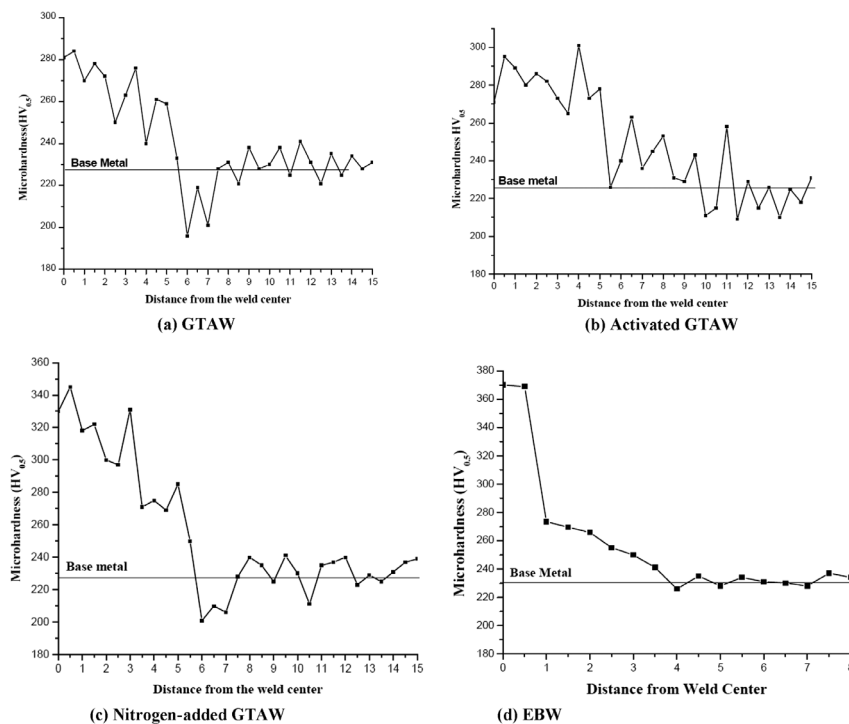


Figure 4: Microhardness profiles for various welding processes

Slika 4: Profil mikrotrdotre pri različnih procesih varjenja

and columnar dendritic structures, as can be seen in **Figures 2a** and **2c**. A short interaction span with an acute energy density causes a low heat input in EBW. As a result, the fusion zone in EBW cools faster resulting in a finer equiaxed dendritic structure.

Typical appearances of the PMZ for various weld types are presented in **Figure 3**. As it can be noticed, the representative PMZ consists of localized regions of austenite that remain solid during the welding, surrounded by irregular boride eutectics. However, the width of PMZ was found to be larger in the case of the GTA and nitrogen-added-GTA welds than that of the activated-flux-GTA welds. This is attributed to slow cooling rates associated with high heat inputs prevailing in the GTA and nitrogen-added-GTA welds. The low heat input associated with high cooling rates almost eliminated the PMZ in electron-beam welding and no localized region of austenite was noticed in **Figure 3d**.

4.3 Mechanical properties

4.3.1 Microhardness

Hardness profiles revealed that FZ exhibited a higher hardness for all the welds. The increase in the hardness of FZ is attributed to the presence of a dendritic microstructure with boride eutectics in the interdendritic regions (**Figure 2**). It was observed that the nitrogen addition in the GTA welds significantly enhances the FZ hardness. It was also noticed that there is a sudden fall in the hardness of PMZ in the case of both the GTA and nitrogen-added GTA welds, while there is no such trend

in the activated GTA and EB welding. The significant reduction in the PMZ hardness is attributed to the difference in the cooling rate, which results in a variation in the size and shape of the eutectic borides formed in PMZ as can be seen from **Figures 3a** to **3d**. It can be seen from **Figure 5** that the fracture during the tensile test in the case of the GTA and nitrogen-added GTA welds, occurs in PMZ, whereas in the case of the other two welds the fracture occurs in the base materials far away from the weld metal.

4.3.2 Tensile properties

In order to obtain joint properties, automatic GTAW was carried out in two passes, one from each side. Though there is no significant variation in the joint efficiencies of the welds, a marginal improvement in the yield strength for the electron-beam and activated-GTA welds was noticed. The GTA and nitrogen-added-GTA welds were found to fracture at PMZ, as shown in **Figure 5**, the region where a loss in the hardness can be clearly noticed due to an irregular distribution of boride eutectics. It was also observed that the activated-GTA and EB welds failed in BM. Low-heat-input welding processes exhibited a significant improvement in the tensile strength compared to high-heat-input welding process.

4.3.3 Impact toughness

It was observed that the welds exhibit the same toughness as that of BM, irrespective of the welding

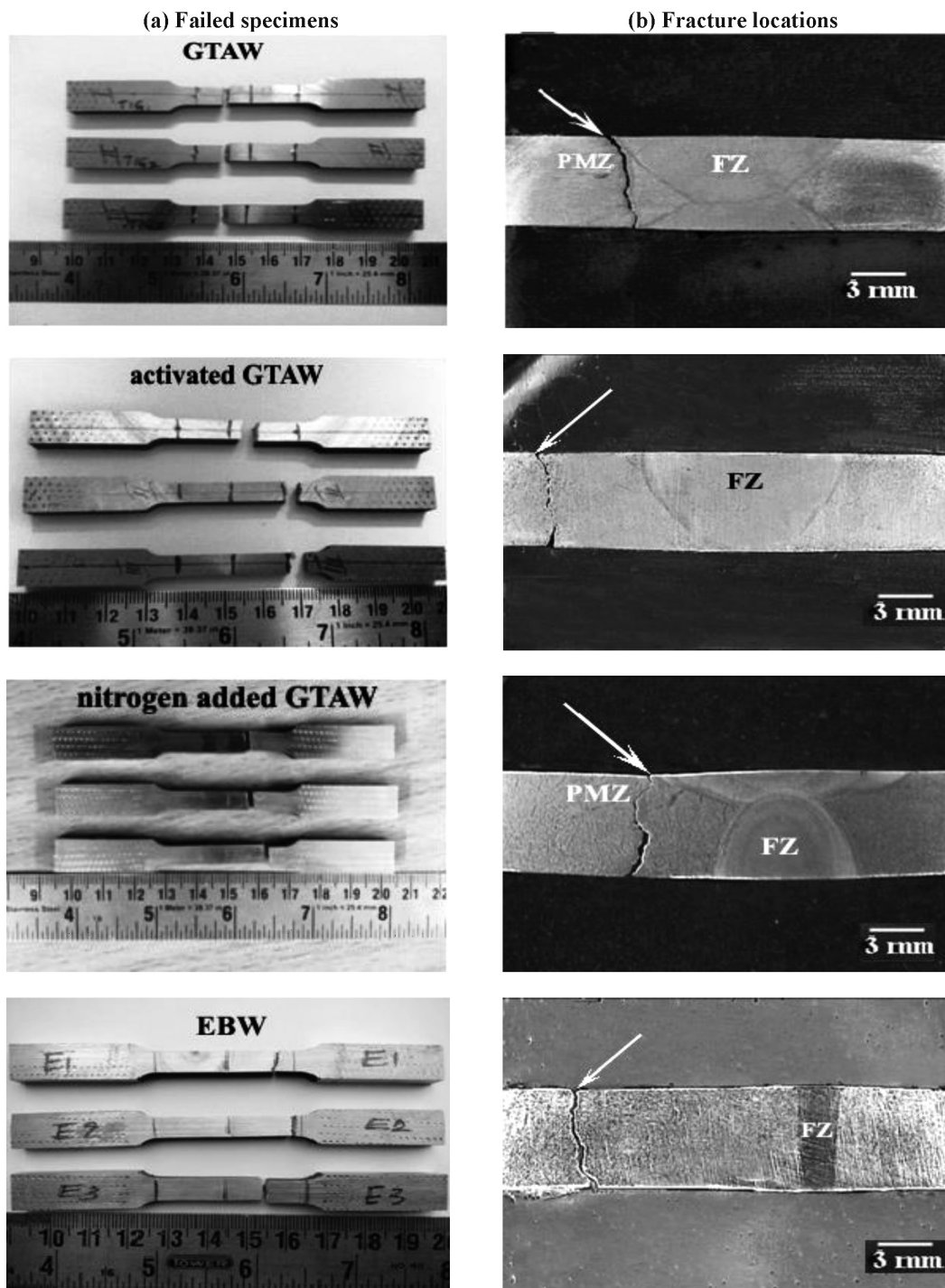


Figure 5: Fracture locations of the welds made with different welding processes: a) tensile-test samples, b) cross-sections
Slika 5: Lokacija preloma zvarov, izdelanih z različnimi postopki varjenja: a) vzorci za natezne preizkuse, b) preseki

process employed. The lower toughness of BM and FZ is mainly due to brittle $(Cr,Fe)_2B$ borides.

5 CONCLUSIONS

1. Defect-free welds of 304B4 borated stainless steels can be easily made using GTA, activated-flux GTA, nitrogen-added GTA and EB welding processes.
2. The activated-flux GTA and EB welding processes substantially enhance both the depth of penetration and the aspect ratio.
3. The fusion-zone microstructure of the activated-flux GTA welds reveals a columnar, austenite dendritic structure with eutectic borides solidified in the interdendritic regions. However, the EB welds exhibit a fine equiaxed dendritic structure.

4. Low-heat-input EBW inhibits the formation of PMZ. A significant loss in the hardness occurs in the PMZs of the GTA and nitrogen-added GTA welds, which is mainly due to the slow cooling rates associated with high heat inputs.
5. A tensile failure occurs in the PMZ area of the GTA and nitrogen-added GTA welds, while the activated-flux GTA and EB welds failed in the base material.

Acknowledgments

The authors would like to acknowledge the technical support of IIT Madras, Defence Research & Development Laboratory (DRDL), Hyderabad and Ador Welding Pvt. Ltd., Chennai.

6 REFERENCES

- ¹ C. V. Robino, M. J. Cieslak, Fusion welding of a modern borated stainless steel, *Welding Journal-Including Welding Research Supplement*, 76 (1997) 1, 12–23, doi:10.2172/10183280
- ² C. V. Robino, M. J. Cieslak, High-temperature metallurgy of advanced borated stainless steels, *Metallurgical and Materials Transactions A*, 26 (1995) 7, 1673–1685, doi:10.1007/BF02670754
- ³ D. A. Moreno, B. Molina, C. Ranninger, F. Montero, J. Izquierdo, Microstructural characterization and pitting corrosion behavior of UNS S30466 borated stainless steel, *Corrosion*, 60 (2004) 6, 573–583, doi:10.5006/1.3287761
- ⁴ H. J. Goldschmidt, Effect of boron additions to austenitic stainless steels – Part I – effect of boron additions to 20%Cr, 25%Ni austenitic steel with and without Nb, Mn and Si, *Journal of the Iron and Steel Institute*, 209 (1971) 11, 900–909
- ⁵ B. Shanmugarajan, J. N. Chary, G. Padmanabham, B. Arivazhagan, S. K. Albert, A. K. Bhaduri, Studies on autogenous laser welding of type 304B4 borated stainless steel, *Optics and Lasers in Engineering*, 51 (2013) 11, 1272–1277, doi:10.1016/j.optlaseng.2013.05.004
- ⁶ T. D. Park, K. K. Baek, D. S. Kim, PWHT effect on the mechanical properties of borated stainless steel GTA weldments for nuclear shield, *Metals and Materials*, 3 (1997) 1, 46–50, doi:10.1007/BF03026105
- ⁷ T. Shinoda, H. Miyake, T. Matsuzaka, T. Matsumoto, H. Kanai, Hot cracking susceptibility of boron modified AISI 304 austenitic stainless steel welds, *Materials Science and Technology*, 8 (1992) 10, 913–921, doi:10.1179/026708392790169777
- ⁸ W. R. Apblett, W. S. Pellini, Factors which influence weld hot cracking, *Welding Journal*, 33 (1954) 2, 83–90
- ⁹ J. C. Borland, R. N. Younger, Some aspects of cracking in welded Cr-Ni austenitic steels, *British Welding Journal*, 7 (1960), 22–59
- ¹⁰ T. Matsumoto, T. Shinoda, H. Miyake, T. Matsuzaka, H. Kanai, Effect of low-melting point eutectic on solidification cracking susceptibility of boron-added AISI 304 stainless steel welds, *Welding Journal-Including Welding Research Supplement*, 74 (1995), 397–405
- ¹¹ ASTM A887-89 (2009) ASM International, West Conshohocken, PA, USA 2009
- ¹² S. Yamamoto, M. Honda, Y. Kobayashi, T. Sakiyama, Y. Ehira, N. Takashi, Boronated stainless steels for thermal neutron shielding, *Jr. Thermal & Nuclear Power Generation*, 41 (1990) 9, 1149–1157
- ¹³ W. Lucas, D. Howse, Activating flux – increasing the performance and productivity of the TIG and plasma processes, *Welding and Metal fabrication*, 64 (1996), 11
- ¹⁴ P. C. J. Anderson, R. Wiktorowicz, Improving productivity with A-TIG welding, *Welding and Metal Fabrication*, 64 (1996) 3, 108–109
- ¹⁵ M. Vasudevan, A. K. Bhaduri, Baldev Raj, Development and evaluation of activated flux for TIG welding of type 304 LN and type 316 LN stainless steels, *Proc. of the Inter. Institute of Welding, International Congress, Chennai 2008*
- ¹⁶ Z. Sun, D. Pan, Welding of titanium alloys with activating flux, *Science and Technology of Welding and Joining*, 9 (2004) 4, 337–344, doi:10.1179/136217104225021571
- ¹⁷ P. Vasantharaja, M. Vasudevan, Studies on A-TIG welding of low activation ferritic/martensitic (LAFM) steel, *Journal of Nuclear Materials*, 421 (2012), 117–123, doi:10.1016/j.jnucmat.2011.11.062
- ¹⁸ C. R. Heiple, J. R. Roper, Effect of selenium on GTAW fusion zone geometry, *Welding Journal*, 60 (1981) 8, 143–145
- ¹⁹ C. R. Heiple, R. Roper, Mechanism for minor element effect on GTA fusion zone geometry, *Welding Journal*, 61 (1982) 4, 97–102
- ²⁰ P. Modenesi, E. R. Apolinario, TIG welding with single-component fluxes, *Journal of Materials Processing Technology*, 99 (2000) 1–3, 260–265, doi:10.1016/S0924-0136(99)00435
- ²¹ S. Lu, H. Fujii, H. Sugiyama, M. Tanaka, K. Nogi, Marangoni convection and welding penetration in A-TIG welding, *Transactions of the Japan Welding Research Institute*, 32 (2003) 79–82, doi:10.1016/j.tafmec.2007.05.004
- ²² H. Fujii, T. Sato, S. Lua, K. Nogi, Development of an advanced A-TIG (AA-TIG) welding method by control of Marangoni convection, *Materials Science and Engineering A*, 495 (2008), 296–303, doi:10.1016/j.msea.2007.10.116
- ²³ H. Y. Huang, S. W. Shyu, K. H. Tseng, C. P. Chou, Evaluation of TIG flux welding on the characteristics of stainless steel, *Science and Technology of Welding and Joining*, 10 (2005) 5, 566–573, doi:10.1179/174329305X48329
- ²⁴ A. Rodrigues, A. Loureiro, Effect of shielding gas and activating flux on weld bead geometry in tungsten inert gas welding of austenitic stainless steels, *Science and Technology of Welding and Joining*, 10 (2005) 6, 760–765, doi:10.1179/174329305X68769
- ²⁵ S. Leconte, P. Paillard, P. Chapelle, G. Henrion, J. Saindrenan, Effect of oxides fluxes on activation mechanisms of tungsten inert gas process, *Science and Technology of Welding and Joining*, 11 (2006) 4, 389–397, doi:10.1179/174329306X129544
- ²⁶ L. Sanbao, Y. Chunli, L. Fengyao, W. Lin, S. Sheng, Effect of activating fluxes on weld mechanical properties in TIG welding, *China Welding*, 10 (2001) 2, 170–174
- ²⁷ K. H. Tseng, C. Y. Hsu, Performance of activated TIG process in austenitic stainless steel welds, *Journal of Materials Processing and Technology*, 211 (2011), 503–512, doi:10.1016/j.jmatprotec.2010.11.003
- ²⁸ D. D. Nage, V. S. Raja, R. Raman, Effect of nitrogen addition on the microstructure and mechanical behaviour of 317L and 904L austenitic stainless steel welds, *Journal of Materials Science*, 41 (2006) 7, 2097–2112, doi:10.1007/s10853-006-3150-5
- ²⁹ K. H. Tseng, C. P. Chou, The study of nitrogen in argon gas on the angular distortion of austenitic stainless steel weldments, *Journal of Materials Processing and Technology*, 142 (2003), 139–44, doi:10.1016/S0924-0136(03)00593-4
- ³⁰ An international patent Tungsten inert gas welding flux for enhancing penetration in single pass for austenitic stainless steels, patent no. PCT/IN06/00442/dt. 8/11/06

MICROSTRUCTURAL EVOLUTION DURING THE TRANSIENT LIQUID-PHASE BONDING OF DISSIMILAR NICKEL-BASED SUPERALLOYS OF IN738LC AND NIMONIC 75

RAZVOJ MIKROSTRUKTURE MED SPAJANJEM S PREHODNO TEKOČO FAZO NEENAKIH SUPERZLITIN NA OSNOVI NIKLJA IN738LC IN NIMONIC 75

Meysam Khakian Ghomi, Saeid Nategh, Shamsoddin Mirdamadi

Islamic Azad University, Science and Research Branch, Department of Materials Engineering, Tehran, Iran
khakian-meysam@yahoo.com, nategh@sharif.ir

Prejem rokopisa – received: 2015-04-01; sprejem za objavo – accepted for publication: 2015-05-08

doi:10.17222/mit.2015.072

The joining of dissimilar nickel-based superalloys, i.e., IN738LC to Nimonic 75, using transient liquid-phase bonding with a Ni-15Cr-3.5B interlayer (MBF-80) was carried out at temperatures of 1080 °C to 1180 °C for different bonding times of 30–150 min. A joint cross-section was surveyed using optical and scanning electron microscopy. Microstructural examinations showed that after short bonding times, the joint microstructure consists of continuous eutectic intermetallic phases and longer bonding times lead to a eutectic-free microstructure. It was clear that for all the bonding times and temperatures, boride phases were precipitated at the interface of the base metal and the interlayer due to boron diffusion in to the base metals. The results also showed that the morphology of the precipitates in the diffusion-affected zone (DAZ) varies from globular to acicular by increasing the bonding time. Completion of the isothermal solidification, which prevents the formation of continuous intermetallic phases at the joint centerline, was studied at different temperatures.

Keywords: IN738LC, Nimonic 75 superalloy, TLP bonding, isothermal solidification, microstructure

Spajanje različnih superzlitin na osnovi niklja IN738LC na Nimonic 75, z uporabo prehodno tekoče faze z vmesnim slojem Ni-15Cr-3,5B (MBF-80), je bilo izvedeno pri temperaturah od 1080 °C do 1180 °C in pri različnih časih spajanja od 30 min do 150 min. Prečni prerez spoja je bil pregledan s svetlobno in z vrstično elektronsko mikroskopijo. Mikrostrukturne preiskave so pokazale, da pri kratkih časih spajanja mikrostruktura sestoji iz zvezne evtektične intermetalne faze, dolgi časi spajanja pa povzročijo mikrostrukturo brez evtektika. Izkazalo se je, da se pri vseh časih in temperaturah spajanja, boridna faza zaradi difuzije bora izloča na meji z osnovnim materialom v osnovni material. Rezultati so tudi pokazali, da morfologija izločkov v difuzijsko vplivani coni (DAZ) z naraščanjem časa spajanja varira, od globularne do acikularne. Dokončanje izotermnega strjevanja, ki prepreči nastanek zvezne intermetalne faze na liniji spajanja, je bilo proučevano pri različnih temperaturah.

Ključne besede: IN738LC, superzlitina Nimonic 75, TLP spajanje, izotermno strjevanje, mikrostruktura

1 INTRODUCTION

IN738LC is one of the most practical casting nickel-based superalloys. IN738LC is strengthened by both solid-solution and precipitation-hardening mechanisms.¹ Due to the presence of coherent γ' precipitates in the alloy with a complex chemical composition and a high stability at high temperatures, the alloy can keep its excellent strength in high-temperature operations and severe conditions, such as gas turbine components. Because of the mentioned properties, the alloy is a good choice for utilization in the first rows of gas-turbine hot sections. Also, this alloy has outstanding strength accompanied by excellent creep, fatigue, oxidation and corrosion resistance at high temperatures.²⁻⁴

Nimonic 75 is an 80/20 nickel-chromium alloy with controlled additions of titanium and carbon. Nimonic 75 first introduced in the 1940s for turbine blades as sealing components and is now mostly used for sheet applications calling for oxidation and scaling resistance coupled with medium strength at high operating temperatures. It

is still used in gas-turbine engineering and also for industrial thermal processing, furnace components and heat-treatment equipment.⁵

The weldability of superalloys is very much dependent on the amount of Al and Ti in their chemical composition. The high precipitation rate of γ' in alloys with a large amount of Al and Ti make them susceptible to crack propagation during welding.⁶⁻⁸ Fusion welding, diffusion bonding and brazing are the three main methods of joining and repairing superalloys that are widely used in power plants and aerospace industries. Solid-state diffusion bonding needs high pressure, time and temperature. Therefore, the process encounters a lot of practical and economic limitations, like growth of grains and precipitates during bonding and lengthy processing causes it to be uneconomic.⁹ Brazing is the other method of joining that uses an interlayer, containing a melting-point depressant like B, Si and P, as the joining media. The joining temperature must be precisely arranged to melt only the interlayer. Brittle boride, silicide and phosphate continuous phases may be developed in the joint

Table 1: Chemical composition of base materials and interlayer in mass fractions, (w/%)**Tabela 1:** Kemijska sestava osnovnih materialov in vmesne plasti, v masnih odstotkih (w/%)

Alloys	Cr	Co	Al	Ti	W	Mo	Ta	Nb	Fe	C	B	Ni
IN738LC	16.23	8.56	3.41	3.45	3.05	1.73	1.57	0.67	0.08	0.09	0.0063	Bal.
Nimonic 75	20.50	–	0.29	0.55	–	–	–	–	4.78	0.10	–	Bal.
MBF-80	14.89	–	–	–	–	–	–	–	–	–	3.72	Bal.

area during the brazing process and can degrade the joint's properties.^{10,11}

Transient liquid-phase (TLP) bonding is a hybrid process of brazing and diffusion bonding.¹ This method possesses the advantages of brazing and diffusion bonding and makes the joint structure very similar to the base material. In contrast to diffusion bonding, the process does not need any pressure due to the use of a liquid interlayer.^{12,13} The superiority of TLP in comparison with brazing is the completion of isothermal solidification in the bonding temperature.¹⁰ Also, TLP is widely used in the joining of metals and ceramics.¹⁴

In the standard models of TLP, there are three individual stages: dissolution, isothermal solidification and solid-state homogenization. Because of the short-range diffusion of melting-point depressant elements in the base metal, the dissolution of the base metal usually needs several minutes. In the isothermal solidification stage, long-term diffusion occurs and therefore the process needs much more time, depending on the bonding temperature and the interlayer type and the time varies from minutes to hours.¹⁵ By optimizing the time and temperature of the bonding, a joint microstructure that is very similar to the base metal with no discontinuity in the microstructure can be achieved.¹⁶

In this paper, the effect of bonding time and temperature on the microstructure evolution of the transient liquid-phase bonding of IN 738LC and Nimonic 75 using MBF-80 filler metal was investigated.

2 MATERIALS AND EXPERIMENTAL PROCEDURES

IN738LC and Nimonic 75 nickel-based superalloys were used as the base metals in this study. Both superalloys were used in the standard solution heat-treated condition. Commercial Ni-Cr-B in the form of amorphous foil (MBF-80) with a 75- μ m thickness was used as the interlayer. The chemical compositions of the base materials and the interlayer are given in **Table 1**.

TLP bonding test coupons were cut using EMD wirecut to a size of 10 mm \times 10 mm \times 5 mm, then they were grounded with a pendulum grinding machine, in order to remove the recast oxide layer from the faying surface of the coupons, and finally cleaned ultrasonically in a acetone bath. The interlayer was cut with a size of 11 mm \times 6 mm and placed between two faying surfaces of the base alloys. In order to prevent the movement of the samples, the assembly was placed in a fixture without any pressure on it. Green stop-off type 1 was used to

prevent the flowing out of the molten interlayer. The solidus and liquidus temperatures of the interlayer are 1050 °C and 1090 °C, respectively.¹⁷ Therefore, the bonding temperatures were selected above 1050 °C. TLP bonding was performed in a furnace under a vacuum of 10⁻⁵ mbar pressure at different temperatures of (1080, 1120, 1150 and 1180) °C and various holding times of (30, 60, 120 and 150) min. In order to investigate the phases formed during the athermal solidification, one test coupon was bonded at 1120 °C for 5 min. The heat-treatment cycle of the bonding is illustrated in **Figure 1**. The heating rate from 950 °C to the bonding temperature was set to 20 °C/min. In order to show the effect of time on the bond strength, a shear test was carried out on all the samples TLP bonded at 1080 °C.

The TLP-bonded test coupons were cut perpendicular to the bonding surface, due to brittleness of the intermetallic phases formed in the bonding centerline, by EDM wirecut and then prepared for metallographic examinations. In order to reveal the microstructure constituent, the samples were etched with Kalling's solution (5 gr CuCl₂ + 100 cc HCl + 100 cc Ethyl alcohol).¹⁸ Metallographic examinations were carried out using optical and scanning electron microscopy.

3 RESULTS AND DISCUSSION

3.1 Microstructure of the joint

The microstructure of the TLP-bonded specimen at 1120 °C and 5 minutes is shown in **Figure 2**. As can be seen, the bonding area can be divided into six distinct zones:

- Base metal - Nimonic side
- Isothermally Solidified Zone – Nimonic 75 Side (ISZ – Nimonic Side)

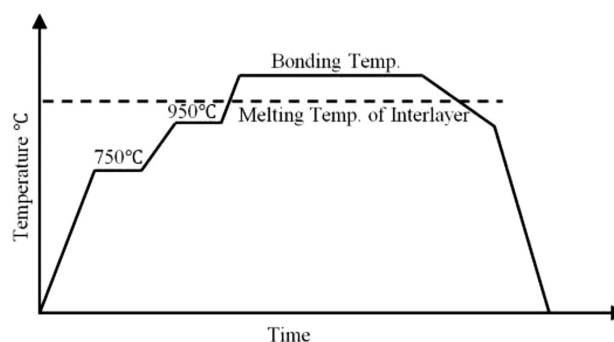
**Figure 1:** Heat-treatment cycle of the TLP bonding test coupons**Slika 1:** Potek cikla toplotne obdelave pri TLP spajanju preizkušancev

Table 2: EDS analysis (x/%) of phase formed in bond line shown in **Figure 2**

Tabela 2: EDS analiza (x/%) faze, ki je nastala na liniji stika, prikazani na **Sliki 2**

	Al	Ti	Cr	Fe	Co	Ni	Nb	Mo	Ta	W
ISZ - Inconel Side	3.12	0.94	19.41	1.23	3.01	70.43	0.64	0.52	0.28	0.41
ISZ - Nimonic Side	0.57	0.46	22.12	4.26	0.35	71.21	0.34	0.40	0.0	0.28
A (Ni-rich Boride)	1.08	3.83	9.18	0.71	2.28	80.70	0.85	0.56	0.80	0.0
B (γ Eutectic)	0.97	0.53	16.27	1.64	2.47	75.84	0.60	0.66	0.30	0.71
C (Cr-rich Boride)	0.41	0.08	89.72	0.15	0.47	5.37	0.46	2.02	0.0	1.31
D (Cr-rich Boride)	0.04	0.05	87.50	0.40	0.69	5.36	1.37	1.97	1.72	0.89
E	0.75	0.36	73.05	2.34	0.0	22.04	0.63	0.44	0.13	0.25
F	0.56	0.84	40.06	4.11	0.03	52.66	0.66	0.52	0.25	0.30

- Athermally Solidified Zone (ASZ)
- Isothermally Solidified Zone – Inconel 738 Side (ISZ – Inconel Side)
- Diffusion Affected Zone – Inconel 738 Side (DAZ – Inconel Side)
- Base metal – Inconel side

As can be seen in **Figure 2a**, the ISZ zone on both sides of the ASZ contains a thin layer of γ solid solution that formed at the solid/liquid interface during isothermal solidification from the base metal to the joint centerline. The chemical composition of the solid solutions formed on the ISZ – Inconel Side and ISZ - Nimonic Side are shown in **Table 2**. A significant difference between these two compositions is related to the chemical compositions of the Nimonic 75 and the IN738LC. Also, in **Figure 2b**, the different phases that are formed during bonding are specified with A to F.

As the interlayer melts, because the liquid and solid phases are not in the equilibrium condition, base-metal dissolution commences. The diffusion of boron into the base metal and the diffusion of base-metal elements like Cr, Fe, Co, Al and Ti into the molten interlayer leads to the equilibrium condition between the liquid and the solid. A chemical analysis of ISZ shows the diffusion of the base-alloy elements that were not present in the primary interlayer. The alloying elements' diffusion from the base metal to the interlayer and also boron diffusion from the interlayer to the base metal increases the liquidus temperature of the interlayer. The dissolution stage continues until the liquidus temperature of the molten interlayer reaches the bonding temperature, and

then the isothermal solidification starts from the solid/liquid interface to the joint centerline.^{2, 19}

As seen in **Table 2**, the chemical composition of the ISZ regions adjacent to the base alloys (Inconel Side and Nimonic Side) are not similar; therefore, we can conclude that the time required to reach equilibrium on each side are not equal. In contrast with the TLP bonding of two similar alloys, in which the isothermal solidification starts simultaneously and the eutectic centerline forms symmetrically, in dissimilar alloys the TLP bonding eutectic centerline lies closer to the alloy so that its equilibrium starts earlier.

A variation of the chemical composition that is due to the interdiffusion of elements of the base alloy and the interlayer is the main driving force of solidification for the ISZ.¹⁹ Since the solid and liquid are in an equilibrium condition during isothermal solidification, the secondary phases cannot form at this stage.^{3,20} The solidification behavior of the remaining liquid during the TLP bonding of pure nickel using the Ni-Cr-B interlayer, before completion of the isothermal solidification, was modeled by K. Ohsasa et al.²¹ The ternary phase diagram of Ni-Cr-B, in which the chemical composition of the interlayer is specified, is shown in **Figure 3**.²² During the cooling of the remaining liquid, which is the main

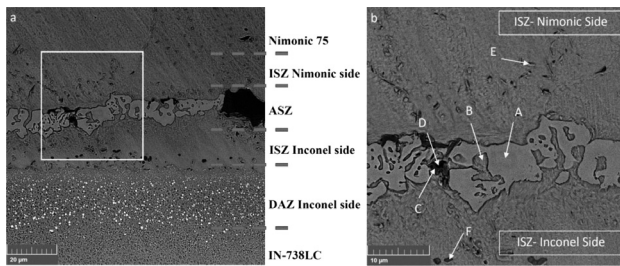


Figure 2: a), b) SEM micrograph of sample bonded at 1120 °C for 5 min

Slika 2: a), b) SEM-posnetek vzorca, spajaneja pri temperaturi 1120 °C, 5 min

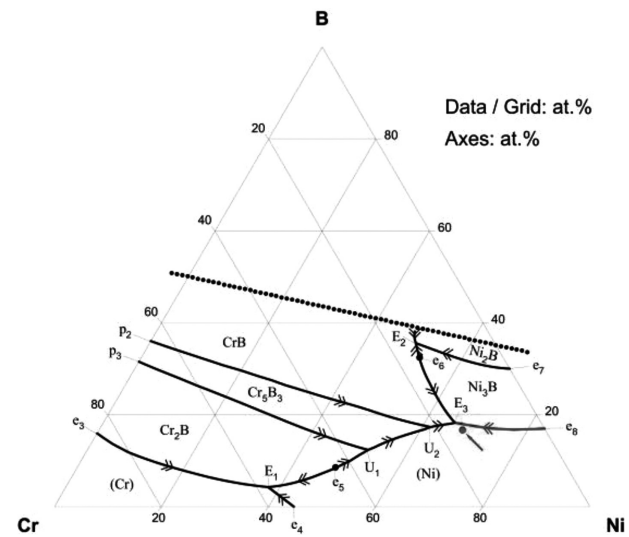


Figure 3: Liquidus projection of ternary phase diagram Ni-Cr-B

Slika 3: Projekcija likvidusa v ternarnem faznem diagramu Ni-Cr-B

driving force for ASZ solidification, γ dendrite is the first phase that forms at 1100 °C²¹ and grows from the solid/liquid interface towards the joint centerline. Solute elements with a partition coefficient less than unity ($k < 1$) are rejected into the liquid. Continuous enrichment of the liquid from the solute elements leads to the solute concentration becoming more than the solubility limit of the solute in the γ and then the secondary solidification constituents are formed between the dendrites (Phases E and F).²⁰ O. Ojo et al.²³ and A. Egbewande et al.¹⁰ observed the formation of these phases in the TLP bonding of IN738 and IN600, by use of a Ni-Cr-B interlayer, respectively.

During the cooling of the liquid and solid-solution growth additional boron is rejected to the liquid, as a result of poor solubility and the low partition coefficient of boron in Ni (0.3 % of amount fractions and ~ 0.008),²⁴ and then at 1042 °C the solidification path coincides with the eutectic line that separates the γ phase stability region from Ni_3B (e_8 line in **Figure 3**) and the γ solid solution and nickel boride eutectic phases are formed simultaneously through a binary eutectic transformation ($L \rightarrow \gamma + \text{Ni}_3\text{B}$).

More cooling leads to the growth of the γ solid solution and the rejection of boron and the formation of nickel borides lead to a reduction of the Ni concentration and an increment in the Cr in the remaining liquid (Cr solubility in Ni boride is relatively low (10.11 % of amount fractions)).¹⁹ Also, the Cr content of the liquid increases by temperature decrement until at 997 °C the liquid transforms into three phases of γ solid solution, nickel boride and chromium boride through a ternary eutectic transformation ($L \rightarrow \gamma + \text{Ni}_3\text{B} + \text{CrB}$).²¹ These phases are shown in **Figure 2b**, and its chemical compositions are shown in **Table 2**.

3.2 Effect of time and temperature on the microstructure of the TLP bonds

In order to investigate the effect of time on the microstructure of the TLP bonds, bonding was performed at 1080 °C for 30, 60, 120 and 150 min. It was clear that the thickness of the intermetallic phases decreases with the increasing time (**Figure 4**). The extent of isothermal solidification during TLP bonding depends on the amount and rate of boron diffusion into the base alloys. The thickness of remaining interlayer, which can transform into a continuous eutectic centerline during cooling, decreases for longer bonding times. It was clear that with an increasing time from 30 to 60 min, the thickness of the centerline eutectic decreases. After 120 min there is no continuous eutectic and after a longer time (150 min) there is a negligible amount of intermetallic phases. The results showed that 150 min is not enough for the completion of isothermal solidification at 1080 °C. **Figure 5** shows the ASZ thickness and the shear strength of the bond at different times. It is clear that a dominant

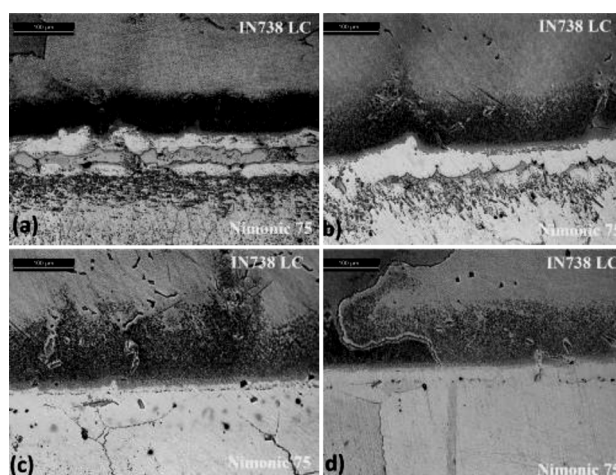


Figure 4: Light micrograph of TLP-bonded specimen at 1080 °C: a) 30 min, b) 60 min, c) 120 min, d) 150 min

Slika 4: Svetlobni posnetek vzorcev, spajanih s TLP, na temperaturi 1080 °C: a) 30 min, b) 60 min, c) 120 min, d) 150 min

increment in strength can be associated with a decrement of the ASZ thickness. The shear strengths of Nimonic 75 and IN738 at room temperature are 650 MPa and 860 MPa, respectively. The results showed that the strength of the TLP-bonded specimen at 1080 °C is less than the strength of the base metals.

Figure 6 shows the optical microstructure of TLP bonding at 1120 °C, 1150 °C after 120 min and 1180 °C after 150 min. It was clear that at bonding temperatures of 1120 °C and 1150 °C there was no centerline eutectic micro-constituents, and isothermal solidification was complete. It can be seen that with increasing bonding temperatures from 1120 °C to 1150 °C, significant microstructural changes occurred in the DAZ of IN738, but no changes happened in the bond line. It is expected that increasing the bonding temperature and consequently increasing the diffusion rate of boron, decreases the time required for completing the isothermal solidification. But as shown in **Figure 6c**, at 1180 °C

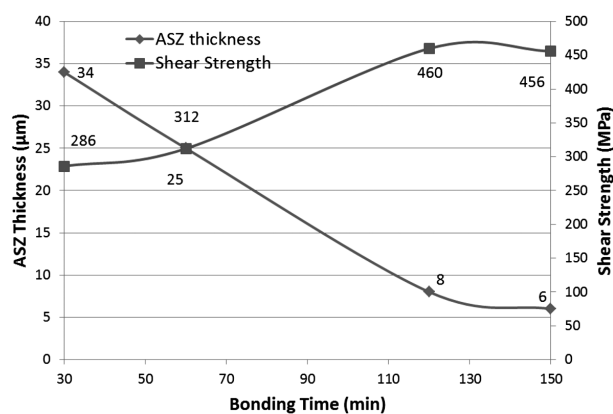


Figure 5: Shear strength and ASZ thickness versus bonding time at 1080 °C

Slika 5: Odvisnost strižne trdnosti in debeline ASZ od časa spajanja na temperaturi 1080 °C

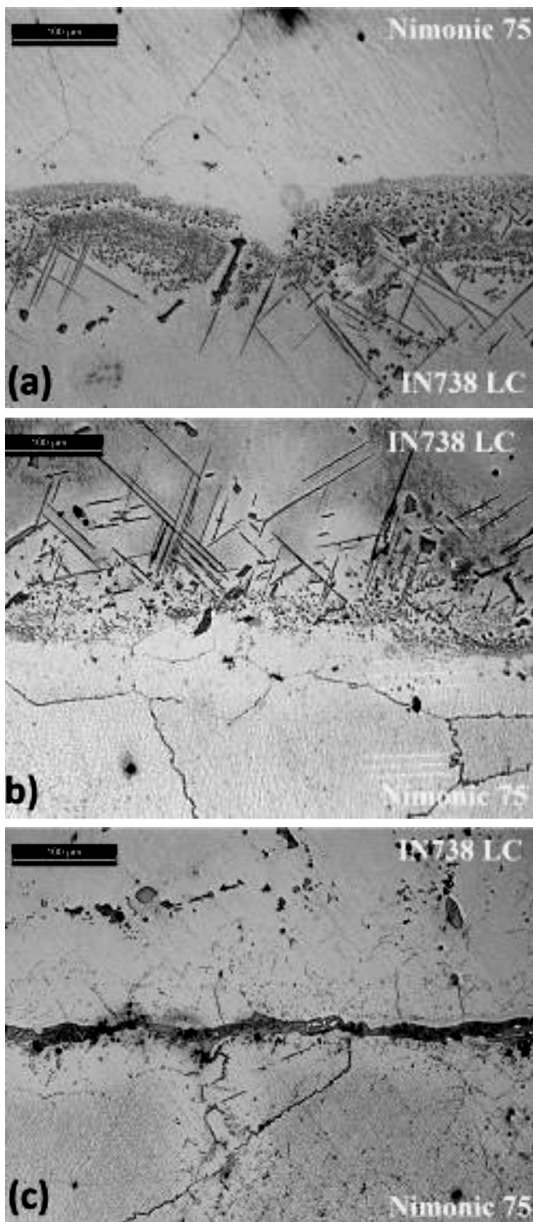


Figure 6: Light micrograph of TLP-bonded specimens at: a) 1120 °C for 120 min, b) 1150 °C for 120 min, c) 1180 °C for 150 min

Slika 6: Svetlobni posnetek vzorcev, spajanih s TLP: a) 1120 °C – 120 min, b) 1150 °C – 120 min, c) 1180 °C – 150 min

there are significant amounts of centerline eutectic in the bonding after 150 min and isothermal solidification was not completed yet. O. Idouw et al.²⁵ reported that in TLP bonding of IN738, increasing the bonding temperature from 1170 °C leads to the diffusion of aluminum and titanium into the molten interlayer and a reduction of the isothermal solidification rate may happen. They reported that the diffusion of titanium to the molten layer leads to the formation of a Ni-Ti rich phase, M₂SC-type sulphocarbide, chromium-rich boride and a γ - γ' centerline eutectic. These phases are very stable and hard to solute. Therefore, they can decrease the rate of isothermal

solidification and the completion of the process will be postponed.

3.3 Precipitation in the diffusion-affected zone (DAZ)

Boride precipitation is expected in the base metal where the concentration of boron is more than its solubility limit in a γ solid solution.²³ The solubility limit of boron in nickel is 0.3 % of amount fractions over the range of 1065–1110 °C, according to the Ni–B binary phase diagram.²⁶ Therefore, the diffusion of boron into the base metal during the holding at bonding temperature leads to the formation of boride precipitates in the DAZ. These precipitates are shown in **Figures 7** and **8** in two morphologies: globular and acicular.

When the distance between the precipitates and the interface increases the morphology of the precipitates changes from globular to acicular. As mention before, dissolution is the first stage of TLP bonding where the base-alloys solute elements diffuse into the base alloy until the equilibrium condition between solid/liquid is achieved. Therefore, the alloying-elements concentration in the base metal layer adjacent to the bond is poorer than the other layers. As shown in **Table 3**, the amount

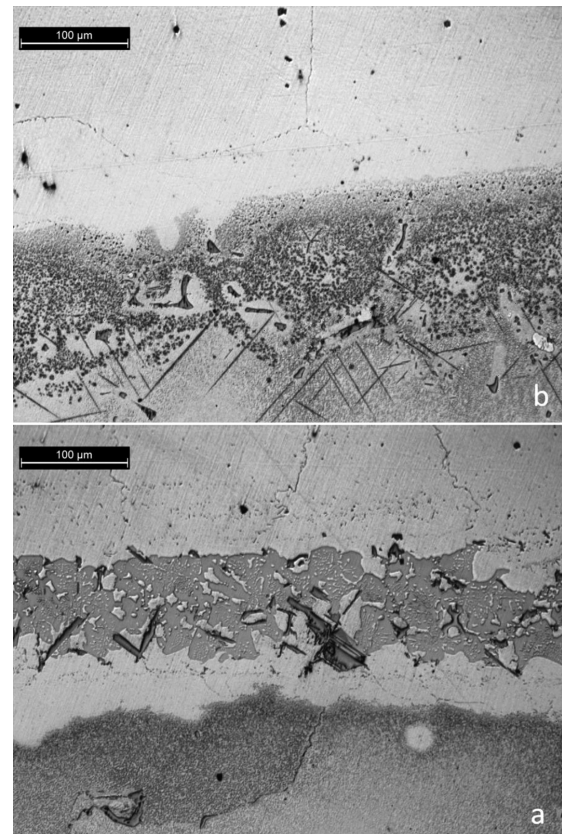


Figure 7: Variation of precipitates' morphology in DAZ at 1120 °C with time from a) 5 min to b) 120 min. The morphology changes from globular to globular/acicular.

Slika 7: Spreminjanje morfologije izločkov v DAZ na temperaturi 1120 °C, v odvisnosti od časa od a) 5 min do b) 120 min. Morfologija se spreminja od globularne do globularno/acikularne.

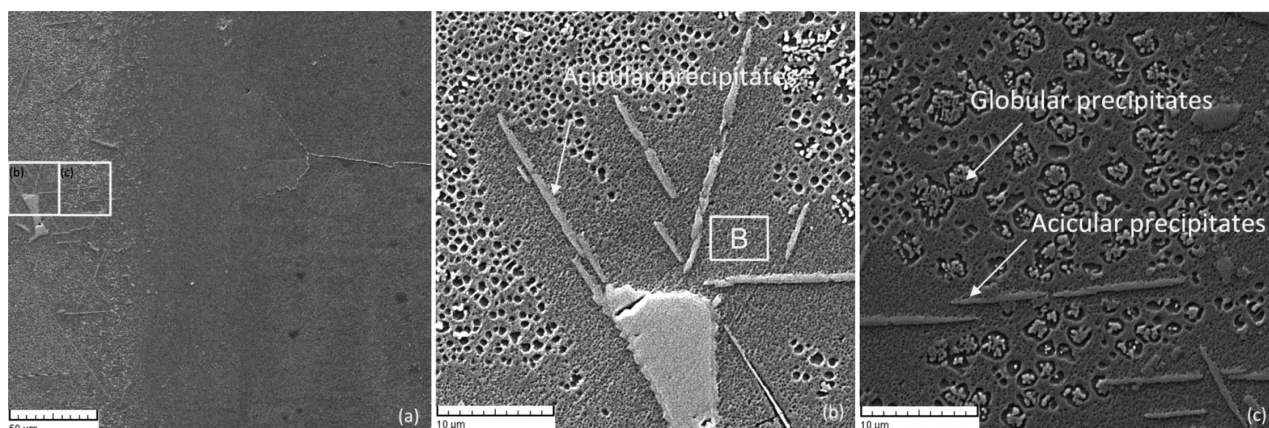


Figure 8: a) SEM micrograph of specimen TLP-bonded at 1150 °C for 150 min, b) and c) specified area in a) showed by b) and c) respectively
Slika 8: SEM-posnetek vzorcev, spajanih s TLP, na temperaturi 1150 C, 150 min, b) in c) določeno področje a) prikazano na b) oz. c)

Table 3: EDS analysis of phases shown in Figure 8 (x/%)

Tabela 3: EDS analiza faz prikazanih na Sliki 8 (x/%)

	Al	Ti	Cr	Co	Ni	Nb	Mo	Ta	W
Acicular Precipitates	2.25	39.45	7.99	2.81	18.78	7.49	5.07	11.46	4.69
Globular Precipitates	8.44	3.53	38.70	4.06	34.68	0.57	5.28	0.61	4.12
B	3.71	0.46	25.65	6.32	60.61	0	0.60	1.15	1.49

of alloying elements in the precipitates closer to the bonding interface (globular precipitates) is less than the ones further than the bond line (acicular precipitates). As seen in **Table 3**, the high chromium content of the globular precipitates leads to a significant depletion of the chromium around them. Since the Cr is the main element for resistance to corrosion of the base alloy, the depletion of Cr around these precipitates leads to a reduction of the matrix's corrosion resistance.²⁷ Moreover, a high concentration of γ' -formers in the precipitates leads to the depletion of Al and Ti in the matrix around the precipitates, and as seen in **Figure 8**, there is no γ' particle around them.

The morphology of the precipitates varies by increasing the bonding temperature from the globular to the acicular morphology, and at 1150 °C the acicular morphology is dominant (**Figures 6a** and **6b**). The reason is probably related to more diffusion of the alloying elements at the higher temperature and greater homogeneity of the chemical composition in the DAZ. The other point that can be gained from **Figure 6c** is that the amount of precipitates in the DAZ decreases by raising the temperature, such that at 1180 °C there is no acicular and globular precipitate. It can be concluded that these precipitates may be dissolved at temperatures lower than 1180 °C.

Figure 7 shows that at 1120 °C, the morphology of the precipitates varies from globular to globular/acicular by increasing the holding time from 5 to 120 min. This phenomenon is related to more diffusion of boron into the base alloy at longer times and implies that the formation of acicular precipitates need more alloying elements than globular precipitates (**Table 3**).

Figure 8 shows the bond interface in a specimen TLP bonded at 1120 °C for 150 min. Boron was detected in all precipitates, but their accurate concentration could not be reported quantitatively due to X-ray absorption of the EDS analyzer window. The compositional analyses shown in **Table 3** suggests that globular precipitates are borides rich in Ni, Cr, Mo, W and Al and acicular precipitates are borides rich in Ti, Ta, Mo, Nb and W. O. Ojo et al.²² and O. Idowu et al.²⁴ observed boride precipitates rich in Cr, W and Mo in TLP bonding of IN738 by a Ni-Cr-B interlayer at 1130 °C. Also, it can be seen that there are lots of very fine γ' around acicular precipitates. The reason is related to the absorption of Ti by these precipitates so that the concentration of the γ' former element is less than normal. Since the Nimonic 75 does not have any boride formers in its chemical composition, no precipitate was observed in its diffusion-affected zone. **Figures 8b** and **8c** show the different zones specified in **Figure 8a**.

4 CONCLUSION

The effect of time and temperature on the TLP bonding of the dissimilar nickel-based super alloys IN738LC and Nimonic 75 using an MBF-80 interlayer was investigated. The following conclusions can be drawn from this study:

- Before completion of the isothermal solidification, the microstructure of the joint centerline consists of three eutectic phases: γ solid solution, Ni-rich boride and Cr-rich boride.
- DAZ precipitates are formed due to boron diffusion from the interlayer to the base metal during a

solid-state transformation. Boride precipitates were observed in the DAZ at bonding temperatures up to 1150 °C. However, at a bonding temperature of 1180 °C, the boride precipitates were not observed.

- At a given bonding temperature, the morphology of the DAZ precipitates changes from globular to globular-acicular with an increasing bonding time.
- Boride precipitation in Nimonic 75 DAZ did not occur due to a lack of boride-forming elements in its chemical composition.
- A reduction in the isothermal solidification rate was observed when TLP bonding at 1180 °C.

5 REFERENCES

- M. Mosallae, A. Ekrami, K. Ohsasa, K. Matsuura, Microstructural evolution in the transient-liquid-phase bonding area of IN-738LC/BNi-3/IN-738LC, *Metallurgical and Materials Transactions A*, 39 (2008) 10, 2389–2402, doi:10.1007/s11661-008-9588-0
- M. Abdelfatah, O. Ojo, On the extension of processing time with increase in temperature during transient-liquid phase bonding, *Metallurgical and Materials Transactions A*, 40 (2009) 2, 377–385, doi:10.1007/s11661-008-9726-8
- M. Pouranvari, A. Ekrami, A. Kokabi, Aging response of transient liquid phase bonded wrought IN718 superalloy: influence of post-bond heat treatment, *Science and Technology of Welding and Joining*, 19 (2014) 2, 105–110, doi:10.1179/1362171813Y.0000000170
- M. Pouranvari, A. Ekrami, A. Kokabi, Diffusion Brazing Metallurgy of IN718/Ni-Cr-Si-B-Fe/IN718, *Welding journal*, 93 (2014) 2, 60s–68s, doi:10.1179/1743284713Y.0000000320
- O. Kalvenes, Studies of the reaction of Nimonic 75 with Co₂, *Corrosion Science*, 4 (1964), 211–220, doi:10.1016/0010-938X(64)90020-4
- O. Ojo, N. Richards, M. Chaturvedi, Effect of gap size and process parameters on diffusion brazing of Inconel 738, *Science and Technology of Welding & Joining*, 9 (2004) 3, 209–220, doi:10.1179/136217104225012175
- M. Pouranvari, A. Ekrami, A. H. Kokabi, Effect of the bonding time on the microstructure and mechanical properties of a transient liquid phase bonded 718 using a Ni-Cr-B filler alloy, *Mater. Tehnol.*, 47 (2013) 593–599
- N. Wikstrom, A. Egbewande, O. Ojo, High temperature diffusion induced liquid phase joining of a heat resistant alloy, *Journal of Alloys and Compounds*, 460 (2008) 1, 379–385, doi:10.1016/j.jallcom.2007.06.066
- X. Wu, R. Chandel, H. Li, Evaluation of transient liquid phase bonding between nickel-based superalloys, *Journal of Materials Science*, 36 (2001) 6, 1539–1546, doi:10.1023/A:1017513200502
- A. Egbewande, C. Chukwukaeme, O. Ojo, Joining of superalloy Inconel 600 by diffusion induced isothermal solidification of a liquated insert metal, *Materials Characterization*, 59 (2008) 8, 1051–1058, doi:10.1016/j.matchar.2007.08.023
- R. Saha, T. Khan, Microstructural developments in TLP bonds using thin interlayers based on Ni-B coatings, *Materials Characterization*, 60 (2009) 9, 1001–1007, doi:10.1016/j.matchar.2009.04.002
- W. Gale, D. Butts, Transient liquid phase bonding, *Science and Technology of Welding & Joining*, 9 (2004) 4, 283–300, doi:10.1179/136217104225021724
- F. Jalilian, M. Jahazi, R. Drew, Microstructural evolution during transient liquid phase bonding of Inconel 617 using Ni-Si-B filler metal, *Materials Science and Engineering: A*, 423 (2006) 1, 269–281, doi:10.1016/j.msea.2006.02.030
- M. Pouranvari, A. Ekrami, A. Kokabi, TLP bonding of cast IN718 nickel based superalloy: Process-microstructure-strength characteristics, *Materials Science and Engineering: A*, 568 (2013), 76–82, doi:10.1016/j.msea.2013.01.029
- Diffusion Brazing, in *ASM Handbook*, ASM International, 2005, 207–221
- M. Pouranvari, A. Ekrami, A. Kokabi, Solidification and solid state phenomena during TLP bonding of IN718 superalloy using Ni-Si-B ternary filler alloy, *Journal of Alloys and Compounds*, 563 (2013), 143–149, doi:10.1016/j.jallcom.2013.02.100
- A. Rabinkin, Brazing with (NiCoCr)-B-Si amorphous brazing filler metals: alloys, processing, joint structure, properties, applications, *Science and Technology of Welding & Joining*, 9 (2004) 3, 181–199, doi:10.1179/136217104225012300
- T. A. Christman, K. B. Small, Guide to etching specialty alloys, *Advanced materials & processes*, (2008) 10192/1881463/amp16602p032.pdf/4d43b19b-45b7-4893-84a7-d6babb9505e5
- M. Pouranvari, A. Ekrami, A. Kokabi, Phase transformations during diffusion brazing of IN718/Ni-Cr-B/IN718, *Materials Science and Technology*, 29 (2013) 8, 980–984, doi:10.1179/1743284713Y.0000000238
- N. Wikstrom, O. Ojo, M. Chaturvedi, Influence of process parameters on microstructure of transient liquid phase bonded Inconel 738LC superalloy with Amdry DF-3 interlayer, *Materials Science and Engineering: A*, 417 (2006) 1, 299–306, doi:10.1016/j.msea.2005.10.056
- K. Ohsasa, T. Narita, T. Shinmura, Numerical modeling of the transient liquid phase bonding process of Ni using Ni-B-Cr ternary filler metal, *Journal of Phase Equilibria*, 20 (1999) 3, 199–206, doi:10.1361/105497199770335721
- A. Bondar, B-Cr-Ni Boron-Chromium-Nickel, *Landolt-Börnstein, Numerical Data and Functional Relationships in Science and Technology (New Series). Group IV, Physical Chemistry*, 2006 153–167, doi:10.1007/978-3-540-47004-5_19
- O. Ojo, N. Richards, M. Chaturvedi, Isothermal solidification during transient liquid phase bonding of Inconel 738 superalloy, *Science and Technology of Welding & Joining*, 9 (2004) 6, 532–540, doi:10.1179/174329304X8702
- Alloy Phase Diagrams, 10 ed, *ASM Handbook*, 3, ASM International, 1992
- O. Idowu, N. Richards, M. Chaturvedi, Effect of bonding temperature on isothermal solidification rate during transient liquid phase bonding of Inconel 738LC superalloy, *Materials Science and Engineering: A*, 397 (2005) 1, 98–112, doi:10.1016/j.msea.2005.01.055
- K. Tokoro, N. Wikstrom, O. Ojo, M. Chaturvedi, Variation in diffusion-induced solidification rate of liquated Ni-Cr-B insert during TLP bonding of Waspaloy superalloy, *Materials Science and Engineering: A*, 477 (2008) 1, 311–318, doi:10.1016/j.msea.2007.05.069
- M. Pouranvari, Isothermal solidification during transient liquid-phase bonding of GTD-111/Ni-Si-B/GTD-111, *Mater. Tehnol.*, 48 (2014) 1, 113–118

WORKABILITY BEHAVIOUR OF Cu-TiB₂ POWDER-METALLURGY PREFORMS DURING COLD UPSETTING

PREOBLIKOVALNOST Cu-TiB₂ PREDOBLIK IZDELANIH Z METALURGIJO PRAHOV MED HLADNIM KOVALNIM PREIZKUSOM

Saikumar Gadakary¹, Asit Kumar Khanra¹, Maharajan Joseph Davidson²

¹National Institute of Technology, Department of Metallurgical and Materials Engineering, Warangal, India

²National Institute of Technology, Department of Mechanical Engineering, Warangal, India
sai.gadakary@gmail.com

Prejem rokopisa – received: 2015-04-07; sprejem za objavo – accepted for publication: 2015-06-17

doi:10.17222/mit.2015.074

An investigation was carried out to find the workability behaviour of a Cu-TiB₂ composite under triaxial stress-state conditions. Initially, the TiB₂ powder was prepared by using a self-propagating high-temperature synthesis (SHS) technique and the same was added to a Cu matrix in order to make Cu-TiB₂ composites. Cylindrical preforms with three different TiB₂ weight percentages (2 %, 4 % and 6 %) with aspect ratios of 0.50, 0.75 and 1 were prepared using a uniaxial load. Then the preforms were pressureless sintered in a tubular furnace with a continuous flow of pure argon gas at 950 °C for a period of 1 h. The cold upsetting test was carried out on the sintered specimens. The relationships between the various stresses, strains and the relative density were determined. The results for the various stress-ratio parameters, namely (σ_0/σ_{eff}) and (σ_m/σ_{eff}), the formability stress index (β_0) under triaxial stress-state conditions were systematically analysed. The formability stress index was found to increase with the increase in preform fractional density and it decreased with the aspect ratios. This was because the preform contains more pores and the porous bed height is high. A statistical fitting method was performed on the curve drawn between the axial strain and the stress-formability index. The compacts with a higher value of the aspect ratio and the initial preform density showed a very high fracture strain.

Keywords: SHS, powder metallurgy, TiB₂, workability, relative density, fracture strain

Izvršena je bila preiskava preoblikovalnosti Cu-TiB₂ kompozita pri triosnem napetostnem stanju. Najprej je bil pripravljen prah TiB₂; s pomočjo napredujoče visoko temperaturne sinteze (SHS), ki je bil dodan Cu osnovi, da bi napravili Cu-TiB₂ kompozit. Z enoosnim stiskanjem so bili pripravljene vzorci cilindrične oblike s tremi različnimi vsebnostmi TiB₂ v masnih deležih (2 %, 4 % and 6 %) in z razmerjem 0,50, 0,75 in 1. Nato so bile predoblike sintrane v cevasti peči pri kontinuirnem pretoku čistega argona na temperaturi 950 °C in trajanju 1 h. Kovni preizkus v hladnem je bil izveden na sintranih vzorcih. Ugotovljena je bila odvisnost med različnimi napetostmi, raztezki in relativne gostote. Sistematično so bili analizirani rezultati različnih parametrov (σ_0/σ_{eff}) in (σ_m/σ_{eff}) ter indeks preoblikovalnih napetosti (β_0) pri triosnem napetostnem stanju. Ugotovljeno je, da indeks preoblikovalne napetosti narašča z naraščanjem gostote predoblike in se zmanjšuje z razmerjem širina-višina. Razlog za to je večje število por v predobliki in zato je višina poroznega vzorca višja. Izvedena je bila tudi statistična obdelava krivulje, narisane med osno napetostjo in indeksom preoblikovalne napetosti. Stiskanci z višjo vrednostjo razmerja med širino in višino ter večjo gostoto predoblike, so pokazali veliko napetost pri porušitvi.

Ključne besede: SHS, metalurgija prahov, TiB₂, preoblikovalnost, relativna gostota, napetost pri porušitvi

1 INTRODUCTION

Powder metallurgy (P/M) is one of the most actively researched manufacturing processes capable of delivering near-net-shaped precision metal parts. This process has delivered a large number of industrial components, such as connecting rods in engines, self-lubricating bearings, gear sets in automobile transmissions, etc.¹⁻² Near-net-shape components can be made and, the process has the capability to greatly reduce machining costs, and can improve material utilization.³⁻⁴ A series of upsetting, bending, rolling and plane strain tests to assess the fracture behaviour of porous materials was carried out.⁵ P/M components involving copper are a highly researched composite materials as alloys with copper as one of the constituents will be stronger and durable.⁶⁻⁸

Copper P/M parts are used extensively in both structural and non-structural applications because of the high corrosion resistance, high thermal and electrical conductivity. The corrosion resistance can be further improved by the application of chemical conversion coatings or anodizing treatment. In general, the physical and mechanical properties of near-full (theoretical) density copper and copper alloy P/M structural parts are comparable to cast and wrought copper-based materials of a similar composition. However, P/M copper parts vary in density from the low-density self-lubricating bearings or filters to the near-full density of the electrical parts.

TiB₂, due to its high melting temperature, hardness, elastic modulus, electro-conductibility and thermal diffusivity, and excellent refractory properties and chemical inertness has been widely used in many industrial

fields. It has applications in rocket nose cones for atmospheric re-entry, ballistic armour, cathodes for Hall-Heroult cells, crucibles for molten metals, metal evaporation boats, and as a coating on cutting tools.⁹⁻¹⁰ It is widely used as cutting-tool composites and wear-resistant parts.¹¹ The TiB₂ powder is synthesized using the SHS method. The main feature of the SHS process is that, it utilizes the high energy released during the exothermic chemical reaction of the reactants to yield a variety of inorganic materials. Once the reactants are ignited by an external source, the reaction front propagates within the solid with a certain velocity to complete the chemical reaction.

The extent of deformation possible without failure is defined by the term "workability". It is the ability of a material to withstand the induced internal stresses of forming before any failure occurs. It is the extent to which a material can be deformed in a specific metal working process without the initiation of cracks.¹²⁻¹⁴ Workability depends on both the material and the process parameters. The workability of dense material is better than with P/M material. The workability can be calculated by interpreting the value of hydrostatic stress and effective stress for a tri-axial state of compression, and the hydrostatic stress can be evaluated from the axial and hoop stresses. The evaluation of different stresses and the failure strain will reveal the workability limits of the P/M composites.¹⁵ M. Abdel-Rahman and E. Sheikh¹⁶ explored the effect of the relative density on the forming limit of P/M compacts during upsetting. J. J. Park et al.¹⁷ developed a constitutive relation involving the Poisson's ratio, relative density and flow stress to predict the plastic deformation behaviour of porous metals. A mathematical equation for the calculation of the flow stress in the case of a simple upsetting of P/M sintered preforms was proposed by R. Narayanasamy et al.¹⁸ Furthermore, the authors developed a new equation for the determination of the hydrostatic stress in the case of the simple upsetting of sintered P/M compacts. Equations for the determination of the flow stress and the hydrostatic stress depending upon two factors, i.e., (i) the

value of Poisson's ratio and (ii) the relative density of the P/M preform in the case of the simple compression test were proposed in the literature.¹⁸ However, copper-based materials are hard to form as they offer resistance to the forming load due to the formation of intermetallic compounds. Thus, it is essential to investigate the deformation behaviour of the Cu-TiB₂-based composite developed in the present work.

The deformation behaviours of Al matrix composites have been studied extensively. There are, however, few research reports on the deformation behaviour of Cu-TiB₂ composites. In the present paper efforts were made to make composites of Cu-TiB₂. The TiB₂ used is synthesized by using self-propagating high-temperature synthesis (SHS). Until now there is no report of workability studies on Cu-TiB₂ composites. The workability studies of the composites using a cold upsetting test are evaluated.

2 EXPERIMENTAL DETAILS

Cu-TiB₂ composite sintered preforms were selected in order to provide a reasonably wide range of study, namely, workability and work-hardening behaviour during cold upset operation. The commercially available copper powder was obtained from Alfa Aesar and the TiB₂ powder was produced using self-propagating high-temperature synthesis (SHS) in our lab, igniting the stoichiometric mixture of 20 g according to Equation (1), in a tubular furnace, maintaining an argon atmosphere. To investigate the particle size, shape and its distribution, copper, TiB₂ powders were studied using a scanning electron microscope (SEM) (**Figure 1**). The Cu-TiB₂ powders with different weight percentages of TiB₂, namely, 2 %, 4 % and 6 %, blend in a mortar mixer in order to obtain a homogeneous mixture.

The powders were compacted in a 25-ton manual pellet press with the closed die set assembly technique. Compacts of 15-mm diameter were prepared with aspect ratios of 0.50, 0.75 and 1. The aspect ratio is the ratio of the height to the diameter of the sample. The approxi-

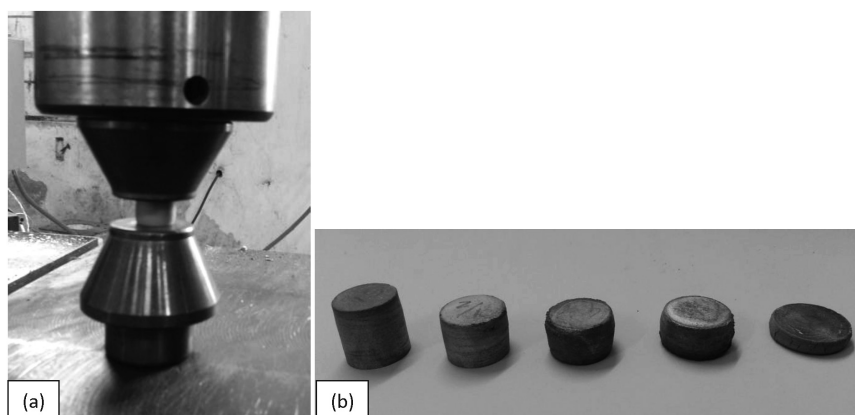


Figure 1: a) Upsetting test setup, b) deformed preforms
Slika 1: a) Sestav za krčilni preizkus, b) predoblike po deformaciji

mate initial preform density is 70 % of the theoretical density. These densities were achieved after sintering. Then the preforms were sintered in a tubular furnace at a temperature of 950 °C for a period of 1 h. To avoid oxidation the preforms were heated in an inert argon atmosphere. After the sintering schedule, the compacts were cooled in the furnace itself. The sintered preforms were cleaned and the dimensional measurement was made before the deformation.

The upsetting tests (**Figures 1a** and **1b**) were conducted on a hydraulic press having a capacity of 50 tons. Extreme care was taken to place the cylindrical specimen within the platens, concentric with the central axis of the hydraulic press (loading direction). Cylindrical preforms were cold upset between the flat platens. Each preform was subjected to an incremental compressive loading in steps until the appearance of visible cracks on the free surface.

Immediately after each incremental loading, the contact diameter at the top (D_{CT}), the contact diameter at the bottom (D_{CB}), the bulged diameter (D_B), the height of the preforms (h_f) and the density (ρ_f) were recorded. Before upsetting, the initial diameter (D_o), the initial height (h_o) and the initial preform density (ρ_o) of the specimens were measured. Moreover, the density measurements of the preforms were carried out using the Archimedes principle. Using the load, the dimensional parameters and density, the different true stresses (i.e., σ_z , σ_θ , σ_m and σ_{eff}) and the different true strains, (i.e., ϵ_z and ϵ_θ) and the workability parameters (β_σ) were determined using the expressions specified below for the triaxial stress-state condition.

For the present investigation, the TiB₂ powders were synthesized in-house as explained by the authors in a previous study.¹⁹ The mixture of titanium oxide (TiO₂), boric acid (H₃BO₃) and magnesium was taken as per the stoichiometric reaction (Equation 1). The powders were mixed in a mortar mixer for about 20 min. A mixture of 20 g was then taken in a stainless-steel boat and was kept

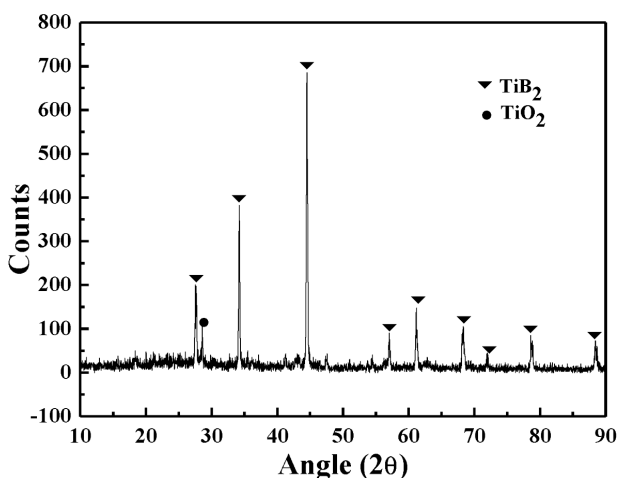


Figure 2: XRD pattern of TiB₂ synthesized powder
Slika 2: Rentgenogram sintetiziranega prahu TiB₂

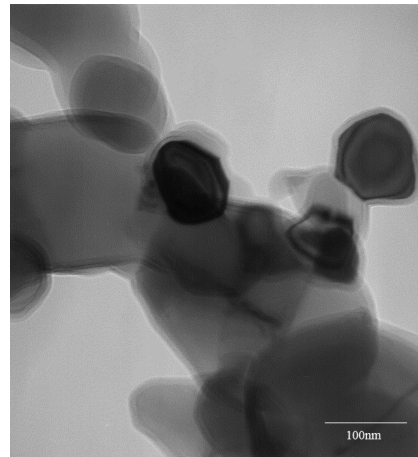
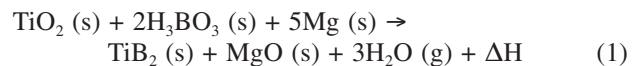


Figure 3: TEM image of TiB₂ synthesized powder
Slika 3: TEM-posnetek sintetiziranega prahu TiB₂

in a tubular furnace (Systems control, Chennai). The complete process was carried out in a highly pure argon atmosphere in order to maintain an inert atmosphere. The furnace was then heated up to 800 °C with a constant heating rate. It was observed that the reaction was taking place with an explosive sound at an approximate temperature of 680 ± 15 °C. The furnace is then left to cool to room temperature.



After cooling, the synthesized powder was taken out. It was observed that the reacted mixture is formed of black lumps, and some amount of white surface layer was seen on the lumps. The powder is then taken out and was crushed into fine powder before going to the leaching process, in order to make the leaching process effective. The leaching process was carried out in diluted HCl, with normality of 2 N. The solution was mixed

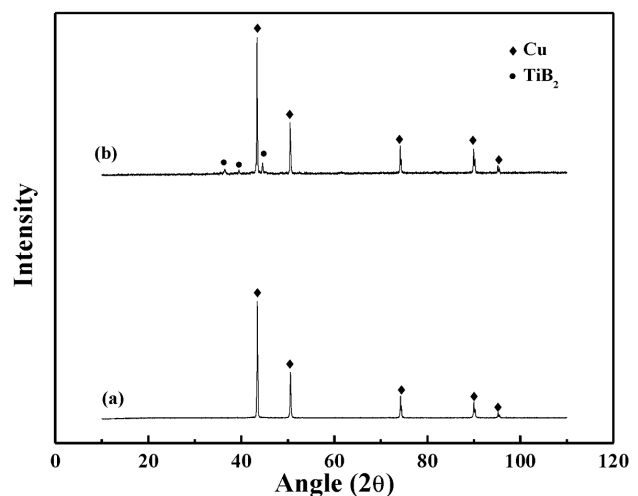


Figure 4: XRD patterns of samples: a) pure Cu and b) Cu-6 (6 % of mass fractions of TiB₂)

Slika 4: Rentgenograma vzorcev: a) čisti Cu in b) Cu-6 (6 % masnega deleža TiB₂)

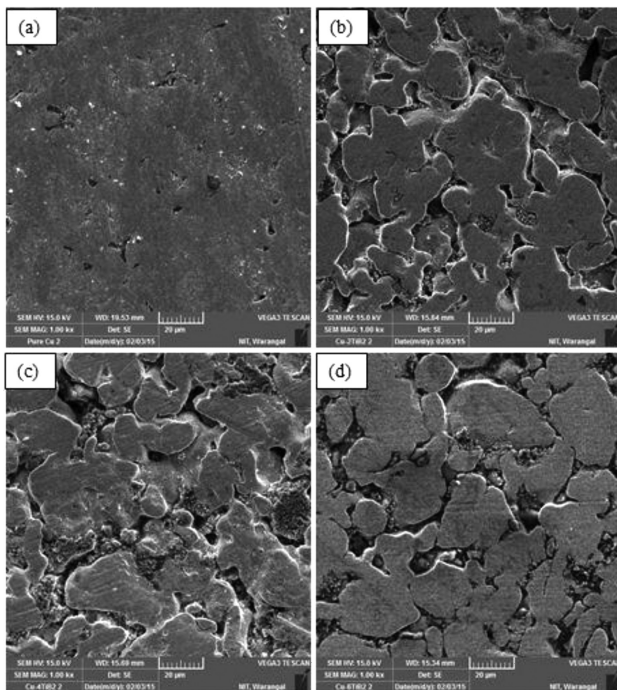


Figure 5: SEM images of: a) pure Cu, b) Cu-2 (2 % of mass fractions of TiB₂), c) Cu-4 (4 % of mass fractions of TiB₂), d) Cu-6 (6 % of mass fractions of TiB₂)

Slika 5: SEM-posnetek: a) čisti Cu, b) Cu-2 (2 % masnega deleža TiB₂), c) Cu-4 (4 % masnega deleža TiB₂), d) Cu-6 (6 % masnega deleža TiB₂)

with the crushed powder and heated up to 120 °C. The process was continued while the solution boils for about 10 min, and then the solution was separated using filter paper. The resulting powder, which was taken after the leaching process, was then dried in an oven for 1 h. The resulting powder is used in the present study.

The XRD patterns of the sample produced by the SHS process after leaching shows the presence of TiB₂ as major phase with TiO₂ as minor phase in **Figure 2**. The TEM image of the synthesized powder is shown in **Figure 3**. The TEM images show the formation of spherical and hexagonal TiB₂ particles.

The XRD pattern of pure Cu and Cu-6 (6 % of mass fractions of TiB₂) is shown in **Figure 4**. The pattern shows the presence of TiB₂ as small peaks and Cu as a major phase. This indicates there is no interaction between the Cu and TiB₂ during the pressureless sintering. It is because of the smaller weight percentage of TiB₂ in the Cu matrix.

The scanning electron microscope images of the Cu-TiB₂ samples are shown in **Figures 5a** and **5d**. Pure Cu is shown in **Figure 5a**. Cu-2 (2 % of mass fractions of TiB₂), Cu-4 (4 % of mass fractions of TiB₂) and Cu-6 (6 % of mass fractions of TiB₂) are shown in **Figures 5b** to **5d**, respectively. The SEM images reveal the surface morphology of the sintered samples. The images show the porosity, the distribution of the powder particles and the sintering behaviour.

3 THEORETICAL ANALYSIS

In the upsetting of P/M parts, the height decreases, the average density increases, and the various stresses increase.²⁰ The expressions for the normal stress (σ_z), normal strain (ϵ_z), hoop stress (σ_θ), hoop strain (ϵ_θ), hydrostatic stress (σ_m), effective stress (σ_{eff}), and effective strain (ϵ_{eff}) were taken from N. Selvakumar et al.²¹ and Narayanasamy et al.²²

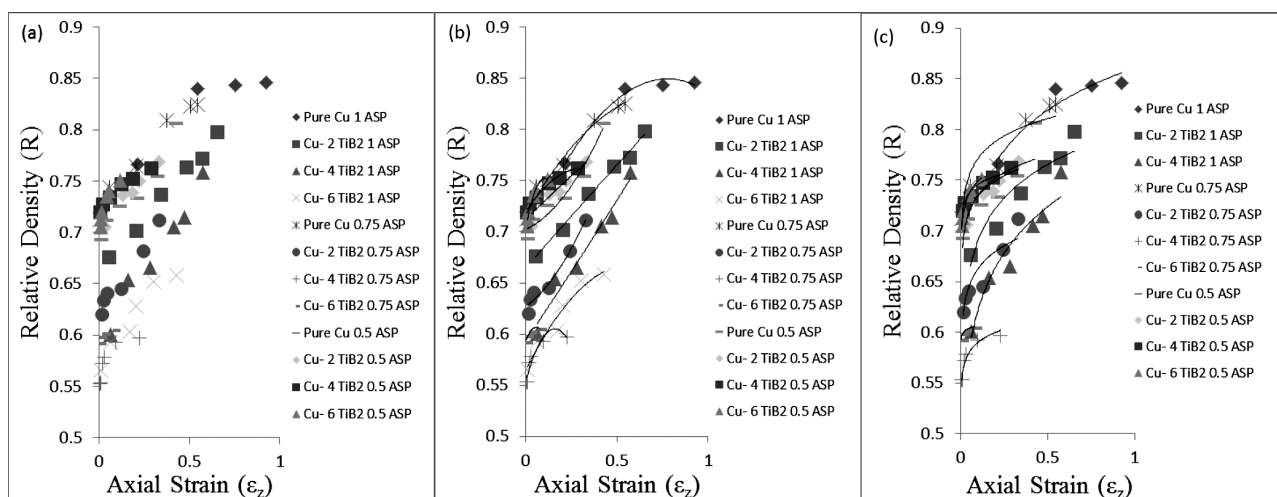


Figure 6: a) Relative density (R) versus axial strain (ϵ_z) for triaxial stress state condition, b) relative density (R) versus axial strain (ϵ_z) for triaxial stress-state condition (power-law curve-fitting results) and c) relative density (R) versus axial strain (ϵ_z) for triaxial stress-state condition (parabolic curve-fitting results)

Slika 6: a) Odvisnost relativne gostote (R) od osne napetosti (ϵ_z) pri triosnem napetostnem stanju, b) odvisnost relativne gostote (R) od osne napetosti (ϵ_z) pri triosnem napetostnem stanju (rezultati urejanja potenčne krivulje) in c) odvisnost relativne gostote (R) od osne napetosti (ϵ_z) pri pogoju triosnega napetostnega stanja (rezultati urejanja parabolične krivulje)

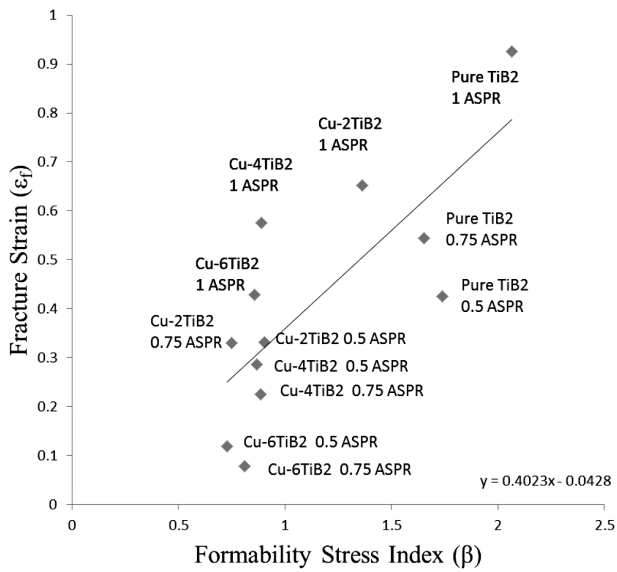


Figure 7: Fracture strain versus formability stress index (β)
Slika 7: Napetost loma v odvisnosti od indeksa preoblikovalne sile (β)

Triaxial Stress State Condition:

$$\alpha = \frac{A}{B} \tag{1}$$

$$A = (2 + R^2)\sigma_\theta - R^2(\sigma_z + 2\sigma_\theta) \tag{2}$$

$$B = (2 + R^2)\sigma_z - R^2(\sigma_z + 2\sigma_\theta) \tag{3}$$

$$\text{Hoop stress, } \sigma_\theta = \left[\frac{2\alpha + R^2}{2 - R^2 + 2R^2\alpha} \right] \sigma_z \tag{4}$$

$$\text{Hydrostatic stress, } \sigma_m = \frac{\sigma_z + 2\sigma_\theta}{3} \tag{5}$$

Effective stress,

$$\sigma_{\text{eff}} = \left[\frac{\sigma_z^2 + 2\sigma_\theta^2 - R^2(\sigma_\theta^2 + 2\sigma_z\sigma_\theta)}{2R^2 - 1} \right]^{0.5} \tag{6}$$

$$\text{Relative density, } R = \frac{\rho_f}{\rho_{\text{th}}} \tag{7}$$

ρ_f is the final density of the compact after deformation and ρ_{th} is the theoretical density of the compact.

$$\text{Formability Stress Index, } \beta = \frac{3\rho_m}{\sigma_{\text{eff}}} \tag{8}$$

4 RESULTS AND DISCUSSION

Figures 6a to 6c show the relationship between the relative densities attained and the axial strain for the Cu-TiB₂ preforms. The compaction load was kept constant for all the samples compacted with different proportions of TiB₂ and copper. It is observed that the initial densification achieved is better for the preforms prepared with copper alone and its relative density is around 75%. This reduces as the percentage of TiB₂ addition increases. The strain to failure was found to be low for the preforms with 6% TiB₂ and it was found to increase as the TiB₂ decreases. Moreover, it can also be inferred that the strain to failure is low for the low initial relative densities.

A statistical curve-fitting technique was adopted for the drawn curves and the prediction equation developed from the curves was checked for its applicability by comparing the correlation coefficient 'R²' values. These values can be used for modelling purposes and can also serve as prediction equations. In the present study, two

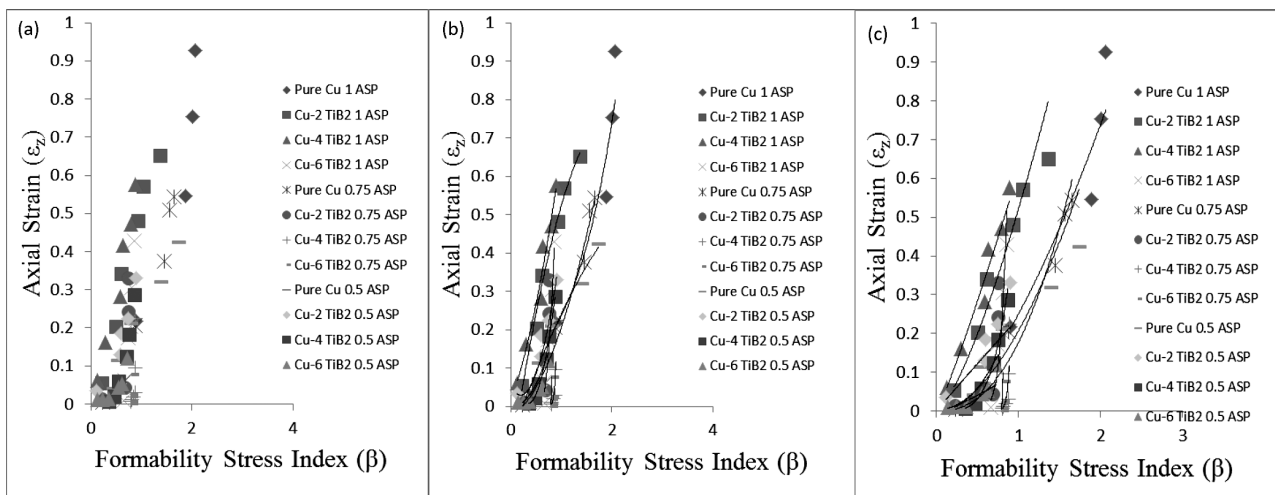


Figure 8: a) axial strain (ϵ_z) versus formability stress index (β) triaxial stress-state condition, b) axial strain (ϵ_z) versus formability stress index (β) triaxial stress-state condition (power-law curve-fitting results), c) axial strain (ϵ_z) versus formability stress index (β) triaxial stress-state condition (parabolic curve-fitting results)

Slika 8: a) odvisnost osne napetosti (ϵ_z) od indeksa preoblikovalne napetosti (β) pri triosnem napetostnem stanju, b) odvisnost osne napetosti (ϵ_z) od indeksa napetosti preoblikovanja (β) pri triosnem napetostnem stanju (rezultati urejanja potenčne krivulje), c) odvisnost osne napetosti (ϵ_z) od indeksa preoblikovalne napetosti (β) pri triosnem napetostnem stanju (rezultati urejanja parabolične krivulje)

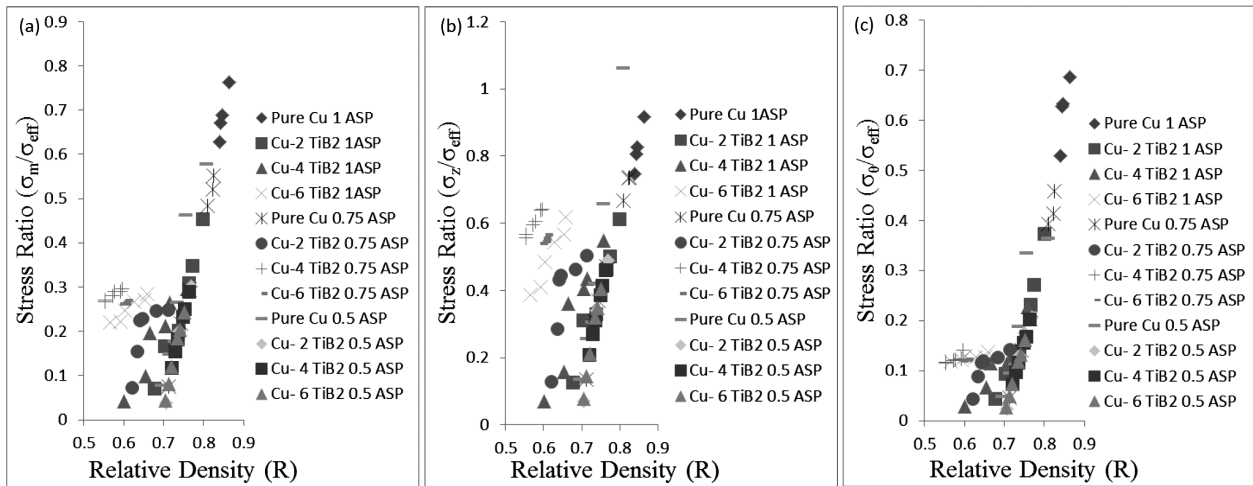


Figure 9: a) Stress ratio (σ_m/σ_{eff}) versus relative density (R), b) stress ratio (σ_z/σ_{eff}) versus relative density (R), c) stress ratio ($\sigma_\theta/\sigma_{eff}$) versus relative density (R)

Slika 9: a) Odvisnost razmerja napetosti (σ_m/σ_{eff}) od relativne gostote (R), b) odvisnost razmerja napetosti (σ_z/σ_{eff}) od relativne gostote (R), c) odvisnost razmerja napetosti ($\sigma_\theta/\sigma_{eff}$) od relativne gostote (R)

different curve-fitting techniques, i.e., the power law and parabolic curve fitting, were used.

As the aspect ratio increases, the fracture strain increases (Figure 7). The fracture strain decreases with the addition of TiB₂. Irrespective of the TiB₂ content, the fracture strain is less for 0.5 aspect ratio preforms. The decrease in the fracture strain indicates that the composite has attained a higher strength level with the addition of TiB₂, with less sacrifice in the strain values. The addition of TiB₂ to a preform with an aspect ratio of 1 has increased the strength with very little loss of fracture strain.

Figures 8a to 8c show the plot drawn between the axial strain and the formability stress index (b). A statistical fit is made using the polynomial function and the power-law function. It is found that the power law

related the parameters with higher accuracy. The addition of TiB₂ decreased the strain further.

For preforms with a higher aspect ratio and a lower initial relative density, the formability stress-index value moves closer to the minimum value. The reason is that this preform contains more pores and the porous bed height is larger or greater. The increase in relative density with increasing deformation is less in this case compared to lower aspect ratio preform. A parabolic curve-fitting technique was applied to relate the formability stress index and the axial strain for a varying aspect ratio and relative density. The polynomial equations obtained for each aspect ratio and relative density along with its regression co-efficient value are presented in Table 1, where it is observed that the constant value decreases with a decreasing amount of relative density, irrespective of the aspect ratio.

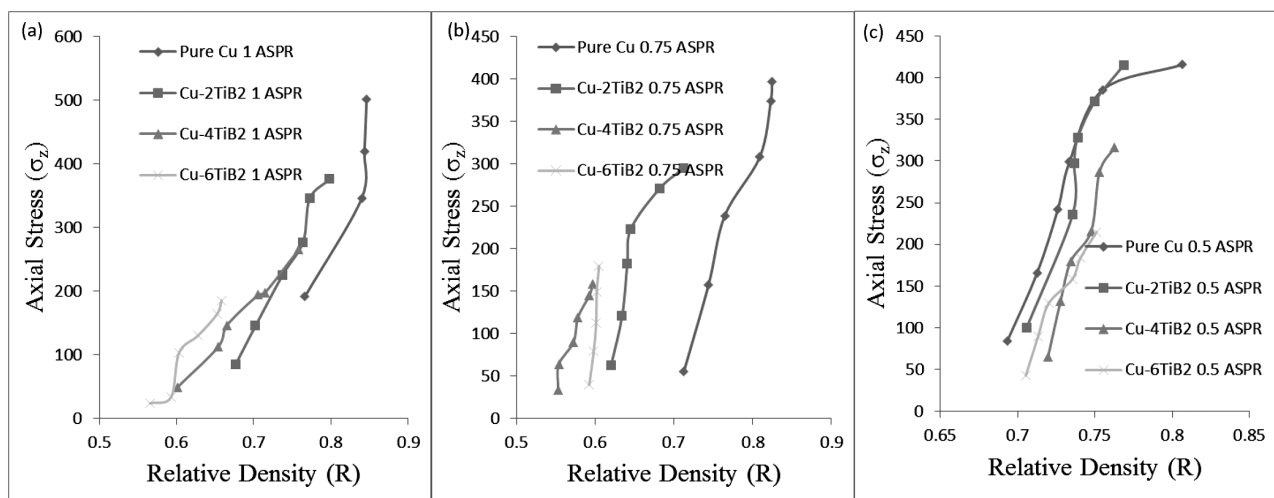


Figure 10: Axial stress (σ_z) versus relative density (R): a) 1 ASPR, b) 0.75 ASPR and c) 0.5 ASPR

Slika 10: Odvisnost osne napetosti (σ_z) od relativne gostote (R): a) 1 ASPR, b) 0,75 ASPR in c) 0,5 ASPR

Table 1: Parabolic curve-fitting equations and R^2 values**Tabela 1:** Enačbe urejanja parabolične krivulje in vrednosti R^2

Sample	Aspect ratio	Equation	R^2 value
Pure Cu	1	$y = -0.2603x^2 + 0.4053x + 0.6916$	0.9863
Cu-2%TiB ₂		$y = -0.0045x^2 + 0.2031x + 0.6646$	0.9915
Cu-4%TiB ₂		$y = 0.0187x^2 + 0.2652x + 0.5934$	0.9671
Cu-6%TiB ₂		$y = -0.307x^2 + 0.3572x + 0.5642$	0.9506
Pure Cu	0.75	$y = -0.2038x^2 + 0.312x + 0.7167$	0.9804
Cu-2%TiB ₂		$y = 0.3857x^2 + 0.1301x + 0.6268$	0.9724
Cu-4%TiB ₂		$y = -2.0138x^2 + 0.645x + 0.5534$	0.8919
Cu-6%TiB ₂		$y = -4.1476x^2 + 0.4749x + 0.593$	0.9105
Pure Cu	0.5	$y = 0.3627x^2 + 0.079x + 0.7022$	0.9525
Cu-2%TiB ₂		$y = -0.0329x^2 + 0.1792x + 0.7117$	0.8193
Cu-4%TiB ₂		$y = -0.4124x^2 + 0.2648x + 0.72$	0.9889
Cu-6%TiB ₂		$y = -4.6848x^2 + 0.9689x + 0.702$	0.9444

Figures 9a to 9c give the plot of the relative density with the stress ratio. The change of density along the axial and hoop stress directions was analysed. **Figure 8a** shows the variation of the relative density with the mean stress ratio. It is found that Cu with 4 % TiB₂ and an aspect ratio of 0.5 yielded high density values with a high load-bearing capacity. The same was true for the axial stress ratio and the hoop stress ratio. The hoop stress is responsible for the initiation of cracks in the preforms. Thus, it is clear that the addition of 4 % TiB₂ improves the density of the preforms and postpones the initiation of cracks. As the relative density increases the stress ratio parameter also increases.

It was found that the relative density increases as the stress-ratio parameter increases. The effect of the aspect ratio on the stress-ratio parameter is found to be minimal for the lower initial preform density preforms. However, as the initial preform density increases, a higher stress ratio parameter is observed for higher initial preform densities with a lower aspect ratio. This shows that the formability increases for the preforms with lower aspect ratios and higher initial preform densities.

The **Figures 10a to 10c** show plots of the axial stress (σ_z) against the relative density R . The experiment was done with preforms that have initial densities ranging from 0.6 to 0.75 and aspect ratios ranging from 0.5 to 1. The axial stress is found to increase rapidly during the initial stage of densification, and thereafter continue to increase with a lesser rate. The increase in stress due to the forming load is followed by the closure of pores in the preform, leading to its densification. This densification is attributed to the combined effect of the geometric and the matrix work-hardening. The preforms with a lower TiB₂ content were found to attain a higher stress value than the TiB₂ preforms. Along with the densification, the load-bearing capability of the preforms also increases, as is evident from the higher stress values in the plot (**Figures 10a to 10c**).

It was found that the preform with 6 % TiB₂ and a 0.5 aspect ratio densified more. Preforms with a high initial

preform density had a higher load-bearing capacity and a longer strain to failure. This is due to the presence of a smaller number of pores. At the same time, the dislocation density increases rapidly during plastic deformation, thereby resulting in a steep axial stress regime with a smaller increase in the corresponding relative density.

5 CONCLUSION

The formability behaviours of sintered Cu-TiB₂ composite preforms was studied. The formability stress index increased with an increase in the initial preform fractional density and decreased with the aspect ratios. A statistical fitting method was performed on the curve drawn between the axial strain and the stress formability index, and the parabolic curve fitting was found to give better predictive results. For the compacts with a higher value of the aspect ratio and initial preform density, the initiation of the crack appeared at a very high fracture strain.

Acknowledgement

This research work has been funded by the Council of Scientific and Industrial Research (CSIR) (sanction letter no. 22/597/12-EMR-II, dated 25/03/2012).

6 REFERENCES

- J. Mascarenhas, Powder metallurgy: a major partner of the sustainable development, Materials Science Forum, 455–456 (2004), 857–860, doi:10.4028/www.scientific.net/MSF.455-456.857
- G. E. Dieter, Mechanical Metallurgy, 3rd ed., McGraw-Hill, New York 1981
- T. J. Griffiths, R. Davies, M. B. Bassett, Compatibility equations for the powder forging process, Powder Metallurgy, 4 (1977), 214–220
- E. Bilgi, H. Erdem Çamurlu, B. Akgün, Y. Topkaya, N. Sevinç, Formation of TiB₂ by volume combustion and mechanochemical process, Mater. Res. Bull., 43 (2008), 873–881, doi:10.1016/j.materresbull.2007.05.001
- A. Nekahi, S. Firoozi, Effect of KCl, NaCl and CaCl₂ mixture on volume combustion synthesis of TiB₂ nanoparticles, Materials

- Research Bulletin, 46 (2011) 9, 1377–1383, doi:10.1016/j.materresbull.2011.05.013
- ⁶ T. S. Srivatsan, G. Guruprasad, D. Black, R. Radhakrishnan, T. S. Sudarshan, Influence of TiB₂ content on microstructure and hardness of TiB₂ – B₄C composite, Powder Technology, 159 (2005), 161–167, doi:10.1016/j.powtec.2005.08.003
- ⁷ X. K. Sun, S. J. Chen, J. Z. Xu, L. D. Zhen, K. T. Kim, Analysis of cold compaction densification behaviour of metal powders, Materials Science and Engineering, A267 (1999), 43–49, doi:10.1016/S0921-5093(99)00052-0
- ⁸ H. A. Kuhn, C. L. Downey, How flow and fracture affect design of preforms for powder forging, International Journal of Powder Metallurgy and Powder Technology, 10 (1974) 1, 59–66
- ⁹ I. Pokorska, Deformation of powder metallurgy materials in cold and hot forming, Journal of Materials Processing Technology, 196 (2008) 1–3, 15–32, doi:10.1016/j.jmatprotec.2007.08.017
- ¹⁰ P. W. Taubenblat, Importance of copper in powder metallurgy, International Journal of Powder Metallurgy, 39 (2003), 25–28
- ¹¹ R. Narayanasamy, V. Anandakrishnan, K. S. Pandey, Some aspects on plastic deformation of copper and copper–titanium carbide powder metallurgy composite preforms during cold upsetting, International Journal of Material Forming, 1 (2008) 4, 189–209, doi:10.1007/s12289-008-0383-7
- ¹² M. Sumathi, N. Selvakumar, R. Narayanasamy, Workability studies on sintered Cu-10SiC preforms during cold axial upsetting, Materials and Design, 39 (2012), 1–8, doi:10.1016/j.matdes.2012.02.004
- ¹³ S. Narayan, A. Rajeshkannan, Workability studies in forming of sintered Fe-0.35C powder metallurgy preform during cold upsetting, Journal of Iron and Steel Research International, 18 (2011), 71–78, doi:10.1016/S1006-706X(12)60012-0
- ¹⁴ G. Dieter, Handbook on workability analysis and applications, ASM publications 1, 2002
- ¹⁵ R. Narayanasamy, V. Anandakrishnan, K. S. Pandey, Effect of carbon content on workability of powder metallurgy steels, Materials Science and Engineering A, 494 (2008), 337–342, doi:10.1016/j.msea.2008.04.022
- ¹⁶ M. Abdel-Rahman, E. Sheikh, Workability in Forging of Powder Metallurgy Compacts, Journal of Materials Processing Technology, 54 (1995), 97–102
- ¹⁷ J. J. Park, Constitutive relations to predict plastic deformations in porous metal during Compaction, International Journal of Mechanical Sciences, 37 (1995), 709–719
- ¹⁸ R. Narayanasamy, R. Ponalagusamy, A Mathematical theory of plasticity for compressible powder metallurgy materials – Part II, Journal of Materials Processing Technology, 97 (2000), 110–113, doi:10.1016/S0924-0136(99)00357-X
- ¹⁹ S. Gadakary, A. K. Khanra, R. Veerababu, Production of nanocrystalline TiB₂ powder through self-propagating high temperature synthesis (SHS) of TiO₂–H₃BO₃–Mg mixture, Advances in Applied Ceramics, 113 (2014) 7, 419–426, doi:10.1179/1743676114Y.0000000188
- ²⁰ R. Narayanasamy, T. Ramesh, K. S. Pandey, S. K. Pandey, Effect of particle size on new constitutive relationship of aluminium–iron powder metallurgy composite during cold upsetting, Material and Design, 29 (2008), 1011–1026, doi:10.1016/j.matdes.2006.06.004
- ²¹ N. Selvakumar, R. Narayanasamy, Phenomenon of strain hardening behaviour of sintered aluminium preforms during cold axial forming, Journal of Materials Processing Technology, 142 (2003), 347–54, doi:10.1016/S0924-0136(03)00605-8
- ²² R. Narayanasamy, T. Ramesh, K. S. Pandey, Some aspects on workability of aluminium–iron powder metallurgy composite during cold upsetting, Materials Science and Engineering, A391 (2005), 418–426, doi:10.1016/j.msea.2004.09.018

EFFECTS OF EXTRUSION SHEAR ON THE MICROSTRUCTURES AND A FRACTURE ANALYSIS OF A MAGNESIUM ALLOY IN THE HOMOGENIZED STATE

VPLIVI STRIŽENJA MED IZTISKANJEM HOMOGENIZIRANE MAGNEZIJEVE ZLITINE NA MIKROSTRUKTURO IN NA ANALIZO PRELOMA

Hongjun Hu¹, Zhao Sun¹, Dingfei Zhang²

¹Chongqing University of Technology, College of Material Science and Engineering, 400050, P.R.China
²Chongqing University, National Engineering Research Center for Magnesium Alloys, 400044, P.R.China
48516686@qq.com

Prejem rokopisa – received: 2015-04-16; sprejem za objavo – accepted for publication: 2015-05-21

doi:10.17222/mit.2015.081

A new type composite extrusion method has been explored that combines extrusion and two continuous shears (referred to as Extrusion-Shear (ES)). To study the effects of extrusion-shear on the microstructures and the mechanical properties of a magnesium alloy for homogenization state, the ES process has been performed on extrusion equipment using an ES die. Grain-size measurements and X-ray diffraction and compression experiments were conducted. The experimental results and fracture analyses were described and discussed. It was found that the microstructures could be refined gradually from part 1 to 4 in the ES die. But a higher temperature could improve the grain growth and coarsen the microstructures. The results showed that fine and uniform microstructures can be achieved using the (ES) process and various types of texture can also be found in the microstructures. From the X-Ray diffraction (0002) the basal plane texture intensity was decreased, and the ES process could weaken the dominant base texture for (0002). The main fracture mechanism for the specimens extruded at 420 °C is transgranular fracture, while it is primarily caused by twins when the extrusion temperature was 450 °C.

Keywords: magnesium alloy, microstructure, texture, grain size, fracture analysis

Uporabljena je bila nova vrsta sestavljene metode iztiskovanja, ki kombinira iztiskovanje in dvojno kontinuirano striženje (ES). Za študij vpliva striženja na mikrostrukturo pri iztiskavanju in na mehanske lastnosti magnezijeve zlitine v homogeniziranem stanju, je bil izvršen ES postopek na napravi za iztiskovanje, z uporabo ES orodja. Izvedene so bile meritve velikosti zrn in rentgenska difrakcija stisnjenih vzorcev. Opisani in ocenjeni so bili rezultati preizkusov in analize preloma. Ugotovljeno je, da le-to postaja mikrostruktura bolj drobnostnata od 1 do 4 v ES orodju. Višje temperature lahko olajšajo rast zrn, kar napravi mikrostrukturo bolj grobnostnato. Rezultati so pokazali, da je mogoče drobnostnato in enakomerno mikrostrukturo doseči s postopkom striženja pri iztiskovanju (ES), v mikrostrukturi pa je moč najti različne vrste tekstur. Iz rentgenske difrakcije se vidi, da intenziteta teksture osnovne ravnine (0002) slabi in da ES postopek zmanjša prevlado osnovne teksture za (0002). Glavni mehanizem preloma vzorcev, iztiskanih pri 420 °C, je transkristalni prelom. Slednjega povzročajo predvsem dvojčki, če je temperatura iztiskovanja 450 °C.

Ključne besede: magnezijeva zlitina, mikrostruktura, tekstura, velikost zrn, analiza preloma

1 INTRODUCTION

A magnesium alloy is increasingly being specified for automotive, transportation, electronics, aerospace, and general engineering applications.¹ Magnesium has the ability to combine a high strength and a lighter weight.²⁻⁴ But the use of magnesium alloys in aerospace and military applications has begun to decline due to the poor service performance.^{5,6} A new type of composite extrusion method has been explored that combines extrusion and shear (referred to as ES). The ES process and the die design and optimization in production practice were obtained by repeated testing on industrial extruders. To study the effects of ES on microstructures and the mechanical properties of a magnesium alloy for the as-cast and homogenized state of magnesium alloys during the ES process, the ES process was performed on extrusion equipment with an ES die. The grain size

measurement and the X-ray diffraction analysis and compression experiments and fracture analysis were made and discussed.

2 EXPERIMENTAL PART

A homogenizing treatment was conducted for AZ31 magnesium alloys (Mg3.02% Al1.01% Zn0.30%Mn), the microstructures of the homogenized state were observed, and the ES processes were performed with different preheated temperatures. The metallurgical experiment, grain size measurement, mechanical property tests and X-ray diffraction analysis were conducted on an extruded AZ31 magnesium alloy. The AZ31 magnesium alloys in the homogenized state were chosen as the materials for the experiment. The material used in this study is the AZ31B Mg alloy. The proof stress of the AZ31 wrought Mg alloy is typically 160–240 MPa, and

the Mg alloy has a lower density and can withstand greater column loading per unit weight. The billets were machined into rounds with a diameter of 80 mm. The process parameters in the manufacturing process are critical to the microstructure evolution and the mechanical properties.

After the homogenization annealing treatment, the specimen and the die were heated to the desired temperatures and kept for 1 h. The experiments were made by pressing with a force of 500 tons on the horizontal extrusion machines with a container diameter of 85 mm. The ES process was conducted with an extrusion speed of 0.5 m/min. The microstructures of the AZ31 magnesium alloy for the homogenized state with preheated temperatures 450 °C and 420 °C for the magnesium alloy, respectively, were observed using a metallographic microscope.

Immediately after the ES processes the rods and die were water quenched in order to fix the metallurgical microstructures, and then the ES die and formed rods, including the billet remaining in ES die, were cut along the plane of symmetry. In order to study the changes of the microstructures at all stages of the ES process, samples taken from products in different parts of the ES die were observed, including microstructural observations and an analysis of the planes that are parallel to the extrusion direction.

All samples were grinded, first coarsely, then finely, with waterproof abrasive paper, no.120, no.280, no.400, no.600, no.800, no.1000, and no.1200. The etchant employed in this experiment was a picric-acid-based etchant including 5 g picric acid, 5 g acetic acid, 100 mL alcohol and 10 mL distilled water. The microstructures were observed under the electron microscope. The specimens used for the metallographic observation and the X-ray diffraction analysis were taken from the parts shown in **Figure 1**. Deformation zone 1 is located within the compression cone, deformation zone 2 is through the

compression cone, deformation zone 3 is the first shearing zone, and deformation zone 4 is the second shearing zone.

An Olympus light microscope was employed to observe the microstructure. The average grain size (\bar{d}) of the microstructure was measured with the cut straight-line method, which is a test method using the "average intercept length" (L) to represent the grain size, where the L can be determined on the polishing plane. The average intercept length of the grains filling the space is as follows:⁷

$$L = 1/NL = LT/PM$$

where NL is the number of grains per unit test line length, M is the macrostructure magnification, LT is the total length of any test lines that get through the microstructure image and P is the intersection number of test lines and the grain boundaries.

The mechanical properties experiments were performed on a CMT-5150 universal electronic testing machine, including compression and tensile failure experiments that were conducted at a speed of 1 mm/min. Before the experiments, deformed specimens were machined into standard compression specimens and tensile specimens with dimensions of $\Phi 8 \times 16$ mm and $\delta 5$, respectively. The tensile and compression fracture tests were conducted to obtain the yield strength, tensile strength, compressive strength, elongation after fracture and the compression ratio of the extruded magnesium alloy. The crystallographic orientation of the homogenized and extruded AZ31 magnesium alloy rod was analyzed qualitatively by X-ray diffraction, which was used to determine the crystallographic orientation of the rods.⁸ Each diffraction peak was calibrated according to the standard X-ray diffraction chart to determine the Miller indices corresponding to the diffraction peaks. The experiments were conducted on a D/Max-1200X X-ray diffractometer, using a scanning angle of 20–80°, a scanning speed of 1° min⁻¹, a Cu target, an acceleration voltage of 40 kV, a filament current of 30 mA and graphite monochromatic as the filter.

3 RESULTS AND DISCUSSION

By comparing the grain sizes from the cross-sections of the magnesium alloy billet after the ES process, it is clear that the grains were significantly refined because the dynamic recrystallization happens during the ES process. In addition, it can also be seen from **Figure 2** that the grains are constantly refined from part 1 to 4 in **Table 1**, and the grain sizes are compared in the same part with different extrusion temperatures. It is well known that the grain size increases with the temperature, which is because a higher temperature would improve the grain growth.^{8,9}

The lamellar microstructures in the first shear zone begin to reduce for the large shear strain caused by the

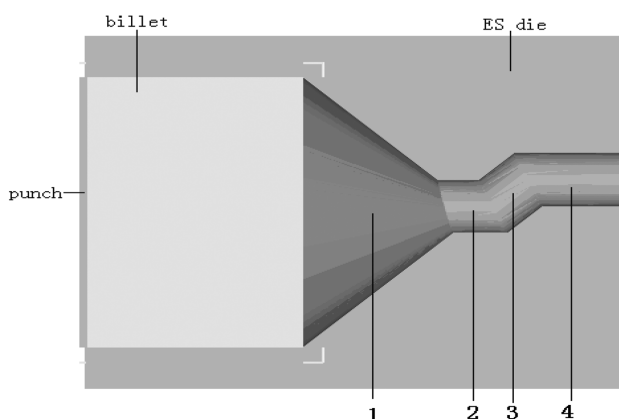


Figure 1: Schematic diagram of ES die with two 120° corner angles, 1 – upsetting zone, 2 – sizing zone, 3 – the first shearing zone, 4 – the second shearing zone

Slika 1: Shematski prikaz ES z dvema zamikoma s kotom 120°: 1 – področje krčenja, 2 – področje dimenzioniranja, 3 – prvo področje striženja, 4 – drugo področje striženja

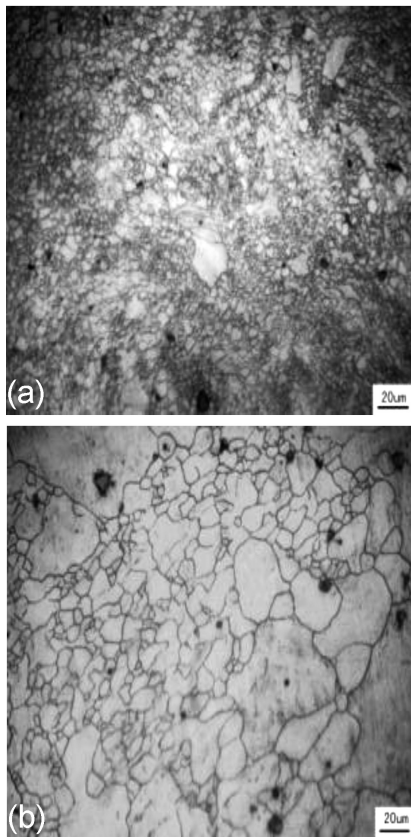


Figure 2: Microstructures of the cross-section with preheated temperatures: a) 420 °C, b) 450 °C

Slika 2: Mikrostrukturni preseka pri temperaturi ogrevanja: a) 420 °C, b) 450 °C

Table 1: Comparison of the grain size during various stages for the ES process

Tabela 1: Primerjava velikosti zrn med različnimi stopnjami ES postopka

	Homogenization state	Temperature	Part 1	Part 2	Part 3	Part 4
Grain size (µm)	188	420 °C	4.9	2.8	2.4	2.1
		450 °C	8.8	8.1	5.6	5.0

shear deformation in this zone and the deformed grains turn into recrystallization grains. In the second shear zone, DRX occurs, but there is still a small amount of fine-grain strips in the center of the rod. The average grain size decreased from about 188 µm to 2–5 µm by using the ES process. The microstructures are not only greatly refined but also relatively uniform because the ES process includes two simple shear steps. The deformation degree of the central parts of the rods increases, allowing more DRX to occur. Therefore, the microstructure becomes smaller and more homogeneous.

From the microstructures of the billet after the ES process it can be observed that the number of dendrites in the α-Mg matrix is greatly reduced, while the second phase and the dendrites' segregation were mostly eliminated in the microstructures. The sizes of the grains

before and after the ES process were measured using the cut line method, as shown in **Table 1**.

The relationship between the average recrystallization grain size (d) and the Zener-Hollomon parameter (Z) during the dynamic recrystallization is given by $-\ln d = A + B \ln Z$. Based on the present ES process, with the extrusion temperature, the accumulative strain increase with the extrusion advancing, the grains will be refined.^{10,11}

The relationship between the average recrystallization grain size (d) and the Zener-Hollomon parameter (Z) during dynamic recrystallization is given by Equation (1):

$$\left(\frac{d}{d_0}\right)^n = 10^{-3} \cdot Z^{-1/3} \quad (1)$$

The temperature-corrected strain rate Z is given by Equation (2):

$$Z = \dot{\epsilon} \exp\left(\frac{Q}{RT}\right) \quad (2)$$

where $\dot{\epsilon}$ is the strain rate, Q is the activation energy for the deformation, T is the temperature and R is the gas constant.

It can be seen from Equation (1) and Equation (2) that the preheated temperature of the billets has a significant impact on the dynamic recrystallization of the fine grains if the structure parameters of the ES dies are the same. So the sizes and the volume fraction of the dynamic recrystallization of the fine grains are inversely proportional to the preheated temperature of the billets. It is obvious that the average sizes of the grains for the lower preheated temperature are finer than those of the higher preheated temperature. It can be observed that the lower temperature could inhibit any further grain growth.

To obtain the orientations of the deformed grains, XRD tests were carried out. The baseline orientation was obtained by using samples that were taken from the longitudinal section in a direction parallel to the extrusion direction of the ES process. The strength of the diffraction lines represents the relative amount of the crystal plane that is parallel to the distribution surface. As can be seen from **Figure 3**, the strongest diffraction peak is the (0002) crystal plane, and the (10 $\bar{1}$ 0) plane is the second-strongest diffraction peak before the ES process. In Mg alloys, a strong basal texture is always found, which resulted in poor ductility at room temperature. Therefore, it is important to control the orientations during the processing. In the upsetting zone I, the strongest diffraction peak is still the (0002) crystal plane. But in the sizing zone, the intensity of the (10 $\bar{1}$ 0) and (10 $\bar{1}$ 1) planes increases very obviously. The crystal plane (10 $\bar{1}$ 1) is the strongest diffraction peak in the last two continuous shearing zones, while the strength of the basal plane (0002) peak clearly decreases. The two shearing steps lead to an increase in the peak-intensity ratio. This shows that the ES process could promote the coexistence

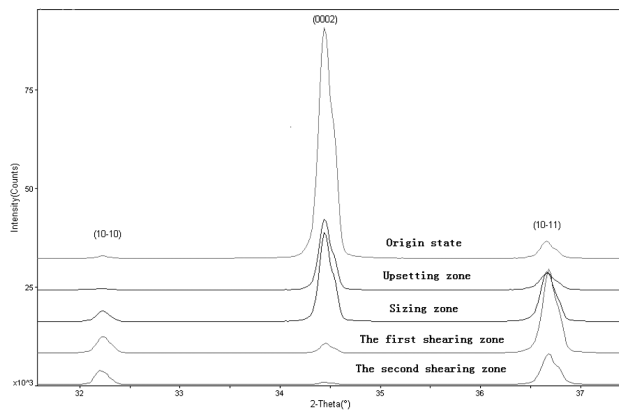


Figure 3: X-Ray diffraction of AZ31 Mg alloy in different parts of the rod in ES dies

Slika 3: Rentgenska difrakcija Mg zlitine AZ31 na različnih delih palice v ES orodju

of the (0002) basal plane and the non-basal planes. From the XRD test, it is clear that the basal texture of (0002) was greatly weakened, and it becomes less dominant after the ES process. The weakening of the basal texture could be attributed to the shear deformation during the ES process. The weakening of the basal texture is expected to enhance the formability of Mg alloys.

Compression and tensile fracture experiments were conducted at room temperature. The fracture behaviors

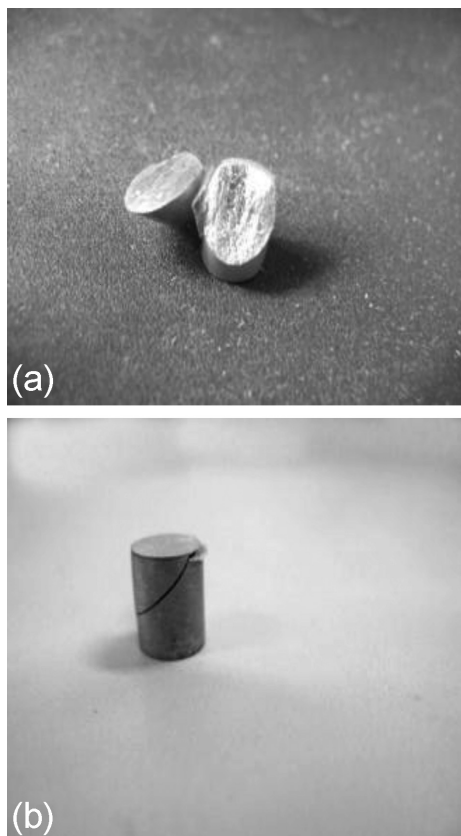


Figure 4: Images of the specimens after compression
Slika 4: Posnetek vzorcev po stiskanju

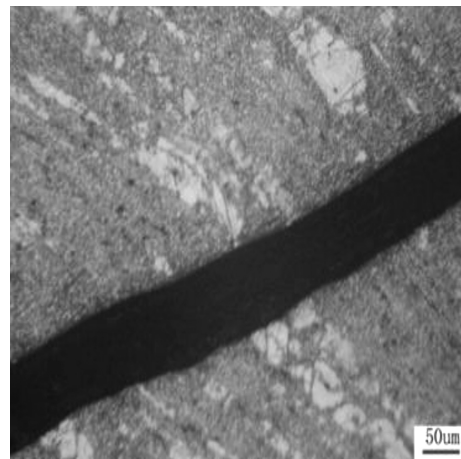


Figure 5: Microstructures of fracture caused by compression in the specimen extruded at 420 °C

Slika 5: Mikrostrukture ob prelomu, ki je nastal pri stiskanju vzorca, iztiskanega na 420 °C

and the regulation of magnesium alloys during the ES process were studied by observing and analyzing the fracture phenomenon, which is important in effectively preventing fractures of the magnesium alloy during the ES process. Macro images of specimens after compression have been shown in **Figure 4**.

As can be seen from **Figure 5**, the main fracture of the specimen extruded at 420 °C is a transgranular fracture, while it is mainly caused by the twins when the extrusion temperature is 450 °C in **Figure 6**. The specimen that was formed at 450 °C would be fractured when the amount of deformation is 10.5 %, while the specimen that was formed at 420 °C would fracture when the amount of deformation is 13.8 %.

The microstructures were refined at an extrusion temperature of 420 °C. Twins were hardly generated in the part for dynamic recrystallization. The internal microstructures of the specimens extruded at 450 °C are uneven, and there is a portion of elongated grains and a

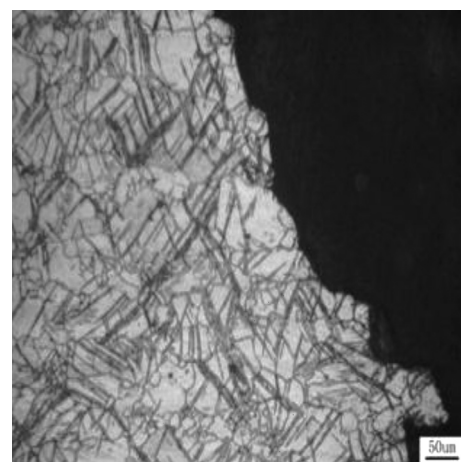


Figure 6: Microstructures for fracture caused by compression in the specimen extruded at 450 °C

Slika 6: Mikrostrukture ob prelomu, ki ga je povzročilo stiskanje vzorca, iztiskanega na 450 °C

large amount of fine dynamic-recrystallization grains distributed among the original grains. The specimens would be subjected to a compressive stress during the compression process at room temperature. Once the slip plane tended to the direction that is parallel to the force direction, the slip systems in the magnesium alloy would stop moving. The increase in the external force usually led to the occurrence of twins. The twins were generated between the elongated original grain boundaries. Once the twins occur, due to changes of the crystal orientation in the twins, the slip plane is no longer parallel to the direction of force, and the primary slip systems would begin. The plastic deformation would not stop before the sample is fractured. When the cracks on the edge of the fracture encounter twins, the expansion path is forced to change. Obviously, the hindrance of twins to the crack propagation leads to an improvement in the material toughness. Cracks on the fracture would be hindered by grain boundaries when they encounter small grains. It is known that the microstructures are inhomogeneous. Twins would be generated among the elongated original grains boundaries. However, it is prone to produce cracks in the twin boundaries. It can be seen from **Figure 6** that a large amount of twins appear near the fracture and the cracks. A large number of twins were generated along the elongated grain boundaries near the fracture. There are interactions between the twins and cracks, and the cracks could induce twins, and twins would promote crack nucleation. The twins and cracks develop rapidly, so a large stress concentration would occur at the tip of the cracks. Twinning and fracture are two processes that release stress concentration. Therefore, the factors in favor of one process are beneficial to the other process. The microstructures would be elongated under tensile stress and a large number of fine twins would be generated because of the severe deformation at the elongated grain boundaries.

The ES process is actually a combination of extrusion and ECAP extrusion to achieve a compound of extrusion and shear processes. In the early extrusion, the microstructures appear to be bent and broken under simultaneous compression and shear.

4 CONCLUSIONS

To study the effects of extrusion-shear on the microstructures and mechanical properties of a magnesium alloy in the homogenized state during the ES process, the ES process was performed on extrusion equipment with the explored ES die. The grain size measurement and the X-ray diffraction analysis, compression experiments and fracture analysis were made and discussed. It can also be seen that the grains are constantly refined from part 1 to 4. The ES process could improve the dynamic recrystallization during deformation. The microstructures become more uniform and finer, when compared to the original states, during the ES process. A higher pre-heating temperature could improve the grain growth and

coarsen the grains. The texture analysis showed that after the ES process there is a variety of types of texture, which could weaken the dominant position of the basal plane texture (0002). The main fracture mechanism of the specimen extruded at 420 °C is transgranular fracture, while it is mainly caused by the twins when the extrusion temperature was 450 °C.

Acknowledgements

This work was supported by the open fund for Key Laboratory of Manufacture and Test Techniques for Automobile Parts (Chongqing University of Technology) Ministry of Education in 2013, and foundation of the post doctorate in Chongqing city and Project Number is Xm201327, the China Postdoctoral Science Foundation funded project, and the Chongqing Natural Science Foundation Project of cstc2014jcyjA50004.

5 REFERENCES

- G. Liu, J. Zhou, J. Duszczyc, Finite element analysis of magnesium extrusion to produce a cross-shaped profile, *J. of Manufacturing Science and Engineering*, 129 (2007) 3, 607–614, doi:10.1115/1.2714590
- H. Hu, D. Zhang, F. Pan, M. Yang, Analysis of the Cracks Formation on Surface of Extruded Magnesium Rod Based on Numerical Modeling and Experimental Verification, *Acta Metallurgica Sinica*, 22 (2009) 5, 353–364, doi:10.1016/S1006-7191(08)60109-X
- K. Siegert, S. Jäger, M. Vulcan, C. Wizemann, Forming tubes, extrusions and sheet metal from magnesium AZ31, *Mater. Sci. Forum*, 488–489 (2005), 499–508, doi:10.4028/www.scientific.net/MSF.488-489.499
- H. Hongjun, Z. Dingfei, Y. MingBo, D. Ming, 201. Grain refinement in AZ31 Magnesium alloy rod fabricated by an ES SPD process, *Transactions of Nonferrous Metals Society of China*, 21 (2010) 2, 243–249, doi:10.1016/S1003-6326(11)60705-X
- L. Li, J. Zhou, J. Duszczyc, Determination of a constitute relationship for AZ31B magnesium and validation through comparison between simulated and real extrusion, *Mater. Process. Technol.*, 172 (2006) 3, 372–380, doi:10.1016/j.jmatprotec.2005.09.021
- M. Chandrasekaran, Y. M. Shyan John, Effect of materials and temperature on the forward extrusion of magnesium alloys, *Mater. Sci. Eng. A*, 381 (2004), 308–319, doi:10.1016/j.msea.2004.04.057
- N. Ogawa, M. Shiomi, K. Osakada, Forming limit of magnesium alloy at elevated temperatures for precision forging, *Int. J. Mach. Tools Manu*, 42 (2002) 5, 607–614, doi:10.1016/S0890-6955(01)00149-3
- R. Ye, Lapovok, M. R. Barnett, C. H. J. Davies, Construction of extrusion limit diagram for AZ31 magnesium alloy by FE simulation, *J. Mater. Process. Technol.*, 146 (2004) 3, 408–414, doi:10.1016/j.jmatprotec.2003.12.003
- S. B. Xu, G. Q. Zhao, X. W. Ma, G. C. Ren, Finite element analysis and optimization of equal channel angular pressing for producing ultra-fine grained materials, *Journal of Materials Processing Technology*, 184 (2007) 1–3, 209–216, doi:10.1016/j.jmatprotec.2006.11.025
- R. Matsumoto, K. Osakada, Development of warm forging method for magnesium alloy, *Materials Transactions*, 45 (2004) 9, 2838–2844, doi:10.2320/matertrans.45.2838
- D. Orlov, G. Raab, T. T. Lamark, M. Popov, Y. Estrin, Improvement of mechanical properties of magnesium alloy ZK60 by integrated extrusion and equal channel angular pressing, *Acta Materialia*, 59 (2011) 1, 375–385, doi:10.1016/j.actamat.2010.09.043

FSW WELDING OF Al-Mg ALLOY PLATES WITH INCREASED EDGE ROUGHNESS USING SQUARE PIN TOOLS OF VARIOUS SHOULDER GEOMETRIES

FSW VARJENJE PLOŠČ IZ Al-Mg ZLITINE S POVEČANO HRAPAVOSTJO ROBOV Z ORODJEM S KVADRATNO KONICO IN RAZLIČNO GEOMETRIJO BOKOV

**Sebastian Balos, Lepasava Sidjanin, Miroslav Dramicanin, Danka Labus Zlatanovic,
Aco Antic**

Faculty of Technical Sciences, Department of Production Engineering, Trg Dositeja Obradovica 6, 21000 Novi Sad, Serbia
danlabus@uns.ac.rs

Prejem rokopisa – received: 2015-04-30; sprejem za objavo – accepted for publication: 2015-06-17

doi:10.17222/mit.2015.088

In the paper, the influence of tool shoulder geometries on the mechanical properties and weld surface roughness of an Al-Mg alloy was studied. Different types of tools were used: with straight and concave profiles. Three concave-shoulder types were applied, with volume ratios of 0.5 and 0.9 of the square pin to the shoulder reservoir and one with three concentric semi-toroidal reservoirs with a volume ratio of 0.5 of the pin to the shoulder reservoir. The tensile and bend properties, hardness profiles and macro-features of welds were examined. It was found that the optimum tensile and bending properties were obtained when applying the tool with concentric reservoirs and the lowest welding speed. In this way, the widest nugget zone at the plate axis is obtained, as well as the thickest nugget-zone layer under the specimen surface, covering the thermomechanical and heat-affected zones. The overlapping of the nugget zone with the thermomechanical and heat-affected zones enables higher proof and ultimate tensile strengths compared to the base material. The surface-roughness parameters of the weld face are lower for the specimens welded with the tools with reservoirs and considerably lower than the base-material edge-surface roughness.

Keywords: friction-stir welding, 5052 aluminum alloy, FSW parameters, joint properties, surface roughness

V članku je prikazana raziskava vpliva geometrije boka orodja na mehanske lastnosti in hrapavost površine zvara Al-Mg zlitine. Uporabljeni sta bili orodji z ravnim in konkavnim profilom. Uporabljene so bile tri vrste konkavnih bokov, z razmerjem volumna 0,5 in 0,9 bočnega rezervoarja ter kvadratne konice in eden s tremi poltoroidnimi koncentričnimi rezervoarji, z razmerjem volumnov 0,5 konica-bok. Preiskovane so bile natezne in upogibne lastnosti, profili trdote in makro izgled zvarov. Ugotovljeno je, da so bile optimalne natezne in upogibne lastnosti dobljene pri uporabi orodja s koncentričnimi rezervoarji pri najmanjši hitrosti varjenja. Na ta način se doseže najširše področje mešanja pod površino vzorca, ki pokriva termomehansko in toplotno vplivano področje. Prekrivanje področja mešanja s termomehanskim in toplotno vplivanim področjem, omogoča višjo mejo plastičnosti in višjo natezno trdnost, v primerjavi z osnovnim materialom. Parametri površinske hrapavosti čela zvara so manjši pri vzorcih zvarjenih z orodji z rezervoarji in so občutno nižji, kot je osnovna hrapavost roba materiala.

Ključne besede: torni vrtilni varjenje, aluminijeva zlitina 5052, parametri FSW, lastnosti spoja, hrapavost površine

1 INTRODUCTION

Friction-stir welding (FSW) is a solid-state metal-joining process that uses a specialized non-consumable rotating tool to join work pieces.¹ It has been shown that FSW is a suitable welding method for joining the materials difficult to join using conventional welding techniques. The most notable are aluminium-zinc-magnesium and aluminium-copper heat-treated alloys.²⁻⁷ Furthermore, Mg-alloys and dissimilar materials have been successfully welded by FSW.⁸⁻¹³ The main advantages of FSW are related to the fact that no melting occurs and, therefore, gas porosity is avoided. Also, no distortion occurs and no shielding gases or welding consumable materials are needed, leading to a relatively low energy input.¹⁴ A decisive influence on the weld performance comes from the welding tool and the parameters such as welding and rotational speeds, as well as the tilt angle, etc. On the other hand, the FSW tool geometry

can be related to the pin and shoulder geometry and the relation between the pin and shoulder size.

The tool has three primary functions: heating, material movement and containment of the heated material between the tool shoulder and the base plate.¹⁵⁻¹⁶ The tool pin influences deformational and frictional heating, as well as shearing the material in front of and moving the material behind the tool.¹⁷⁻²⁰ The geometry of the FSW tool pin can vary considerably: round and flat-bottom cylindrical or threaded pins were found to be adequate for aluminium-alloy plates of up to 12 mm.¹⁷ Truncated cone pins were developed to weld plates thicker than 12 mm at higher welding speeds, while fluted pins add deformation to the weld line, increasing the possible welding speeds even further.¹⁵ Polygonal pins offer 12–25 % reduced traversing and forging forces at a comparable strength as fluted pins.²¹ However, thin metallic plates were reported to be welded with pinless tools as well.²²

The shoulder of FSW tools influences a number of weld features: from the most basic ones such as the weld appearance and roughness, to microstructural characteristics influencing the weld strength.^{23–25} These features are obtained through the forging action aimed at a proper containment and consolidation of the base material.²⁵ A number of shoulder designs emerged. The most basic shoulder type is straight in the profile, without any curvature. However, now the most common type is the concave shoulder of a certain volume (reservoir), usually requiring tilting of the tool by 2–4°.

Both mentioned types of shoulder enable a relatively simple fabrication and cleaning after the welding process.^{14–15,19} An alternative is a shoulder with features such as scrolls, ridges or concentric circles, generally aimed at increasing the welding speed, the deformation and the frictional heating.^{15,26–28} Convex shoulder tools with scrolls are characterized with an improved ability to weld curvatures, base material with mismatch tolerances and different-thickness workpieces.¹⁵ Finally, the friction-stir spot welding (FSSW) of polymers can be used with a one-piece tool or a tool with a pin and a sleeve to allow dissimilar polymers to be mixed in lap joints.^{29–30}

Another variable is the tool material, which is tailored to the material to be welded. Aluminium and magnesium alloys can be welded using tool steels, most typically hot-work tool steel such as H13. However, copper and copper alloys demand the use of nickel- or tungsten-alloy tools, while steel welding is most often done with polycrystalline cubic boron-nitride (PCBN) or tungsten-carbide (WC) material.¹⁵

The aim of this paper is to study the influence of different shoulder geometries on mechanical and weld-surface properties. Namely, regardless of what type of shoulder geometry is applied, a careful optimization of welding parameters is needed to obtain adequate mechanical properties as well as an acceptable weld-face surface roughness, since rough weld tracks most often require rework.²³ Therefore, the machining of quality weld tracks is desirable and can be achieved with an efficient FSW tool that combines this outcome with high mechanical properties, without the need for a tool tilt, improving the tool life and used on a relatively rough edge-surface textures of plates.

2 EXPERIMENTAL WORK

In this paper, the base material consisted of Al-Mg EN-AW5052-0 plates of 5 mm. The chemical composition of the aluminium alloy determined with an optical emission spectrometer ARL 3580 is given in **Table 1**. The mechanical properties of the workpiece material, tested with a WPM ZDM 5/91 tensile-testing machine, on the basis of three specimens, are given in **Table 2**.

The plates were machined to dimensions of 300 mm × 65 mm, with the average roughness of the edge to be welded of $R_a = 7.67 \mu\text{m}$ and the maximum peak rough-

ness (R_z) of $29.8 \mu\text{m}$, corresponding to the sawing process.³¹ The samples were tightly placed into a steel fixture into a 130-mm-wide groove and secured by clamps. The fixture was fitted onto an adapted Prvo-majska UHG universal milling machine with a power of 5.2 kW. The tool used was made of X38CrMoV5-1 (H11) hot-work tool steel, having had its chemical composition tested with an ARL 2460 optical emission spectrometer, as given in **Table 3**. The hardness of all the FSW tools was 53 HRC, as measured with a WPM HPO-250 device. Four different tool geometries were used, all with four-sided pins of equal dimensions, **Figure 1**. It can be seen that three basic geometries were used: a straight profile without a reservoir (0-type), two concave shoulders with shoulder-to-pin ratios of 0.5 and 0.9 (5- and 9-type) and a feature shoulder with three concentric circles and the overall volume-to-pin ratio of 0.5 (53-type tool). FSW was done without a tool tilt, with a rotational speed of 925 min^{-1} and three welding speeds,

Table 1: Chemical composition of EN-AW 5052 aluminium alloy (in mass fractions, w/%)

Tabela 1: Kemijska sestava aluminijeve zlitine EN-AW 5052 (v masnih odstotkih, w/%)

Cu	Mn	Mg	Si	Fe	Zn	Ti	Al
0.09	0.09	2.78	0.24	0.38	0.046	0.015	balance

Table 2: Mechanical properties of EN-AW 5052-0

Tabela 2: Mehanske lastnosti EN-AW 5052-0

Proof strength R_{pBM} (MPa)	Ultimate tensile strength R_{mBM} (MPa)	Elongation A_{BM} (%)	Vickers hardness number HV5
124±10	193±3	22±1	60±1

Table 3: Chemical composition of X38CrMoV5-1 tool steel (in mass fractions, w/%)

Tabela 3: Kemijska sestava orodnega jekla X38CrMoV5-1 (v masnih odstotkih, w/%)

C	Si	Mn	P	S	Cr	Mo	V	Fe
0.37	1.01	0.38	0.017	0.0005	4.85	1.23	0.32	balance

Table 4: Specimen-group designation system

Tabela 4: Sistem označevanja vzorcev

Shoulder cavity/pin volume ratio	Number of shoulder cavities	Area of the shoulder surface parallel to the base metal (mm^2)	Tool designation	Welding speed (mm/min)	Specimen group designation
0	0	374	0	17	01
0	0			46	04
0	0			91	09
0.5	1	163	5	17	51
0.5	1			46	54
0.5	1			91	59
0.5	3	226	53	17	531
0.5	3			46	534
0.5	3			91	539
0.9	1	163	9	17	91
0.9	1			46	93
0.9	1			91	99

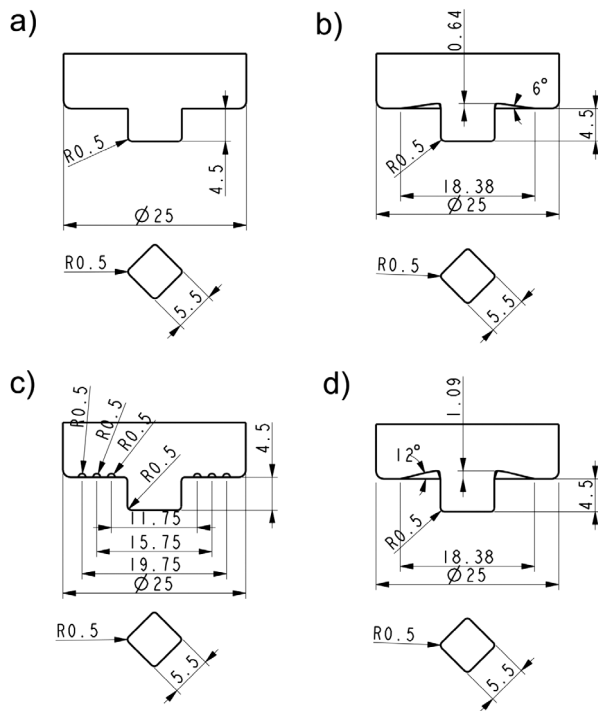


Figure 1: FSW tools: a) straight profile without a reservoir (0-type), b) concave shoulder with the shoulder-to-pin volume ratio of 0.5 (5-type), c) feature shoulder with three concentric circles with the overall volume-to-pin ratio of 0.5 (53-type) and d) concave shoulder with the shoulder-to-pin volume ratio of 0.5 (9-type) 0.9

Slika 1: FSW orodja: a) raven profil brez hranilnika (0-vrsta), b) konkaven bok z razmerjem volumna na boku in konici 0,5 (5-vrsta), c) oblikovan bok s tremi koncentričnimi krogi z razmerjem skupni volumen-konica 0,5 (53-vrsta) in d) konkavni bok z razmerjem volumnov bok-konica 0,5 (9-vrsta) 0,9

Table 5: Tensile properties and standard deviations, joint efficiencies, fracture locations and angles of bend to the first crack

Tabela 5: Natezne lastnosti in standardni odkloni, učinkovitost spojev, položaj porušitev in koti pri upogibanju do prve razpoke

	R_p (MPa)	R_m (MPa)	A (%)	Joint efficiency			Number of fractures × side of fracture	Number of fractures × fracture location	Angle of bend to the first crack-weld root (°)*	Angle of bend to the first crack-weld face (°)*
				R_{pFSW}/R_{pBM} 100 (%)	R_{mFSW}/R_{mBM} 100 (%)	A_{FSW}/A_{BM} 100 (%)				
01	125±20	171±39	6±2	101	89	27	3×AS	2×NZ/TMAZ 1×TMAZ/HAZ	22	(180)
04	134±8	182±22	10±2	108	94	45	3×AS	2×TMAZ/HAZ 1×NZ/TMAZ	23	(180)
09	125±8	153±10	4±3	102	80	18	3×AS	3×NZ/TMAZ	17	(180)
51	147±8	191±3	10±2	125	103	45	2×AS 1×RS	3×TMAZ/HAZ	26	(180)
54	138±15	160±14	7±2	111	83	32	3×AS	3×NZ/TMAZ	16	(180)
59	120±24	146±23	6±3	97	76	27	3×AS	3×NZ/TMAZ	12	(180)
531	160±2	198±5	13±2	129	103	59	3×RS 1×AS	2×TMAZ/HAZ 1×NZ/TMAZ	(180)	(180)
534	155±5	196±7	10±3	125	102	45	2×AS 1×RS	3×TMAZ/HAZ	55	(180)
539	125±3	153±7	7±3	101	80	32	3×AS	2×TMAZ/HAZ 1×NZ	18	(180)
91	154±7	198±3	12±3	118	99	55	2×AS 1×RS	2×TMAZ/HAZ 1×NZ/TMAZ	66	(180)
94	128±26	151±44	7±3	103	79	32	3×AS	2×NZ/TMAZ 1×TMAZ/HAZ	17	(180)
99	123±11	143±29	6±3	99	74	27	3×RS	3×NZ/TMAZ	7	(180)

*Numbers in parentheses indicate that the cracking did not occur until the test was completed (until 180°)

*Številka v oklepajih kažejo, da ni prišlo do razpoke, dokler ni bil test zaključen (pri 180°)

(17, 46 and 91) mm/min. Therefore, a designation system was devised, **Table 4**. The plunge depth of tool shoulder was 0.3 mm for all the FSW specimens.

The properties of the FSW workpieces were determined with tensile, bending, hardness testing and metallographic examination. The tensile and bending testing was determined with the WPM ZDM 5/91 testing machine, according to the EN 895 and EN 910 standards, respectively. Hardness was determined with a VEB HPO-250 Vickers testing machine, with a 5-kg load. The hardness measurements were done at a 1.5-mm distance between the indentations to obtain the hardness profiles. The metallographic examinations were done after the standard metallographic preparation: grinding with sandpapers (grit 220 to 2000), polishing with diamond suspensions (6, 3, 1 and ¼ µm abrasive-grain sizes) and etching with Keller's reagent (2 mL HF, 3 mL HCl, 5 mL HNO₃, 190 mL H₂O). The obtained metallographic specimens were then examined with a Leitz Orthoplan light microscope.

Roughness parameters including the average roughness (R_a), ten-point mean roughness (R_y) and the maximum peak roughness (R_z) were determined with a Mitutoyo SJ-301 surface-roughness tester.

3 RESULTS

3.1 Mechanical properties

The results of the tensile and bend testing are shown in **Table 5**. The tool design, that is, the tool-shoulder

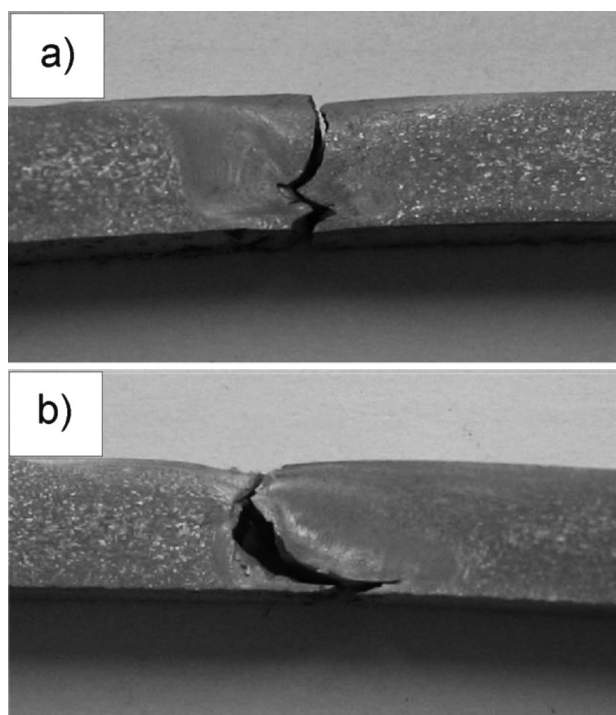


Figure 2: Fracture locations for tensile specimens: a) NZ on RS (specimen 539), b) NZ/TMAZ on AS (specimen 54)

Slika 2: Položaja preloma pri nateznem preizkušancu: a) NZ na RS (vzorec 539), b) NZ/TMAZ na AS (vzorec 54)

geometry clearly influences the tensile properties. The lowest values were obtained with the 0-type tool, followed by the 9-type tool, the 5-type tool and, finally, the highest mechanical properties were obtained with the 5- and 53-type tools. Furthermore, a clear correlation exists between the welding speed and the tensile properties for the 5-, 53- and 9-type tools. At lower welding speeds, the proof and tensile strengths, as well as the elongation increase. In the case of the 0-type tool, the highest tensile properties were achieved with a welding speed of 46 mm/min. The same trend can be observed for joint efficiencies, which are related to the base-material tensile properties. Thus, the highest joint efficiencies were obtained with the 531 specimen group

(129 % proof-strength efficiency, 103 % ultimate-tensile-strength efficiency and 59 % elongation efficiency), followed by the 534 and 91 specimen groups. The lowest efficiencies were achieved with the 01, 09 and 99 specimen groups.

No clear influence of the welding speed on the tensile-property standard deviation can be observed. However, comparing the specimen groups obtained with different tools, a clear trend can be seen: the highest standard deviations were achieved with the straight profile shoulder (the 0-type tool; 01, 04, 09 specimen groups), while the lowest deviation was obtained with the three-circular-groove tool (the 53-type tool; 531, 534, 539 specimen groups). For the 0-type tool, the general trend shows a reduction in the standard deviations with an increase in the welding speed. An opposite trend can be observed with the 5-type tool. In the cases of the 53- and 9-type tools, no clear correlation between the standard deviation and the welding speed can be made. Furthermore, no clear correlation between the tool shoulder design, the welding speed or the tensile/bend properties, and the side of fracture or the fracture location can be observed.

The fracture location for all the specimen groups is either in NZ/TMAZ (nugget zone/thermomechanical zone) or TMAZ/HAZ (thermomechanical zone/heat affected zone), with only one NZ fracture. The more frequent side of fracture was the advancing side (AS), in contrast to the retreating side (RS). Some cases of the fracture during the tension test are shown in **Figure 2**.

Angles of bend to the first crack can be positively correlated to tensile properties. Namely, as the tensile properties are higher, the angle of the first crack in the weld root is also higher. In the case of 531, the specimen was bent to 180 ° without cracking in the weld root. No cracking occurred in either specimen weld face. Some cases of bend testing are shown in **Figure 3**.

Hardness profiles are shown in **Figure 4**. All the hardness profiles have a similar general shape, with the maximum attained hardness values at the middle of the chart, that is, in the NZ. However, some clear trends can be observed for all the specimen groups welded with the



Figure 3: Bending to the first crack: a) specimen 04, b) specimen 531

Slika 3: Upogibanje do prve razpoke: a) vzorec 04, b) vzorec 531

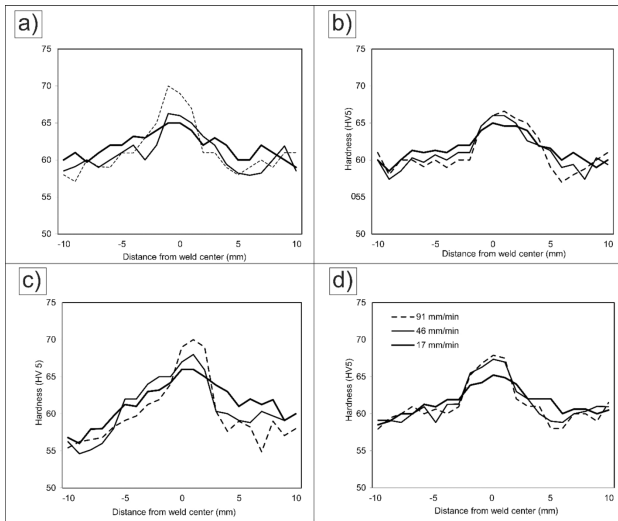


Figure 4: Hardness profiles of specimens welded with a tool rotational speed of 925 min^{-1} : a) 0-type tool, b) 5-type tool, c) 53-type tool, d) 9-type tool (welding speeds are indicated by different lines, shown in **Figure 4d**)

Slika 4: Profili trdote vzorcev zvarjenih s hitrostjo vrtenja 925 min^{-1} : a) 0 – vrsta orodja, b) 5 – vrsta orodja, c) 53 – vrsta orodja, d) 9 – vrsta orodja (hitrosti varjenja so prikazane z različnimi linijami, obrazloženi na **Sliki 4d**)

same FSW tool. Firstly, the hardness in the NZ is higher for the specimens welded at higher welding speeds. Secondly, an increase in the welding speed causes a drop in the hardness values for the TMAZ and HAZ zones (approximately 3–10 mm on either side of the NZ).

3.2 Metallographic examinations

The results of the metallographic examinations of the representative specimens obtained with the 5- and

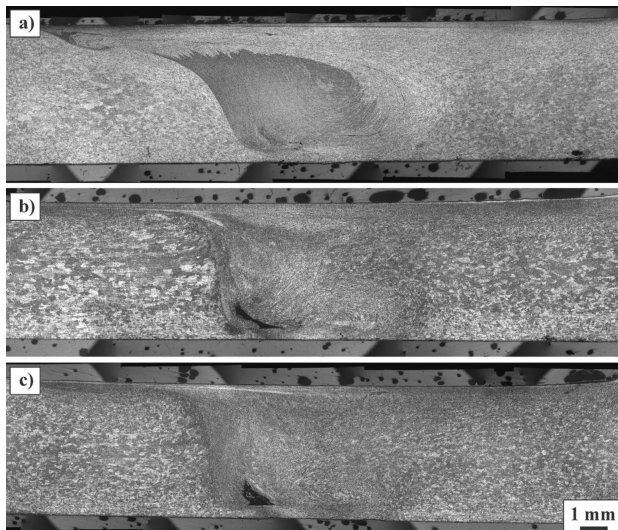


Figure 5: Macrographs of specimens welded with 5-type tool (rotational speed of 925 min^{-1}): a) specimen 51 (welding speed of 17 mm/min), b) specimen 54 (46 mm/min), c) specimen 59 (91 mm/min)

Slika 5: Makroposnetki vzorcev zvarjenih z orodjem vrste 5 (hitrost vrtenja 925 min^{-1}): a) vzorec 51 (hitrost varjenja 17 mm/min), b) vzorec 54 (46 mm/min), c) vzorec 59 (91 mm/min)

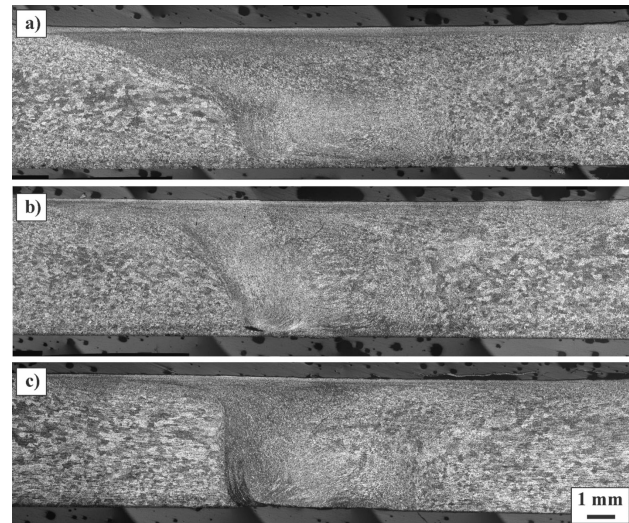


Figure 6: Macrographs of specimens welded with 53-type tool (rotational speed of 925 min^{-1}): a) specimen 531 (17 mm/min welding speed), b) specimen 534 (46 mm/min), c) specimen 539 (91 mm/min)

Slika 6: Makroposnetki vzorcev zvarjenih z orodjem vrste 53 (hitrost vrtenja 925 min^{-1}): a) vzorec 531 (hitrost varjenja 17 mm/min), b) vzorec 534 (46 mm/min), c) vzorec 539 (91 mm/min)

53-type tools are shown in **Figures 5** and **6**. It can be seen that multiple relatively small, tunnel-like defects occur in Specimen 51, **Figure 5a**. However, in Specimens 54 and 59, single larger tunnel-like defects appear at the bottom section of the NZ, on the advancing side. Also, by increasing the welding speed, a more pronounced tunnelling occurs. A similar trend of the increasing defect size can be seen in **Figure 6**, relating to the specimens welded with the 53-type tool. In Specimen 531, welded at the lowest welding speed, no tunnel-like defect occurs, while in Specimens 534 and 53, small-sized closed and open tunnels (root defects) occur.

The variation in the welding speed causes a change in the transition line between NZ and TMAZ on the advancing and retreating sides. This becomes closer to a vertical (normal to the specimen surface) as the welding speed increases. This means that the thickness of the refined zone under the specimen surface is higher in the specimens treated at a lower welding speed.

The macrostructures of the HAZ and TMAZ zones also vary depending on the type of tool used, as well as the welding speed. In **Figure 5**, for the 5-type tool, the lowest and the highest welding speeds of 17 and 91 mm/min result in a finer microstructure. The same can be observed for Specimen 534, welded with the 53-type tool at the medium welding speed, **Figure 6**.

3.3 Roughness of the weld face

Roughness parameters of the FSW weld faces are given in **Table 6**. It can be seen that the obtained results are generally lower than those for the edges of the base material ($R_a = 7.67 \mu\text{m}$; $R_z = 29.8 \mu\text{m}$). The highest surface roughness is obtained with the 0-type tool

without a reservoir in the shoulder, followed by the 53-type tool and 5-type tool, while the lowest roughness was achieved with the 9-type tool with the largest reservoir. No clear correlation between the roughness parameters and the welding speed can be observed.

4 DISCUSSION

In this paper, the influence of the shoulder configuration of the FSW tool with a square pin was evaluated in relation to the weld tensile, bend and hardness properties, macro-analysis and the surface roughness of the weld faces of the Al5052 plates with a high edge roughness.

The tensile/bending properties and macro-imaging are well correlated. Tunnel and root defects have a considerable influence on the weld properties, causing a decrease in the weld proof strengths, tensile strengths, elongations, corresponding efficiencies, as well as the bending angles to the first crack. Therefore, tunnel-free specimens had the highest mechanical properties and the corresponding weld efficiencies.

Such results can be explained with the nature of the square-pin-tool interaction with the surrounding material at various welding speeds. At a constant rotational speed, a relatively low welding speed causes an increase in the stirring-impulse frequency at a given weld length, leading to a more effective weld filling and defect avoidance. These results support the findings from reference²⁰, where a similar, relatively low welding speed was applied for FSW, with a square pin tool, of an Al-alloy-based metal-matrix composite reinforced with TiB₂ particles. Furthermore, in reference³², where the influence of a tunnelling-type defect on the mechanical and metallurgical properties of an Al-Mg alloy was studied, a low welding speed was more effective than high welding speeds, even with the tools having concave shoulders with large reservoirs. Furthermore, a similar finding was reported by Balos and Sidjanin in reference³², where a three-sided pin and an unusually large reservoir were used to promote the appearance of a tunnel-like defect. In reference³², the highest mechanical properties were obtained with the lowest welding speed (17 mm/min) and the highest rotational speed (1230 min⁻¹). The theory that refers to the frequency of impulse stirring at a given weld length is in a marked contrast to the findings of I. Radisavljevic et al.³³, who reported that the avoidance of a tunnel-like defect depends on the ratio of the rotation to the welding speed, but with the application of a threaded-pin tool.

Two specimens welded at the lowest speed, 01 and 51, also developed a tunnel-like defect. This phenomenon is the result of the tool-shoulder geometry and, therefore, its influence on the material flow. A straight-profile pin without a reservoir (the 0-type tool) provides lower mechanical properties than the 5-type tool, **Table 5**, indicating that even a relatively small

reservoir provides a more convenient material flow. This allows the material to move not only perpendicularly to the tool axis, as forced by the pin, but also parallelly to the tool axis, making the tunnel-like defect smaller (the 5-type tool) or eliminating it at a lower welding speed (the 53- and 9-type tools).

The welding speed also has a marked influence on the hardness of NZ. It can be seen that the increase in the welding speed causes a rise in the hardness of NZ for all the specimen groups. This is the result of the added deformation that comes from the increased welding speed due to the pushing action of the pin while passing through the material. On the other hand, NZs of the specimens welded at a lower welding speed are wider compared to the ones of the specimens welded at a higher welding speed. The hardness values of the TMAZ and HAZ zones vary; however, for the majority of the specimens (welded with the 0-, 5- and 9-type tools), a lower welding speed results in a higher average hardness compared to the medium and high welding speeds. This means that the welding speed of 17 mm/min enables lower hardness variations throughout the weld. These results are supported by the macrographs of the welds, where a change in the NZ is observed.

With the increase in the welding speed, the NZ to TMAZ transition line, at the advancing side, becomes closer to a vertical (normal to the specimen surface), while, at the retreating side, the NZ to TMAZ transition line gradually diminishes. This observation is supported by the hardness measurements, which suggest that the hardness drops more gradually in TMAZ at RS than in AS. The reason for such results is difficult to determine, but the major influence may come from the tool-shoulder geometry, which influences the material flow, causing a higher amplitude and lower frequency for the specimens welded with the 5-type tool or a lower amplitude and higher frequency for the specimens welded with the 53-type tool. Furthermore, this also influences the thickness of the NZ under the specimen surface. Namely, a thicker refined NZ under the specimen surface and over the TMAZ and HAZ zones can have a beneficial effect on the mechanical properties. This elongated layer can be regarded as very important for achieving higher proof strength and ultimate tensile strength than those of the base metal.

The results for the weld face roughness strongly depend on the shoulder contact area and the angle of the shoulder contact surface with the reservoir. It can be seen that the 5- and 9-type tool-shoulder contact areas are equal. This implies that a larger angle found for the 9-type-tool outer/external portion of the reservoir has a beneficial influence on the surface-profile finishing, preventing excessive adhesion of the base metal to the tool material. On the other hand, for the 0-type tool, a larger contact area (374 versus 163 mm²) proved to have an adverse effect, probably due to the adhesion of the base material. For the 53-type tool, a larger angle of the

concentric reservoirs has a secondary importance compared to a larger contact area (226 versus 163 mm²) and the existence of the secondary, tertiary and quaternary contacts between the tool shoulder and the base material that have a negative effect on the roughness parameters. According to the results shown in **Table 6**, there is no firm correlation between the roughness parameters and the welding speed.

Table 6: Roughness parameters obtained with different tools and FSW speeds

Tabela 6: Parametri hrapavosti, dobljeni z različnimi orodji in pri različnih hitrostih FSW

	R_a (μm)	R_y (μm)	R_z (μm)
01	3.24	32.13	21.64
04	2.41	14.51	17.33
09	4.17	20.85	26.14
51	2.48	15.27	13.10
54	1.35	12.69	8.05
59	2.05	10.40	8.94
531	1.46	12.78	8.29
534	2.51	18.30	14.07
539	2.02	12.90	11.59
91	1.95	16.84	12.89
94	1.14	10.94	6.46
99	1.11	7.32	5.84

5 CONCLUSIONS

According to the presented results, some conclusions can be drawn:

- The tool with a square pin and three concave reservoirs, with a reservoir-to-pin volume ratio of 0.5 enables proof and ultimate tensile strengths to surpass those of the base metal. The main reason for such mechanical properties is the characteristic shape of NZ that overlaps with TMAZ and HAZ.
- The welding speed of 17 mm/min enables the avoidance of the tunnel-like defect. This way, a full 180° bending over the weld root can be achieved.
- Low welding speeds are needed for achieving an increase in the stirring-impulse frequency at a given weld length. This enables a more effective weld filling and defect avoidance.
- Weld surface-roughness parameters are considerably lower for the specimens welded with the tools with reservoirs than with the tools without a reservoir.
- A relatively rough edge-surface texture of the base-metal specimens can be successfully overcome with a careful optimization of the tool geometry and welding speed, providing higher proof and ultimate tensile strengths compared to the base metal.

Acknowledgement

The authors are very grateful to Mr. Ninkovic Mladen from the company Unimet DOO in Novi Sad, Serbia, for

his valuable help in determining the roughness parameters of the specimens.

6 REFERENCES

- ¹ W. M. Thomas, E. D. Nicholas, J. C. Needham, M. G. Murch, P. Templesmith, C. J. Dawes, International Patent Application No. PCT/GB92/02203, GB Patent Application No. 9125978.8 (Dec. 1991) and U.S. patent No. 5, 460, 317 (Oct. 1995)
- ² H. Khodaverdizadeh, A. Mahmoudi, A. Heidarzadeh, E. Nazari, Effect of friction stir welding (FSW) parameters on strain hardening behavior of pure copper joints, *Materials and Design*, 35 (2012), 330–334, doi:10.1016/j.matdes.2011.09.058
- ³ G. Ypekoglu, B. G. Kiral, S. Erim, G. Cam, Investigation of the effect of temper condition on the friction-stir weldability of a7075 Al-alloy plates, *Mater. Tehnol.*, 46 (2012) 6, 627–632
- ⁴ L. Fratini, G. Buqa, D. Palmeri, J. Hua, R. Shivpuri, Material flow in FSW of AA7075–T6 butt joints: numerical simulations and experimental verifications, *Science and Technology of Welding and Joining*, 11 (2006), 412–421, doi:10.1179/174329306X113271
- ⁵ R. S. Mishra, Z. Y. Ma, Friction stir welding and processing, *Materials Science and Engineering R*, 50 (2005), 1–78, doi:10.1016/j.mser.2005.07.001
- ⁶ P. L. Threadgill, A. J. Leonard, H. R. Shercliff, P. J. Withers, Friction stir welding of aluminium alloys, *International Materials Review*, 54 (2009) 2, 49–93, doi:10.1179/174328009X411136
- ⁷ L. Magnusson, L. Kallman, Mechanical Properties of Friction Stir Welds in Thin Sheet of Aluminium 2024, 6013 and 7475, *Proc. of the 2nd International Symposium on Friction Stir Welding*, Gothenburg, Sweden 2000, 26–28
- ⁸ N. Afrin, D. L. Chen, X. Cao, M. Jahazi, Microstructure and tensile properties of friction stir welded AZ31B magnesium alloy, *Materials Science and Engineering A*, 472 (2008), 179–186, doi:10.1016/j.msea.2007.03.018
- ⁹ G. M. Xie, Z. Y. Ma, L. Geng, Effect of microstructural evolution on mechanical properties of friction stir welded ZK60 alloy, *Materials Science and Engineering A*, 486 (2008), 49–55, doi:10.1016/j.msea.2007.08.043
- ¹⁰ S. M. Chowdhury, D. L. Chen, S. D. Bhole, X. Cao, Tensile properties of a friction stir welded magnesium alloy: Effect of pin tool thread orientation and weld pitch, *Materials Science and Engineering A*, 527 (2010), 6064–6075, doi:10.1016/j.msea.2010.06.012
- ¹¹ T. Debroy, H. K. D. H. Bhadeshia, Friction stir welding of dissimilar alloys – a perspective, *Science and Technology of Welding & Joining*, 15 (2010) 4, 266–270, doi:10.1179/174329310X1272649607240
- ¹² O. Frigaard, A Process Model for FSW of Age Hardening Aluminium Alloys, Ph.D. Thesis, Norwegian University of Science and Technology, 1999
- ¹³ J. Quyang, R. Kovacevic, Material flow and microstructure in the friction stir butt welds of the same and dissimilar aluminum alloys, *Journal of Materials Engineering and Performance*, 11 (2002) 1, 51–63, doi:10.1007/s11665-002-0008-0
- ¹⁴ Z. Barlas, U. Ozsarac, Effects of FWS parameters on joint properties of AlMg3 alloy, *Welding Journal*, 91 (2012), 16–22
- ¹⁵ R. S. Mishra, M. W. Mahoney, Friction Stir Welding and Processing, ASM International, Materials Park, Ohio, USA 2007
- ¹⁶ A. Zivkovic, The influence of tool geometry on FSW process, Ph.D. Thesis, University of Belgrade, 2010
- ¹⁷ R. Rai, A. De, H. K. D. H. Bhadeshia, T. DebRoy, Review: friction stir welding tools, *Science and Technology of Welding & Joining*, 16 (2011) 4, 325–342, doi:10.1179/1362171811y.0000000023
- ¹⁸ Y. N. Zhang, X. Cao, S. Larose, P. Wanjara, Review of tools for friction stir welding and processing, *Canadian Metallurgy Quarterly*, 51 (2012) 3, 250–261, doi:10.1179/1879139512y.0000000015

- ¹⁹ P. Podrzaj, B. Jerman, D. Klobcar, Welding defects at friction stir welding, *Metalurgija*, 54 (2015), 387–389
- ²⁰ W. Yuan, R. S. Mishra, S. Webb, Y. L. Chen, B. Carlson, D. R. Herling, G. J. Grant, Effect of tool design and process parameters on properties of Al alloy 6016 friction stir spot welds, *Journal of Materials Processing Technology*, 211 (2011) 6, 972–977, doi:10.1016/j.jmatprotec.2010.12.014
- ²¹ P. A. Colegrove, H. R. Shercliff, Development of Trivex friction stir welding tool, Part 1 – two-dimensional flow modelling and experimental validation, *Science and Technology of Welding and Joining*, 9 (2004) 4, 345–351, doi:10.1179/136217104225021670
- ²² D. Klobčar, J. Tušek, A. Smolej, S. Simončič, Parametric study of FSSW of aluminium alloy 5754 using a pinless tool, *Weld World*, 59 (2015), 269–281, doi:10.1007/s40194-014-0208-x
- ²³ D. A. Burford, B. M. Tweedy, C. A. Widener, Influence of shoulder configuration and geometric features on FSW track properties, 6th International Symposium on Friction Stir Welding, Saint-Sauveur, Montreal, Canada, Paper No. 36, 2006
- ²⁴ G. Bussu, P. E. Irving, Fatigue Performance of Friction Stir Welded 2024-T3 Aluminium Joints, 1st International Symposium on Friction Stir Welding, TWI, United Kingdom 1999
- ²⁵ M. J. Peel, A. Steuwer, P. J. Withers, T. Dickerson, Q. Shi, H. Shercliff, Dissimilar friction stir welds in AA5083-AA6082, Part I: Process parameter effects on thermal history and weld properties, *Metallurgical and Materials Transactions A*, 37 (2006) 7, 2183–2193, doi:10.1007/BF02586138
- ²⁶ S. J. Vijay, N. Murugan, Influence of tool pin profile on the metallurgical and mechanical properties of friction stir welded Al–10 wt.% TiB₂ metal matrix composite, *Materials and Design*, 31 (2010) 7, 3585–3589, doi:10.1016/j.matdes.2010.01.018
- ²⁷ S. Brinckmann, A. Strombeck, C. Schilling, J. F. Santos, D. Lohwasser, M. Kocak, Mechanical and Toughness Properties of Robotic-FSW Repair Welds in 6061-T6 Aluminum Alloys, Proceedings of the Second International Conference on Friction Stir Welding, Gothenburg, Sweden, 2000
- ²⁸ C. J. Dawes, W. M. Thomas, Development of Improved Tool Designs for Friction Stir Welding of Aluminum, Proceedings of the First International Conference on Friction Stir Welding, Thousand Oaks, CA, 1999
- ²⁹ T. Pan, Friction stir spot welding (FSSW) – a literature review, SAE Technical Paper 2007-01-1702, 2007, doi:10.4271/2007-01-1702
- ³⁰ P. H. F. Oliveira, S. T. Amancio-Filho, J. F. Dos Santos, E. Hage, Preliminary study on the feasibility of friction spot welding in PMMA, *Materials Letters*, 64 (2010), 2098–2101, doi:10.1016/j.matlet.2010.06.050
- ³¹ E. P. Degarmo, J. T. Black, R. A. Kohser, *Materials and Processes in Manufacturing*, 9th ed., John Wiley and Sons, New York 2003, 60
- ³² S. Balos, L. Sidjanin, Effect of tunneling defects on the joint strength efficiency obtained with FSW, *Mater. Tehnol.*, 48 (2014) 4, 491–496
- ³³ I. Radisavljevic, A. Zivkovic, N. Radovic, Avoidance of tunnel type defects in FSW welded Al 5052-H32 plates, *Welding & Welded Structures*, 1 (2012) 1, 5–11

IMPROVEMENT OF SELECTIVE COPPER EXTRACTION FROM A HEAT-TREATED CHALCOPYRITE CONCENTRATE WITH ATMOSPHERIC SULPHURIC-ACID LEACHING

IZBOLJŠANJE SELEKTIVNE EKSTRAKCIJE BAKRA IZ TOPLOTNO OBDELANEGA KONCENTRATA HALKOPIRITA Z LUŽENJEM Z ŽVEPLENO KISLINO NA ZRAKU

Elif Uzun¹, Mustafa Zengin², İsmail Atılgan¹

¹Karabuk University, Department of Metallurgy and Material Science Engineering, 78050 Karabuk, Turkey

²Kalimakina Company, Department of Mining, 16059 Bursa, Turkey
elifuzun@karabuk.edu.tr

Prejem rokopisa – received: 2015-05-04; sprejem za objavo – accepted for publication: 2015-05-13

doi:10.17222/mit.2015.091

The present work focuses on the extraction of Cu, suitable for production, directly from a leach solution of a chalcopyrite concentrate as an alternative to the conventional smelting and refining method. Firstly, the main aspects of the kinetics of chalcopyrite leaching in a sulphuric-acid solution and transformation reactions of chalcopyrite at high temperatures were briefly reviewed. Secondly, atmospheric-acid leaching experiments were performed as a function of the acid content and temperature under agitation. Direct leaching experiments resulted in very low and scattered Cu recoveries, hence revealing a sulphide passivation layer on the chalcopyrite. In order to get rid of this layer, the sulphides in the chalcopyrite were transformed into sulphates with heat treatment at 500 °C prior to the leaching process, in which a high dissolution of species was obtained. Finally, the leaching of the pre-heated concentrate resulted in a 99.82 % Cu extraction. Consequently, optimized process parameters were proposed by comparing the Cu extraction and the increased purity of the pregnant solution without Fe impurities.

Keywords: chalcopyrite concentrate, leaching, heat treatment, passivation layer, copper extraction, selectivity

Namen tega dela je ekstrakcija bakra (Cu), ki bi bila primerna za neposredno proizvodnjo iz lužine koncentrata halkopirita, kot alternative običajni metodi s taljenjem in rafinacijo. Najprej je bil opravljen pregled glavnih vidikov kinetike izluževanja halkopirita v raztopini solne kisline in reakcij pretvorbe halkopirita pri visokih temperaturah. Nato so bili izvedeni preizkusi izluževanja na zraku v kislini, v odvisnosti od vsebnosti kisline in temperature z mešanjem. Neposredni preizkusi izluževanja so pokazali zelo nizko in raztreseno pridobitev bakra, ker se je halkopirit prekril s sulfidnim pasivacijskim slojem. Da bi se tega sloja znebili, so bili sulfidi v halkopiritu pretvorjeni v sulfate, s toplotno obdelavo pri 500 °C pred postopkom izluževanja, pri katerem je bilo doseženo dobro raztapljanje vzorca. Končno je bilo doseženo 99,82 % izluževanje bakra (Cu) iz predogretega koncentrata. Posledično so bili predlagani optimalni parametri procesa s primerjavo ekstrakcije bakra (Cu) in povečane čistosti nosilne raztopine brez nečistoč železa (Fe).

Ključne besede: koncentrat halkopirita, izluževanje, toplotna obdelava, pasivacijska plast, ekstrakcija bakra, selektivnost

1 INTRODUCTION

Copper has been one of the most important metals for over five thousand years.¹ Production of copper was easy for high-grade copper ores, for which traditional batch-smelting techniques were used before their grades were degraded. Afterwards, beneficiation of lower-grade ores was realised with the flotation technique prior to the smelting process. However, the traditional smelting technique became costly as the ore grades further decreased. On the other hand, there is currently an imbalance between the copper supply and the world demand.² In dealing with this problem, nowadays researchers are working hard to decrease process costs.

Chalcopyrite (CuFeS₂) is one of the most abundant and widely spread copper-bearing minerals,³ accounting for approximately 70 % of the Earth's copper.⁴

In traditional smelting processes, the chalcopyrite concentrate of a desired grade is obtained with a multi-

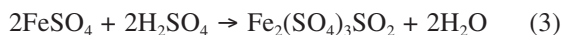
stage flotation of a sulphide ore, having fine grains of chalcopyrite dispersed in a matrix of various sulphide minerals and quartz.^{1,4} The chalcopyrite concentrate is then smelted in reverberatory flash furnaces.^{5,6} A major problem with smelting is the pollution of the environment, especially with sulphur dioxide.¹ At the same time, there is a decline in the copper-ore grades, often remarked upon as a future challenge in the production of copper for industry.⁷

Hydrometallurgical processes, an alternative to smelting, offer a high potential for treating chalcopyrite concentrate, apart from heap leaching, since they result in increased metal recoveries and reduced air pollution.⁴ In acidic media (sulfuric, hydrochloric and nitric acid), the concentrate can be leached under atmospheric or elevated pressures.⁸⁻¹⁴ Among them, the most promising one is sulfuric acid, since it can be readily produced at lower costs as the ore and, hence, the concentrate contain considerable amounts of sulphur.

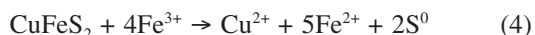
The kinetics of leaching in sulfuric-acid media have been extensively analysed as chalcopyrite can be dissolved in a strong sulfuric acid.¹⁵ The main reactions are as follows:



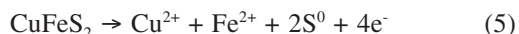
and



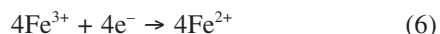
These reactions are very slow at atmospheric pressure because of the formation of a sulphide passivation layer on the chalcopyrite surface during the leaching process.¹⁶ There have been many efforts at the lab scale to overcome the difficulty of the concentrate being oxidized in the presence of several species (ferric ions, cupric ions, bacteria, pyrite oxygen, etc.).^{17–22} Additionally, some researches have been done to increase the leach rate by favouring anodic reaction between the passivation layer and pyrite using the following redox reactions (4, 5, 6):¹⁶



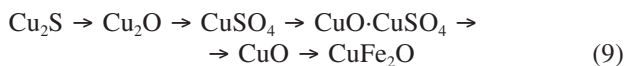
Anodic half-cell reaction: chalcopyrite oxidation



Cathodic half-cell reaction: reduction of ferric ions



Another process for increasing the leach rate can be roasting before leaching due to the fact that an oxidized and/or sulphatized concentrate has a higher dissolution rate because of the altered sulphide passivation layer.^{23–28} So, the pre-heating of chalcopyrite concentrate before the leaching in a different ambient would be an important step for the extraction of copper. As the passivation layer is composed of sulphur, it requires a sulphatization or oxidation process at elevated temperatures from 500–1000 K in an oxidizing ambient. Probable reactions during this treatment are extensively analysed in the literature.^{1,29} Among them, the most important ones for low temperatures are briefly given, in light of the relevant literature. L. Meunier et al.²⁹ studied the behaviour of chalcopyrite in a stream of air in a lower-temperature regime of 573–8230 K. The following reactions were mainly formed:



The first reaction (7) describes direct oxidation of chalcopyrite with released sulphur dioxide, occurring preferentially at temperatures higher than 900 K. At lower temperatures, sulphides are transformed into sulphates, as shown with reactions (8), (9) and (10). In the first step, Cu and Fe are separated from chalcopyrite in the form of sulphide and elemental sulphur. And then, these sulphides are oxidized as iron sulphide can be

gradually transformed to magnetite and then hematite, as given in (9); copper sulphide can be easily converted into copper sulphate at low temperatures, and sequentially into tenorite and copper iron oxide at higher temperatures, as given in (10). Here, the produced copper iron oxide is reported to have a higher intrinsic resistance to an acidic attack than tenorite.³⁰ As a result, chalcopyrite can be transformed into sulphates and oxides, which can be dissolved in sulphuric acid in line with the following reaction:



The main aim of this work is to improve the leaching rate of chalcopyrite concentrate in a sulphuric-acid solution under atmospheric pressure in order to have a high Cu recovery at a low process cost. So, only sulphuric-acid solution without any catalysis was used for the leaching experiments since it can be produced from the same concentrate. In the first stage, direct leaching experiments were performed to disclose the low dissolution rate of chalcopyrite. This rate resulted in a limited extraction of Cu due to the existence of a sulphide layer on chalcopyrite and was, therefore, too far from establishing an industrial process. In the second stage, the concentrate was pre-heated at 500 °C to increase the extraction of Cu by converting sulphides into sulphates in the concentrate. In this case, the dissolution rate was found to increase enormously and a Cu extraction higher than 99.8 % was obtained in a leaching time of 180 min. Finally, a compromise between Cu and Fe extractions was made to have the pregnant solution free of Fe as much as possible.

2 EXPERIMENTAL WORK

2.1 Materials, analysis and characterization of samples

The agitated acid leaching method was used at atmospheric pressure for the Cu extraction from the chalcopyrite concentrate obtained from a newly discovered copper mine in the Kastamonu-Hanönü region of Turkey. The concentrate was produced by means of beneficiation of the sulphide copper ore via the flotation technique in a pilot-scale plant. In the first step, mineralogical/elemental analyses of the concentrate were obtained and summarized in **Table 1**. We can briefly say that the concentrate consists of 65 % chalcopyrite, 30 % pyrite and 5 % sphalerite.

In this work, mineralogical analyses of the samples were investigated with an X-ray diffractometer (Rigaku Primus IV) and elemental analyses were carried out with an inductively coupled plasma-atomic adsorption spectrometer (ICP-OES, Perkin Elmer Optima 2100DV) and an atomic absorption spectrometer (AAS, Perkin Elmer Analyst 400). Additionally, a particle-distribution analysis was performed by means of an optical analysis (Nikon EPIHOT 200); thus, the sizes of the chalcopyrite particles were found to be in the range of 1–60 µm

and 80 % of the particles were below 45 μm . During the leaching operations, sulphuric acid with a purity of 96 % and a density of 1.84 g/cm^3 , obtained from the MERCK Company, and distilled water were used. The pre-heating and drying of the samples was done using a furnace (Protherm PL442T) and a stove (drying oven, MAS DT104), respectively. Finally, Cu and Fe extraction percentages were determined with the weighting method, using an ordinary lab scale with a 1 mg resolution.

Table 1: Mineralogical/elemental analysis of chalcopyrite concentrate
Tabela 1: Mineraloška/elementna analiza koncentrata halkopirita

Mineral/ Element	SiO ₂	S	Cu	Zn	Au (g/t)	Fe
%	1.12	36.44	21.10	21.26	0.39	33.34

2.2 Experimental methods

Leaching experiments were performed in an 800 mL pyrex reactor, using the batch method. The reactor was placed in a bath, whose temperature was controlled by a temperature controller via a thermocouple within an error of ± 1 °C. The agitation of the leach solution was continuously maintained by an external propeller, rotated at a constant speed of 350 min^{-1} throughout the processes. The complete system is shown in **Figure 1a**. Throughout this work, a constant volume of 600 cc of the leaching solution was used and its temperature was increased to the preselected value prior to the addition of 60 ± 0.5 g of the concentrate, which maintained a constant solid-content weight-to-volume ratio (w/v) of 1/10 in the solution. With the addition of the concentrate, the leaching process was commenced. After the process was finished, or a sample was taken out of the reactor, the residue was obtained using white-band filter paper. Upon determining its weight and carrying out elemental analyses, the amounts of Cu and Fe were determined and used for the calculation of the extraction percentage.

The process flowchart of this work is given in **Figures 1b** and **1c**, for direct and pre-heated leaching pro-

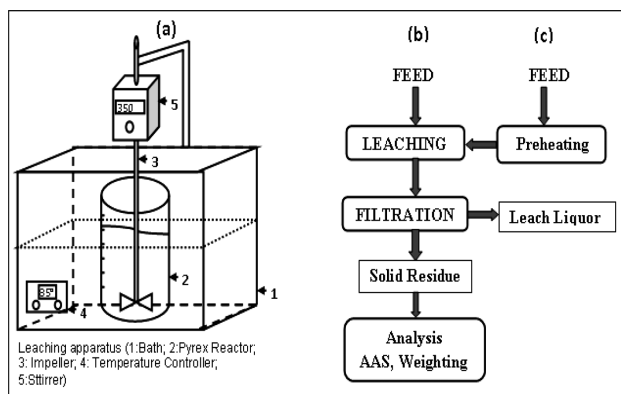


Figure 1: Experimental setup: a) flowchart of direct, b) pre-heated and c) leaching processes

Slika 1: Eksperimentalni sestav: a) potek neposrednega, b) toplotno predobdelanega in c) izluževalnega procesa

cesses, respectively. Initially, direct-leaching experiments without any pre-treatment of the concentrate were performed and very low extraction percentages were obtained. Secondly, the leaching process halted at the end of every 60-min period and the pregnant solution was replaced with a fresh solution in order to see the effect of acid consumption. Finally, the concentrate was pre-heated in air ambient at 773 K for 2 h in order to achieve an alteration of sulphide minerals.

3 RESULTS AND DISCUSSION

3.1 Direct atmospheric acid leaching

Experiments of direct leaching were performed with the parameters of temperature and sulphuric-acid concentration under atmospheric pressure for 360 min. The parameters and corresponding Cu % extraction results are reported in **Table 2**. Although the results of the Cu % extraction given in **Table 2** are somehow scattered, a net increase by the temperature is observed. Thus, the effect of the acid concentration seems to be lower than that of the temperature as the temperature increases. More importantly, the Cu % extraction stays below 17 %, which is in agreement with the results reported in the literature.³¹ This behaviour contradicts the one explained above, in which galvanic reactions are reported to dominate the process due to the addition of pyrite, for the redox potential to be between 400 and 500 mV.¹⁵ In our case, as the concentrate has 30 % pyrite, galvanic effects may also be expected for the reactions without any electric field. However, a probable built-in redox potential seems to stay below 400 mV, since pyrite stays undissolved. Otherwise, pyrite should be dissolved at the redox potential of 500 mV.^{32–33} Another evidence of this is the XRD analysis of the leach residue, given in **Figure 2**, where the pyrite and chalcopyrite peaks are clearly seen. This confirms that the dissolution processes of chalcopyrite and pyrite in sulphuric acid are very slow when there is no control of the redox potential of the leach solution.

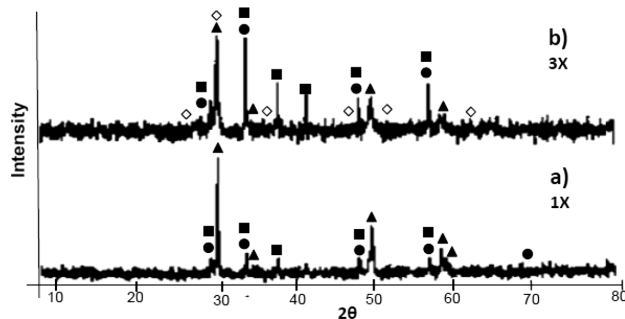


Figure 2: XRD spectra of: a) chalcopyrite concentrate and b) residue of direct leaching process with 105 g of acid content at 85 °C for 360 min (chalcopyrite: ▲; pyrite: ■; sphalerite: ●; jarosite: ◇)

Slika 2: Rentgenograma: a) koncentrat halkopirita in b) ostanek neposrednega 360 min izluževanja pri 85 °C in vsebnosti kisline 105 g (halkopirit: ▲; pirit: ■; sfalerit: ●; jarožit: ◇)

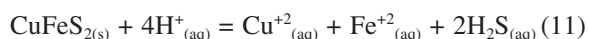
Table 2: Results of direct-leaching experiments lasting for 360 min
Tabela 2: Rezultati preizkusa 360 min neposrednega izluževanja

Temperature (C)	Acid concentration (g/L)	% Cu extraction
Room Temperature (25)	15	8.99
	45	15.83
	75	12.97
45	15	14.46
	45	12.10
	75	13.55
85	15	15.01
	45	16.42
	75	14.06

On the other hand, an increase in the acid concentration from 45 g/L to 75 g/L at room temperature and 85 °C seems to cause a decrease in Cu recoveries of 2.86 % and 2.36 %, respectively. This might be explained with the rapid formation of the sulphur layer, reported in the literature.⁶

3.2 Effect of acid consuming

The proposed reactions for the chalcopyrite leaching, given with Equations (1) to (3), are acid-consuming processes. The most proton-consuming (acid-consuming) reaction is given below:^{2,34}



It is hypothesized that it is governed by two steps: (i) a rapid dissolution to establish the equilibrium (11) between the soluble species at the chalcopyrite surface and the bulk solid and (ii) a rate-determining diffusion of the soluble species away from the surface.

In order to test the effect of the above reaction, the influence of the acid consumption on the copper extraction was investigated with a solid-liquid ratio of 1/20 g/L in a H₂SO₄ concentration of 105 g/L at 60 °C. Before the process was started, a fresh acidic solution was prepared and held at a process temperature of 60 °C. At the end of every 60-minute period of leaching, agitation was stopped for the solid species to precipitate in the leaching bath. Five minutes after the completed precipitation, 560 mL of the solid-free leach liquor was drained out of the reactor. At this step, a 1-mg residue was taken out of the reactor to analyse the copper content via AAS. Then, the process was continued with an addition of 560 ml of the fresh solution of 105 g/L H₂SO₄ concentration into the reactor at 60 °C. This procedure was repeated every 60 min throughout the process.

The effect of the acid consumption was tested by determining the Cu content of the residue for each sampling. The results are given in **Table 3**, where a smooth decrease in the copper grade of the leach residue from 17.70 % to 17.10 % is clearly seen at 60 min and 300 min., respectively. However, the dissolution rate of Cu decreases in time and may tend to stop at around 17 %. This blockage would be caused by the passivation layer grown on the surface of chalcopyrite minerals to

resist the leaching kinetics, as reported in the literature.^{15,35} It may be concluded that the acid consumption has little effect on direct leaching of the chalcopyrite concentration since the results are not scattered as in the previous case.

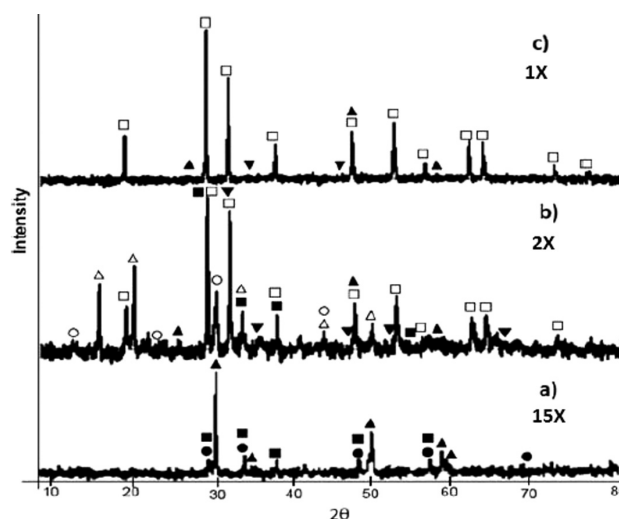
3.3 Atmospheric acid leaching of pre-heated chalcopyrite concentrate

The experiments above showed that the leaching of a chalcopyrite concentrate in a sulphuric-acid solution is hardly possible for industrial applications without an alteration of the passivation layer formed around chalcopyrite minerals.

Table 3: Copper concentration of the residue for each sampling when 560 mL of leach liquor was replaced with a new one**Tabela 3:** Vsebnost bakra v ostanku za vsako vzorčenje, ko je bilo 560 mL tekočine za izluženje zamenjane z novo

Leaching time (min)	Added fresh solution (mL)	Cu % of leach residue
60	560	17.70
120	560	17.40
180	560	17.23
240	560	17.10
300	560	17.10

Therefore, the concentrate was subjected to pre-heating at 773 K for 2 h in an atmospheric ambient before the leaching process. The change in the mineralogical property of the concentrate was determined with an XRD analysis whose spectra before and after the treatment are given in **Figure 3**. Dominant peaks of chalcopyrite and pyrite of the unprocessed concentrate are seen in **Figure**

**Figure 3:** XRD spectra of: a) chalcopyrite concentrate, b) heated concentrate and c) residue of leaching process with 150 g acid content at 85 °C for 360 min (chalcopyrite: ▲; pyrite: ■; sphalerite: ●; iron sulphate: ○; hematite: □; chalcocyanide: △; tenorite: ▼)**Slika 3:** Rentgenogrami: a) koncentrat halkopirita, b) toplotno obdelan in c) ostanka neposrednega 360 min izluževanja pri 85 °C, z vsebnostjo kisline 150 g (halkopirit: ▲; pirit: ■; sfalerit: ●; železov sulfat: ○; hematit: □; halkocianit: △; tenorit: ▼)

3a. But, in **Figure 3b**, the chalcopyrite peaks are disappeared whereas the pyrite peaks are still seen for the heated concentrate; here, hematite, iron sulphate and chalcocyanide peaks appear as dominant peaks.^{36,37} Moreover, a trace of tenorite is found to have little peaks in **Figure 3b**. It can be concluded from the results that the chalcopyrite in the concentrate is almost converted to CuSO_4 and CuO , which are soluble in a sulphide-acid solution, and to those compounds (hematite and iron sulphide) resistant to an acid solution.^{1,35}

The Cu and Fe extraction percentages in the leaching experiments of the pre-heated chalcopyrite concentrate were determined with the weighting method, via an elemental AAS analysis of the residue. The Cu extraction results for three different acid concentrations and temperatures as a function of the leach duration are given in **Figure 4**. The first thing to be mentioned is the fact that the leaching process seems to be nearly finished within 60 min as the lowest Cu extraction obtained is almost over 90 % for the lowest acid content and the lowest temperature. Additionally, the time dependence on the Cu extraction becomes almost flat at 85 °C, depicted in **Figure 4**, so that the reactions are nearly finished and independent of the acid concentration. Moreover, only hematite peaks are clearly observed and any trace of Cu bearing species is hardly found on the XRD graph given in **Figure 3c**, obtained for the residue of the experiment with the highest Cu recovery of 99.8 %. This enormous increase in comparison with the former experiments, obtained with the so-called direct leaching method, is

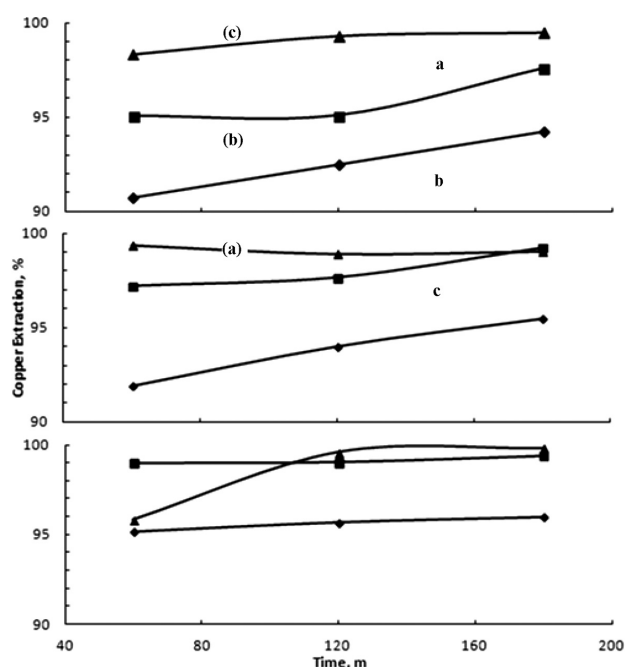


Figure 4: Copper extraction versus leaching time at: a) 90 g/L H_2SO_4 , b) 120 g/L H_2SO_4 , c) 150 g/L H_2SO_4 acid concentrations (■ 85 °C; ▲ 65 °C; ◆ 45 °C)

Slika 4: Ekstrakcija bakra v odvisnosti od časa izluževanja pri koncentraciji kisline: a) 90 g/L H_2SO_4 , b) 120 g/L H_2SO_4 , c) (■ 85 °C; ▲ 65 °C; ◆ 45 °C)

certainly caused by the alteration of the sulphides in the concentrate of the latter case.

The pre-heating of the concentrate in air ambient makes it soluble in sulphuric acid, i.e., the solubility of CuSO_4 is higher than for Cu_2S , CuS and CuFeS_2 . In addition, an increase in the solubility of hematite in a strong acid is also reported in³⁸.

Thus, a pregnant solution may also have FeSO_4 species making it hard to produce pure Cu directly from the solution (liquor).

Therefore, an optimization between purity and Cu recovery is necessary for the copper production, since Fe incorporated into the Cu structure especially deteriorates the electrical characteristics of copper. In other words, iron incorporation into copper should be as low as possible.

The optimization of the copper production was carried out by selecting the leaching process between the Cu and Fe recoveries, which were determined from the residue with the AAS analysis. The selectivity was calculated by subtracting Fe % from the Cu % recovery as a measure of the Cu purity in the solution, depicted in **Figure 5**, where Cu recoveries of over 97 % are reported for 65 °C and 85 °C. For example, the highest Cu extraction of 99.82 % was obtained from the process with the parameters of the temperature, 85 °C, acid concentration, 150 g/L, and duration, 180 min, as seen in **Figure 4c**; the highest Fe extraction of 37.31 % was also obtained, and hence, the selectivity of the leaching process was reduced to 62.51 %. In the figure, the selectivity goes through a peak with the acid concentration at 65 °C, but it decreases and seems to reach saturation at 85 °C. This behaviour is the evidence of an increased solubility of hematite at high acid concentrations and temperatures. As a result, the optimum leaching condition can be chosen as the peak on **Figure 5**, for the parameters of 65 °C and the 120 g/L acid concentration. Weaker acid concentrations and lower temperatures seemingly result in a low Cu extraction, in which some Cu is disposed in the residue.

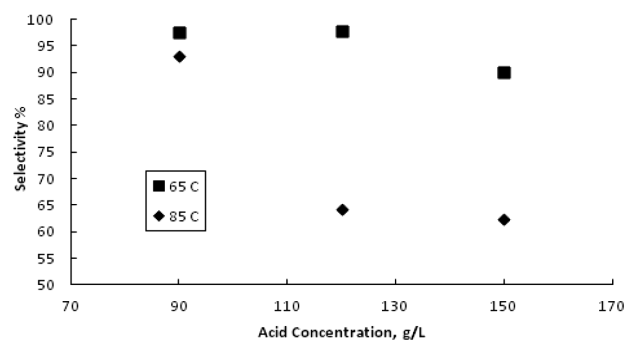


Figure 5: Selectivity of Cu in the solution with respect to the acid concentration for leaching processes of 180 min

Slika 5: Selektivnost Cu v raztopini, glede na koncentracijo kisline pri trajanju izluževalnega postopka 180 min

4 CONCLUSION

In the course of developing a hydrometallurgical process as an alternative to the conventional smelting and refining method, the production of Cu directly from the leach solution of the chalcopryrite concentrate would be a cornerstone. The most important step in this process is to have a Fe-free solution since Fe can be incorporated into the Cu structure during the subsequent electrowinning step. An observation of the selectivity between Cu and Fe can be taken as a measure of the purity of the produced copper. For achieving this aim, the main aspects of the kinetics of chalcopryrite leaching in the sulphuric acid solution is briefly reviewed in the light of the relevant literature. Additionally, transformation reactions of chalcopryrite at high temperatures are studied because direct leaching of chalcopryrite is a very slow process.

Direct-leaching experiments were performed at three different temperatures of (25, 45 and 85) °C, and acid concentrations of (15, 45 and 75) g/L. They resulted in very low Cu recoveries, below 15 %, due to the existence of a sulphide layer around the chalcopryrite species. In addition, a slight decrease in the acid concentration was observed at 85 °C, indicating acid consumption during the process.

Acid consumption was checked with a solid-liquid ratio of 1/20 g/L of a 105 g/L H₂SO₄ concentration at 60 °C. Its effect was measured with the change in the Cu concentration in the leach residue over time. The Cu concentration was found to decrease initially and have a saturation tendency, confirming that the leaching process was limited by the motion of the species through the passivation layer around chalcopryrite.

Finally, the pre-heating of the concentrate before the leaching at 500 °C for 120 min was found to have converted sulphides into sulphates. The subsequent leaching experiments were performed as a function of the acid concentration in g/L, the temperature and the time, using a solid-to-liquid ratio of 1/10 w/v at a stirring speed of 350 min⁻¹ under atmospheric pressure. As a result, a high dissolution rate was obtained because of the Cu recovery of over 90 % in the leaching process of 60 min. Thus, very high Cu recoveries of up to 99.82 % were achieved. Besides, over 36 % of Fe was found to have dissolved in the concentrate during the reactions because of the increased dissolution rate of hematite due to the increase in the temperature and acid concentration of the solution. Finally, the optimum selectivity of Cu and Fe was determined for the process with the acid concentration of 120 g/L, the temperature of 65 °C and the leach duration of 180 min. These can be taken as the proposed process parameters for the Cu production, optimized for the balance between the purity and Cu recovery.

Acknowledgment

Authors wish to thank ARGETEST Co. for experimental facilities. This work was supported by a grant from the Karabuk University BAP Project and, in part, by ASYA MADEN Co.

5 REFERENCES

- ¹ S. Prasad, B. D. Pandey, Alternative processes for treatment of chalcopryrite – A review, *Minerals Engineering*, 11 (1998) 8, 763–781, doi:10.1016/S0892-6875(98)00061-2
- ² H. R. Watling, Chalcopryrite hydrometallurgy at atmospheric pressure: 1. Review of acidic sulfate, sulfate-chloride and sulfate-nitrate process options, *Hydrometallurgy*, 140 (2013), 163–180, doi:10.1016/j.hydromet.2013.09.013
- ³ Y. N. Li, A. P. Kawashima, A. R. Chandra, A. Gerson, Review of the structure and fundamental mechanism and kinetics of the leaching of chalcopryrite, *Adv. Coll. Int. Sci.*, 197–198 (2013), 1–32, doi:10.1016/j.cis.2013.03.004
- ⁴ M. Loncnar, M. Zupancic, P. Bukovec, A. Toklic, The effect of water cooling on the leaching behavior of EAF slag from stainless steel production, *Mater. Tehnol.*, 42 (2009) 6, 315–321
- ⁵ A. K. Biswas, W. G. Davenport, *Extractive metallurgy of copper*, 2nd Edition, Pergamon Press, New York 1974, 64–69
- ⁶ Ö. Gök, G. C. Anderson, Dissolution of low-grade chalcopryrite in acidified nitride electrolyte, *Hydrometallurgy*, 134–135 (2013), 40–46, doi:10.1016/j.hydromet.2013.01.021
- ⁷ www.indexmundi.com/en/commodities/minerals/copper/copper-t20.html
- ⁸ P. B. Munoz, J. D. Miller, Wodsworth, Reaction mechanism for the acid ferric sulfate leaching of chalcopryrite, *Metall. Trans. Process Metall.*, 103 (1979), 149–158, doi:10.1007/BF02652458
- ⁹ R. Romero, A. Mazueios, I. Palencia, F. Cerranza, Copper recovery from chalcopryrite concentrates by BRISA process, *Hydrometallurgy*, 70 (2003), 205–215, doi:10.1016/S0304-386X(03)00081-1
- ¹⁰ D. Dreisinger, N. Abed, A fundamental study of the reductive leaching of chalcopryrite using metallic iron, part I: kinetic analysis, *Hydrometallurgy*, 66 (2002), 37, doi:10.1016/S0304-386X(02)00079-8
- ¹¹ F. Habashi, Action of nitric acid on chalcopryrite, *Soc. Min. Eng. AIME*, 254 (1973b), 224–228
- ¹² T. Hiroto, M. Kinoshito, Y. Awokira, H. Majima, The leaching of chalcopryrite with ferric chloride, *Metall. Trans. B – Process Metall.*, 17 (1973), 19–28, doi:10.1007/BF02670815
- ¹³ N. Hiroyoshi, H. Miki, T. Hirajina, M. Tsunekawa, A model for ferrous promoted chalcopryrite leaching, *Hydrometallurgy*, 57 (2000), 31–38, doi:10.1016/S0304-386X(00)00089-X
- ¹⁴ N. Hiroyoshi, H. Kitagawa, M. Tsunekawa, Effect of solution composition on the optimum redox potential for chalcopryrite leaching in sulphuric acid solutions, *Hydrometallurgy*, 91 (2008), 144–149, doi:10.1016/j.hydromet.2007.12.005
- ¹⁵ J. M. S. Koleini, V. Aghazadeh, A. Sandström, Acidic sulphate leaching of chalcopryrite concentrates in presence of pyrite, *Minerals Engineering*, 24 (2011), 381–386, doi:10.1016/j.mineng.2010.11.008
- ¹⁶ T. R. Ingraham, R. Kerby, Roasting in extractive metallurgy – a thermodynamic and kinetic review, *Can. Metall.*, 6 (1967) 2, 89–119, doi:10.1179/cm.1967.6.2.89
- ¹⁷ H. C. Linge, A study of chalcopryrite dissolution in acidic ferric nitrate by potentiometric titration, *Hydrometallurgy*, 2 (1976), 51–64, doi:10.1016/0304-386X(76)90013-X
- ¹⁸ E. M. Cordoba, J. A. Munoz, M. L. Blazquaz, F. Gonzalez, A. Ballester, Passivation of chalcopryrite during its chemical leaching with ferric ion at 68 °C, *Minerals Engineering*, 22 (2009), 229–235, doi:10.1016/j.mineng.2008.07.004

- ¹⁹ D. G. Dixon, D. D. Mayne, K. G. Boxter, Galvanox – a novel galvanically assisted atmospheric leaching technology for copper concentrate, *Can. Metall. Q.*, 47 (2008), 327–336, doi:10.1179/cm.2008.47.3.327
- ²⁰ J. E. Dutrizac, R. J. C. McDonald, T. R. Ingraham, The kinetics of dissolution of synthetic chalcopryrite in aqueous acidic ferric sulphate solutions, *AIME*, 245 (1969), 955–959
- ²¹ R. P. Hackl, D. B. Dreisinger, E. Peters, J. A. King, Passivation of chalcopryrite during oxidative leaching in sulfate media, *Hydrometallurgy*, 39 (1995), 25–48, doi:10.1016/0304-386X(95)00023-A
- ²² J. D. Miller, H. Q. Portilla, Silver catalysis in ferric sulfate leaching of chalcopryrite, In: J. Laskowski (Ed), XII International Min. Proc. Cont., Elsevier, Amsterdam 1979, 851–901
- ²³ G. Debernardi, J. C. Gentina, P. Albistur, G. Slanzi, Evaluation of processing options to avoid the passivation of chalcopryrite, *International Journal of Mineral Processing*, 125 (2013), 1–4, doi:10.1016/j.minpro.2013.09.001
- ²⁴ C. Li, J. Li, J. Lu, X. Lu, R. Wang, X. Zhao, Bioleaching of chalcopryrite by *Acidithiobacillus ferrooxidans*, *Minerals Engineering*, 53 (2013), 184–192, doi:10.1016/j.mineng.2013.08.008
- ²⁵ M. Nicol, H. Miki, L. Velasquez, The dissolution of chalcopryrite in chloride solutions: Part 3, Mechanisms, *Hydrometallurgy*, 103 (2010), 86–95, doi:10.1016/j.hydromet.2010.03.003
- ²⁶ K. Kaplun, N. Li, A. Kawashima, R. Gerson, Cu and Fe chalcopryrite leach activation energies and the effect of added Fe³⁺, *Geochimica et Cosmochimica Acta*, 75 (2011), 5865–5878, doi:10.1016/j.gca.2011.07.003
- ²⁷ D. Dreisinger, Copper leaching from primary sulfides: Options for biological and chemical extraction of copper, *Hydrometallurgy*, 83 (2006), 10–20, doi:10.1016/j.hydromet.2006.03.032
- ²⁸ E. Ghahremaninezhad, D. Asselin, G. Dixon, Electrochemical evaluation of the surface of chalcopryrite during dissolution in sulfuric acid solution, *Electrochimica Acta*, 55 (2010), 5041–5056, doi:10.1016/j.electacta.2010.03.052
- ²⁹ L. Meunier, H. Vanderpoorten, Roasting reactions of chalcopryrite, *ATB Met.*, 1 (1957), 31–35
- ³⁰ J. K. Gerlack, E. D. Gock, S. K. Ghosh, Activation and leaching of chalcopryrite concentrates with dilute sulfuric acid, *International Symposium on Hydrometallurgy*, Chicago, USA 1973, 403–416
- ³¹ A. F. Tshilombo, Mechanism and kinetics of chalcopryrite passivation and depassivation during ferric and microbial leaching, PhD thesis, UBC, 2004
- ³² L. M. Ou, R. A. He, Q. M. Feng, Influencing factors of pyrite leaching in germ free system, *J. Cent. South Univ. Technol.*, 14 (2007) 1, 28–31, doi:10.1007/s11771-007-0006-3
- ³³ M. J. Nicol, I. Lazaro, The role of non-oxidative processes in the leaching of chalcopryrite, In: P. A. Riveros, D. Dixon, D. B. Dreisinger, J. Menacho, (Eds), *Copper 2003-Cobre 2003*, vol. VI, Canadian Institute of Mining, Metallurgy and Petroleum, Montreal 2003, 367–381
- ³⁴ M. Gericke, Y. Govender, A. Pinches, Tank bioleaching of low-grade chalcopryrite concentrates using redox control, *Hydrometallurgy*, 104 (2010), 414–419, doi:10.1016/j.hydromet.2010.02.024
- ³⁵ N. Li, S. Lo, C. Hu, C. Hsieh, C. Chen, Stabilization and phase transformation of CuFeO₄ sintered from simulated copper-laden sludge, *Journal of Hazardous Materials*, 190 (2011), 597–603, doi:10.1016/j.jhazmat.2011.03.089
- ³⁶ M. Krogovic, I. Boskovic, M. Vukcevic, R. Zejak, M. Knezevic, R. Mitrovic, B. Zlaticanin, N. Jacimovic, The influence of the mineral content of clay from the white bauxite mine on the properties of the sintered product, *Mater. Tehnol.*, 45 (2011) 6, 609–612
- ³⁷ M. Vukcevic, D. Turovic, M. Krogovic, I. Boskovic, M. Ivanovic, R. Zejak, Utilization of geopolymerization for obtaining construction materials based on red mud, *Mater. Tehnol.*, 47 (2013) 1, 99–104
- ³⁸ J. MacCarthy, A. Nusrati, W. Skinner, J. Addai, Dissolution and Rhedogical Behaviour of Hematite and Quartz Particles in Aqueous Media at pH 1, *Chemical Engineering Journal*, 92 (2014), 2509–2522, doi:10.1016/j.cej.2009.05.010

HOMOGENIZATION OF AN Al-Mg ALLOY AND ALLIGATORING FAILURE: ALLOY DUCTILITY AND FRACTURE

HOMOGENIZACIJA Al-Mg ZLITINE IN KROKODILJENJE: DUKTILNOST ZLITINE IN PRELOM

Endre Romhanji, Tamara Radetić, Miljana Popović

University of Belgrade, Faculty of Technology and Metallurgy, Department of Metallurgical Engineering,
Karnegijeva 4, POB 35-03, 11 120 Belgrade, Serbia
endre@tmf.bg.ac.rs

Prejem rokopisa – received: 2015-06-01; sprejem za objavo – accepted for publication: 2015-06-12

doi:10.17222/mit.2015.110

High-strength Al-Mg alloys have a propensity toward hot fracture and failure by alligating during hot rolling. In this study the effect of homogenization conditions on the susceptibility of an Al-5.1Mg-0.7Mn alloy toward alligating was investigated. It was found that the plates homogenized in a temperature range of 460–520 °C were prone toward alligating, but once homogenized at 550 °C they were not prone toward it any longer. The characterization of the fracture showed a predominance of the intergranular ductile fracture, but the type of the constitutive particles filling the voids changed with the homogenization regime. Grain decohesion and grain-boundary embrittlement show that certain thermal treatments resulted in a microstructure that promoted slip localization.

Keywords: Al-Mg alloy, thermo-mechanical processing, hot working, ductility, embrittlement

Pri Al-Mg zlitinah z visoko trdnostjo se med vročim valjanjem pogosto pojavijo razpoke in krokodiljenje. V študiji je bil preiskovan vpliv pogojev pri homogenizaciji na občutljivost zlitine Al-5,1Mg-0,7Mn na krokodiljenje. Ugotovljeno je, da so plošče, ki so bile homogenizirane v temperaturnem območju 460-520 °C, občutljive na pojav krokodiljenja, medtem ko plošče homogenizirane pri 550 °C, niso bile občutljive na krokodiljenje. Pregled prelomov je pokazal, da prevladuje interkristalni žilav prelom, vendar pa se je z režimom homogenizacije spreminjala tudi vrsta delcev v jamicah. Dekohezija med zrni in krhkost po mejah zrn kažeta, da se določena toplotna obdelava odraža na mikrostrukturi, ki lokalizira drsenje.

Ključne besede: Al-Mg zlitina, termomehanska predelava, vroča predelava, duktilnost, krhkost

1 INTRODUCTION

One of the main concerns in the fabrication of high-strength Al-Mg alloy sheets is their proclivity toward hot fracture and formation of defects such as edge cracking, central bursts and alligating during hot rolling.^{1,2} The alligating defect is characterized by an opening of rolled slab ends due to a crack formation along the central horizontal plane of the slab. In addition to the inefficiencies associated with the material loss, the failure caused by it can introduce serious damage to the equipment.

It is considered that alligating arises due to an inhomogeneous deformation and a variation in the residual-stress states across the width of a rolled material.³ The modeling based on the upper-bound approach allowed the development of the criteria for its occurrence in terms of the roll-gap shape factor, $\Delta = h/l$ (h is the average sheet thickness of the rolling gap, l is the arc of contact).⁴ The prediction of a failure due to the alligating taking place at $\Delta > 1.35$ was verified by cold rolling an Al6061-T6 alloy. However, other reports show alligating taking place at Δ of 0.5–1.5.^{1,2} Some studies^{5,6} consider the development of a sharp notch at the concave front of a slab and the resulting triaxial state of the stress at the notch tip to be responsible for the

failure. Similarly, the presence of a complex state of the stress and the concave shape of the front end of a slab play important roles in the alligating during the cold rolling of spheroidized steel.⁷

However, the effects of other factors, such as homogenization conditions and the microstructures of the Al-Mg alloys, on the alligating are far less understood. This work reports about the effect of the homogenization conditions on the occurrence of the alligating in an Al-5.1Mg-0.7Mn alloy during hot-rolling experiments.

2 EXPERIMENTAL WORK

The material used in this study was an Al-Mg alloy with higher Mg and Zn contents than a standard AA 5083 alloy; its composition was within the lower limits of an AA 5059 alloy (**Table 1**). The alloy, supplied by Impol-Seval Rolling Mill–Serbia, was industrially DC cast.

Prior to hot rolling, plates 25 mm × 30 mm × 55 mm were homogenized, following one of the regimes given in **Figure 1**. Hot rolling was performed at a two-high rolling mill (a roll diameter of 200 mm). The applied schedule of hot-rolling passes (n_i , $i = 1 - 8$) was designed by gradually increasing the reduction from 1.5 % in the

Table 1: Chemical compositions of the studied alloy and standard AA 5083 and AA 5059 alloys, in mass fractions (w%)

Tabela 1: Kemijska sestava uporabljene zlitine in zlitini AA 5083 in AA 5059 po standardu, v masnih deležih (w%)

	Mg	Mn	Cu	Fe	Si	Zn	Cr	Ti	Sr	Zr
Alloy	5.13	.72	.013	.34	.11	.51	.008	.025	.003	-
AA5083	4.0-4.9	0.4-1.0	<.1	<.4	<.4	<.25	0.05-0.25	<.15	<.005	<0.05
AA5059	5.0-6.0	0.6-1.2	<.25	<.5	<.45	.4-.9	<0.25	<.2	<0.05	0.05-0.25

Table 2: Hot-rolling outcome and characteristic parameters after the homogenization treatments

Tabela 2: Stanje po vročem valjanju in značilni parametri po homogenizaciji

Homogenization procedure	Outcome	h_0 (mm)	h_f (mm)	Total reduction (%)	"Alligatoring" pass	
					Partial reduction (%)	h/l
Regime I 460 °C/ 16 h → HR	Alligatoring	20.4	14.6	28.4	18	0.90
	Alligatoring	20.4	13.7	32.8	19	0.86
Regime II 430 °C/12 h + 520 °C/16h Cooling → 500 °C/1 h → HR	Alligatoring	25	13.5	46.0	20	0.82
	Alligatoring	25	14.0	44.0	18	0.89
	Success	25	6.5	74.0	/	/
	Alligatoring	21	11.8	43.0	20	0.76
Regime III 430 °C/12 h + 550 °C/16 h Cooling → 500 °C/1 h → HR	Success	25	6.0	76.0	/	/
	Success	25	6.1	75.6	/	/
	Success	25	6.0	76.0	/	/
	Success	21	7.0	67.6	/	/

first pass to 35 % at the end (**Figure 1**). The temperature of the plates at the exit of each pass was in a 380–400 °C range. After each rolling pass, the plate was reheated for 10 min.

SEM characterization of the fractured surfaces was conducted with JEOL JSM-6610LV at 20 kV, equipped with an EDS detector and Tescan Mira 3XMU at 10 kV.

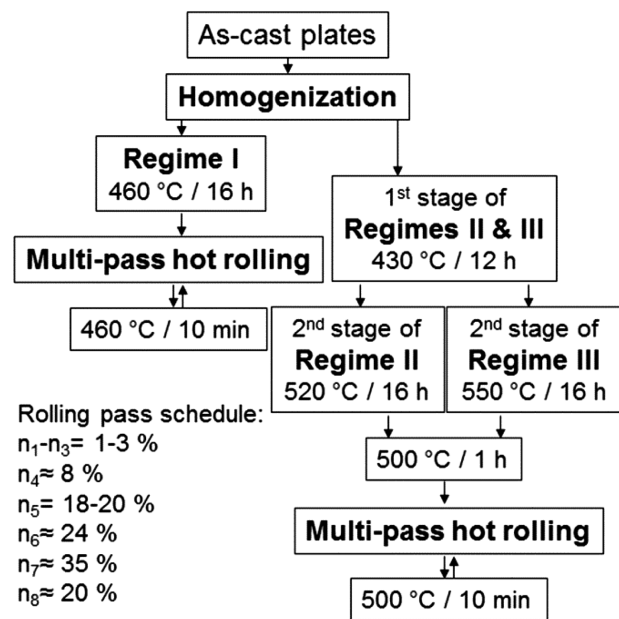


Figure 1: Schematic representation of the thermo-mechanical treatment: homogenization and hot-rolling schedules

Slika 1: Shematski prikaz termo-mehanske obdelave: potek homogenizacije in vročega valjanja

3 RESULTS

3.1 Hot rolling

The effects of different homogenization treatments on the hot-rolling outcome are shown in **Table 2**. The hot rolling of the plates homogenized according to Regimes I and II failed due to the alligatoring. The critical passes corresponded to the partial reductions of ≈ 20 %. The alligator crack (**Figure 2a**) opened at the front side in all the cases.

The total reduction for the plates homogenized following Regime I was ≈ 30 %, while Δ was 0.85–0.90 at the failure pass.

The hot rolling of three out of four plates homogenized according to Regime II failed. In the passes leading to the alligatoring, Δ was in a range of 0.76–0.89. However, the plates homogenized according to Regime II showed higher hot ductility than in the case of Regime I since the total reduction at failure was ≈ 45 %.

The plates homogenized at the highest temperature (Regime III) did not alligator and all of them were suc-

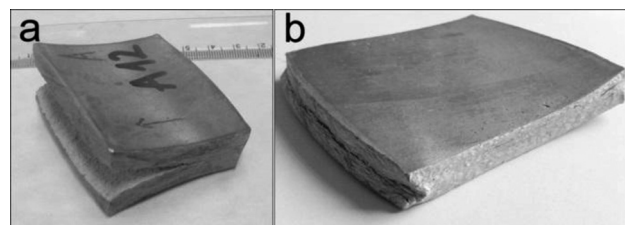


Figure 2: a) Image of an alligatoring defect after hot rolling with the total reduction of 44 %, b) concave front profile of the plate that did not alligator (total reduction of 74 %)

Slika 2: a) Posnetek napake krokodiljenja po vročem valjanju s celotno redukcijo 44 %, b) konkavni sprednji del plošče, kjer ni bilo krokodiljenja (celotna redukcija 74 %)

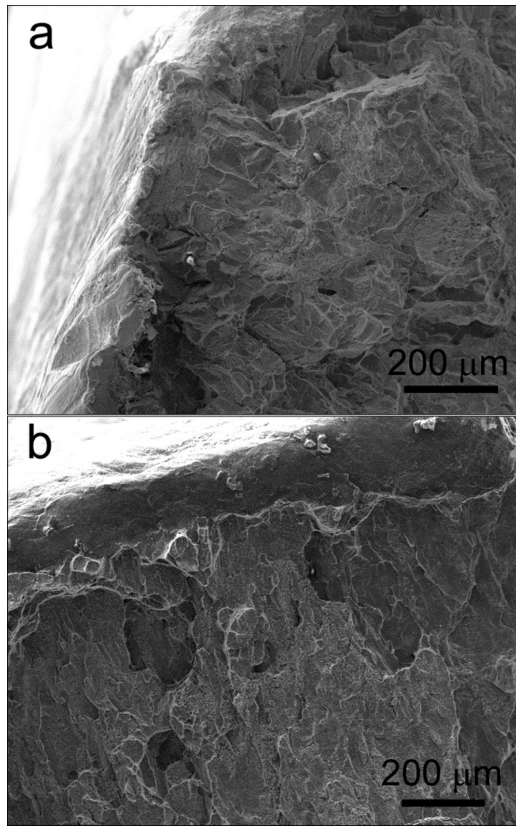


Figure 3: Secondary-electron SEM micrographs of the front edge of a plate: a) Regime I, b) Regime II

Slika 3: SEM-posnetek prednjega roba plošče s sekundarnimi elektroni: a) Režim I, b) Režim II

cessfully hot rolled with a total reduction of up to $\approx 70\text{--}75\%$.

The fronts of the plates developed a concave profile during the hot rolling, with the formation of a groove at the centerline as the deformation progressed (**Figure 2b**). The shape of the side profile varied with the position along a slab. Some lateral spreading was observed at high total reductions.

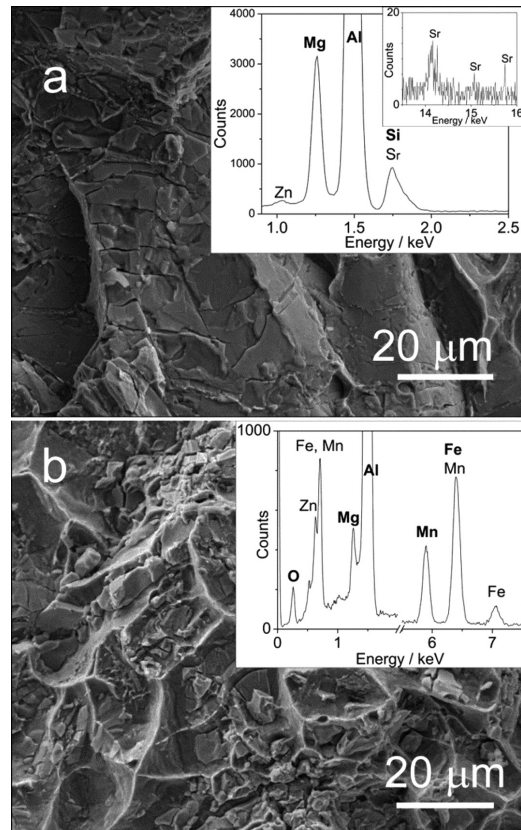


Figure 4: Secondary-electron SEM micrographs of ductile intergranular fractures and EDS of the broken constitutive particles: a) Regime I, b) Regime II

Slika 4: SEM-posnetek s sekundarnimi elektroni duktilnega, interkristalnega preloma in EDS-analiza polomljenega delca: a) Režim I, b) Režim II

3.2 Fractography

A macroscopic examination of the fracture surfaces revealed two distinct regions, similarly to the report on spheroidized steel.⁷ The narrow region at the front edge of a fractured plate, 1–2 mm in width, was characterized

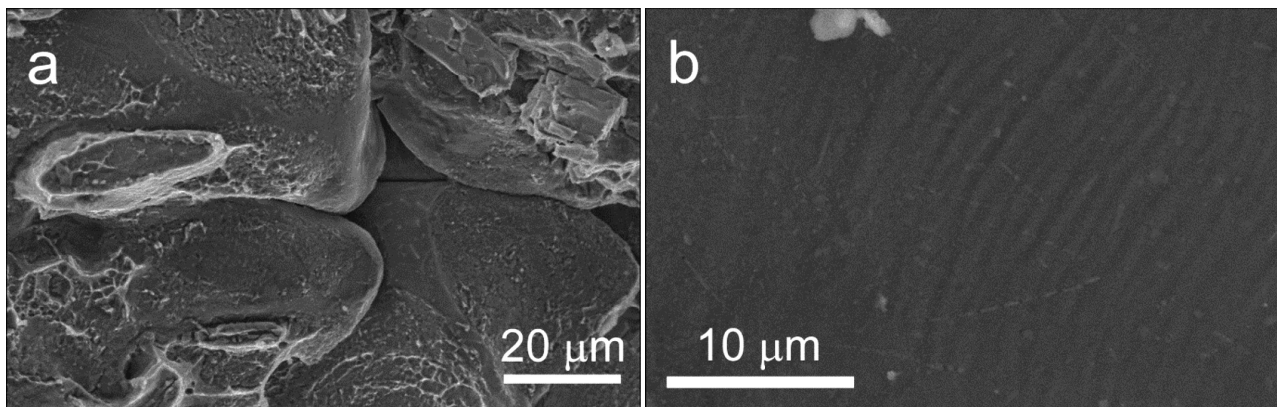


Figure 5: Secondary-electron SEM micrographs of a brittle intergranular fracture (Regime I): a) smooth grain surfaces, b) slip-line traces and shearing of dispersoids

Slika 5: SEM-posnetek s sekundarnimi elektroni krhkega, interkristalnega preloma (Režim I) : a) gladka površina zrn, b) sledovi drsnih linij in striženje disperzoidov

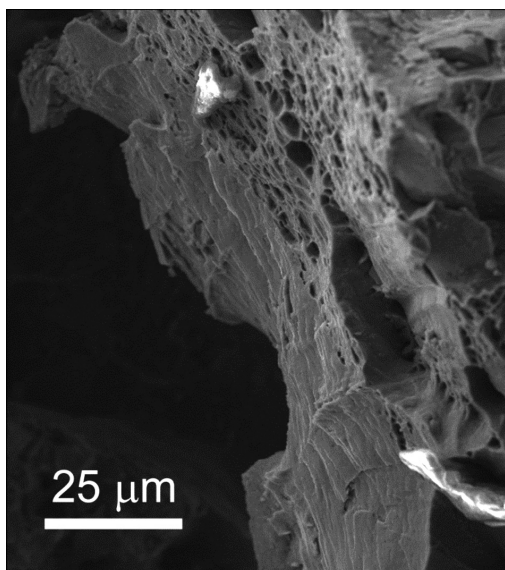


Figure 6: Secondary-electron SEM micrograph of a cleavage (Regime I)
Slika 6: SEM-posnetek s sekundarnimi elektroni cepilnega loma (Režim I)

with a number of ridges consisting of high elevations and depressions. It was more prominent on the plates homogenized according to Regime II than Regime I. The topography of the rest of the fracture was more leveled. A dull surface typical of a ductile fracture was sprinkled with tiny sparkles indicating the presence of cleavage facets.

A SEM characterization of the plates homogenized according to Regime I showed that the fractured surface extended to the very end of the front edge (**Figure 3a**). A hem, with markings from the front side of the plate, was observed only at a few points.

On the plates homogenized according to Regime II, the hem with the front-side marks extended over the entire front edge, being 100–200 μm wide (**Figure 3b**). Adjacent to it was a region of shallow, elongated dimples that is characteristic for a shear fracture and void sheeting. Away from the edge, the predominant fracture mode was ductile intergranular fracture for all the alligatored plates (**Figure 4**).

An intergranular fracture proceeded due to a coalescence of voids created by a break-up of constitutive particles. However, there was a distinction between the broken constituent particles filling the voids, depending on the homogenization regime. Most of the particles of the plates homogenized according to Regime I had a thin plate-like morphology (**Figure 4a**). The EDS analysis showed that those particles were a Mg-Si-Sr rich phase. On the plates homogenized according to Regime II, a mixture of a plate like Mg-Si-Sr and more irregularly shaped $Al_6(Fe,Mn)$ was observed (**Figure 4b**).

Another difference was that a grain decohesion and a brittle intergranular fracture were observed only on the plates homogenized according to Regime I. Smooth grain surfaces of the brittle intergranular fracture par-

tially covered with fine dimples nucleated at grain-boundary dispersoids are shown in **Figure 5**.

A cleavage, with a typical river pattern (**Figure 6**), was observed on the plates homogenized according to both Regime I and II.

4 DISCUSSION

A failure by alligatoring is frequently ascribed to a deformation inhomogeneity across the plate cross-section due to a low reduction and an induced distribution of stresses.^{1–4} The results of this study, i.e., the alligatoring occurring at high reductions of 20 % and $\Delta = 0.75–0.9$, show that it may not be critical. Rather, the state of the stress leading to the alligatoring might be related to the metal flow in the roll gap. The lateral spread along the centerline was greater than in the surface layer due to the friction at the roll surfaces leading to a groove formation at the front.⁵ The groove could have acted as a notch and provided a stress concentration for the crack initiation.^{5,6} However, the results show that the grooving is unlikely the sole cause of the alligatoring. On the plates homogenized according to Regime II, the fracture by the void sheeting adjacent to the groove (**Figure 3a**) is a sign of shear stresses and a low stress triaxiality.⁸

Furthermore, the deepest grooves were observed on the plates that did not fail during the hot rolling. On the other hand, on the least ductile plates, homogenized according to Regime I, incipient grooving was observed only at a few points along the front profile. Since deformation conditions were identical for all the plates, but the material response varied with the homogenization treatment (**Table 2**), it is clear that different ductilities and predispositions toward the alligatoring were related to the microstructures developed during the thermal treatment. Fracture features such as the change in the type of the constitutive particles filling the voids point in that direction. The observed grain decohesion and grain-boundary embrittlement can be related to the slip localization and dispersoid distribution that will be described in Part II of this study.

5 CONCLUSION

It was demonstrated that ductility and predisposition toward alligatoring during hot rolling depend on the homogenization treatment of the Al-5.1Mg-0.7Mn alloy. An increase in the homogenization temperature improved the ductility and the plates homogenized at 550 °C (Regime III) did not alligator. Ductile intergranular fracture is the dominant fracture mechanism, but on the plates homogenized at the lowest temperature (Regime I), grain decohesion and brittle intergranular fracture were also observed. Changes in the fracture mode and the type of the constitutive particles broken with the homogenization treatment pointed out that the propensity

toward alligatoring is controlled by microstructural changes.

Acknowledgment

This research was supported by the Ministry of Education, Science and Technological Development, Republic of Serbia, and Impol-Seval Aluminium Rolling Mill, Sevojno, under contract grant TR 34018.

6 REFERENCES

- ¹ M. M. Al-Mousawi, A. M. Daragheh, S. K. Ghosh, D. K. Harrison, Some physical defects in metal forming processes and creation of a data base, *Journal of Materials Processing Technology*, 32 (1992) 1–2, 461–70, doi:10.1016/0924-0136(92)90202-4
- ² J. G. Lenard, Workability and Process Design in Rolling, In: G. Dieter, H. A. Kuhn, S. L. Semiatin (eds.), *Handbook of Workability and Process Design*, ASM International, Materials Park, Ohio, USA 2003, 258–277
- ³ J. A. Schey, Fracture in rolling processes, *Journal of Applied Metalworking*, 1 (1980) 2, 48–59, doi:10.1007/BF02833609
- ⁴ S. Turczyn, The effect of the roll-gap shape factor on internal defects in rolling, *Journal of Materials Processing Technology*, 60 (1996) 1–4, 275–282, doi:10.1016/0924-0136(96)02342-4
- ⁵ A. J. Meadows, W. J. Pearson, Discussion: Edge Cracking, Lamination, and Surface Cracking in Hot and Cold Rolling, *Journal of the Institute of Metals*, 92 (1964) 8, 254–255
- ⁶ R. Couch, R. Becker, M. Rhee, M. Lee, Development of a rolling process design tool for use in improving hot roll slab recovery, Report UCRL-TR-206843 (2004), Lawrence Livermore National Laboratory, USA 2004; available at <https://e-reports-ext.llnl.gov/pdf/312127.pdf>
- ⁷ L. Xu, G. S. Daehn, Alligatoring and damage in the cold rolling of spheroidized steels, *Metallurgical and Materials Transactions A*, 25 (1994) 3, 589–598, doi:10.1007/BF02651600
- ⁸ F. Bron, J. Besson, A. Pineau, Ductile rupture in thin sheets of two grades of 2024 aluminium alloy, *Materials Science and Engineering*, 380A (2004) 1–2, 356–364, doi:10.1016/j.msea.2004.04.008

ASSESSMENT OF TUBULAR LIGHT GUIDES WITH RESPECT TO BUILDING PHYSICS

OCENA CEVASTIH VODNIKOV SVETLOBE GLEDE NA GRADBENO FIZIKO

František Vajkay, David Bečkovský, Vladimír Tichomirov

Brno University of Technology, Faculty of Civil Engineering, Institute of Building Structures, Veveří 95, 602 00 Brno, Czech Republic
vajkay.f@fce.vutbr.cz

Prejem rokopisa – received: 2013-10-01; sprejem za objavo – accepted for publication: 2015-06-08

doi:10.17222/mit.2013.204

Architecture and the building industry consist of several minor fields, which come together when a building is designed and erected. One of them is the field of building physics. It primarily focuses on the evaluation of constructions, structures and spaces with respect to thermo-technical conditions, daylighting and many more. It is believed that among the above-mentioned sub-fields of building physics, daylighting is the most important because it influences the health of every human being. Daylighting enables people to see the colours and objects surrounding them. Therefore, buildings have to be equipped with a kind of daylighting system. In the past, spaces located either in the centres of buildings or in the underground areas were illuminated solely on the basis of luminaries. Nowadays, indirect daylighting systems like optical fibres or tubular light guides may also be utilized.

In Central Europe, the application of tubular light guides in buildings increases every year. The manufacturers say that this is an important and maintenance-free system. It is a system that brings light into any building, thus helping to save money. On the other hand, the designing of tubular light guides is complicated as it has to deal with daylighting, thermo-technical aspects and moisture. A huge amount of light guides is problematic due to the condensation of water inside the pipes, which is a side effect of a non-air-tight solution, or just due to an incorrect thermal analysis. The paper focuses on different aspects of designing light-guiding systems through computer simulations.

Keywords: tubular light guide, illuminance, luminance, building physics, computer simulations

Arhitektura in gradbeništvo sestojita iz več glavnih področij, ki se združijo, ko je objekt načrtovan in zgrajen. Eno od takih področij je gradbena fizika. To je področje, ki je usmerjeno predvsem na oceno konstrukcije, zgradbe in prostora glede na termo-tehnične pogoje, dnevno svetlobo in podobno. Med omenjenimi podpodročji gradbene fizike je najbolj pomembna dnevna svetloba, ker vpliva na zdravje vsakega človeka. Dnevna svetloba omogoča, da vidimo barve in predmete okrog sebe. Zato morajo biti zgradbe opremljene s sistemom za dnevno svetlobo. Včasih so bili prostori, locirani v sredini zgradbe ali v podzemlju, osvetljeni samo na osnovi svetlobnih teles. Danes pa lahko uporabljamo tudi posredne sisteme za dnevno svetlobo z optičnimi vlakni ali s cevastimi vodniki svetlobe.

V centralni Evropi uporaba cevastih vodnikov svetlobe v zgradbah iz leta v leto narašča. Proizvajalci trdijo, da je to pomemben sistem, ki ne potrebuje vzdrževanja. Sistem omogoča svetlobo v zgradbi, kar pomaga pri zmanjšanju stroškov. Vendar pa je načrtovanje cevastih vodnikov svetlobe zapleteno, glede na to ali gre za dnevno svetlobo ali termo-tehnično načrtovanje in vlago. Velik delež vodnikov svetlobe ima težave zaradi kondenzirane vlage znotraj cevi, kar je stranski učinek nevodotesne izvedbe ali pač samo nepravilne termične analize. Članek je usmerjen na različne vidike računalniške simulacije pri načrtovanju sistema za prevajanje svetlobe.

Ključne besede: cevast vodnik svetlobe, osvetljenost, svetilnost, gradbena fizika, računalniška simulacija

1 INTRODUCTION

Lighting design of indoor spaces is a rarely discussed discipline of the building industry. More often than not, it is in the shadows of the fields related to the thermo-technical processes organised in a building,¹ although the light makes it possible for humans to see their surroundings, since the visible part of optical radiation (i.e., the visible light) causes certain photochemical reactions in the eye balls. The information perceived by the eye balls is then processed in the brain.² When more light enters the eyes through the corneas we can distinguish more details of the surroundings. This property should be reflected on the daylighting design of indoor spaces as well. Human beings spend about 80 % of their lives indoors and it is necessary to think about

how natural light can enter a building. Usually architects use one of the available direct daylighting systems, like:

- windows and their variants,
- roof lights.

However, as we need to make buildings more compact because of land prices or we use the underground areas, architects are required to use indirect daylighting systems as well.

Representatives of these are optic-fibre systems (widely applied in the USA, but not in the EU) and tubular light guides.

Tubular light guides are a type of indirect daylighting system. Their history can be traced back to ancient Egypt, when the predecessors of light guides were used to illuminate sanctuaries.³ Only after their reinvention in the 19th century and their further development that

started at the end of the 20th century, they become what they are today.⁴ Each light guide consists of at least three elements:

- the copula (the external cover made from a material with high light transmission),
- the tube (the pipe with a special surface finish that has a high light-reflectance value),
- the diffuser (the internal finish of light guides distributing the light).

Tubular light guides can differ in every aspect. They can have different lengths and diameters of the tube, and also different copulas and diffusers. However, once the elements ordered are assembled on a construction site and later built into the building, some issues might arise because of the unexpected physical properties of the building. One of these may be associated with the daylighting of the building since light guides are difficult to design. The other difficulty might be a result of the thermal design, as water vapour often condenses inside the pipe.

The paper is focused on the available computer tools, which can be used to monitor the resulting properties of the light guides within the selected test case.

2 EXPERIMENTAL SECTION

Indoor spaces in the centres of buildings or underground areas can be illuminated with indirect daylighting systems using natural light, or with luminaries. Tubular light guides already proved to be efficient in this respect, at least during daytime. The first half of this section is focused on this particular topic.

The second half of the experimental section deals with the thermo-technical simulations of the chosen tubular-light-guide system, since it passes through the envelope, especially through the roof.

The dimensions of the room assessed were 7 m × 2.5 m and the room represented a corridor. The tubular light guides were located along the longitudinal axis of the space. The plan of the room including the light-guide positions is shown in **Figure 1**.

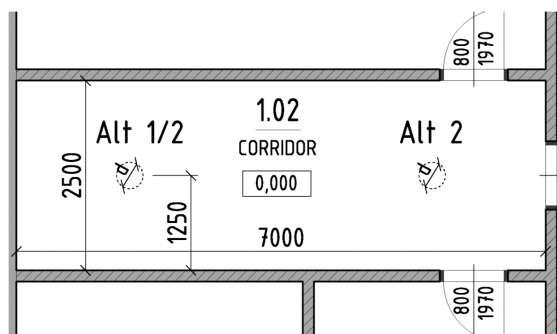


Figure 1: Plan of the corridor including the positions of designed tubular light guides

Slika 1: Načrt hodnika, ki vključuje položaj načrtovanih cevstih vodnikov svetlobe

2.1 Daylighting design

One of the most useful computer simulation tools is HOLIGILM.⁵ It was developed to assess the amount of the visible light transmitted by straight tubular light guides. It is simple to use, fast and it provides a graphical output. Nonetheless, it cannot evaluate the internally reflected component of daylight in the same way as Radiance or Velux Daylight Visualizer.

Although all 15 sky-type definitions described by CIE⁶ are implemented in HOLIGILM, considering the local codes of European countries including the Czech Republic, the simulations were done only for the CIE overcast-sky conditions.⁷

The properties of the tubular light guides input to HOLIGILM were as follows:

- transparency of the copula: $t_c = 95 \%$,
- surface reflectance of the pipe (Spectralight Infinity compound): $r_p = 99.7 \%$,
- transparency of the thermally insulating element dividing the pipe into two segments: $t_{te} = 95 \%$,
- transparency of the diffuser (to be on the safe side of the calculations): $t_d = 75 \%$.

Seeing that HOLIGILM does not have any input fields for additional light-transmitting parts like the thermally insulating element, the total light transmittance of the diffuser had to include that value as well; hence, this value was set to 71 % instead of 75 %.

The total length l of the tubular light-guide pipe is 4.5 m and its diameter d is 0.530 mm.

Since the space is used as a corridor two distances (l_1) were set between the diffuser and the working plane:

- 2.15 m corresponding to the distance to the base location of the working plane at 0.85 m above the floor since in each room there may be some furniture;
- 3.0 m at the floor level so that the corridor is suitable for movements.

2.2 Thermo-technical design

Thermo-technical calculations were carried out in Agros2D. Agros2D is a free multi-platform alternative to ANSYS Workbench and COMSOL Multiphysics.

The aims were:

- to find out whether water vapour can condense within the pipe,
- to determine the point-wise thermal conductivity of the structure.⁸

The thermal-conductivity coefficients of the structural elements were set as follows:

- acryl: $l_a = 0.2 \text{ W m}^{-2} \text{ K}$,
- the thermal insulation of mineral wool around the pipe: $l_{i1} = 0.040 \text{ W m}^{-2} \text{ K}$,
- the thermal insulation of mineral wool as part of the roof: $l_{i2} = 0.040 \text{ W m}^{-2} \text{ K}$,
- the pipe: $l_p = 0.220 \text{ W m}^{-2} \text{ K}$,
- steel: $l_s = 50.0 \text{ W m}^{-2} \text{ K}$,
- the lambda value of air depends on its volume.

3 RESULTS

3.1 Daylighting design

It was assumed that the luminous efficacy of a tubular light guide of this length under the CIE Overcast Sky conditions would prove to be insufficient to illuminate the working plane at 0.85 m above the floor level. The resulting illuminance levels were rather low. The values varied from 0 lx to 100 lx (equivalent to 0 % and 1 % of daylight factor, **Figure 2**). With an additional light guide, it was possible to shift these values. For example, the minimum value grew by 40 lx (**Figure 3**).

Seeing that the design only included the sky component of the daylight factor and that the light-transmittance value of the light guide was reduced by the thermally insulating element, it can be concluded that the values were extraordinarily high. The peaks beneath the light guides, at a distance of 2.15 m, increased by 10 lx, from 100 lx to 110 lx.

Since illuminance decreases with the increasing distance, when considering the results described previously, the evaluation at the floor level was done under the assumption that two tubular light guides should be used to illuminate the designed space.

As anticipated, the resulting light levels dropped. The peak values beneath the light guides receded to 58 lx (**Figure 4**).

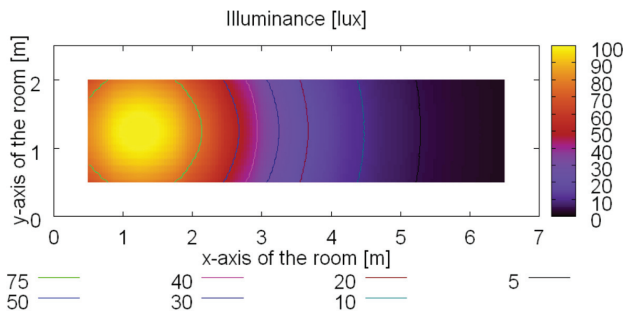


Figure 2: Illuminance-contour plot at 2.15 m beneath the diffuser for one tubular light guide

Slika 2: Diagram obrisa osvetljenosti pri 2,15 m pod difuzorjem pri enem cevastem vodniku svetlobe

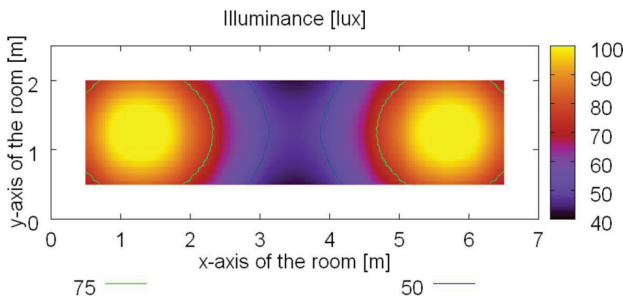


Figure 3: Illuminance-contour plot at 2.15 m beneath the diffuser for two tubular light guides

Slika 3: Diagram obrisa osvetljenosti pri 2,15 m pod difuzorjem pri dveh cevastih vodnikih svetlobe

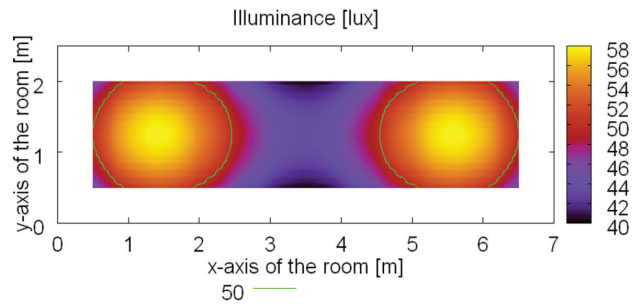


Figure 4: Illuminance-contour plot at 3.0 m beneath the diffuser for two tubular light guides

Slika 4: Diagram obrisa osvetljenosti pri 3 m pod difuzorjem pri dveh cevastih vodnikih svetlobe

3.2 Thermo-technical simulations

The results presented on **Figure 5** were obtained with the simulations provided under common boundary conditions. External and indoor air temperatures were set to $-15\text{ }^{\circ}\text{C}$ and $20\text{ }^{\circ}\text{C}$ and the corresponding relative air humidity inputs were 84 % for the exterior and 50 % for the interior.

As can be seen on **Figure 5**, the contact surface temperature on the interface of the light guide and the roof varies between $16\text{ }^{\circ}\text{C}$ and $20\text{ }^{\circ}\text{C}$.

Other results can be connected to the overall thermal conductivity of the light pipe, which is evaluated just like in the case of windows.

The simulations pointed out that the U point-wise thermal conductivity of the structure is 0.37 W K^{-1} . This value is smaller than the one required by the Czech legislation; therefore, the light guide meets the necessary conditions.

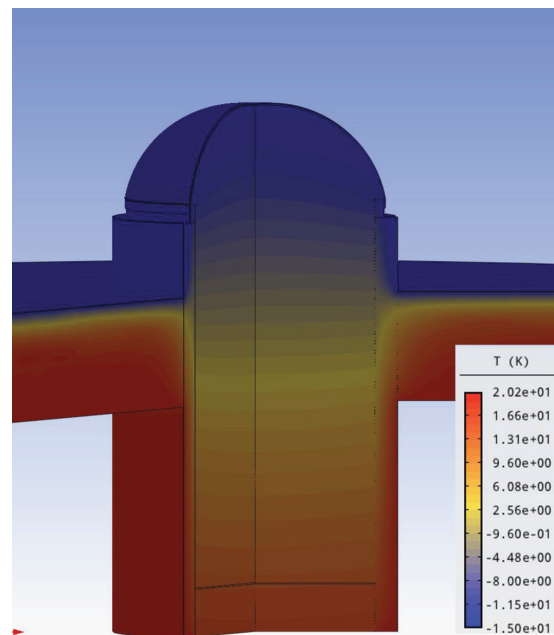


Figure 5: Temperature profile of the light guide

Slika 5: Temperaturni profil vodnika svetlobe

4 DISCUSSION

Tubular light guides are a type of daylighting system, used to illuminate a room or a bigger space inside a building or construction, in which natural light is hardly available. However, an emphasis should be put onto the ways a light guide can be designed with respect to daylighting, thermo-technical requirements and other factors.

The above results for daylighting were determined solely with HOLIGILM. The software can draw luminance maps for the diffuser and determine the total luminous flux beneath the optical interface. It is useful for simulations when a tubular light guide is regarded as a luminary, practically artificial light source. For the artificial-lighting design, luminaries are represented as IES data files. Light guides can also be designed in this way instead of using the approach based on a natural-light source. This approach is useful because HOLIGILM cannot determine the internally reflected component of the daylight factor, but only the sky component. Another disadvantage of HOLIGILM is that the room used can only have a rectangular shape. On the contrary, when the internally reflected component of the daylight factor is neglected, the results may be obtained for rooms of any shape. However, simulations for different sky types created by the software tools using one of the global illumination models can be important in future since the use of photorealistic rendering slowly but steadily rises year by year.

As for the thermo-technical design of light guides, it can be said that they lack one crucial parameter. That is the motion of the air inside and outside the pipe. The pipe is commonly manufactured from plain metal sheets, thus, when put together, the joints are not sealed by sealants. Therefore, at some places, there can be leakage of air, with a possibility of water vapour entering the light-guiding system. This water can condense inside the pipe at any time, especially in winter. The condensed water may damage the surrounding structures. Also, the fact that the thermal conductivity of the resulting structure can be evaluated just because it goes through the envelope of a building leaves some space for improvements. Another approach similar to that of the determination of the thermal conductivity may or may not be correct and should be researched in detail via long-term monitoring, not just by the means of computer simulations.

5 CONCLUSION

The design and application of tubular light-guiding systems have a flaw: most of their parameters regarding building physics are determined solely by computer simulations, which are not required to correspond to reality.

This could be changed by the means of experimental activities, which are planned within the Faculty of Civil Engineering. Through a comprehensive long-term monitoring, several characteristics could be observed, such as the movement of the air in the pipe, temperature rises and the effects of air humidity in the light guides.

Acknowledgement

This paper was prepared within project No. LO1408 "AdMaS UP – Advanced Materials, Structures and Technologies", supported by the Ministry of Education, Youth and Sports under National Sustainability Programme I.

6 REFERENCES

- ¹ P. Charvat, T. Mauder, M. Ostry, Simulation of Latent-Heat Thermal Storage Integrated with Room Structures, *Mater. Tehnol.*, 46 (2012), 239–242
- ² P. Boyce, P. Raynham, *SLL Lighting Handbook*, CIBSE, London 2009
- ³ F. Moore, *Concepts and Practice for Architectural Daylighting*, Van Nostrand Reinhold, New York 1985, 290
- ⁴ J. Mohelnikova, F. Vajkay, Study of Tubular Light Guides Illuminance Simulations, *LEUKOS*, 5 (2009), 267–277, doi:10.1582/LEUKOS.2008.05.04.001
- ⁵ M. Kocifaj, S. Darula, R. Kittler, HOLIGILM: Hollow light guide interior illumination method – An analytic calculation approach for cylindrical light-tubes, *Solar Energy*, 82 (2008) 3, 247–259, doi:10.1016/j.solener.2007.07.003
- ⁶ Commission Internationale de l'Eclairage, CIE DS 011.2/E: 2002 Spatial distribution of daylight – CIE standard general sky, Vienna: Commission Internationale de l'Eclairage, 2002
- ⁷ Czech Standardization Institute, ČSN 73 0580 Daylighting in buildings – Part 1: Basic Requirements, Prague, Czech Standardization Institute, 2007
- ⁸ Czech Standardization Institute, ČSN 73 0540 Thermal protection of buildings – Parts 1,2,3,4 Prague, Czech Standardization Institute, 2005 and 2011

CREEP BEHAVIOUR OF A SHORT-FIBRE C/PPS COMPOSITE

VEDENJE KRATKIH VLAKEN C/PPS KOMPOZITOV PRI LEZENJU

Tomáš Fíla¹, Petr Koudelka², Daniel Kytýř², Jiří Hos¹, Jan Šleichrt¹

¹Czech Technical University in Prague, Faculty of Transportation Sciences, Konviktská 20, 110 00 Prague 1, Czech Republic

²Institute of Theoretical and Applied Mechanics, Academy of Sciences of the Czech Republic, Prosecká 76, 190 00 Prague, Czech Republic
xfila@fd.cvut.cz

Prejem rokopisa – received: 2014-08-22; sprejem za objavo – accepted for publication: 2015-04-24

doi:10.17222/mit.2014.208

Composite materials with a polymeric matrix reinforced by carbon fibres are nowadays widely used as high-tech structural materials with excellent mechanical properties (particularly their stiffness and strength). The application of this type of composite to structural parts exposed to thermal loading has recently been proposed. Such an application requires an investigation and analysis of the mechanical behaviour under long-term exposure to simultaneous thermal and mechanical loading. In this paper the measurements and results of the creep behaviour of a composite with a polyphenylene sulphide matrix reinforced with chopped poly-acrylonitrile carbon fibres (C/PPS) are presented. The measured compound is proposed for use as a structural material for a jet-engine frame in the aerospace industry and the internal parts of aircraft with possible thermal loading. A custom experimental device designed for the creep measurements of composite materials was used for measurements of the developing strain at a constant tensile stress and temperature. Short-term creep tests with continuous strain monitoring were performed at a constant stress level at several elevated temperatures below and above the glass-transition temperature of the matrix. The strain was measured using the digital image correlation (DIC) method. The measured data were processed to find the strain-to-time dependency and the creep-compliance-to-time dependency. The creep-compliance-to-time data were also fitted using Findley's creep law for polymers to evaluate the model parameters and to analyse the applicability of the model for a PPS polymer reinforced with chopped carbon fibres.

Keywords: creep, short fibre composite, C/PPS, Findley's model, DIC

Kompozitni materiali s polimerno osnovo, okrepljeno z ogljikovimi vlakni, se dandanes pogosto uporabljajo kot visokotehnoški konstrukcijski materiali z izjemnimi mehanskimi lastnostmi, še posebej to velja za njihovo togost in trdnost. Pred kratkim je bila predlagana uporaba kompozita te vrste za konstrukcijske dele, ki so izpostavljeni toplotni obremenitvi. Takšna uporaba zahteva raziskavo in analizo mehanskega vedenja pri dolgotrajni izpostavljenosti istočasni toplotni in mehanski obremenitvi. Prispevek predstavlja meritve in rezultate deformacijskega vedenja kompozitov z matrico iz polifenilen sulfida, okrepljenega z razcepljenimi poliakrilonitrilnimi ogljikovimi vlakni (C/PPS), ki naj bi se uporabljali kot konstrukcijski materiali za ogrodje reaktivnih motorjev v letalski in vesoljski industriji ter za notranje dele letal, ki so pod potencialno toplotno obremenitvijo. Za merjenje napredovane deformacije pri konstantni natezni obremenitvi in temperaturni obremenitvi, je bila uporabljena posebna preizkusna naprava, izdelana za merjenje deformacije kompozitov. C/PPS vzorci so bili postavljeni v toplotno komoro in segreti. Vzorci so bili nato s pomočjo stiskalnice izpostavljeni konstantni natezni sili. Kratkotrajni preizkusi lezenja, z nadzorovanjem neprekinjene natezne sile, so bili opravljeni pri konstantnih stopnjah obremenitve pri različnih temperaturah, ki so bile višje ali nižje od temperature prehoda v steklasto stanje osnove. Deformacija vzorca je bila izmerjena z uporabo metode korelacije digitalne slike (DIC). Namen izmerjenih podatkov je bil poiskati odvisnosti deformacije od časovne komponente in lezenja. Podatki o času in sili lezenja so bili usklajeni s Findleyevim zakonom lezenja za polimere za oceno parametrov modela in analizo veljavnosti modela za PPS polimere, ki so okrepljeni razcepljenimi ogljikovimi vlakni.

Ključne besede: lezenje, kompozit s kratkimi vlakni, C/PPS, Findleyev model, DIC

1 INTRODUCTION

Composite materials with various matrices reinforced by short or continuous fibres are nowadays widely used as general structural materials with good mechanical properties (particularly their stiffness and strength). One of the very popular composite compounds that are widely used in the aviation industry consists of a polyphenylene sulphide (PPS) matrix and carbon-fibre reinforcement. This material, in continuous fibre form, is typically used in the production of external aircraft components because of its excellent mechanical properties, chemical resistance to aerospace fluids and low density.¹ Composite compounds with carbon fibres and PPS matrices (C/PPS) also have a good resistance to heat and flames. Therefore, they are able to meet the smoke and toxicity requirements of aviation legislation¹ and recently

they have been used for the construction of aircraft's interior parts, particularly seats.^{1,2}

Attempts to simplify the fabrication process for aircraft parts and to reach a higher cost efficiency in terms of production have led to the introduction of C/PPS in the form of a material reinforced by chopped or short carbon fibres.³ The parts used in the aviation industry, e.g., seats, manufactured using a composite with a short reinforcement can be easily fabricated using injection moulding and their shape can be very complex and thick.³ However, such composites consist of unit cells with discrete boundaries, various fibre arrangements and distributions. Thus, these materials exhibit significantly lower strengths and are in comparison with continuous-fibre reinforcements susceptible to the occurrence of creep.⁴ For this reason the creep behaviour of short-fibre composites has to be properly described and taken into

account as one of the most important parameters for an estimation of a part's lifetime.

In this study a series of isothermal creep measurements was performed with the composite compound consisting of a PPS matrix reinforced with short carbon fibres fabricated using an untested method involving heating cables (details of the manufacturing method are classified, and thus only the main features of the method will be described in the text). The tested material is planned to be used for the construction of monocoque shell parts of the fuselage and for structural parts with large volumes (such as engine suspension, etc.) and thin reinforcements with possible thermal loading.

2 EXPERIMENTAL PART

Material samples with a dog-bone shape were tested in a custom-designed device for uniaxial creep tests at a constant stress level. The creep was measured on a set of samples at various temperatures above and below the glass-transition temperature of the matrix. The strain was observed using a digital single-lens-reflex (DSLR) camera and evaluated using the digital image correlation technique (DIC). As a result, the strain-time and the creep-compliance-time dependencies were evaluated and the creep behaviour of the tested compound was described.

2.1 Material

The material samples were manufactured as a new type of cost-efficient material. The composite compound (Carbon AS4/PPS, TenCate Advanced Composites) consists of a polymeric polyphenylene sulphide (PPS) matrix and chopped carbon fibres with a length of approximately 10 mm. The material was fabricated as a 2.5-mm-thick sheet using the technique of mixing chopped fibres with PPS particles and baking in a mould with heating cables at 310–340 °C under 4 MPa



Figure 1: Image of a C/PPS sheet used to prepare a specimen
Slika 1: Posnetek C/PPS pločevine, ki je bila uporabljena za pripravo vzorca

pressure. The outer parts of the sheet were manufactured with an 8 mm thickness for the clamping of the samples into sample holders. Part of the sheet is depicted in **Figure 1**.

2.2 Specimen preparation

The dog-bone-shaped specimens were cut from a sheet of material using a water-jet cutting machine. The middle part of the specimen was prepared with a width of 10 mm. The overall length of the specimen was 160 mm, the maximum width was 25 mm and the thickness of the middle part was 2.5 mm. The maximum distortion caused by the water-jet cutting was experimentally determined to be better than 0.15 mm (in all dimensions on both surfaces of the specimen). Such a manufacturing tolerance was considered to be sufficient for the experiment and the surfaces were not additionally modified. All the specimens were measured before the test and particular dimensions were used for the evaluation of the experiment. The dimensions were selected to be similar to the dimensions of small longitudinal reinforcements used in, e.g., aircraft seats. The specimen surface was sprayed using an airbrush with a granite effect for better pixel identification in the DIC technique. A specimen with a granite coating is displayed in **Figure 2**.

2.3 Experimental setup

The experimental setup consists of a custom-designed experimental device for the creep measurements and a DSLR camera with accessories.

The creep experimental device was designed for uniaxial creep testing at a constant stress level. The device consists of a heating chamber SFL 3119 (Instron, USA) with a temperature range of –70 °C to 350 °C, a rigid structural steel frame, two independent aluminium alloy lever arms with ratio of 1:10 and set of dead weights. The device is equipped with two load cells (VTS Zlín, Czech Republic) with a loading capacity up to 10 kN. The strain can be measured in two possible ways: extensometers or DIC. Two custom-designed extensometers (VTS Zlín, Czech Republic) with a maximum measur-

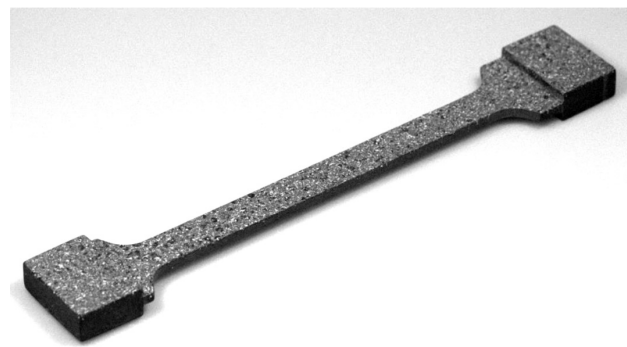


Figure 2: Image of a specimen with sprayed granite coating on its surface

Slika 2: Prikaz vzorca s prevleko iz granita na površini

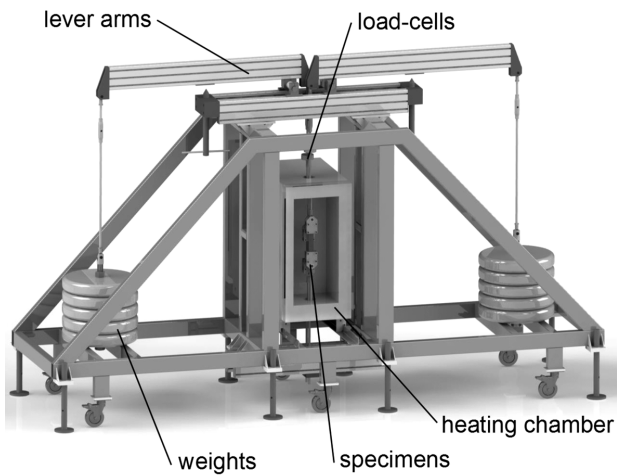


Figure 3: Visualization of the custom-designed device for the creep measurements

Slika 3: Prikaz posebne naprave za merjenje deformacije

able extension of 10 mm and a heat resistance up to 150 °C allow the accommodation of two samples in the device's heating chamber and their independent loading. In contrast the DIC allows the measurement of only a single specimen, but it is not limited by the maximum temperature because all of the measuring equipment is situated outside the heating chamber. The experimental device is shown in **Figure 3**.

The DIC was used as a tool for an evaluation of the strain held in the experiments. The specimen in the heating chamber was observed with a DSLR camera EOS 550D (Canon, Japan) with a macro-objective



Figure 4: Image of the experimental setup and a specimen mounted in the thermal chamber

Slika 4: Prikaz preizkusnega sklopa in vzorca, ki je bil nameščen v toplotni komori

EF100mm/1:2.8L Macro (Canon, Japan) situated on a tripod in front of the heating chamber. The sample surface was illuminated with a laboratory LED light source KL 2500 (Shott, Germany). The overall view of the experimental setup is shown in **Figure 4**.

2.4 Experiment

Prior to the experiment the specimen was put in the heating chamber and the positions of the illuminators and the camera stand were adjusted. The reference image of the sample surface in the heating chamber was taken to verify the focalization, the field of view and to detect and eliminate possible reflections of illuminating light on the chamber window. The unloaded specimen was then heated to a given temperature and for a 30-min period was held to reach a uniform temperature distribution throughout all the heated parts. After that the image-capturing sequence was started and the specimen was loaded with a constant tensile force of 1.5 kN (one measurement with a loading force of 2.5 kN was also performed). The loading force was selected according to data obtained during quasi-static measurements in tension of specimens with an identical shape. A value of 1.5 kN was situated in a linear elastic region of the material and represented approximately 70 % of the material's yield strength. The creep test was continued until specimen rupture or for at least 20 h. The glass-transition temperature of the matrix material was according to the manufacturer's datasheet approximately 85 °C and therefore the creep tests were performed at temperatures of 60 °C (certainly below the glass-transition temperature), 90 °C (slightly above the glass-transition temperature), 110 °C, 130 °C and 140 °C (significantly above the glass-transition temperature). Images were taken at equidistant time intervals and were labelled with a unique timestamp for precise synchronization of the DIC and the experiment time. The strain was evaluated from the image sequence using custom DIC software⁵ based on the Lucas-Kanade algorithm.⁶

3 RESULTS AND DISCUSSION

The evaluated strain-time dependencies are shown in **Figure 5**. The creep-compliance-time dependencies were calculated from the data using the following Equation (1):^{7,8}

$$J_c(t) = \frac{\varepsilon_c(t)}{\sigma_c} \quad (1)$$

where $J_c(t)$ represents the creep compliance in time t , $\varepsilon_c(t)$ is the actual creep strain in time t (excluding the initial strain) and σ_c is the applied constant tensile stress. A graph of the creep-compliance-time dependency is shown in **Figure 6**.

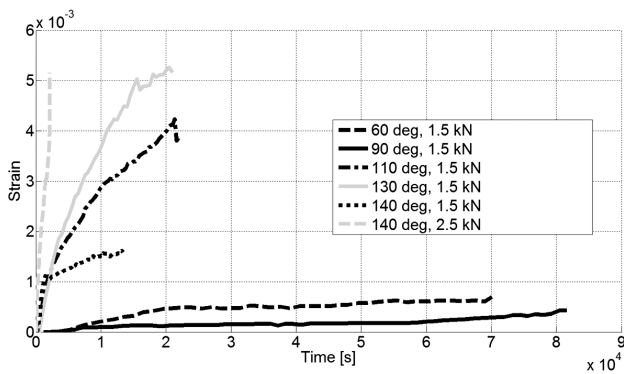


Figure 5: Graph of measured strain-time dependencies
Slika 5: Diagram odvisnosti izmerjenih obremenitev in časa

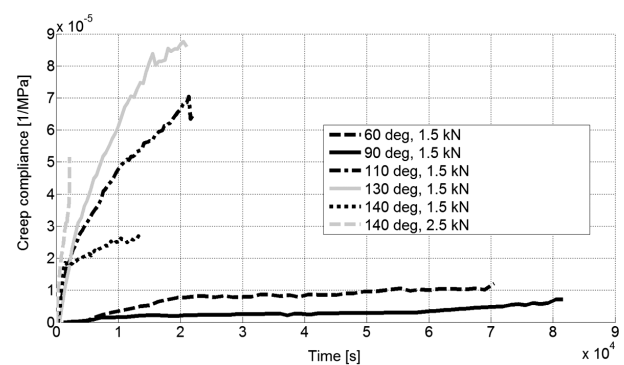


Figure 6: Graph of measured creep-compliance-time dependencies
Slika 6: Diagram odvisnosti izmerjenega lezenja od časa

The creep-compliance data were also fitted using Findley’s creep law for polymers, assuming steady-state creep behaviour according to the Equation (2):⁸

$$\overline{J_c(t)} = b_0 t^{b_1} \quad (2)$$

where $\overline{J_c(t)}$ represents the predicted creep compliance in time t (in seconds) and b_0, b_1 are material parameters evaluated by a regression of the experimental data. The evaluated regression curves are shown in Figure 7 and the calculated material parameters are summarized in Table 1.

Table 1: Evaluated parameters of Findley’s creep model

Tabela 1: Ocenjeni parametri Findleyevega modela lezenja

Temperature (°C)	Loading (kN)	b_0	b_1
60	1.5	4.432×10^{-10}	0.9386
90	1.5	2.286×10^{-9}	0.6818
110	1.5	2.419×10^{-7}	0.5711
130	1.5	1.271×10^{-7}	0.6712
140	1.5	1.078×10^{-6}	0.3475
140	2.5	1.832×10^{-7}	0.7044

Based on the experimental data it can be stated that the creep behaviour of the tested material was brittle above the glass-transition temperature. The test of each specimen above this temperature ended with a sudden

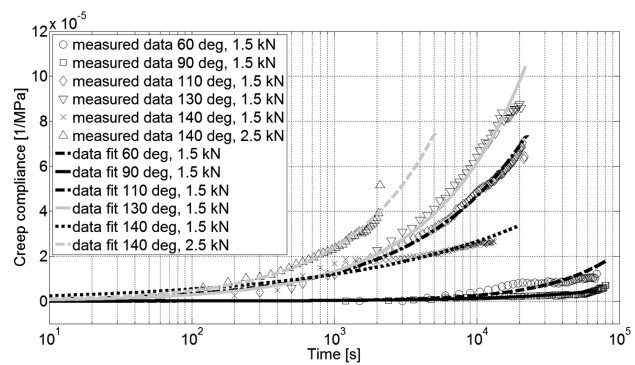


Figure 7: Graph of fits of Findley’s creep model on the experimental data

Slika 7: Prikaz prilagoditev Findleyevega modela lezenja na podatke pri preizkusu

specimen rupture after a short time period (max. approx. 6 h).

Creep under (test at 60 °C) and slightly above (test at 90 °C) the glass-transition temperature can be considered immeasurable because the measured maximum displacements of approximately 10 μm correspond only to double the pixel-size of the DIC image (approx. 5 μm) and thus subject to the noise and reliability of the method.

The majority of the measured dependencies agreed with the standard polymer creep theory and their creep strain-rate increased with increasing temperature or loading. A regression analysis showed a good correlation of the experimental data and Findley’s creep model for polymers (Figure 7). The fitted model’s parameters have different values than usual for clear polymers⁸⁻¹⁰ because of the brittle behaviour of the material and the short times to specimen failure. Still, Findley’s creep model can be considered as suitable for a description of the creep behaviour for the used C/PPS compound.

However, disagreement with the basic theory can be seen in the test with a loading of 1.5 kN at a temperature of 140 °C that exhibited a lower strain rate than expected. The strain rate at the beginning of the test was appropriate for the temperature, but at a strain of approximately 1×10^{-3} a sudden decrease was observed and the strain remained low until specimen rupture (Figure 5). Moreover, several specimens ruptured during the initial loading at forces even 3 times lower than the testing force of 1.5 kN and are not presented in the results. This discrepancy was caused by significant imperfections detected in the material’s microstructure (missing matrix binder, etc.) caused by an imperfect fabrication process and size effect due to the combination of a random material structure and the small width of the specimen (10 mm). Hence, the delivered material was considered to be unsuitable for parts with small dimensions in terms of structural and thermal loading.

4 CONCLUSIONS

A set of isothermal creep tests with constant loading of the C/PPS composite with chopped fibres was performed. The C/PPS material was fabricated with an innovative technique of baking in a mould using heating cables. The experiments were performed at several different temperatures below and above the glass-transition temperature and the strain was evaluated using the DIC technique. The experimental results showed a good correlation with the standard creep theory for polymers and with Findley's creep law. However, the used fabrication technology brought several imperfections to the material's structure, which together with the size effect caused by small dimensions of the specimen, led to a discrepancy in the results. Thus, the tested material was considered unsuitable for small structural parts exposed to structural and thermal loading and so further improvements to the fabrication process are required.

Acknowledgements

The research was supported by The Technology Agency of Czech Republic (grant No. TA03010209), by the Grant Agency of the Czech Technical University in Prague (grant No. SGS15/225/OHK2/3T/16) and by RVO: 68378297. All the support is gratefully acknowledged.

5 REFERENCES

- ¹ M. Favaro, Evaluation of a low cost thermoplastic composite for aircraft interior applications, Proceedings of SAMPE 2010 Conference, Seattle, USA 2010
- ² Composites becoming the standard in aircraft seats, JEC Composite Magazine, 43 (2006) 23, 34
- ³ R. Bockstedt, J. Sajna, Low cost composites based on long carbon fiber thermoplastics, Proceedings of SAMPE 1993 Conference, Anaheim, USA, 1993
- ⁴ V. Monfared, M. Mondali, A. Abedian, Steady state creep behaviour of short fiber composites by mapping logarithmic functions (MF) and dimensionless parameter (DP) techniques, Archives of Civil and Mechanical Engineering, 12 (2012), 455–463, doi:10.1016/j.acme.2012.08.001
- ⁵ I. Jandjsek, J. Valach, D. Vavřík, Optimization and Calibration of Digital Image Correlation Method, Proceedings EAN 2010, Czech Republic, 2010, 121–126, doi:http://hdl.handle.net/11104/0190791
- ⁶ B. Lucas, T. Kanade, An iterative image registration technique with an application to stereo vision, Proceedings of IUW, 1981, 121–130
- ⁷ W. Callister, Fundamentals of Material Science, John Wiley, 2001
- ⁸ S. Vaitkus, I. Gnip, V. Kersulis, S. Vejelis, Prediction of Creep Strain of the Expanded Polystyrene (EPS) in Long-term Compression, Materials Science, 13 (2007) 4, 293–296
- ⁹ Y. Guo, R. Bradshaw, Isothermal physical aging characterization of Polyether-ether-ketone (PEEK) and Polyphenylene sulfide (PPS) films by creep and stress relaxation, Mech Time-Depend Mater, 11 (2007) 1, 61–89, doi:10.1007/s11043-007-9032-7
- ¹⁰ Y. Guo, R. Bradshaw, Long-term creep of polyphenylene sulfide (PPS) subjected to complex thermal histories: The effect of nonisothermal physical aging, Polymer, 50 (2009) 16, 4048–4055, doi:10.1016/j.polymer.2009.06.046

INCREASING MICRO-PURITY AND DETERMINING THE EFFECTS OF THE PRODUCTION WITH AND WITHOUT VACUUM REFINING ON THE QUALITATIVE PARAMETERS OF FORGED-STEEL PIECES WITH A HIGH ALUMINIUM CONTENT

POVEČANJE MIKROČISTOČE IN DOLOČITEV UČINKA PROIZVODNJE, Z VAKUUMSKIM RAFINIRANJEM ALI BREZ, NA KVALITATIVNE PARAMETRE KOVANEGA JEKLA Z VISOKO VSEBNOSTJO ALUMINIJA

Vladislav Kurka¹, Jaroslav Pindor¹, Jana Kosňovská¹, Zdeněk Adolf²

¹Material and metallurgical research, Ltd, Pohranicni 693/31, 703 00 Ostrava-Vítkovice, Czech Republic
²VŠB – Technical University of Ostrava, 17. listopadu 15/2172, 708 33 Ostrava-Poruba, Czech Republic
vladislav.kurka@mmvyzkum.cz

Prejem rokopisa – received: 2014-10-13; sprejem za objavo – accepted for publication: 2015-03-24

doi:10.17222/mit.2014.258

The quality production technology for the W.Nr. 1.8504 steel was developed. The aim of the work was to achieve the required internal micro-purity and determine the effects of different production technologies on the qualitative parameters of forged-steel pieces. Firstly, polygonal ingots weighing 1600 kg were produced, using the metallurgical units, in a controlled-atmosphere induction-melting furnace (IF) without vacuum treatment, and in a vacuum and pressurized induction-melting furnace (VPIM) with vacuum treatment. The ingots were subsequently reshaped by open-die forging into bars with a rectangular cross-section. The effect of the ingot-production technology was evaluated by comparing the forged-steel pieces in terms of their purity, macrostructure and microstructure.

Keywords: vacuum, inclusion, aluminium, steel

Izvršen je bil razvoj kakovostne proizvodne tehnologije jekla W.Nr. 1.8504. Namen je bil doseči zeleno notranjo mikročistočo in ugotoviti vpliv različnih tehnologij proizvodnje na kvalitativne parametre odkovkov. Najprej so bili izdelani poligonalni kovani ingoti z maso 1600 kg, z uporabo naslednjih metalurških agregatov: v indukcijski talilni peči s kontrolirano atmosfero (IF) brez vakuumskega rafiniranja in v vakuumski ter indukcijski talilni peči (VPIM) s povišanim tlakom in z vakuumskim rafiniranjem. Nato so bili ingoti s prostim kovanjem preoblikovani v palice s pravokotnim prerezom. Vpliv tehnologije proizvodnje ingotov je bil ocenjen s primerjavo odkovkov z vidika čistosti, makro in mikrostrukture.

Ključne besede: vakuum, vključki, aluminij, jeklo

1 INTRODUCTION

Aluminium is primarily used in steel as a deoxidising agent as well as an alloying element. In a melt, aluminium occurs in the dissolved form, in a solid solution as aluminium metal, aluminium oxide Al_2O_3 and, in an interaction with nitrogen, also as aluminium nitride AlN .¹ An increased aluminium content in steel reduces its formability due to the mechanical effect of its precipitates, and alternatively also due to its local ferrite affecting the structural state. An increased concentration of strongly ferrite generating aluminium may occur in the vicinity of dissolved AlN particles. AlN is separated in steel in the form of acicular crystals, usually on the grain borders. The quality of W.Nr.1.8504 (hereinafter referred to as the "steel") is, with regard to its chemical composition, intended for surface nitration. Nitration is a saturation of the steel surface with nitrogen that creates hard nitrides with the alloying elements Al, Cr, Ti and V. **Figure 1** shows an example of a nitrated steel layer. The process of nitration takes place at temperatures of 500 °C – 540 °C for about 50 h,² when the nitrated steel layer

achieves a 0.3 mm thickness in 30 h, and a 0.5 mm thickness in 50 h. The process depends on the temperature, pressure, chemical composition of the steel and atmospheric composition.

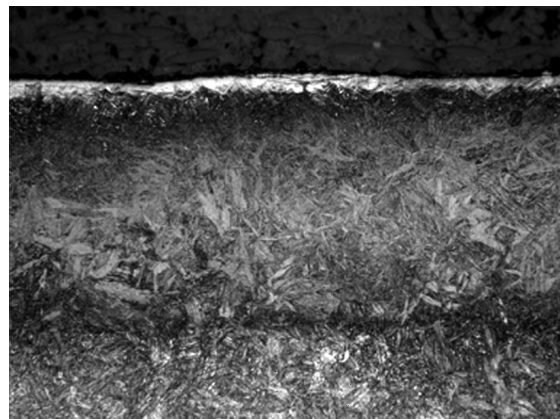


Figure 1: Example of a nitrated steel layer²

Slika 1: Primer nitrirane plasti na jeklu²

Nitrogen is thus an element that creates AlN nitrides with Al in steel, which are very hard and non-malleable. On the steel surface, it creates a hard, abrasion-resistant area. AlN nitrides inside the steel are non-malleable inclusions that impair the micro-purity of the steel. This work is concerned with the elimination of AlN inclusions from the WNr1.8504 quality steel with 0.8 % – 1.1 % of mass fractions of high Al.

An important step in the elimination of the AlN-type inclusions with a high aluminium content from steel is the reduction of the nitrogen content to the minimum level.

1.1 Nitrogen in steel

Nitrogen in steel not only reacts with iron but also with other dissolved elements, forming a wide variety of compounds. These are dominated by nitrides, but carbonyl nitrides, oxynitrides, cyanonitrides, complex binary nitrides and other phases of variable compositions can occur as well. Their existence depends on a number of factors, such as the composition of the steel, the melting method, the temperature, the pressure, the thermal treatment, etc.⁴ In our case, aluminium nitrides form under the liquidus temperature and re-dissolve in the steel at temperatures of 900 °C – 1100 °C, where the dissolution rate is a function of the material temperature and structure.⁵ Increased frequency and size of, for example, the AlN particles may lead to the generation of inter-crystalline steel fractures. The effects of the elements on the solubility of nitrogen in molten iron at a temperature of 1600 °C and a nitrogen pressure of 100 kPa are presented in **Figure 2**.⁴

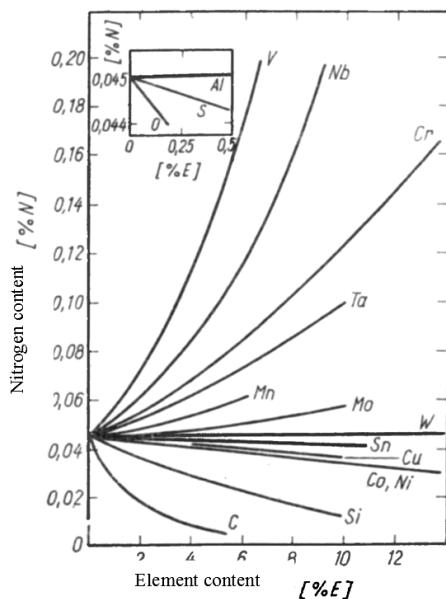


Figure 2: Effects of elements on the solubility of nitrogen in molten iron at a temperature of 1600 °C and a pressure of 100 kPa⁴

Slika 2: Vpliv elementov na topnost dušika v staljenem železu pri 1600 °C in tlaku 100 kPa⁴

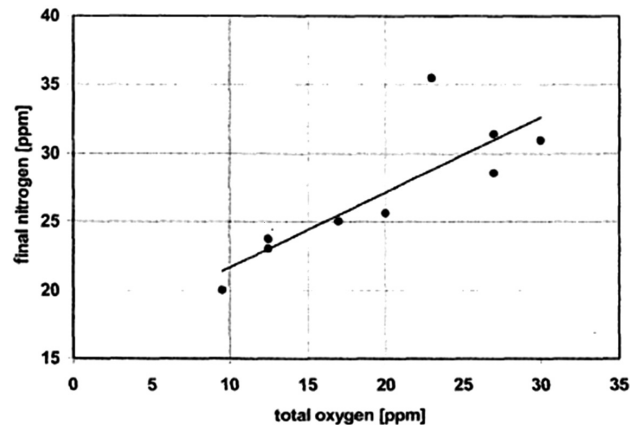


Figure 3: Nitrogen removal by tank degassing as a function of the total oxygen content⁶

Slika 3: Zmanjšanje vsebnosti dušika pri odstranjevanju plina v komori, kot funkcija skupne vsebnosti kisika⁶

Surface-active elements such as sulphur and oxygen hinder the removal of nitrogen from the molten steel during vacuuming (nitrogen diffusion in argon bubbles during bubbling) and from the vacuum above the steel surface. If reducing the nitrogen content, e.g., to a required value below 0,004 % of mass fractions, very low values of sulphur and oxygen need to be ensured at the same time. See **Figures 3** and **4** for a graphic illustration of this dependence.⁶

1.2 Solubility of nitrogen in steel

The solubility of nitrogen in steel and the effects of individual elements are described in detail in a previous paper.⁷ The transition of nitrogen in steel is governed by Sievert's law, which presupposes its atomic dissolution. The dependence of the nitrogen content in an iron melt at pressure is described with relationship (1):

$$[\%N]_{Fe} = \frac{K_N}{f_N} \cdot \sqrt{\{p_{N_2}\}_{rel.}} \quad (1)$$

where:

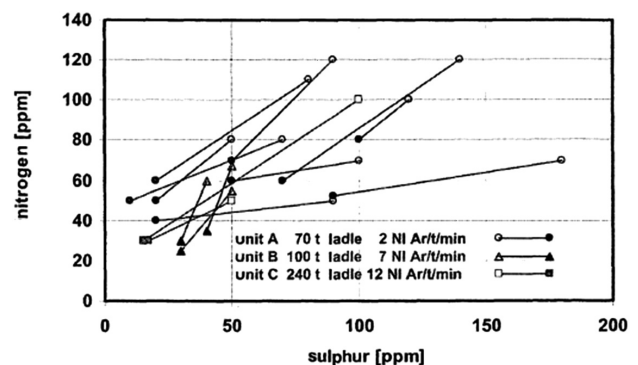


Figure 4: Nitrogen removal by tank degassing as a function of sulphur content⁶

Slika 4: Zmanjšanje vsebnosti dušika pri odstranjevanju plina v komori, kot funkcija skupne vsebnosti žvepla⁶

K_N is the equilibrium constant of the dissolution process (in mass fractions, (w/%) maximum, f_N is the nitrogen activity coefficient in iron melt,¹ $\{p_{N_2}\}_{rel.}$ is the relative partial nitrogen pressure above iron melt.¹

The equilibrium constant K_N expresses the nitrogen solubility in iron under standard conditions, i.e., its maximum content under a pressure of 0.1 MPa $\{p_{N_2}\}_{rel.} = 1$ a $f_N = 1$. The temperature dependence of nitrogen solubility is expressed with Equation (2):

$$\lg K_N = -\frac{188}{T} - 1.246 = \lg[\%N]_{Fe} \quad (2)$$

and the adequate dependence of the reaction-free enthalpy on the temperature is expressed with relationship, Equation (3):

$$\Delta G^0 = 3600 + 23.86T \quad (3)$$

As it is clear from Equation (2), the solubility of nitrogen at a temperature of 1600 °C is 0.045 % of mass fractions, but it drops significantly when the melt solidifies. It slightly increases in iron γ , and then drops in iron α to approximately 0.0015 % of mass fractions at 600 °C.

The nitrogen solubility in steel is significantly affected by the presence of alloying elements, particularly in highly alloyed corrosion-resistant steels. The effect of alloying elements is manifested in the value of active coefficient f_N :

$$\lg f_N = \sum e_N^X [\%N] \quad (4)$$

This effect can be expressed by means of interaction coefficients $e_{N(1873K)}^X$. The temperature dependence of the interaction coefficients expressing the effects of elements on the nitrogen activity was described by Chipman and, according to the author⁸, it is expressed with Equation (5):

$$e_{N(T,K)}^X = \left(\frac{3280}{T} - 0.75 \right) \cdot e_{N(1873K)}^X \quad (5)$$

Therefore, the dependence of the nitrogen solubility on the temperature can be expressed with Equations (6) and (7):

$$\lg[\%N]_{steel} = \lg K_N - \lg f_N + \frac{1}{2} \lg \{p_{N_2}\}_{rel.} \quad (6)$$

$$\lg[\%N]_{steel} = \left(-\frac{188}{T} - 1.246 \right) - \sum \left(\frac{3280}{T} - 0.75 \right) \cdot e_{N(1873K)}^X + \frac{1}{2} \lg \{p_{N_2}\}_{rel.} \quad (7)$$

An improvement of the calculation is, especially for highly alloyed steels (e.g. CrNi steels) conditioned not only by the knowledge of the first values of the interaction coefficients but also of the second values and the cross-interaction coefficients, Equation (8):

$$\lg[\%N]_{steel} = \lg[\%N]_{Fe} - \sum e_N^X \cdot [\%X^2] - \sum r_N^X \cdot [\%X^2] - \sum r_N^{X,Y} \cdot [\%X] \cdot [\%Y] \quad (8)$$

For significantly corrosion-resistant steel alloys, these values are quoted by, e.g., Z. Buzek⁸ in **Table 1**.

Table 1: Values of interaction coefficients 1, 2, and cross-interaction coefficients⁸

Tabela 1: Vrednosti interakcijskih koeficientov 1, 2 in navzkrižnih koeficientov⁸

X (in mass fractions, (w/%)	$e_{N(1873K)}^X$	$r_{N(1873K)}^X$	$r_{N(1873K)}^{X,Y}$
Cr	-0.0468	+0.00034	-
Nb	-0.0667	+0.00019	+0.00136 (Cr-Nb)
Mo	-0.0106	-	+0.00002 (Cr-Mo)
Ni	+0.0107	-	-0.00041 (Cr-Ni)
Si	+0.047	-	-0.00149 (Cr-Si)

1.3 Elimination of AlN from WNr1.8504 quality steel

Elimination of the AlN inclusions from steel commenced with the evaluation of standardly produced steel with production-technology adjustments. The objective of the work was a reduction of the nitrogen content and thus the occurrence of AlN in the final product. In MMR, ingots were produced in an atmospheric induction-melting furnace (hereinafter referred to as the IF) with a nominal batch weight of 1750 kg, and in a vacuum and pressurized induction-melting furnace (hereinafter referred to as the VPIM), in which vacuum degassing (VD) at a minimum pressure of 40 Pa (a), or vacuum oxygen decarburisation (VOD) can be carried out by using of an oxygen-argon nozzle.

One polygonal ingot for forging, V2A, was produced from each melt, weighing approximately 1650 kg. With every melt, the ingot was filled from the bottom through the casting system. The ingots were forged by open-die forging into bars of the following dimensions: 140–160 mm × 90–110 mm.

The melts were produced and found as follows:

Melt 1 – Production of the melt in the IF with casting on an atmospheric casting bed under a protective argon atmosphere.

Melt 2 – Production of the melt in the VPIM, vacuum refined with VD, with casting on an atmospheric casting bed under a protective argon atmosphere.

Melt 3 – Production of the melt in the VPIM, vacuum refined with VD, with casting under a protective argon atmosphere in a cofferdam.

The chemical composition of the steel according to the standard³ and the chemical compositions of the monitored and evaluated melts and forged pieces are shown in **Table 2**. All the melts and forged pieces featured the required standardised chemical composition. The content of nitrogen in the forged piece from Melt 1 was 0,0132 % of mass fractions. This amount was reduced to the value of 0.0108 % of mass fractions,

Table 2: Chemical compositions of standardised³ WNr1.8504, the melts and forged pieces (in mass fractions (w/%))**Tabela 2:** Kemijska sestava normiranega³ jekla WNr1.8504, taline in odkovkov (v masnih deležih (w/%))

1.8504		C	Si	Mn	P	S	Cr	Al _{diss.}	Al _{bound}	Al _{total}	N
Standard	min	0.30	0.15	0.60	–	–	1.20	–	–	0.800	–
	max	0.37	0.35	0.90	0.035	0.035	1.50	–	–	1.100	–
Melt 1	melt	0.33	0.30	0.81	0.017	0.006	1.39	–	–	1.20	–
	forged piece	0.33	0.30	0.82	0.012	0.007	1.42	1.08	0.02	1.10	0.0132
Melt 2	melt	0.33	0.27	0.70	0.015	0.007	1.44	–	–	1.11	–
	forged piece	0.34	0.26	0.73	0.011	0.008	1.45	1.07	0.02	1.09	0.0108
Melt 3	melt	0.35	0.24	0.76	0.018	0.007	1.47	–	–	0.97	–
	forged piece	0.35	0.23	0.77	0.010	0.007	1.48	0.94	0.02	0.96	0.0108

through the VD process, in the pieces forged from Melts 2 and 3.

Elements of C, S, N were determined with the thermochemical method using equipment LECO CS 230 and LECO TCH 600. Metal samples were melted in an induction (for C and S) or resistor (for N) furnace in a gas stream. The gas was analysed for the absorption of infrared radiation (for SO₂ and CO₂) and the change in the thermal conductivity was measured (for N₂). Elements Si, Mn, P, S, Cr were determined with an X-ray spectrometry apparatus, ARL ADVANT'X IntelliPower THERMOFISHER SCIENTIFIC. The method of sequential X-ray fluorescence spectrometry is based on the excitation of characteristic X-rays of the elements present in a sample using an X-ray lamp. The Al element was determined on Optima 3000SC PERKIN ELMER. The analysed sample was dissolved in acids and transferred into the solution, and then it was measured using optical emission spectrometry with inductively bounded plasma.

The pieces forged from all the melts were subjected to non-destructive ultrasound testing according to SEP 1921/84 Group 3, Class C/c. All the forged pieces fully conformed to the evaluation.

The work further presents an evaluation of the micro-purity of the pieces forged from Melts 1 to 3, according to ASTM E45-10, method A. This method classifies the inclusions by their shape and light reflec-

tivity only, so their chemical composition plays no role. For the above reason, a spectral microanalysis was also performed with a scanning electron microscope JEOL JSM-5510, equipped with an energy-dispersive analyser from Oxford Instruments, with which the chemical compositions of the inclusions were determined. Last but not least, the work presents an evaluation of the forged pieces' macrostructures.

1.4 Micro-purity of the pieces forged from Melt 1 in the IF

First of all, micro-purity was evaluated on the pieces forged from Melt 1 in the IF. Very coarse inclusions, spot D (oxidic inclusions), were observed in the specimens that often exceeded the allowed limit of 12 µm, specified in the classification of these inclusions. The biggest inclusion achieved the size of 49 µm; the spot-D (oxidic) inclusions were not quite standard, i.e., globular. They featured a rather sharp-edged shape with a variable size. Then there was a smaller quantity of specimens with the inclusions arranged in lines, often in combination with sulphides that were, using the relevant standard etalon, evaluated as the B type – line Al₂O₃. A very low number of slightly shaped A-type inclusions were then observed in some places, exceeding the thickness of 6 µm that is specified for the coarse A-type inclusions. Examples of non-metallic inclusions are shown in **Figures 5 and 6**;

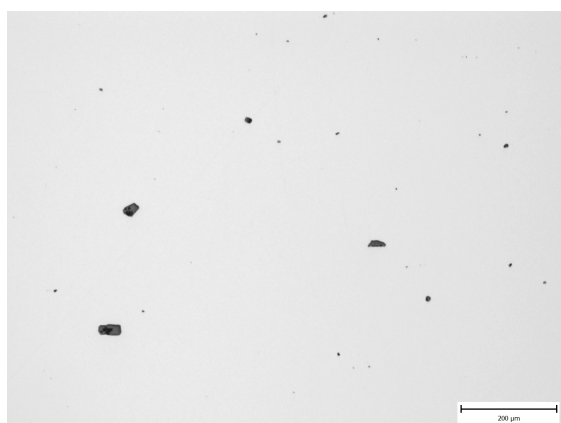


Figure 5: Non-metallic inclusions in the piece forged from Melt 1. Magnified 65x.

Slika 5: Nekovinski vključki v odkovku iz taline 1. Povečava 65x.

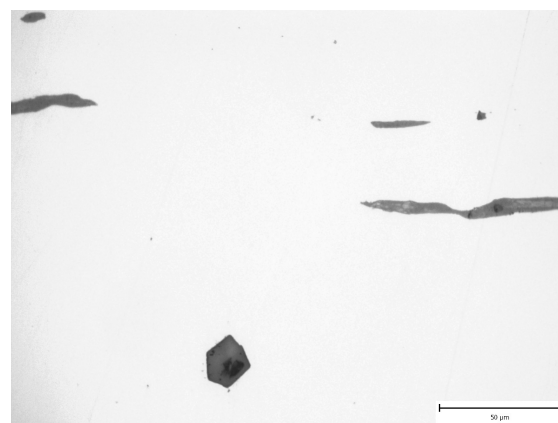


Figure 6: Non-metallic inclusions in the piece forged from Melt 1. Magnified 330x.

Slika 6: Nekovinski vključki v odkovku iz taline 1. Povečava 65x.

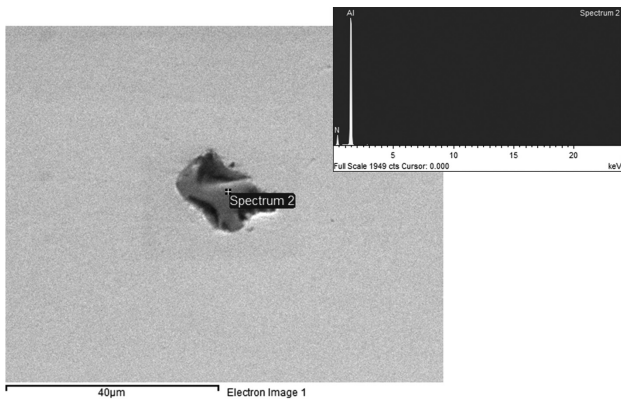


Figure 7: EDX spectrum of non-metallic AlN particles in the piece forged from Melt 1

Slika 7: EDX-spekter nekovinskih delcev AlN, v odkovku iz 1. taljenja

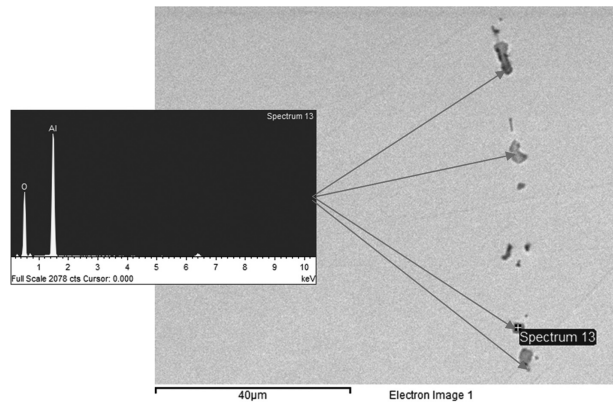


Figure 8: EDX spectrum of non-metallic Al₂O₃ particles in the piece forged from Melt 1

Slika 8: EDX-spekter nekovinskih delcev Al₂O₃, v odkovku iz 1. taljenja

see **Figures 7 and 8** for the chemical compositions of the most frequent inclusions.

Table 3 shows the results of the micro-purity evaluation; the table also includes the largest inclusion found in the tested metal specimens.

1.5 Micro-purity of the pieces forged from Melt 2 in the VPIM through the VD process and casting under Ar atmosphere

During the examination of the polished state, most often non-metallic inclusions of D- and A-type complexes were observed in the tested chains, as shown in **Figures 9 and 10**. Oval inclusion particles were often locally dispersed in the metallic matrix in the forged pieces, sometimes achieving a diameter of 48 µm. The results of the micro-purity evaluation of Melt 2 are shown in **Table 3**.

Locally occurring complex non-metallic particles on the tested specimen surfaces were classified into groups with the closest shape similarity. The majority of the tested inclusions were observed to be globular particles



Figure 9: Non-metallic inclusions in the piece forged from Melt 2. Magnified 65×.

Slika 9: Nekovinski vključki v odkovku iz taline 2. Povečava 65×.



Figure 10: Non-metallic inclusions in the piece forged from Melt 2. Magnified 330×.

Slika 10: Nekovinski vključki v odkovku iz taline 2. Povečava 330×.

(D type) or elongated sulphides (A type). Small-scale tiny lines of B-type inclusions were observed in the forged-piece matrix as well.

The microanalysis detected the chemical compositions of the most frequent inclusions of the AlN type

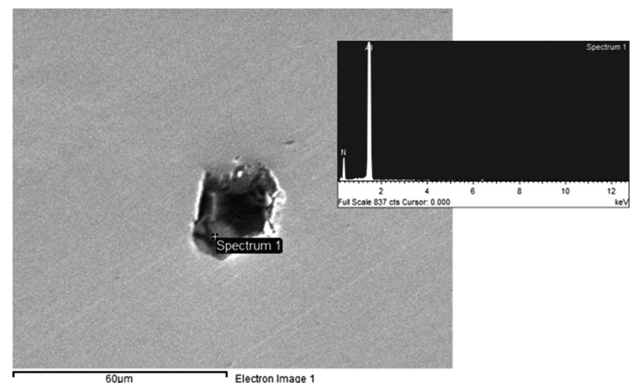


Figure 11: EDX spectrum of non-metallic AlN particles in the piece forged from Melt 2

Slika 11: EDX-spekter nekovinskih delcev AlN, v odkovku iz taline 2

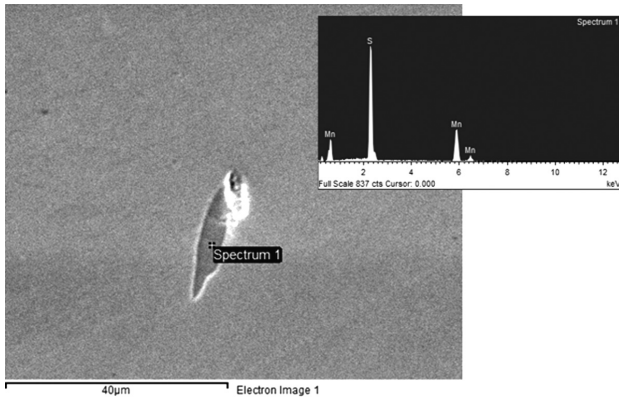


Figure 12: EDX spectrum of non-metallic MnS particles in the piece forged from Melt 2

Slika 12: EDX-spekter nekovinskih delcev MnS, v odkovku iz taline 2

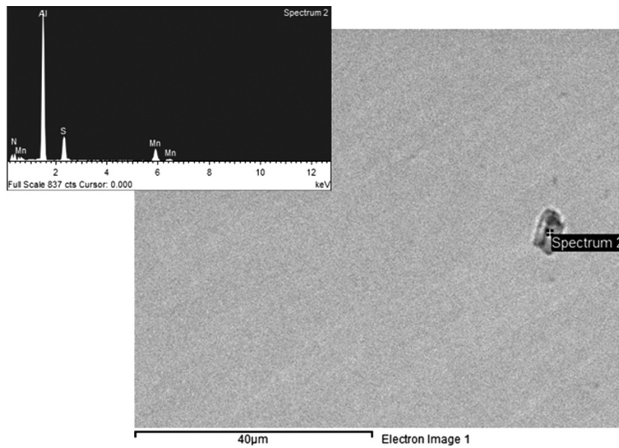


Figure 13: EDX spectrum of non-metallic AlN-MnS particles in the piece forged from Melt 2

Slika 13: EDX-spekter nekovinskih delcev AlN-MnS, v odkovku iz taline 2



Figure 14: Non-metallic inclusions in the piece forged from Melt 3. Magnified 65x.

Slika 14: Nekovinski vključki v odkovku iz taline 3. Povečava 65x.

(**Figure 11**), the MnS type (**Figure 12**), or the complex AlN-MnS type inclusions (**Figure 13**).

1.6 Micro-purity of the piece forged from Melt 3 in VPIM through the VD process and casting in the cofferdam under Ar

As in the previous cases, the presence of a high amount of coarse inclusions was detected in this forged piece; due to their shape, these inclusions were classified as D-type inclusions (oxidic inclusions). Their size significantly exceeded the admissible diameter of up to 12 µm specified for the D-type inclusions. The occurrence of these inclusions was frequent and they achieved the size of up to 50 µm; however, their shape was not typically globular but rather angular, as shown in **Figures 14** and **15**. The occurrence of oxidic inclusions in a line arrangement was less frequent.

Besides the oxidic inclusions, A-type inclusions were observed in the specimen, or complexes of these inclusions, the occurrence of which was relatively frequent. The results of the non-metallic inclusion evaluation are listed in **Table 3**. The microanalysis revealed that, unlike in Melt 2, AlN-type inclusions were the most frequent in Melt 3, as shown in **Figures 16**, **17** and **18**.

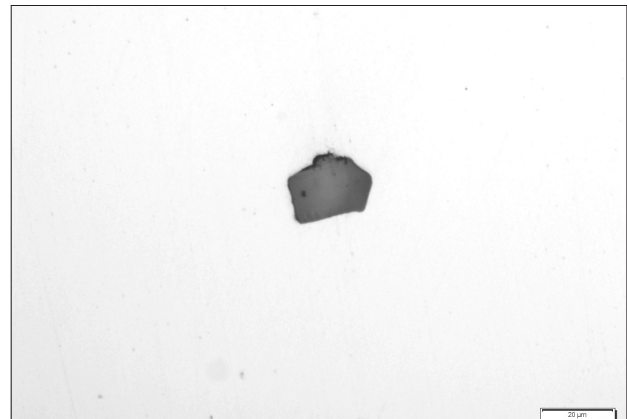


Figure 15: Non-metallic inclusions in the forged piece in Melt 3. Magnified 330x.

Slika 15: Nekovinski vključki v odkovku iz taline 3. Povečava 330x.

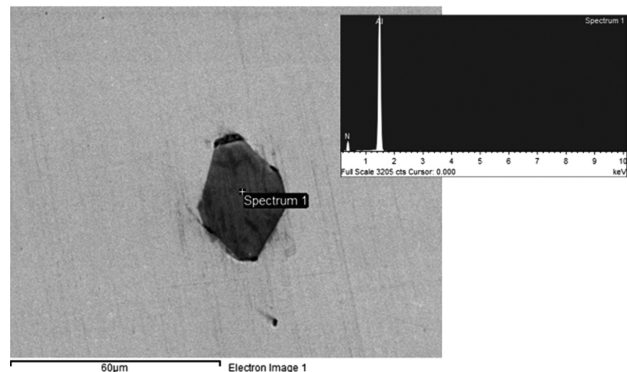


Figure 16: EDX spectrum of non-metallic AlN particles in the piece forged from Melt 3

Slika 16: EDX-spekter nekovinskih delcev AlN, v odkovku iz taline 3

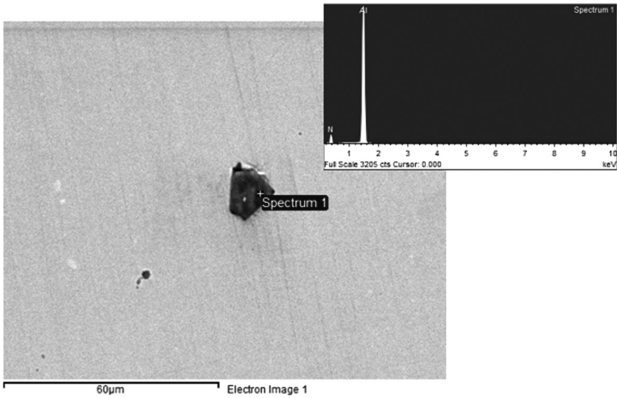


Figure 17: EDX spectrum of non-metallic AlN particles in the piece forged from Melt 3

Slika 17: EDX-spekter nekovinskih delcev AlN, v odkovku iz taline 3

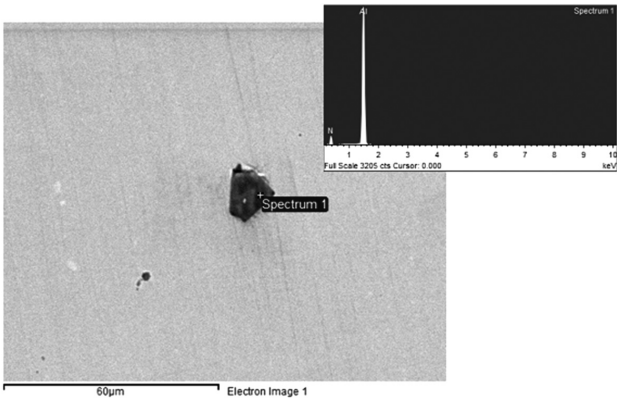


Figure 18: EDX spectrum of non-metallic AlN particles in the piece forged from Melt 3

Slika 18: EDX-spekter nekovinskih delcev AlN, v odkovku iz taline 3

1.7 Macrostructure evaluation

The macrostructures of the forged pieces were revealed by etching in 10 % HNO₃. Unequally distributed insignificant segregations of a darker contrast were revealed in the specimen of the piece forged from Melt 1, as shown in **Figure 19**. More or less uniform macrostructures of the surfaces were observed for the specimens forged from Melts 2 and 3, as shown in **Figures 20** and **21**.

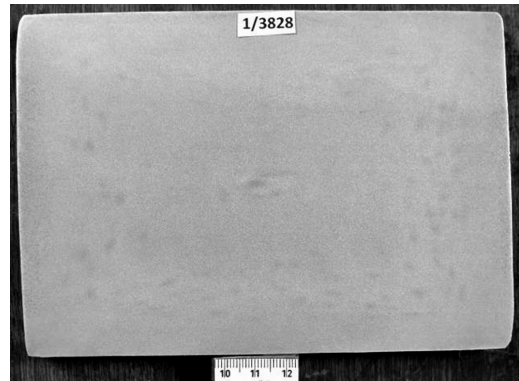


Figure 19: Macrostructure of the piece forged from Melt 1

Slika 19: Makrostruktura odkovkov iz taline 1

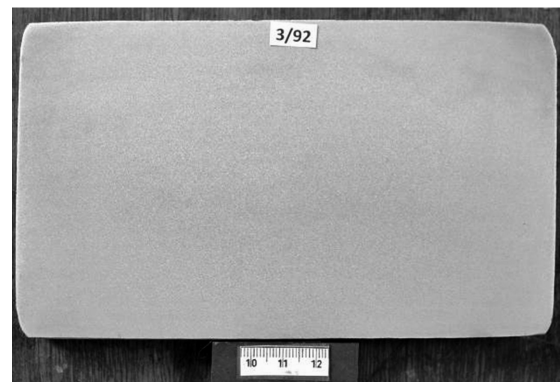


Figure 20: Macrostructure of the piece forged from Melt 2

Slika 20: Makrostruktura odkovkov iz taline 2

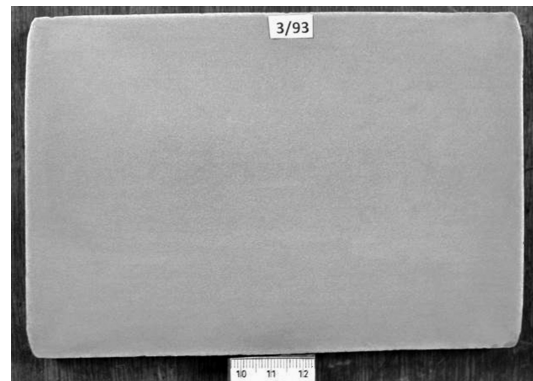


Figure 21: Macrostructure of the piece forged from Melt 3

Slika 21: Makrostruktura odkovkov iz taline 3

Table 3: Micro-purity evaluation according to the ASTM E45-10 standard, method A, and the largest D-type inclusions found in the pieces forged from Melts 1 to 3

Tabela 3: Vrednotenje mikročistoče po standardu ASTM E45-10, metoda A in največji najdeni vključki vrste D v vzorcih iz odkovkov iz taline 1 do 3

Specimen	Maximum contamination, method A								Maximum dimension of D-type inclusion µm
	Type A sulphides		Type B aluminates		Type C silicates		Type D oxides		
	Fine	Coarse	Fine	Coarse	Fine	Coarse	Fine	Coarse	
Melt 1	1	1	2	2			2	2	49
Melt 2	2	2	2	1	–	–	2	2	48
Melt 3	2	1	2	–	–	–	2	2	50

2 CONCLUSION

The objective of the presented work was to increase the inner purity of a WNr1.8504 high-quality forged piece. For this reason, three production technologies (melts) were evaluated in this work.

As the performed analysis of the chemical compositions and non-destructive ultrasound tests indicate, the atmospheric induction furnace and the vacuum and pressurized induction-melting furnace with casting outside and inside the cofferdam are suitable for the production of this material.

However, from the macrostructural point of view, the production of melt in the atmospheric induction-melting furnace proved to be unsuitable.

With respect to the micro-purity determined with the microanalysis of the detected particles and nitrogen content in the forged pieces, none of the three technologies can be applied to achieve a reduced content of mostly AlN inclusions. The production technology for Melt 3 in the VPIM, with the VD process and the casting in the cofferdam under a protective argon atmosphere, eliminated the portion of oxidic and complex inclusions but not the AlN inclusions.

The experiments showed that vacuum degassing (VD) helps to reduce the Al content. The content of nitrogen was reduced by 0.0024 % of mass fractions, from 0.0132 % of mass fractions (the steel made in the IF) to 0.0108 % of mass fractions (the steel made in the VPIM). Based on this fact, the authors are preparing another experiment that will eliminate the nitrogen content using vacuum oxygen decarburization (VOD)

because the melt is mixed better with VOD than with VD. VOD includes a more efficient degassing process because, generally, a high oxygen content in a melt decreases the solubility of nitrogen. For this process, a newly manufactured oxygen-argon nozzle will be used.

Acknowledgement

This paper was created within Project No. LO1203 "Regional Materials Science and Technology Centre – Feasibility Program" funded by the Ministry of Education, Youth and Sports of the Czech Republic.

3 REFERENCES

- ¹ J. Šenberger, Z. Bůžek, A. Záděra, K. Stránský, V. Kafka, *Metalurgie oceli na odlitky*, VUTIUM, Brno 2008, 311
- ² Introduction to Metallography, PACE Technologies, <http://www.metallographic.com/Technical/Metallography-Intro.html>, 24.09.2014
- ³ *Stahlschlüssel 2007*, Verlag Stahlschlüssel Wegst GmbH., ver. 5.01.0000, Marbach 2007
- ⁴ T. Myslivec. *Fyzikálně chemické základy ocelářství*, SNTL – Nakladatelství technické webliteratury, Prague 1971, 448
- ⁵ J. Višek, *Hodnocení růstu zrna uhlíkových a nízkolegovaných nástrojových ocelí v závislosti na přítomnosti AlN*, <http://stc.fs.cvut.cz/pdf/VisekJaroslav-338820.pdf>, 24.9.2014
- ⁶ G. Stolte, *Secondary Metallurgy*, Verlag Stahleisen GmbH, Germany 2002, 217
- ⁷ V. Kurka, Z. Adolf, J. Pindor, *Producing Steel with High Nitrogen Content in Induction Melting Furnaces*, European Oxygen Steel-making Conference, Třinec, 2014
- ⁸ Z. Buzek, *Basic thermodynamic calculations in the steel industry*, *Hutnické aktuality*, 29 (1988) 7

USE OF THE ABI TECHNIQUE TO MEASURE THE MECHANICAL PROPERTIES OF ALUMINIUM ALLOYS: EFFECT OF HEAT-TREATMENT CONDITIONS ON THE MECHANICAL PROPERTIES OF ALLOYS

UPORABA ABI TEHNIKE ZA MERJENJE MEHANSKIH LASTNOSTI ALUMINIJEVIH ZLITIN: VPLIV POGOJEV TOPLOTNE OBDELAVE NA MEHANSKE LASTNOSTI ZLITIN

Oleksandr Trudonoshyn^{1,2}, Maxim Puchnin¹, Olena Prach^{1,3}

¹Czech Technical University in Prague, Karlovo náměstí 13, 12135, Prague 2, Czech Republic

²Friedrich Alexander Universität Erlangen Nürnberg, Martenstraße 5, 91058 Erlangen, Germany

³Technische Universität Darmstadt, Karolinenplatz 5, 64289 Darmstadt, Germany
trudonoshyn@fhotm.kpi.ua

Prejem rokopisa – received: 2014-12-08; sprejem za objavo – accepted for publication: 2015-05-04

doi:10.17222/mit.2014.295

Effects of chemical composition and heat treatment on the microstructures and mechanical properties were investigated with automated ball-indentation tests, scanning and transmission electron microscopy, and energy-dispersive X-ray analysis. In this work, the automated ball-indentation (ABI) technique was compared with the standard mechanical tests. The ABI method is based on load-controlled multiple indentations into a polished surface by a spherical indenter. The indentation depth is progressively increased to the specified maximum limit with intermediate partial unloading. This technique allows us to measure the yield strength, the stress-strain curve, the strength coefficient and the strain-hardening exponent. For all the test materials and conditions, the ABI-derived results were in very good agreement with those obtained with conventional standard test methods. We analyzed the effect of heat treatment on the alloys with different chemical compositions. Heat treatment leads to changes in the mechanical properties of the alloys, which are the results of several processes.

Keywords: Al-alloys, heat treatment, tensile strength, yield strength, ABI hardness test

Vpliv kemijske sestave in toplotne obdelave na mikrostrukturo in mehanske lastnosti je bil preiskovan z avtomatiziranim preizkusom trdote z vtiskovanjem kroglice, z vrstično in presevno elektronsko mikroskopijo in energijsko disperzijsko rentgensko spektroskopijo. V tem delu je bila tehnika avtomatskega vtiskovanja kroglice (ABI) primerjana s standardnimi mehanskimi preizkusi. ABI metoda temelji na kontrolirani obtežitvi pri večkratnem vtiskovanju krogličnega telesa v polirano površino. Globina vtiskovanja postopoma narašča do maksimalne določene globine z vmesnimi razbremenitvami. Ta tehnika omogoča merjenje meje tečenja, krivulje raztezek-obremenitev, koeficienta trdnosti in eksponenta napetostnega utrjevanja. Za vse preizkušane materiale in pogoje, so se dobljeni ABI rezultati dobro ujemali z rezultati dobljenimi iz običajnih metod preizkušanja. Preučevan je bil vpliv toplotne obdelave na zlitine z različno kemijsko sestavo. Toplotna obdelava povzroči spremembo mehanskih lastnosti zlitin, kar je posledica večih procesov.

Ključne besede: Al-zlitine, toplotna obdelava, natezna trdnost, meja tečenja, trdota pri ABI preizkusih

1 INTRODUCTION

A large number of aluminum alloys have been developed for casting, but most of them are varieties of six basic types (according to the AA Al alloy designation system): Al-Cu (2XX.X), Al-Cu-Si (or Mg) (3XX.X), Al-Si (4XX.X), Al-Mg (5XX.X), Al-Zn-Mg (7XX.X) and Al-St (8XX.X).¹ In this context, the alloys of the Al-Mg-Si (6XXX) system have been widely used in producing sheets, extruded parts and thin-wall castings.

It was reported by H. Sternau et al.² that an AlMg5Si2Mn alloy (HPDC) shows high mechanical properties such as ductility (up to 18 %), yield strength (up to 220 MPa) and tensile strength (up to 350 MPa), compared with the other casting alloys.

When comparing the AlSi7Mg and AlMg5Si2Mn casting alloys, the most evident difference is in the fact that the highest strength of AlSi7Mg is achieved only

after the heat treatment, whereas AlMg5Si2Mn exhibits its highest properties in the as-cast condition.

Heat-treatable Al-Mg-Si alloys are important for the investigation because of the possible hardening process, which leads to specific properties. The hardening effects are shown when the dislocations interact with the precipitates, which act as obstacles to the dislocation motion.^{1,3} It is well known that the ductility of such alloys decreases with the increasing Si content. Brittle coarse Si particles usually make further deformation difficult.³

In this regard, it is important to apply not only the optimum chemical composition of the material but also the optimum heat-treatment conditions. The main task of this paper is to investigate the influence of heat treatment on the mechanical properties and structure of Al-Mg-Si-Mn alloys.

Table 1: Nominal compositions of the alloys (Al – bal.), in mass fractions (w/%)**Tabela 1:** Nominalna sestava zlitin (Al – ostalo), v masnih deležih (w/%)

Alloys	Mg	Si	Mn	Fe	Ti	Cu	Zn	Comment
AlMg6Mn (M3)	6.0	0.4	0.6	0.3	0.1	0.1	0.1	Al-1Mg ₂ Si-5Mg
AlMg7SiMn (MS1)	7.0	1.0	0.6	0.02	0.1	0.05	0.05	Al-3Mg ₂ Si-5Mg
AlMg7Si2Mn (MS2)	7.0	2.0	0.6	0.02	0.1	0.05	0.05	Al-6Mg ₂ Si-3Mg
AlMg5Si2Mn (MS9)	5.0	2.0	0.6	0.02	0.1	0.05	0.05	Al-6Mg ₂ Si-1Mg
AlMg7Si3Mn (MS3)	7.0	3.0	0.6	0.02	0.1	0.05	0.05	Al-9Mg ₂ Si-1Mg
AlMg7Si4Mn (MS4)	7.0	4.0	0.6	0.02	0.1	0.05	0.05	Al-10.5Mg ₂ Si-0.5Si
AlMg7Si5Mn (MS5)	7.0	5.0	0.6	0.02	0.1	0.05	0.05	Al-10.5Mg ₂ Si-1.5Si
AlSi7Mg (S1)	0.3	6.9	0.02	0.2	-	0.05	0.05	Al-7Si

The ABI test is used to measure material properties when a conventional technique cannot be applied (welded parts, brittle materials, samples with a high porosity and the parts currently used).^{4,5} As shown previously⁶, the results obtained with this method achieve good compatibility with those of the conventional methods.

2 MATERIALS AND METHODS

The chemical compositions of the evaluated alloys are shown in **Table 1**.⁶

Two types of heat treatment were applied. The first type was the solution treatment, carried out in an electric resistance furnace. After the solution treatment, the specimens were quenched at water at room temperature. The second type of heat treatment was T6, combining solution treatment at 570 °C (60 min), quenching in water at room temperature and artificial aging at 175 °C during various periods.

Indentation tests were carried out using a special device (patent CZ 304637 B1), which, due to its design,

is capable of continuously recording the load and indentation depth of the used indenter. The system includes: a recording device, an analog-to-digital converter, a PC with software and an Instron 5582 tensile-testing machine as the force-producing mechanism. The maximum indentation load was 2.5 kN and the indenter diameter was 5 mm. Plane-parallel samples were used for ABI (automatic ball indentation) testing.

Series of measurements were carried out for all the samples. The obtained *HB* hardness was compared with the hardness, measured with a standard testing machine. In the case of a good reproducibility of the results (an error of the order of 10 %) from the obtained curve (**Figure 1**), values of the yield strength and tensile strength were calculated.

The hardness was calculated with Equation (1):

$$HB = \frac{P}{\pi Dh} \quad (1)$$

where *HB* is the Brinell hardness, *P* is the load (kN), *D* is the diameter of the indenter (mm), *h* is the indentation depth (mm) (**Figure 1**).

For the determination of the tensile strength (*R_m*), we used Equation (2):⁷

$$R_m = c \cdot HB \quad (2)$$

where *c* is the coefficient of uncertainty. For the presented series of alloys, we used the following value of this coefficient – 2.8.⁶

For the determination of the yield strength (*R_{p0.2}*), the methodology proposed in ⁷, together with Equation (3), was used. The Meyer hardness was calculated with Equation (4):

$$R_{p0.2} = c \cdot HM \quad (3)$$

$$HM = \frac{P}{\pi a^2} \quad (4)$$

where *c* is the coefficient of uncertainty (2.8), *HM* is the Meyer hardness and *a* is the contact radius.

Using the values of the indentation depth (*h*), according to Equations (5) and (6), strain values (*ψ*) and the contact radius (*a*) were determined. The value of deformation for the yield stress was 0.2 %, by analogy with the tensile tests.

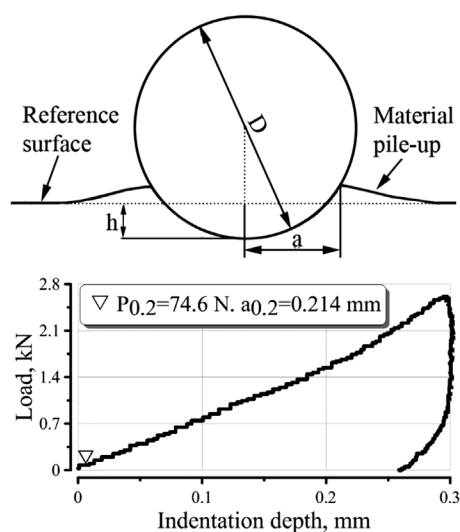


Figure 1: Scheme for determining: a) contact radius, b) indentation curve for the AlMg6Mn alloy

Slika 1: Shematski prikaz za določanje: a) kontaktnega premera, b) krivulja vtiskovanja pri zlitini AlMg6Mn

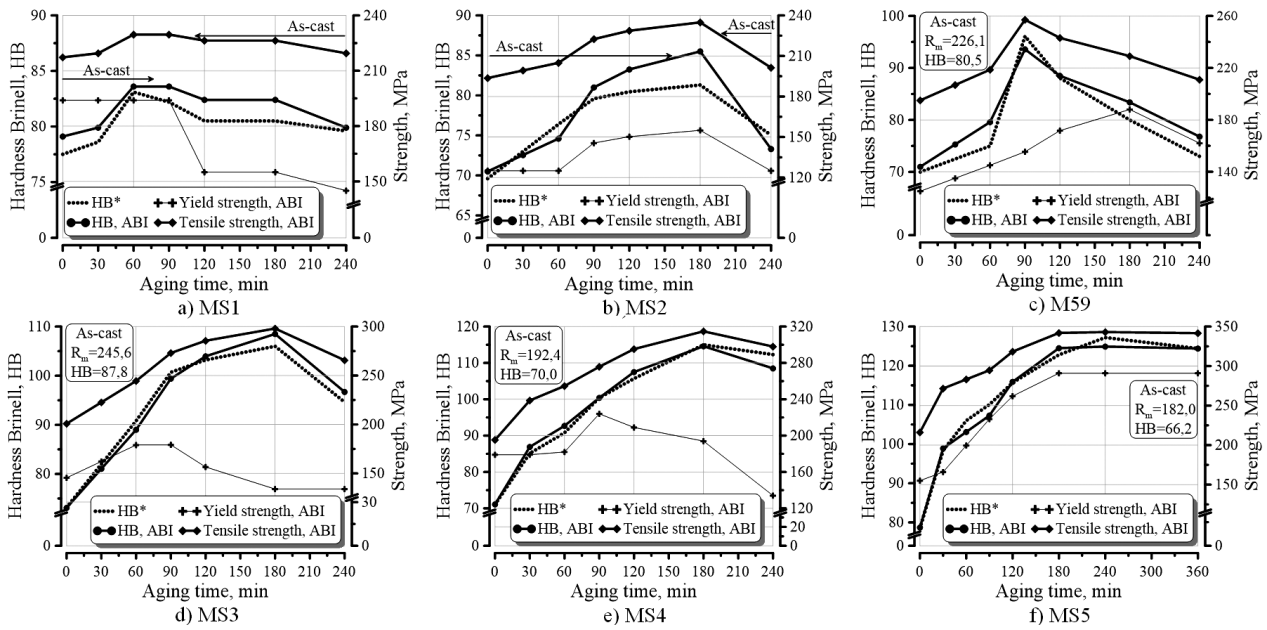


Figure 2: Mechanical properties.*Classical method
Slika 2: Mehanske lastnosti.*Klasična metoda

$$\psi = \frac{h}{D} \tag{5}$$

$$a = \sqrt{Dh - h^2} \tag{6}$$

3 RESULTS AND DISCUSSION

3.1 Mechanical properties

The values of the *HB* hardness and ABI tests are summarized in Figure 2. Figure 4 represents the dependencies of the load-indentation depth, which were recorded in the ABI study. The differences between two curves given in the diagrams (Figure 4) may be connected with the changes in the value of the load (*P*), leading to a diversity in the indentation depth and differences in the hardness of the materials (*HB*).⁶

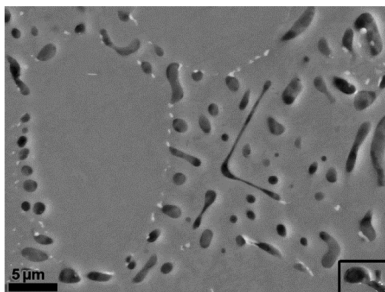
Figure 4 shows indentation curves of the alloys in the as-cast state and after the heat treatment (*T*₆).

As the result of the solution treatment, both *HB* and tensile-strength values are significantly decreased (except for the LP5 alloy). In addition, artificial aging leads to an increase in all the mechanical properties of the alloys.

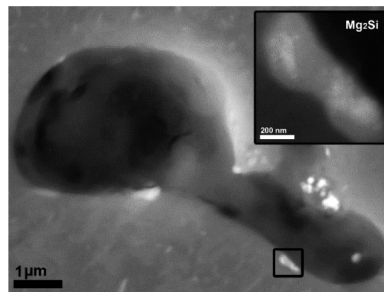
The change during the heat treatment is the result of several processes, which occur during the heating.

3.2 Processes which occur during homogenization

The first process is the eutectic spheroidisation (Figure 3a). A higher solution-treatment temperature leads to a faster eutectic-lamella decomposition into smaller segments and to the spheroidising effect. In ^{8,9} is pre-



a)



b)

Element	Concentration, in mass fractions (w/ %)
O	1.6
Mg	0.6
Al	78.7
Si	5.7
Mn	7.8
Fe	5.6

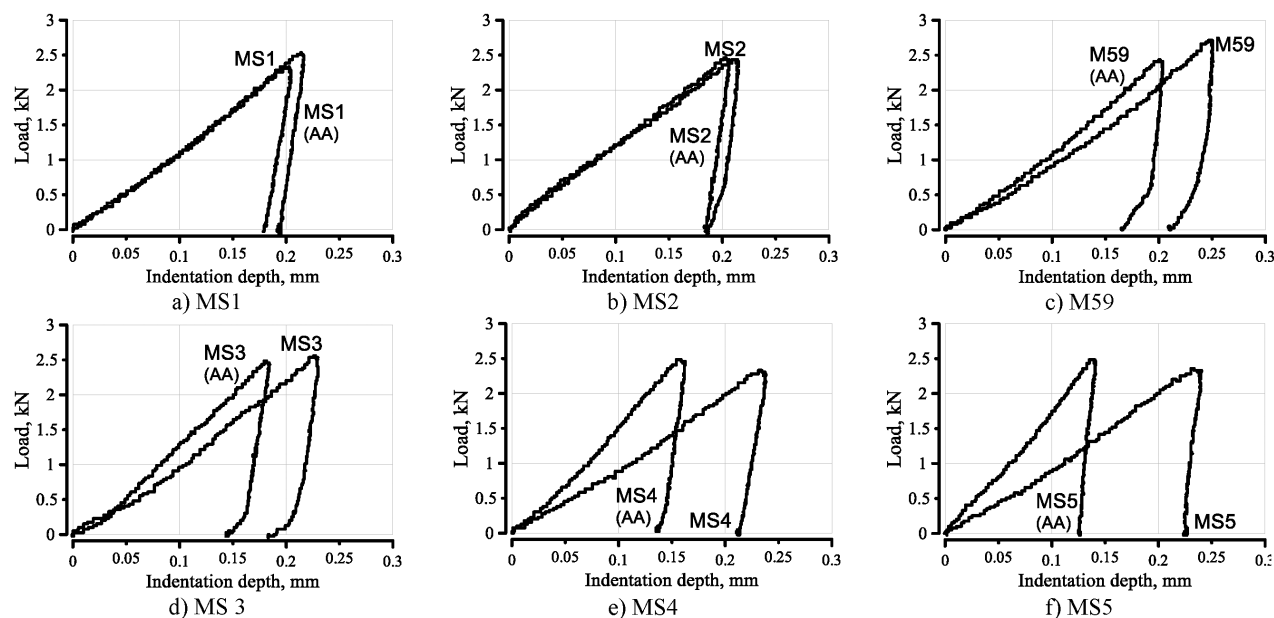
c)

Figure 3: Processes which occur during homogenization: a) spheroidisation of eutectic lamellas, b) formation of α-(Al₁₅(Mn,Fe)₃Si₂) dispersoids, c) chemical composition (EDX) of Al₁₅(Mn,Fe)₃Si₂ dispersoids

Slika 3: Procesi med homogenizacijo: a) sferoidizacija lamel evtektika, b) nastajanje disperzioidov α-(Al₁₅(Mn,Fe)₃Si₂), c) kemijska sestava (EDX) disperzioidov Al₁₅(Mn,Fe)₃Si₂

Table 2: Average compositions of Mn-containing phases in the MS4 and MS5 alloys, measured with EDX**Tabela 2:** Povprečna sestava faz, ki vsebujejo Mn v zlitinah MS4 in MS5, izmerjenih z EDX

Phase stoichiometry	Condition	Chemical composition, in mass fractions (w/%)						
		O	Mg	Al	Si	Mn	Fe	Cu
δ -Al ₄ (Mn,Fe)Si ₂ (acicular-shaped)	AC	1.5	1.1	60.4	26.8	7.6	2.2	0.4
β -Al ₅ (Mn,Fe)Si (blocky-shaped, stable)	ST	0.5	0.2	59.2	11.9	25.1	2.4	0.7

**Figure 4:** ABI indentation curves**Slika 4:** ABI krivulje pri vtiskovanju

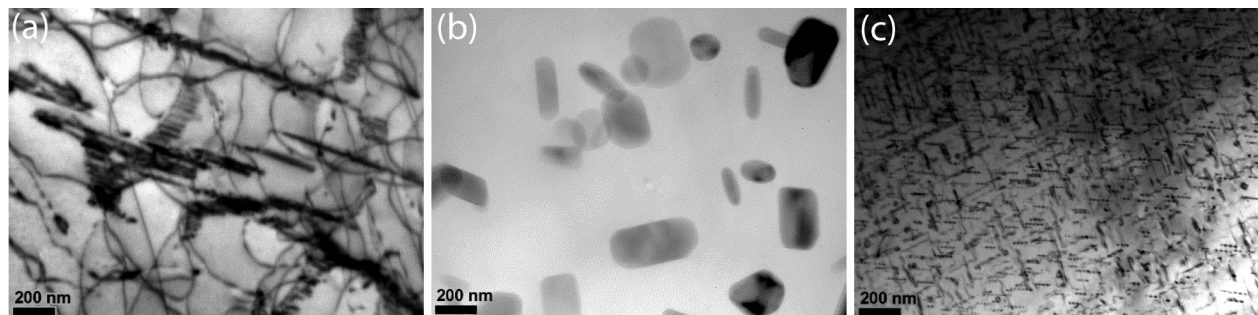
sented a model of the spheroidisation of eutectic lamellas in the alloys of the Al-Mg-Si system. This process leads to a decrease in the hardness of the alloys.

The second process is the dissolution of the primary Mn-containing phases, forming dispersoids, which include Mn, Si and Fe (**Figure 3**).¹⁰ Particle morphology is shown in **Figures 3b** and **5b**. These particles can be identified as the α -(Al₁₅(Mn,Fe)₃Si₂) phase (**Figure 3c**). A lack of coherence of phase α -(Al₁₅(Mn,Fe)₃Si₂) with α -Al probably affects (along with a disintegration of eutectic cells) the decrease in the hardness of the alloys. A dissolution of the β '-Mg₉Si₅ particles also occurs during the homogenization.

The last process occurs in alloys MS4 and MS5. This is a transformation of metastable acicular-shaped δ -phases to a more stable state due to diffusion processes.^{11–13} After the solution treatment, the excess silicon from the δ -phase dissolves in the α -aluminum solid solution.⁶ As it can be seen from **Table 2** and **Figure 5f**, this process improves the hardness even after the homogenization.

3.3 Processes which occur during aging

The remaining processes occur in the solid solution and consist of the formation of nanoscale precipitates via a decomposition of a supersaturated solid solution

**Figure 5:** TEM bright-field images of the precipitates in the AlMgSiMn casting alloy: a) as-cast state, b) after homogenization, c) after artificial ageing**Slika 5:** TEM-posnetek (svetla polja) izločkov v AlMgSiMn livni zlitini: a) lito stanje, b) po homogenizaciji, c) po umetnem staranju

(SSSS) during aging (**Figure 5**). It is established that in the Al-Mg-Si alloys, the decomposition of the super-saturated solid solution takes place during aging and the precipitation sequence is $SSSS \rightarrow GP-I \rightarrow \beta'' \rightarrow \beta' \rightarrow \beta-Mg_2Si$ where GP-I is the Guiner-Preston zone.^{12,13}

Solid-solution grains contain plate-like particles. One of their sides is connected with curved lines, which might be identified as dislocations.

Authors in^{14,15} reported that these particles are formed after natural aging as a result of a heterogeneous nucleation of dislocations. They must be particles of the $\beta'-Mg_9Si_5$ phase. A direct relationship between the dislocation density and the number of particles it is shown in^{14,15}.

As can be seen from the graphs (**Figures 4a and 4b**), heat treatment does not have a significant effect on the mechanical properties (both the hardness and tensile strength) of the alloys with extra magnesium.

According to the test results (**Figure 4**), heat treatment of the alloys with extra silicon improves the mechanical properties. With the increasing time of artificial aging (at 175 °C), the hardness of the alloys with extra silicon grows. This is due to a sufficient amount of silicon in solid solution needed for forming a larger number of strengthening particles.

4 CONCLUSIONS

A higher solution-treatment temperature leads to a faster eutectic-lamella decomposition into smaller segments and to the spheroidising effect, which causes a sharp reduction in the mechanical properties.

Homogenization leads to a dissolution of the primary Mn-containing phases and a formation of dispersoids $\alpha-(Al_{15}(Mn,Fe)_3Si_2)$.

Homogenization leads to a transformation of the metastable acicular-shaped δ -phase into a more stable state (α or β) due to diffusion processes.

Artificial aging at 175 °C leads to a formation of strengthening particles in α -Al, causing an increase in the hardness and tensile strength of the alloys. The difference between the best results for the mechanical properties of the alloys with excess Mg after the heat treatment and the properties of the as-cast alloys, is not significant.

Comparing the AlSi7Mg and AlMg5Si2Mn casting alloys, the most evident difference is the fact that the highest strength for AlSi7Mg is achieved only after the heat treatment, whereas AlMg5Si2Mn exhibits its highest properties in the as-cast condition.

Acknowledgments

The authors gratefully thank the Visegrad Fund and DAAD for their support of the research. Trudonoshyn O. and Prach O. would like to thank Mykhalenkov K. for stimulating the investigations and helping us formulate the discussion.

This work was supported by the Ministry of Education, Youth and Sport of the Czech Republic, program NPU1, project No LO1207 and SGS13/186/OHK2/3T/12 – Research on the influence of surface treatment on the improvement of service life and reliability of exposed water-turbine components.

5 REFERENCES

- I. N. Fridlyander, V. G. Sister, O. E. Grushko, V. V. Berstenev, L. M. Sheveleva, L. A. Ivanova, Aluminium alloys: promising materials in the automotive industry, *Metal Science and Heat Treatment*, 44 (2002) 9–10, 365–370, doi:10.1023/A:1021901715578
- H. Sternau, H. Koch, A. J. Franke, Magsimal-59, an AlMgMnSi-type squeeze-casting alloy designed for temper F, *Aluminium Rheinfelden GmbH*, P. O. Box 11 40, D-79601 Rheinfelden, Germany
- S. Zajac, B. Bengtsson, C. Jonsson, Influence of cooling after homogenization and reheating to extrusion on extrudability and final properties of AA6063 and AA6082 alloys, *Materials Science Forum*, 396–402 and 675–680, doi:10.4028/www.scientific.net/MSF.396-402.399
- H. Lee, J. H. Lee, G. M. Pharr, A numerical approach to spherical indentation techniques for material property evaluation, *Journal of the Mechanics and Physics of Solids*, 53 (2005), 2037–2069, doi:10.1016/j.jmps.2005.04.007
- K. Sharma, P. K. Singh, V. Bhasin, K. K. Vaze, Application of Automated Ball Indentation for Property Measurement of Degraded Zr2.5Nb, *Journal of Minerals & Materials Characterization & Engineering*, 10 (2011) 7, 661–669
- M. Puchnin, O. Trudonoshyn, O. Prach, Use of ABI technique to measure mechanical properties in aluminium alloys, Part 1: Effect of chemical composition on the mechanical properties of the alloys, *Mater. Tehnol.*, 50 (2016) 2, 247–252, doi:10.17222/mit.2014.294
- P. I. Stoev, V. I. Moschenok, Definition of Mechanical Properties of Metals and Alloys on Hardness, *Bulletin of V. N. Karazin Kharkiv National University*, 601 (2003) 2(22), 106–112
- C. Phongphisutthinan, H. Tezuka, T. Sato, Semi-Solid Microstructure Control of Wrought Al-Mg-Si Based Alloys with Fe and Mn Additions in Deformation-Semi-Solid-Forming Process, *Materials Transactions*, 52 (2011) 5, 834–841, doi:10.2320/matertrans.L-MZ201119
- S. Otarawanna, C. M. Gourlay, H. I. Laukli, A. K. Dahle, Microstructure Formation in AlSi4MgMn and AlMg5Si2Mn High-Pressure Die Castings, *Metallurgical and Materials Transactions A*, 40A (2009), 1645–1659, doi:10.1007/s11661-009-9841-1
- L. Lodgaard, N. Ryum, Precipitation of dispersoids containing Mn and/or Cr in Al-Mg-Si alloys, *Materials Science and Engineering*, 283A (2000), 144–152, doi:10.1016/S0921-5093(00)00734-6
- O. Trudonoshyn, O. Prach, V. Boyko, K. Mykhalenkov, Selection and Optimization of Heat Treatment Process to Improve the Mechanical Properties of Casting Alloys of the Al-Mg-Si System, *Casting Processes*, 106 (2014) 4, 12–21
- G. A. Edwards, K. Stiller, G. L. Dunlop, M. J. Couper, The Precipitation Sequence in Al-Mg-Si Alloys, *Acta Mater.*, 46 (1998) 11, 3893–3904, doi:10.1016/S1359-6454(98)00059-7
- C. Ravi, C. Wolverton, First-principles study of crystal structure and stability of Al-Mg-Si-(Cu) precipitates, *Acta Materialia*, 52 (2004), 4213–4227, doi:10.1016/j.actamat.2004.05.037
- V. Boyko, T. Link, N. Korzhova, K. Mykhalenkov, Microstructure characterization of AlMg5Si2Mn casting alloy, *Materials Science and Technology (MS&T) 2013*, Montreal, Quebec, Canada 2013, 1331–1338
- V. Boyko, O. Prach, O. Trudonoshyn, K. Mykhalenkov, Microstructure and Natural Hardening of AlMg5Si2Mn Casting Alloy, *Bulletin of NTUU "KPI"*, (2014), 47–54

INVESTIGATION OF THE EFFECT OF HOLDING TIME AND MELT STIRRING ON THE GRAIN REFINEMENT OF AN A206 ALLOY

PREISKAVA VPLIVA ČASA ZADRŽEVANJA IN MEŠANJA TALINE NA ZMANJŠANJE VELIKOSTI ZRN ZLITINE A206

Neşet Akar¹, Ziya Tanyel³, Kadir Kocatepe¹, Ramazan Kayikci²

¹Gazi University, Department of Metallurgical and Materials Engineering, Ankara, Turkey

²Sakarya University, Department of Metallurgical and Materials Engineering, Sakarya, Turkey

³Gazi University, Graduate School of Natural and Applied Sciences, Ankara, Turkey
rkayikci@sakarya.edu.tr

Prejem rokopisa – received: 2014-12-12; sprejem za objavo – accepted for publication: 2015-06-17

doi:10.17222/mit.2014.302

Effects of melt stirring and holding time were studied with an Al-4.5 % of mass fractions of Cu (A206) alloy. The optimum level of a grain refiner was determined in conjunction with both continuously stirred and non-stirred melts during the holding time. Results showed that a mass fraction of a Ti addition of as low as 0.03 % was sufficient to obtain the 82 µm average grain size, while a Ti addition exceeding the mass fraction of 0.03 % showed no significant effect on the grain size of castings. The grain refinement tends to fade with a long holding time in a non-stirred liquid. The results also showed that an effective grain refinement of the A206 alloy can be achieved with a long holding time as long as the liquid alloy is continually stirred.

Keywords: grain refinement, melt stirring, holding time, Al-4.5Cu alloy, A206 alloy

Raziskan je bil vpliv mešanja in časa zadrževanja taline zlitine Al-4,5 % masnega deleža Cu (A206). Določena je bila optimalna količina udrobnjevalca zrn, v povezavi s stalnim mešanjem ali brez mešanja taline med zadrževanjem. Rezultati so pokazali, da je bilo že 0,03 % masnega deleža dodatka Ti, dovolj za doseganje povprečne velikosti zrn 82 µm, medtem ko dodatek Ti večji od 0,03 % masnega deleža, ni pokazal vpliva na velikost zrn ulitkov. Učinkovitost drobnjenja zrn se zmanjša pri dolgih časih zadržanja in brez mešanja taline. Rezultati so pokazali še, da je mogoče doseči učinkovito drobnjenje zrn tudi pri dolgih časih zadrževanja, dokler se talina stalno meša.

Ključne besede: drobnjenje zrn, mešanje taline, čas zadrževanja, zlitina Al-4.5Cu, zlitina A206

1 INTRODUCTION

Al-Cu alloys are one of the most important Al-based alloys because they provide good castability and excellent mechanical properties.¹⁻⁶ Due to their superior mechanical properties, Al-Cu alloys can be used in many areas such as aircraft construction, military field and automobile manufacturing.⁴ Grain refinement of Al-Cu alloys significantly improves the microstructure and mechanical properties.⁷⁻⁹ Along with many advantages, hot tearing, which frequently occurs during solidification due to a long freezing range, is a severe problem in producing cast components with these alloys. Previous works on casting and solidification of Al-Cu alloys consistently indicated that hot tearing can be eliminated with a good grain refinement.^{1-4,7-9} Grain refinement was also found to be effective for reducing the amount of the porosity and size of the pores, and improving the feeding of cast Al-Cu alloys.⁹ Titanium and boron are added in the form of Al-Ti-B master-alloy rods to cast aluminium alloys for the grain refinement. Rod-type additions were found to be more effective for providing, controlling and optimizing TiB₂ particles than the salt form.^{10,11} It was reported in recent years that Al-Ti-C master alloys are

also effective grain refiners.^{4,12} Due to its high refining potential, an Al5Ti1B alloy in the rod form is one of the most commonly used grain refiner and has been widely accepted in controlling the grain size and microstructures of aluminium alloys in industrial applications.¹³

The A206 alloy is a well-known Al-Cu casting alloy and a research on grain refinement with this alloy indicated that a proper grain refinement can be achieved with a 0.15–0.30 % titanium mass fraction of the final cast part.¹⁴ On the contrary, in recent years other researchers^{3,5,7-9} showed that modern grain refiners containing Al-Ti and B are more suitable for an acceptable grain refinement of A206 alloys if the Ti content is lower than 0.15 %.

Despite a number of studies conducted in the past to investigate the grain refinement of Al-Cu alloys,^{3,5-9,12,15-16} studies on the effects of the holding time and melt stirring on the grain-refinement process have not been published. Therefore, in this work, the optimum amount of the grain refiner for the A206 alloy, using an Al5Ti1B rod-shape grain refiner, in combination with the holding time and melt stirring, was studied.

2 EXPERIMENTAL PROCEDURES

A206 alloys with two different chemical compositions were prepared using commercial-purity Al ingots and commercially pure Cu wires in a new SiC crucible. The final chemical compositions of these alloys before the grain-refiner additions are given in **Table 1**. A Spectro-type optical spectrometer was employed to perform a chemical analysis of the alloys throughout this study. An industrial electrical-resistance furnace with a 600 kg capacity and a SiC crucible were used for the melting.

An Al5Ti1B master alloy was introduced into the liquid A206 alloy at 730 °C followed by rotary degassing for 10 min with dry argon. The temperature of the liquid metal in the melting furnace was continuously controlled with a K-type thermocouple connected to the control unit of the furnace to ensure the holding of the liquid at 730 °C.

Grain-refining experiments were carried out using the Alcan standard grain-refining test¹⁰ with two sets of samples. In the first set of experiments, samples were taken from the crucible at 730 °C, before the grain-refiner addition. Samples were also taken after each addition of the Al5Ti1B rod-type master alloy introducing (0.01, 0.02, 0.03, 0.05, 0.1, 0.2, 0.3) % Ti contents into the liquid alloy. After each addition, the liquid alloy was re-degassed for 10 min at 730 °C. This resulted in 10-min intervals between the sample-taking processes.

The second set of experiments was carried out to determine the effects of the holding time coupled with melt stirring on the grain refinement. To implement this, a new heat of the A206 alloy was melted in a new crucible and heated up to 730 °C. The Al5Ti1B master alloy was introduced into the melt to obtain a 0.05 % Ti content within the alloy. After a 10-min degassing treatment, the purging argon was turned off and the molten alloy was continuously stirred using the graphite lance of the rotary degassing unit with a rotating speed of 150 min⁻¹ for 90 min. Samples for the Alcan grain-refining tests were taken during the whole stirring period, in 30-min intervals from the beginning to the end.

Finally, the melt was re-degassed for 10 min and held for another 90 min without any stirring actions. During this second 90-min period, Alcan test samples were also

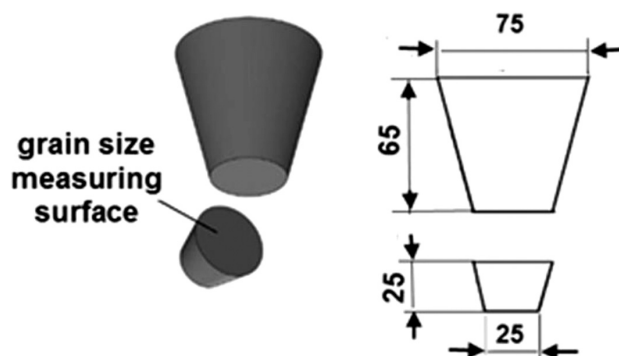


Figure 1: Alcan test dimensions and grain-size measuring surface
Slika 1: Dimenzije Alcan preizkušanca in površina za merjenje velikosti zrn

taken in 30-min intervals, in the same manner as explained above. At the end of this period, the melt was re-stirred for only 1 min and the final sample was taken.

The specimens for the metallographic examinations were cut as shown in **Figure 1**. The surface of each specimen was electro-polished using 5 mL of HClO₄, 15 mL of 2-Butoxyethanol, 60 mL of ethanol and 20 mL of distilled water. The average grain size was determined with the linear intercept method according to the ASTM E112 standard, at different regions of each sample.

3 RESULTS AND DISCUSSION

3.1 Grain-size measurements

The mean values of the measured grain sizes with various Ti contents are shown in **Table 2**, which indicates that the titanium contents in the alloy were determined within a narrow variance. **Table 2** also shows that the grain size of the samples decreased dramatically with the addition of the Al5Ti1B master alloy regardless of the titanium content. The average grain size versus the Ti content is also shown in **Figure 2**. **Figure 2** indicates that the addition of the grain refiner, even with a Ti content as low as 0.01 %, resulted in a remarkable reduction in the grain size of the alloy. **Figure 2** also indicates that the lowest grain size of the alloy is about 80 μm, which was obtained with a 0.03 % Ti content. A higher Ti con-

Table 1: Chemical compositions of A206 alloys before the grain refinement, in mass fractions (w%)

Tabela 1: Kemijska sestava zlitin A206, pred udrobnjenjem zrn, v masnih deležih (w%)

Experiment number	in mass fractions (w%)								
	Si	Fe	Cu	Mn	Mg	Zn	B	Ti	Al
1	0.041	0.105	4.510	0.281	0.214	0.098	0.001	0.000	bal.
2	0.039	0.107	4.610	0.353	0.199	0.084	0.002	0.007	bal.

Table 2: Average grain size of the samples with different Ti contents

Tabela 2: Povprečna velikost zrn pri vzorcih z različno vsebnostjo Ti

Ti (w%)	Target	0	0.01	0.02	0.03	0.05	0.1	0.2	0.3
	Realized	0	0.013	0.019	0.032	0.044	0.098	0.194	0.292
Average grain size (μm)	970	112	92	82	81	79	81	79	

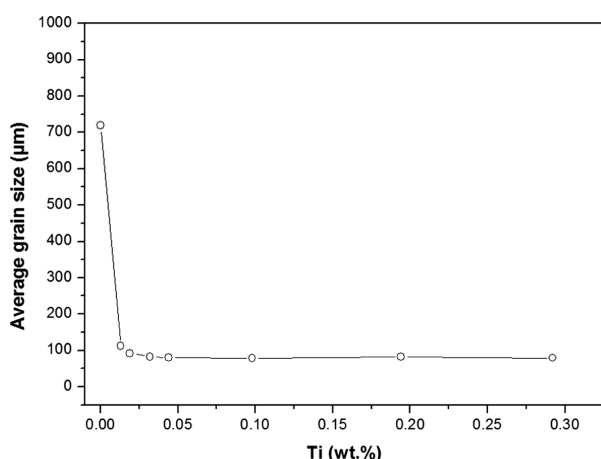


Figure 2: Effect of the Ti content on the grain size of the A206 alloy
Slika 2: Vpliv vsebnosti Ti na velikost zrn zlitine A206

tent within the A206 alloy did not further reduce the grain size of the samples. These results are in good agreement with the previous work carried out by Sigworth and co-workers.^{3,7-8}

The relationship between the titanium recovery and the microstructure is given in **Figure 3**. **Figure 3a** shows the microstructure of the sample obtained with no grain-refiner addition. The microstructure consists of coarse dendrites, heterogeneously distributed in equiaxed grains. **Figure 3b** shows a small addition of Ti, as low as a 0.01 % mass fraction, which caused the grain refinement of the A206 alloy. However, a Ti content of up to 0.05 % was found to be more effective for further reducing the average grain size of the alloy, as seen in **Figure 3c**. The microstructure obtained with a 0.3 % mass fraction of Ti in the melt is shown in **Figure 3d**. It indicates that the increased amount of Ti no longer affected the reduction of the grain size of the A206 alloy used in this study.

The Al5Ti1B master alloy is an effective grain refiner of Al-Cu alloys as it increases the number of heterogeneous nucleation sites for achieving a finer equiaxed grain structure.¹⁰ **Figure 3** clearly shows that a Ti content exceeding the mass fraction of 0.01 % is adequate to turn

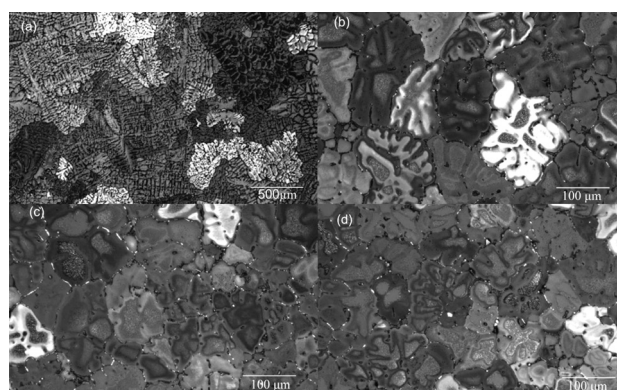


Figure 3: Microstructure of the A206 alloy with different Ti additions: a) 0 % of mass fractions, b) 0.01 % of mass fractions, c) 0.05 % of mass fractions and d) 0.3 % of mass fractions

Slika 3: Mikrostruktura zlitine A206 z različnimi dodatki Ti: a) 0 % masnega deleža, b) 0,01 % masnega deleža, c) 0,05 % masnega deleža in d) 0,3 % masnega deleža

the solidification morphology of the alloy from a fully dendritic to a globular or near-dendritic structure. Thus, the grain refinement of the A206 alloy by adding the Al5Ti1B master alloy can be expected to increase the mechanical properties of A206 castings via reducing the amount of solidification defects such as hot tearing, micro-shrinkage and micro-segregation. These results are in good agreement with the report from H. Kamali et al.⁵ who reported that Ti additions of 0.05–0.3 % showed no significant effect on the grain size, although the minimum Ti mass fractions of 0.05 % was necessary to eliminate the hot-tearing defects.

3.2 Effects of the holding time and melt stirring on the grain size

In the present study, possible effects of melt stirring during the holding period after the master-alloy addition were also investigated. Experiments were carried out with the castings from two different heats of stirred and non-stirred melts. Samples were cast in 30-min intervals throughout the 90-min holding time, during which the amount of Ti was fixed at around 0.05 % of mass fractions.

Table 3: Effect of the holding time on the average grain size

Tabela 3: Vpliv časa zadrževanja na povprečno velikost zrn

Liquid-metal condition	Holding time (min)	Ti recovery (w%)	B recovery (w%)	Ti:B ratio	Average grain size (µm)
Heat 1 Stirred melt	0	0.049	0.009	5.4	84
	30	0.046	0.008	5.8	84
	60	0.047	0.008	5.9	85
	90	0.048	0.009	5.3	84
Heat 2 Non-stirred melt	0	0.046	0.009	5.1	84
	30	0.036	0.005	7.2	88
	60	0.035	0.004	8.8	102
	90	0.031	0.003	10.3	111
	90*	0.048	0.009	5.3	85

(90*) Stirring after 90 min.

A summary of the quantitative results obtained from the test samples throughout these experiments are shown in **Table 3**. Titanium and boron measured in the samples, cast with the stirred melt, show that both elements remained at almost their initial values during the 90-min holding time. Accordingly, the initial Ti:B ratio also remained constant, which was around 5:5. The average grain size of the stirred melt was about 85 μm regardless of the holding time. These results emphasise the fact that the refining efficiency of the Al5Ti1B type master alloy is consisted, at least during the 90-min holding time, even with the Ti recovery as small as 0.05 % of mass fractions of Ti in the A206 alloy. On the other hand, the results obtained for the non-stirred melt reveal that both titanium and boron recovery decreased with the increasing holding time. Interestingly, the diminution in boron was faster compared to titanium, especially in the first 30 min of the holding time, for the non-stirred melt. Therefore, the measured Ti:B ratio shows a continuous increase as the period of the holding time increases.

In **Table 3**, the average measured grain size for the samples of the non-stirred melt also shows a consisted increase with the holding time. This is associated with the diminishing of the Ti and B recovery and the ever increasing Ti:B ratio with the increasing holding time for the non-stirred heat. It is also obvious from **Table 3** that

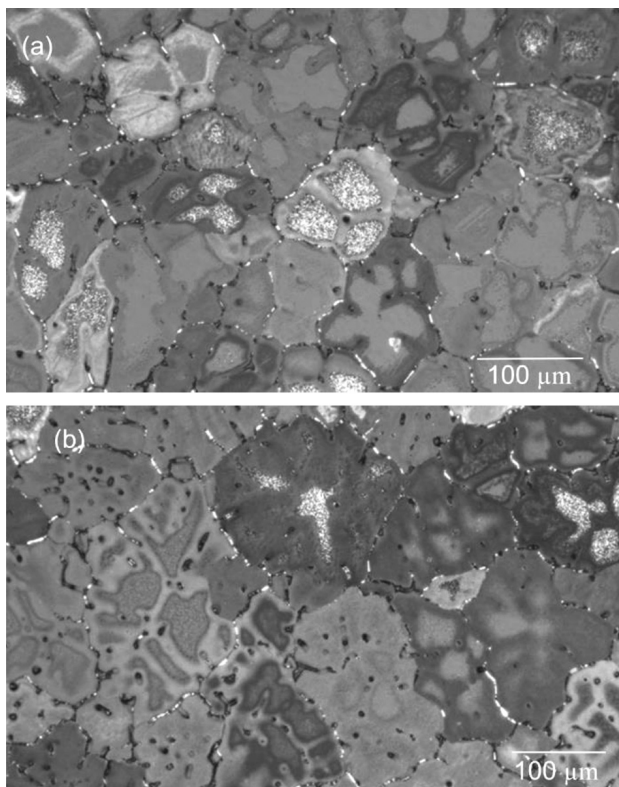


Figure 4: Microstructures of Alcan test samples after a 90 min holding time and an Al5Ti1B master-alloy addition. Samples were cast from: a) continuously stirred melt and b) non-stirred melt.

Slika 4: Mikrostruktura Alcan preizkušancev po 90 min zadrževanju po dodatku predzlitine Al5Ti1B. Vzorci so bili uliti iz: a) kontinuirno mešane taline in b) taline brez mešanja.

an immediate stirring action followed by a 90-min holding time facilitated the Ti and B levels as well as the Ti:B ratio to remain almost at their initial values. This also caused a similar consequence in the measured grain size. These results are in good agreement with a number of previous studies on Al-Cu alloys. Grain-refining studies on non-stirred melts were concluded so that the grain size increased continuously with the increasing holding time;^{11–12,16} however, it began to decrease when the stirring action was resumed.¹⁶

The phenomenon of decreasing Ti and B with the increasing holding time in the non-stirred A206 alloy can be attributed to the settling of TiB₂. This compound has been widely accepted as one of the potential nucleation sites during the solidification of aluminium.^{19–22} Since the density of a solid TiB₂ compound is higher (4.48 g/cm³)¹⁷ than that of the liquid A206 alloy (2.78 g/cm³), it is quite probable that some potential TiB₂ nuclei are disqualified because they sink to the bottom of the crucible as the holding time increases.

The microstructures representing the Alcan test samples obtained from the heats after the 90-min holding time are shown in **Figures 4a** and **4b**. A comparison of the two microstructures provides an explanation of the difference between the stirred and the non-stirred melts. The larger grain size for the non-stirred melt in **Figure 4b** can be associated with a weaker grain-refining action of the master alloy during the 90-min holding. This can also be related to the fading of the potential nuclei probably due to the gravity action of the TiB₂ compound.¹⁸

4 CONCLUSIONS

The grain-refining effects of the Al5Ti1B rod-type master alloy on a commercial A206 alloy with different addition levels were studied. The effects of the holding time under stirring and no-stirring conditions were also studied. From the experimental results, the following conclusions can be drawn:

- 1) Different amounts of titanium recovery ranging from 0.01 to 0.3 were formed in the A206 alloys. Measurements showed that the grain size of the Alcan test samples decreased dramatically with an addition of the Al5Ti1B master alloy regardless of the titanium recovery.
- 2) The smallest average grain size of the A206 alloy was 82 μm , achieved with a 0.03 % of mass fraction of Ti recovery in the melt. Increasing the Ti recovery up to a 0.3 % of mass fractions did not result in a further decrease in the grain size of the A206 alloy.
- 3) Grain-size measurements for two different heats showed that the average initial grain size of the samples increased from 84 μm to 111 μm at the end of the 90-min holding time for the non-stirred liquid. However, a constant grain size was achieved for the stirred melt throughout the holding period.
- 4) The results obtained for the non-stirred melt revealed that both titanium and boron recovery decreased with

the increasing holding time. During the holding period, the diminution in boron was larger compared to titanium, as measured on the cast samples. This was attributed to the formation of a TiB_2 compound in the melt, which is widely accepted as a heterogeneous nucleation site for aluminium. Since the density of TiB_2 is higher than that of the liquid A206 alloy, the compound tends to settle in the non-stirred melt, which may be the reason for the fading of the grain-refining efficiency as the holding time increases.

- 5) The refining efficiency of the Al5Ti1B-type master alloy can be stimulated via re-stirring the melt. The results showed that an immediate stirring action followed by a 90-min holding time reverted Ti and B and also the Ti:B ratio almost to their initial conditions. The Alcan test samples of the re-stirred melt also showed a well-refined grain structure.

Acknowledgements

Authors thank Mr. Ahmet Cevdet Altun at Altun Döküm A.Ş., Konya, Turkey, for the casting experiments carried out at the premises of the company.

5 REFERENCES

- ¹ H. K. Kamga, D. Larouche, M. Bournane, A. Rahem, Mechanical properties of aluminium-copper B206 alloys with iron and silicon additions, *International Journal of Cast Metals Research*, 25 (2012), 15–25, doi:10.1179/1743133610Y.0000000012
- ² H. K. Kamga, D. Larouche, M. Bournane, A. Rahem, Hot tearing of aluminum-copper B206 alloys with iron and silicon additions, *Materials Science and Engineering*, 527A (2010), 7413–7423, doi:10.1016/j.msea.2010.08.025
- ³ G. K. Sigworth, F. DeHart, Recent developments in the high strength aluminum-copper casting alloy A206, *AFS Transactions*, 111 (2003), 341–354
- ⁴ T. Wang, T. Gao, P. Zhang, J. Nie, X. Liu, Influence of a new kind of Al-Ti-C master alloy on the microstructure and mechanical properties of Al-5Cu alloy, *Journal of Alloys and Compounds*, 589 (2014), 19–24, doi:10.1016/j.jallcom.2013.11.187
- ⁵ H. Kamali, M. Emamy, A. Razaghian, The influence of Ti on the microstructure and tensile properties of cast Al-4.5 Cu-0.3 Mg alloy, *Materials Science and Engineering A*, 590 (2014), 161–167, doi:10.1016/j.msea.2013.10.032
- ⁶ Y. D. Kwon, Z. H. Lee, The effect of grain refining and oxide inclusion on the fluidity of Al-4.5 Cu-0.6 Mn and A356 alloys, *Materials Science and Engineering A*, 360 (2003), 372–376, doi:10.1016/S0921-5093(03)00504-5
- ⁷ G. K. Sigworth, Improved hot crack resistance, U.S. Patent US6, 645, 321, 11. 11. 2003
- ⁸ G. K. Sigworth, Providing melt of aluminum base alloy, maintaining dissolved titanium in range of 0.005 to 0.05 wt.% to improve resistance of alloy to hot cracking, adding nucleating agent selected from metal carbides, aluminides, borides, solidifying, U.S. Patent US6, 368, 427, 9. 4. 2002
- ⁹ G. K. Sigworth, T. A. Kuhn, Grain refinement of aluminum casting alloys, *AFS Transactions*, 115 (2007), 1–12
- ¹⁰ G. P. Jones, J. Pearson, Factors affecting the grain-refinement of aluminum using titanium and boron additives, *Metallurgical Transactions B*, 7 (1976), 223–234, doi:10.1007/BF02654921
- ¹¹ K. Sato, M. C. Flemmings, Grain refining of Al-4.5 Cu alloy by adding an Al-30TiC master alloy, *Metallurgical and Materials Transactions A*, 29 (1998), 1707–1710, doi:10.1007/s11661-998-0093-2
- ¹² P. Cooper, A. Barber, Review of the latest developments and best use of grain refiners, 2th International Melt Quality Workshop, Prague, Czech Republic 2003
- ¹³ Alcan AA206 Primary Foundry Alloys 206.2, A206.2 and B206.2, Alcan Primary Products Corporation Inc., Robards, KY, USA 2004
- ¹⁴ S. Li, K. Sadayappan, D. Apelian, Role of Grain Refinement in the Hot Tearing of Cast Al-Cu Alloy, *Metallurgical and Materials Transactions B*, 44 (2013), 614–623, doi:10.1007/s11663-013-9801-4
- ¹⁵ M. A. Kearns, S. R. Thistlewaite, P. S. Cooper, In W. Hale (Ed.), *Light Metals TMS*, Warrendale 1996
- ¹⁶ H. Li, T. Sritharan, Y. M. Lam, N. Y. Leng, Effects of processing parameters on the performance of Al grain refinement master alloys Al-Ti and Al-B in small ingots, *Journal of Materials Processing Technology*, 66 (1997), 253–257, doi:10.1016/S0924-0136(96)02536-8
- ¹⁷ L. Zhou, Z. Fan, Effect of Free Ti on Grain Refinement of Aluminium Inoculated with Potent TiB_2 Particles, *Materials Science Forum*, 790–791 (2014), 155–160, doi:10.4028/www.scientific.net/MSF.790-791.155
- ¹⁸ P. S. Mohanty, J. E. Gruzleski, Mechanism of grain refinement in aluminium, *Acta Metallurgica et Materialia*, 43 (1995) 5, 2001–2012, doi:10.1016/0956-7151(94)00405-7
- ¹⁹ P. S. Mohanty, J. E. Gruzleski, Grain refinement mechanisms of hypoeutectic Al-Si alloys, *Acta Materialia*, 44 (1996) 9, 3749–3760, doi:10.1016/1359-6454(96)00021-3
- ²⁰ C. Wang, M. Wang, B. Yu, D. Chen, P. Qin, M. Feng, Q. Dai, The grain refinement behaviour of TiB_2 particles prepared with in situ technology, *Materials Science and Engineering A*, 459 (2007), 238–243, doi:10.1016/j.msea.2007.01.013
- ²¹ Z. Fan, Y. Wang, Y. Zhang, T. Qin, X. R. Zhou, G. E. Thompson, T. Pennycook, T. Hashimoto, Grain refining mechanism in the Al/Al-Ti-B system, *Acta Materialia*, 84 (2015), 292–304, doi:10.1016/j.actamat.2014.10.055
- ²² X. Wang, Z. Liu, W. Dai, Q. Han, On the Understanding of Aluminium Grain Refinement by Al-Ti-B Type Master Alloys, *Metallurgical and Materials Transactions B*, (2014), doi:10.1007/s11663-014-0252-3

INVESTIGATING THE INFLUENCE OF CUTTING SPEED ON THE TOOL LIFE OF A CUTTING INSERT WHILE CUTTING DIN 1.4301 STEEL

PREISKAVA VPLIVA HITROSTI REZANJA NA ZDRŽLJIVOST VLOŽKA ZA REZANJE PRI REZANJU JEKLA DIN 1.4301

Rozmarína Dubovská¹, Jozef Majerík², Robert Čep³, Karel Kouřil⁴

¹University of Hradec Kralove, Faculty of Education, Department of Technical Subjects, Rokitanského 62, 500 03 Hradec Králové, Czech Republic

²Alexander Dubcek University of Trenčín, Faculty of Special technology, Department of Engineering, Pri Parku 19, 911 05 Trenčín, Slovakia

³Technical University of Ostrava VŠB, Faculty of Mechanical Engineering, Department of Machining and Assembly, 17.listopadu 15, 708 33 Ostrava, Czech Republic

⁴Brno University of Technology, Faculty of Mechanical Engineering, Institute of Manufacturing Technology, Technická 2896/2, 616 69 Brno, Czech Republic
robert.cep@vsb.cz

Prejem rokopisa – received: 2015-02-10; sprejem za objavo – accepted for publication: 2015-05-20

doi:10.17222/mit.2015.036

The main aim of this paper is to assess the tool life $T = f(v_c)$ during the dry turning of 1.4301 austenitic stainless steel with a CNMG 120408 coated carbide cutting insert. Experimental tests of the selected material were realized in an Aero Turn BT-380 CNC machine tool with a Fanuc 21i TB control system. The effect of the applied cutting parameters on the surface finish, tool wear, tool life and surface roughness were investigated during the realized experiments. The aim of the present paper is to focus scientific research on the impact of the various cutting speeds during the outer longitudinal turning. The presented approach and results will be helpful for understanding the machinability of 1.4301 austenitic stainless steel during dry turning. This paper, together with the achieved results, is a basis to optimize the performance of the machining (i.e., turning) of austenitic stainless steel 1.4301 used for special industrial applications with their dominant functional areas.

Keywords: austenitic stainless steel, CNC turning, cutting speed, tool life, surface finish

Glavni namen članka je oceniti preiskovano zdržljivost orodja $T = f(v_c)$ pri struženju, brez mazanja avstenitnega nerjavnega jekla 1.4301, s karbidnim rezalnim vložkom CNMG 120408 s prevleko. Preizkusi izbranega materiala so bili izvršeni na CNC stroju Aero Turn BT-380 s Fanuc 21i TB kontrolnim sistemom. Med preizkusi je bil preiskovan vpliv uporabljenih parametrov pri rezanju na kvaliteto površine, obrabo orodja, zdržljivost orodja in hrapavost. Namen članka je usmeriti raziskavo na vpliv različnih uporabljenih vrednosti hitrosti rezanja pri zunanem vzdolžnem struženju. Vsi predstavljeni približki in rezultati bodo pomagali pri razumevanju obdelovalnosti avstenitnega nerjavnega jekla 1.4301 pri struženju brez mazanja. Dobljeni rezultati so osnova za optimiranje struženja avstenitnega nerjavnega jekla 1.4301, ki se ga, na podlagi posebnih lastnosti, uporablja pri posebnih industrijskih namenih.

Ključne besede: avstenitno nerjavno jeklo, CNC struženje, hitrost rezanja, zdržljivost orodja, kvaliteta površine

1 INTRODUCTION

High productivity and reliability are necessary in today's very highly competitive world of production. In this context, the appropriate selection of cutting tool geometry and tool material is crucial to be competitive, especially in the field of difficult-to-machine materials, such as stainless steels.^{1,2} Problems such as poor surface finish and high tool wear are common in the machining of austenitic stainless steel. The authors³ carried out turning tests on the 1.4301 austenitic stainless steel to determine the optimum machining parameters. Austenitic stainless steel is among the difficult-to-cut material and difficulties such as poor surface finish and rapid tool wear are common.⁴⁻⁸ Stainless steels are widely used in several industrial sectors, such as engine production, the medical and chemical industries. Their high strength, low thermal conductivity, high ductility and high tendency towards work hardening are the main factors for

their poor machinability.⁹ The turning of parts made of austenitic stainless represents nearly 24 % of all machined parts made of steel. Various special chemical compositions of stainless steels are a challenge for all machining technologies. High-speed machining (HSM) is applied with significantly higher cutting speeds v_c with relatively small cross-sections being cut. HSM technology is realized with extremely hard and heat-resistant cutting tools.¹⁰ With the trend in technology development, stainless steel has been broadly adopted because it has the characteristics of high toughness, low thermal conductivity, and a high strain hardening coefficient. This has a negative effect on the surface finish of a machined product and results in a reduced tool life.¹¹ Such is the case for austenitic stainless steels, which in spite of being materials of high economic and technological value, their behaviour with respect to machining is still not well understood in some aspects. There are

not reliable and updated technological data about austenitic stainless steels in industry.¹² The austenitic stainless steel AISI 304 (according to DIN 1.4301) is the second most widely used anti-corrosive material with excellent corrosion resistance, cold formability and weldability. The steel 1.4301 is resistant to water, steam, humidity, edible acids, weak organic and inorganic acids.¹³ Austenitic stainless steel is not hardenable. However, its strength can be increased by cold forming. It is characterized by the need for a solution treatment to ensure corrosion resistance in contact with a wide range of substances. The AISI 304 is approved for a thermal stress of 300 °C. When machining the 1.4301 it is necessary to work with sharp cutting tools of high-speed alloyed steel or cemented carbides because of the tendency to harden. The steel 1.4301 (AISI 304) is used in the engineering and nuclear industries, in architecture, in transport facilities, the food industry, the pharmaceutical and cosmetic industries, the construction of chemical apparatus and vehicles, the manufacture of surgical instruments, sanitary installations, objects and appliances and works of art. The shape of the individual components for the automotive industry and subsequently the time and relative complexity of the conversion work and tool paths for CNC (Computer Numerical Control) program preparation led to the establishment of internal and external graphics support for the creation of individual programs.¹⁴ CNC machines are commonly used in automated factories for producing machined parts. In this study, the AISI 304 austenitic stainless steel was used to help the manufacturers. In this work, the values for the flank wear were investigated and in this way the best cutting parameters were determined. Apart from classic methods, it was also investigated that the process sound generated during machining could be used to assess machinability.¹⁵ Surface integrity is an important factor in evaluating the machinability of the steels.¹⁶ Numerous experimental investigations have been carried out over the years to study the effect of the cutting parameters and tool geometries on the workpieces' surface integrity using several types of workpiece materials.¹⁷ Currently, companies prefer to order material according to DIN or AISI.

2 MATERIALS AND METHODS

The basic factor that causes the flank wear of carbide tools is the high temperature of the cutting edge. In order to increase tool life, we have to reduce this temperature. For machining is necessary to use a stable and solid CNC machine tool with the appropriate cooling. The workpiece material and cutting tools must be firmly clamped in the CNC machine with a small overhang. It is important to create the conditions for cutting, to prevent the formation of vibrations. Progressive solutions in terms of cutting tools seem to be new cutting materials for machining stainless, especially austenitic, steels.

There are cutting tools with changeable cutting inserts with a fine-grained or ultrafine-grained substrate. The carbide grain size is from 0.3 µm to 0.5 µm. On the cemented carbide is deposited a multilayer with the coatings type TiC+Al₂O₃+TiN on the surface, the substrate is WC+Co. The austenitic stainless steels are generally annealed for austenitizing, so that they are heated to 1000–1150 °C. Subsequently, they are quickly cooled in water or air, to prevent the precipitation of the carbides at the grain boundaries. This resulted in a homogeneous austenitic structure. The structure increases with the resistance of these steels to intergranular corrosion and the metallurgical point of view is correct. The disadvantage is a significant increase in the ductility and plasticity of these steels, which is highly undesirable during operation. From the metallurgical point of view, the distinguishing feature of poor machinability is the kinematic coarse austenite, almost carbides. The sign of good machinability is a fine-grained austenite with plenty of finely distributed carbides. Machinability is related to the economy of production. The aim is to produce the maximum performance with the available resources. Machinability influences and even determines the cutting forces, heat and cutting temperature, chip formation, wear and tool life, but also the surface integrity. Cutting parameters such as the cutting speed v_c and the feed rate f play critical roles in the cutting temperature and the surface roughness in the turning processes. The surface roughness, which is used for the evaluation of the product quality, is an important performance characteristic in turning processes.¹⁸ That is, cutting speeds out of the range recommended by tool manufacturers (cutting speed in the range of $v_c = 180\text{--}250\text{ m min}^{-1}$) were tested. The objective was to analyse the effect of cutting speed over the work material–toolpair.¹⁹ I. Korkut et al.¹⁹ and I. Ciftci et al.²⁰ reported that during the turning of AISI 304 austenitic stainless steel using a multilayer (CVD) coated tool, the tool flank wear decreases with an increasing cutting speed up to 180 m min⁻¹ and the surface roughness values decrease with the increasing the cutting speed. The poor performance of the tool at lower cutting speeds can be explained by the influence of the heat on the cutting tool. That is because, metal cutting involves the generation of a large amount of heat and in the machining of AISI 304 stainless steel it is not dissipated rapidly due to the low thermal conductivity of this material. The heat generation principally occurs in three areas: the shear zone, the rake face and on the clearance side of the cutting edge.²⁰ W. Grzesik et al.²¹, studied the machinability of AISI 304 and C45 steel using CVD TiC, TiN/ TiC and TiN/Al₂O₃/TiC coated and uncoated (P20) cemented carbide tools. They found that in the case of TiC and TiN/Al₂O₃/TiC coating the specific cutting pressure decreases and for the TiC/TiN coating it increases. In another study they found a low value of the surface roughness for the coating TiC/Al₂O₃/TiN. In addition, they found that as the

cutting speed increases the cutting force and the contact length decreases. A. Hosokawa et al.²² reported that during its own realization of turning tests of stainless steel (AISI 304) were carried out in order to examine the tool-wear characteristics. W. I. H. Liew²³ investigated the wear characteristics of PCBN (polycrystalline cubical boron nitride) tools in the ultra-precision machining of stainless steel.²² During lathe turning, the machined surface is work hardened. This work-hardened surface is machined on the next lathe turning step, which accelerates the tool wear.²³ This results in the degradation of the surface quality and the acceleration of the adhesive wear of the tools used.²⁴ All of these experiments determine that the purpose and the machinability significantly affect the cutting process. The machining of high-strength materials can cause brittle fracture of the cutting edge parts. This is due to the high cutting forces during machining. In a practical assessment of the size of the wear it is most common to use parameters such as the width of the wear pads on the back of the VB_k and the depth of the groove at the forefront of the KT (according to ISO 3685). The intensity of the wear may affect the cutting conditions. The biggest influence is the cutting speed, then the feed rate and a smaller minimum is the depth of cut. When turning austenitic stainless steels, they are a generally chosen criterion of the flank wear VB_k , given the increase in cutting forces with increasing wear. There is also an increase in the temperature and the intensity of the wear of the cutting tool. The duration of the work of the cutting tool with a target of VB_k wear, the tool life T can be determined within minutes of the machining time, the number of machined parts or the cutting tool path. The cutting tool's ability to restore its sharpness or setting a new cutting edge with a cutting tool exchange. In practice we try to choose the criterion of wear, so that we have the maximum tool life. Selection criteria and the process limits the wear and machined surface roughness achieved, increased cutting

forces, and the emergence of oscillations in the system's working. We are talking about the technological criterion of wear. The tool life depends on the cutting conditions, the geometry of the cutting wedge-shaped tools, the cutting material, the fluency of the cutting process, the method and type of operation and the workpiece material.

3 EXPERIMENTAL DETAILS

The main aim of the paper was the measurement of the tool life $T = f(v_c)$ for various cutting speeds. The experiments were performed in the tool AERO TURN BT-380 CNC machine (**Figure 1**) with a maximum spindle speed $n_{max} = 4500 \text{ min}^{-1}$ and performance $P_c = 11.5 \text{ kW}$ with a turret for clamping the cutting tools (**Figure 2**) and a CNC control system FANUC Series Oi – TC. The workpiece material was austenitic stainless steel 1.4301 (microstructure can be seen in **Figure 3**), $\varnothing 60 \text{ mm} \times 200 \text{ mm}$, hardness HB 190. The clamping was in a three-jaw chuck with the turned inside diameter $\varnothing 60 \text{ mm}$ in length $l = 15 \text{ mm}$, clamping the workpiece by the tail stock. The cutting tool was a side cutting tool holder $\kappa_r = 95^\circ$, with geometry PCLNR 2525 (PRAMET Tools). The carbide cutting insert was CNMG 120408E-NM, carbide type GC 2025 (PRAMET Tools), used for rough machining of the austenitic stainless steels (SEM microstructure of cutting edge's appearance can see in **Figure 4**).

Cutting conditions:

- Depth of cut $a_{p0} = 1.0 \text{ mm}$,
- Feed rate $f_0 = 0.15 \text{ mm/rev}$,
- Cutting speed $v_{c1} = 250 \text{ m min}^{-1}$, $v_{c2} = 200 \text{ m min}^{-1}$, $v_{c3} = 150 \text{ m min}^{-1}$ with usage of the coolant E5%.



Figure 1: Overall view of the AERO TURN BT-380 CNC machine tool

Slika 1: Izgled CNC stružnice AERO TURN BT-380

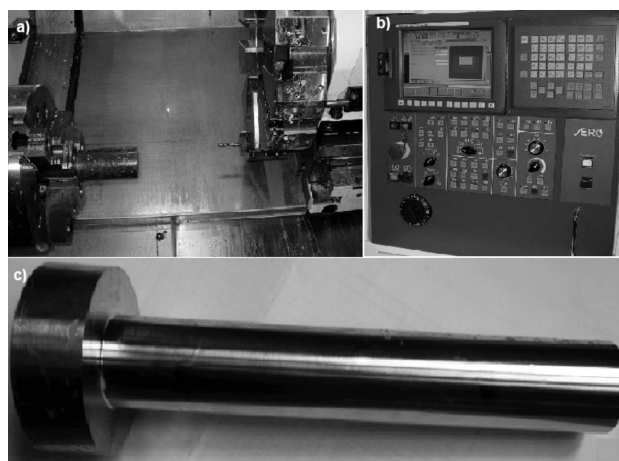


Figure 2: a) Cutting area of CNC machine tool with clamped workpiece, b) control panel of the AERO TURN BT-380 CNC machine tool with system FANUC Series Oi – TC, c) view of the workpiece (tested part) used for the turning experiments

Slika 2: a) Področje CNC struženja z vpetim obdelovancem, b) kontrolna plošča CNC stružnice AERO TURN BT-380 s sistemom FANUC Serije Oi-TC, c) izgled obdelovanca (vzorca) na katerem so bili izvršeni preizkusi struženja

4 RESULTS AND DISCUSSION

To determine the dependence of $T = f(v_c)$ we must satisfy the condition $v_{cmax} = 2.5 v_{cmin}$ and the cutting-tool wear criteria of $VB_k = 0.2$ mm. The scheme of the gradual removal of material during the turning in the virtual interface of the CATIA V5 Lathe Machining system is shown in **Figure 5**. The turning tests were carried out for the following values of the cutting speeds $v_{c1} = 250$ m min⁻¹, $v_{c2} = 200$ m min⁻¹, $v_{c3} = 150$ m min⁻¹, and the cutting speed $v_{c4} = 100$ m min⁻¹ was determined by the calculation method. The CNC machine tool calculates $v_c = \text{const.}$ directly from the turning diameter. For the average diameter $\varnothing 58$ the cutting speed $v_c = 250$ m min⁻¹ and the spindle speed $n = 1348$ min⁻¹. For the maximum removed diameter the cutting speed $v_c = 254$ m min⁻¹. With each cut the spindle speed of the CNC machine tool also changes. With a change of the diameter from $\varnothing 60$ mm to $\varnothing 30$ mm there is also a change of the feed velocity v_f . Even the machining time for one cut also changes as follows.

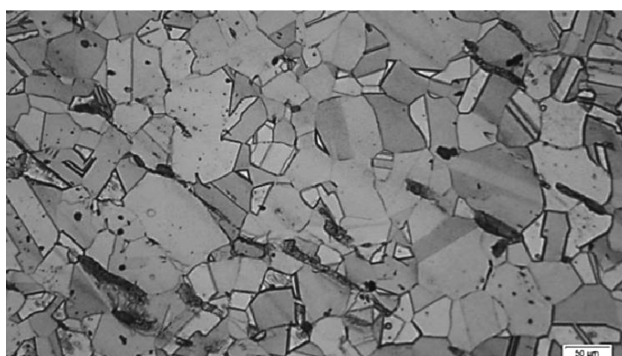


Figure 3: The microstructure of DIN 1.4301 (AISI 304) with an austenitic structure. The microstructure consists of large grains of austenite (grey) and small grains of carbides (black).¹³

Slika 3: Avstenitna mikrostruktura jekla DIN 1.4301 (AISI 304). Mikrostruktura je sestavljena iz velikih zrn avstenita (sive barve) in majhnih karbidnih zrn (črne barve).¹³

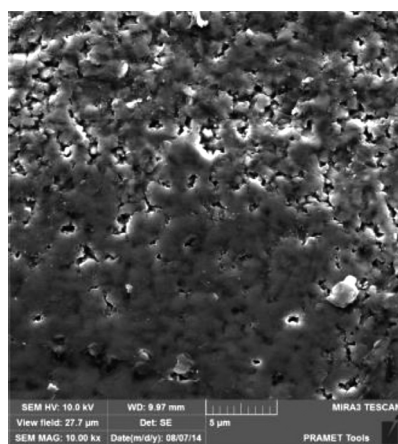


Figure 4: Surface morphology of the CNMG 120408E-FM carbide cutting insert (edge) surface appearance, SEM image

Slika 4: SEM-posnetek morfologije površine CNMG 120408E-FM karbidnega rezalnega vložka (rob)

Different criteria can be used for the measurement of tool life such as the average of the maximum flank wear, the surface roughness and the number of components per tool. In this experimental investigation the criterion of an average flank wear $VB = 0.2$ mm was considered for the tool-life measurement. Fernández-Abbia et al.^{1,2} reported that the cutting speed in the range of 200 to 300 m min⁻¹ is favourable for the machining of 1.4301 stainless steel. After each pass, the cutting insert was used for a measurement of the tool wear and thus wear progress was obtained. **Figure 6** shows the tool-life curves at (150, 200, 250) m min⁻¹ cutting speed for a constant feed rate and depth of cut. The tool life demonstrates three wear stages. Flank wear VB of carbide insert at $v_{c2} = 200$ m min⁻¹ can be seen in **Figure 7**.

Table 1: The calculation table to determine the tool life T (min)

Tabela 1: Tabela za izračun časa T (min) zdržljivosti orodja

N	v_{ci}	T_i	$\log v_{ci}$	$\log T_i$	$\log \frac{v_{ci}}{T_i}$	$\log v_{ci}^2$
1	150	48.8	2.17609	1.68842	3.67416	4.73537
2	200	28.9	2.30103	1.46090	3.36157	5.29474
3	250	19.5	2.39794	1.29003	3.09343	5.75012
Σ	–	–	6.87506	4.43935	10.12915	15.77998

Auxiliary calculation $(\Sigma \log v_{ci})^2 = 6.87506^2 = 47.2664$

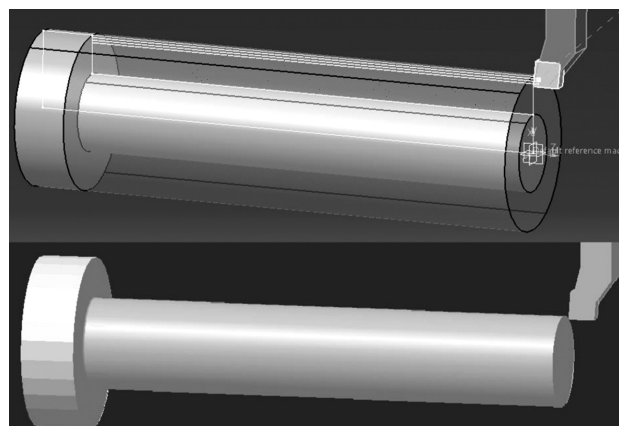


Figure 5: 3D simulation of the longitudinal turning process in CATIA
Slika 5: CATIA tridimenzionalna simulacija vzdolžnega procesa struženja

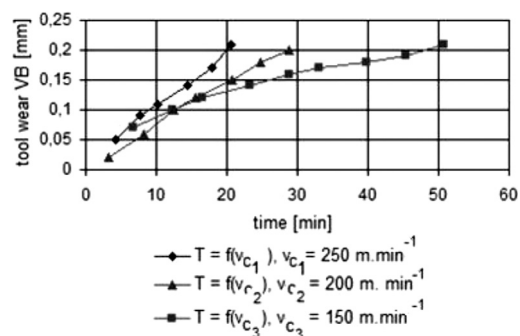


Figure 6: The graphical dependence of the tool flank wear on the machining time during the turning of DIN 1.4301

Slika 6: Grafična odvisnost obrabe boka orodja od časa struženja jekla DIN 1.4301

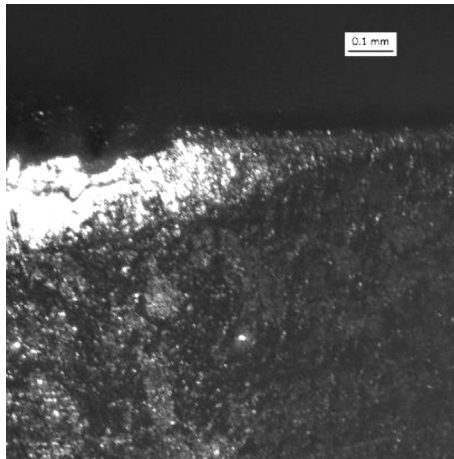


Figure 7: Flank wear VB of cemented carbide insert at cutting speed $v_{c2} = 200 \text{ m min}^{-1}$, established criterion of the flank wear $VB = 0.2 \text{ mm}$
Slika 7: Obraba roba VB karbidnega vložka pri hitrosti rezanja $v_{c2} = 200 \text{ m min}^{-1}$, uveljavljeno merilo za obrabo roba $VB = 0,2 \text{ mm}$

In the process of investigating the quality indicators in terms of the surface integrity during the turning of 1.4301 austenitic stainless steel, the authors of the article also dealt with the dependence of the arithmetic mean surface roughness $Ra = f(v_c)$ in changing the fillet radius of the used cutting tool (the difference can see in **Figure 8**). The surface roughness measurement was carried out on the machined surfaces using a Taylor Hobson measuring device. The value reported represents the average of the surface roughness value obtained from at least three measurements. The surface quality of the machined surface is mainly dependent on the used cutting conditions and it plays a significant role in the functionality and fatigue life of the component.

The measured spindle speeds n_i , the feed velocity rates v_{fi} and the machining times for the individual cuts were determined from a calculation. Sample no. 4 was machined with the same method and with the same cutting parameters as the sample no. 3. Flank wear control was carried out after 23.3 min, 28.8 min, and 33.06 min, and then the sample no. 5 was machined with a

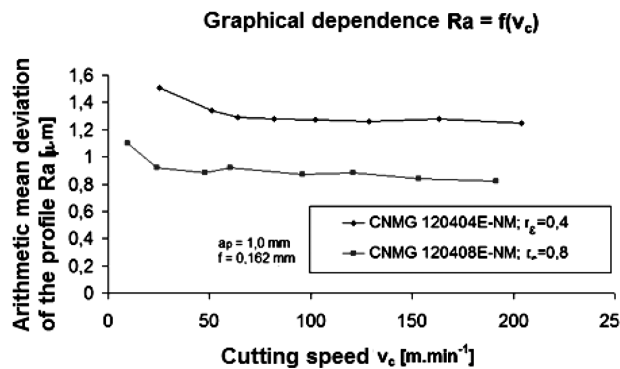


Figure 8: The graphical dependence $Ra = f(v_c)$ in the turning of DIN 1.4301 steel with CNMG 12048E with different r_ϵ

Slika 8: Grafična odvisnost $Ra = f(v_c)$ pri struženju jekla DIN 1.4301 z CNMG 12048E, z različnimi r_ϵ

flank wear measurement after 39.83 min, 45.33 min, and 50.83 min. The measured values of the flank wear VB_{max} for $v_{c1} = 250 \text{ m min}^{-1}$, $v_{c2} = 200 \text{ m min}^{-1}$, $v_{c3} = 150 \text{ m min}^{-1}$, with $a_p = 1.0 \text{ mm}$ and $f = 0.15 \text{ mm/rev}$ are determined in this experiment. Then follows an exchange (rotation) of the cutting insert again. Then continued the completion of the turning of sample no. 5 from the diameter $\varnothing 40 \text{ mm}$ to the diameter $\varnothing 30 \text{ mm}$ on the $L = 180 \text{ mm}$ with $v_{c2} = 200 \text{ m min}^{-1} = \text{const.}$ with the same cutting parameters $a_p = 1.0 \text{ mm}$, $f = 0.15 \text{ mm/rev}$, with usage of coolant. The measured spindle speeds n_i , the feed velocity rates v_{fi} and the machining times for the individual cuts were determined using a calculation. During this phase of the experiment we turned samples no. 5, 6, 7, and 8 from the overall number of 10 pieces. The graphical dependence of the cutting tool wear on the machining time for the cutting speeds v_{c1} , v_{c2} , v_{c3} from the turning of austenitic stainless steel 1.4301 with a cutting parameter depth of cut $a_p = 1.0 \text{ mm}$ and feed rate $f = 0.15 \text{ mm/rev}$, with coolant is shown in **Figure 6**. Three points of the measurement in the dependence $T = f(v_c)$ according to the relevant equation and determines the shape of the curve as linear in the logarithmic coordinates. For the calculation we used values directly from **Table 1**. The PRAMET Tools (Sandvik Group Sweden) is recommended for the tool life of the cemented cutting inserts with the coating type GC 2025 at the cutting speed $v_c = 250 \text{ m min}^{-1}$ with the value of tool life $T = 18 \text{ min}$, establishing the criterion of wear $VB_k = 0.2 \text{ mm}$. Since the cemented carbide insert type GC 2025 has a multilayer coating $\text{TiN} + \text{Al}_2\text{O}_3 + \text{TiC}$ on the fine-grained substrate $\text{WC} + \text{Co}$ it achieves an even higher durability.

There is an analytical description for determining the dependence of the tool life $T = f(v_c)$ with a value of $v_c = 100 \text{ m min}^{-1}$ in the following section. The linear regression of the single parameter is:

$$\hat{y} = b_0 \cdot x_0 + b_1 \cdot x_1 \quad (1)$$

Then the x_0 is a fictitious value, which has a value of 1 for the integer scale. For the logarithmic scale of $\log 10 = 1$, the x_1 is an independent variable, the b_0 is an additive constant, which shows the growth on the axis "y", and the b_1 indicates the slope of the regression function. The values b_0 , b_1 are then calculated using the following Equation (2) (x) to (y):

$$b_1 = \frac{N \cdot \sum_{i=1}^N (\lg T_i \cdot \lg v_{c_i}) - \sum_{i=1}^N \lg T_i \cdot \sum_{i=1}^N \lg v_{c_i}}{N \cdot \sum_{i=1}^N (\lg^2 v_{c_i}) - \left(\sum_{i=1}^N \lg v_{c_i} \right)^2} \quad (2)$$

Substituting b_1 into the Equation (2) we obtain the constant b_0 , Equation (3):

$$b_0 = \frac{\sum_{i=1}^N \lg T_i - b_1 \sum_{i=1}^N \lg v_{c_i}}{N} \quad (3)$$

where i to N is the number of measurements

$$b_1 = \frac{3 \cdot (10.12915) - (4.43935 \cdot 6.87506)}{3 \cdot 15.77998 - 47.2664} = -1.81327$$

$$b_0 = \frac{4.43935 - (-1.81327) \cdot 6.87506}{3} = 5.63523$$

$$\hat{y} = b_0 \cdot x_0 + b_1 \cdot x_1 = 5.63523 \cdot x_0 - 1.81327 \cdot x_1$$

The introduction of the substitution for $b_0 = \log C_T$ and for $\hat{y} = \log T$ is then $C_T = 10^{5.63523} = 431,748 \cdot 10^3$. Then the value is $\text{tg } \alpha = 1.81327$, thereof $\alpha = \text{arctg } 1.81327$ and consequently the size of the angle is $\alpha = 61^\circ 21'$. The inclination angle of the line in the logarithmic coordinates is $-b_1 = m = \text{tg } \alpha$, and from which we obtain the value of the angle α .

The shape of the linear regression for the tool life has the following form:

$$\log T = \log C_T - m \log v_c \quad (4)$$

The equation according to Taylor (2) for the material 1.4301 (AISI 304) will be in the following form for the cutting conditions $a_p = 1$ mm and $f = 0.15$ mm/rev.

$$T = \frac{431.748 \cdot 10^3}{v_c^{1.81327}}$$

Then for the tool-life calculation of cutting edge for the cutting speed $v_{c4} = 100$ m min⁻¹ the following formula is used:

$$\frac{T_4}{T_1} = \left(\frac{v_{c1}}{v_{c4}} \right)^m \quad \text{then } T_4 = 19.5 \left(\frac{250}{100} \right)^{1.81327} = 102.7 \text{ min}$$

5 CONCLUSIONS

The main aim of the presented paper is an experimental determination of the tool life depending on the cutting speed according to Taylor in turning the austenitic stainless steel 1.4301 (AISI 304). The cutting speed and the feed rate have a significant effect on the flank wear. The tool life is significantly influenced by the cutting parameters, the surface roughness and the flank wear. The obtained results are statistically processed using a linear regression analysis with the method of least squares. The results and values are shown in **Table 1**, and the graphical dependence of the flank wear VB_k on the time is shown in **Figure 6**. The flank wear (**Figure 7**) and the tool life of the cemented carbide insert were monitored so that there is no reduction in the quality of the surface finish. These areas were defined by the technical documentation. For the cemented carbide insert wear always occurs at one point when there is a variable depth of cut (can see in **Figure 7**). For example, this can be avoided by using of the CNC program preparation in the three-dimensional CATIA interface (**Figure 5**). The CNC program divides the allowance for machining so that the next depth of cut was slightly smaller than the previous one. The advantage of this cycle is the fact that the cutting tool is not still loaded in the same area, but over the range of applied depth of cuts. When machining austenitic stainless steels we should follow these rules,

which help to increase the durability of the cutting edge of the carbide cutting tool and thus the quality of the machined surface.

- The first rule is basically to use cutting inserts coated with CVD+PVD (for example, TiC+Al₂O₃+TiN on the cutting tool surface).
- The second is to use a washer of cemented carbide directly below the cemented carbide inserts.
- The third rule is to visually diagnose and timely eliminate the causes of premature damage to the cutting edge (notch).
- The fourth rule is to use the best applications for the changeable cutting inserts for dimensionally demanding workpieces.

In terms of the defined cutting parameters the greatest impact comes from the cutting speed v_c , a lower feed rate f and the least depth of cut a_p . We did not study more tool life depending $T = f(f)$ and $T = f(a_p)$ for this reason in CNC machine tools, and the size of the observed flank wear. This creates space for the realization of further research in this area. The applied, discovered knowledge from the literature sources and the experiments conducted here can be used in the future for the manufacture of specific parts on CNC machine tools with new, progressive cutting tools.

Acknowledgement

This paper was supported in the frame of the project "Alexander Dubček University of Trenčín – Faculty of special technology wants to offer high-quality and modern science/research and education", ITMS code 26110230099, based on the Operational Programme Education. Modern education for knowledge society / The project is co-funded by European Social Fund and also includes the results of the grant VEGA no. 1/9428/02 titled "The technological heredity of the machined surfaces – surface integrity".

6 REFERENCES

- ¹ A. I. Fernández-Abia, J. Barreiro, J. Fernández-Larrinoa, L. N. López de Lacalle, A. Fernández-Valdivielso, O.M. Perreira, Behaviour of PVD coatings in the turning of austenitic stainless steels, *Procedia Engineering*, 63 (2013), 133–141, doi:10.1016/j.proeng.2013.08.241
- ² A. I. Fernández-Abia, J. Barreiro, L. N. López de Lacalle, S. Martínez, Effect of very high cutting speeds on shearing, cutting forces and roughness in dry turning of austenitic stainless steels, *International Journal of Advanced Manufacturing Technology*, 57 (2011) 1–4, 61–71, doi:10.1007/s00170-011-3267-9
- ³ M. A. Xavier, M. Adithan, Determining the influence of cutting fluids on tool wear and surface roughness during turning of AISI 304 austenitic stainless steel, *Journal of Material Processing Technology*, 209 (2009) 2, 900–909, doi:10.1016/j.jmatprotec.2008.02.068
- ⁴ A. P. Kulkarni, G. G. Joshi, V. G. Sargade, Dry turning of AISI 304 austenitic stainless steel using AlTiCrN coated insert produced by HPPMS technique, *Procedia Engineering*, 64 (2013), 737–746, doi:10.1016/j.proeng.2013.09.149

- ⁵ S. S. Wagh, A. P. Kulkarni, V. G. Sargade, Machinability studies of austenitic stainless steel (AISI 304) using PVD cathodic arc evaporation (CAE) system deposited AlCrN/TiAlN coated carbide inserts, *Procedia Engineering*, 64 (2013), 907–914, doi:10.1016/j.proeng.2013.09.167
- ⁶ S. Emura, M. Kawajiri, X. Min, S. Yamamoto, K. Sakuraya, K. Tszaki, Machinability improvement and its mechanism in SUS304 austenitic stainless steel by precipitated hexagonal boron nitride, *ISIJ International*, 53 (2013) 10, 1841–1849, doi:10.2355/isijinternational.53.1841
- ⁷ J. Paro, H. Hänninen, V. Kauppinen, Tool wear and machinability of X5CrMn18 stainless steel, *Journal of Materials Processing Technology*, 119 (2001) 1–3, 14–20, doi:10.1016/S0924-0136(01)00877-9
- ⁸ F. Koné, C. Czarnota, B. Haddag, M. Nouari, Modeling of velocity-dependent chip flow angle and experimental analysis when machining 304L austenitic stainless steel with groove coated-carbide tools, *Journal of Materials Processing Technology*, 213 (2013) 7, 1166–1178, doi:10.1016/j.jmat-protec.2013.01.015
- ⁹ S. E. Cordes, Thermal stability of γ -alumina PVD coatings and analysis of their performance in machining of austenitic stainless steels, *CIRP Journal of Manufacturing Science and Technology*, 5 (2012) 1, 20–25, doi:10.1016/j.cirpj.2011.11.003
- ¹⁰ R. Čep, A. Janásek, A. Slíva, M. Neslušán, M. Binder, Experimental tool life tests of indexable inserts for stainless steel machining, *Tehnicki Vjesnik*, 20 (2013) 6, 933–940
- ¹¹ V. T. G. Naves, M. B. Da Silva, F. J. Da Silva, Evaluation of the effect of application of cutting fluid at high pressure on tool wear during turning operation of AISI 316 austenitic stainless steel, *Wear*, 302 (2013) 1–2, 1201–1208, doi:10.1016/j.wear.2013.03.016
- ¹² A. I. Fernández-Abia, J. Barreiro, L. N. López de Lacalle, S. Martínez-Pellitero, Behavior of austenitic stainless steels at high speed turning using specific force coefficients, *International Journal of Advanced Manufacturing Technology*, 62 (2012) 5–8, 505–515, doi:10.1007/s00170-011-3846-9
- ¹³ R. K. C. Nkhoma, C. W. Siyasiya, W. E. Stumpf, Hot workability of AISI 321 and AISI 304 austenitic stainless steels, *Journal of Alloys and Compounds*, 595 (2014), 103–112, doi:10.1016/j.jallcom.2014.01.157
- ¹⁴ J. Jambor, Improving the quality of the machining process through new technologies, *Annals of DAAAM for 2012 & Proceedings – World Symposium Intelligent Manufacturing & Automation*, 23 2012, 623–626
- ¹⁵ Z. Tekiner, S. Yesilyurt, Investigation of the cutting parameters depending on process sound during turning of AISI 304 austenitic stainless steel, *Materials and Design*, 25 (2004) 6, 507–513, doi:10.1016/j.matdes.2003.12.011
- ¹⁶ T. Akasawa, H. Sakurai, M. Nakamura, T. Tanaka, K. Takano, Effects of free-cutting additives on the machinability of austenitic stainless steels, *Journal of Materials Processing Technology*, 143–144 (2003) 1, 66–71, doi:10.1016/S0924-0136(03)00321-2
- ¹⁷ M. Kaladhar, K. Venkata Subbaiah, C. Srinivasa Rao, Parametric optimization during machining of AISI 304 austenitic stainless steel using CVD coated Duratomic™ cutting insert, *International Journal of Industrial Engineering Computations*, 3 (2012) 4, 577–586, doi:10.5267/j.ijiec.2012.04.002
- ¹⁸ M. Aydin, C. Karakuzu, M. Uçar, A. Cengiz, M. A. Cavuşlu, Prediction of surface roughness and cutting zone temperature in dry turning processes of AISI304 stainless steel using ANFIS with PSO learning, *Int. Journal of Advanced Manufacturing Technology*, 67 (2013) 1–4, 957–967, doi:10.1007/s00170-012-4540-2
- ¹⁹ I. Korkut, M. Kasap, I. Ciftci, U. Seker, Determination of optimum cutting parameters during machining of AISI 304 austenitic stainless steel, *Materials and Design*, 25 (2004) 4, 303–305, doi:10.1016/j.matdes.2003.10.011
- ²⁰ I. Ciftci, Machining of austenitic stainless steels using CVD multi-layer coated cemented carbide tools, *Tribology International*, 39 (2006) 6, 565–569, doi:10.1016/j.triboint.2005.05.005
- ²¹ W. Grzesik, The role of coatings in controlling the cutting process when turning with coated indexable inserts, *Journal of Material Processing Technology*, 79 (1998) 1–3, 133–143, doi:10.1016/S0924-0136(97)00491-3
- ²² A. Hosokawa, T. Ueda, R. Onishi, R. Tanaka, T. Furumoto, Turning of difficult-to-machine materials with actively driven rotary tool, *CIRP Annals – Manufacturing Technology*, 59 (2010) 1, 89–92, doi:10.1016/j.cirp.2010.03.053
- ²³ W. I. H. Liew, B. K. A. Ngoi, Y. G. Lu, Wear characteristics of PCBN tools in the ultra-precision machining of stainless steel at low speeds, *Wear*, 254 (2003) 3–4, 265–277, doi:10.1016/S0043-1648(03)00002-4
- ²⁴ M. Hua, W. Xicheng, L. Jian, Friction and wear behaviour of SUS 304 austenitic stainless steel against Al₂O₃ ceramic ball under relative high load, *Wear*, 265 (2008) 5–6, 799–810, doi:10.1016/j.wear.2008.01.017

NiAl INTERMETALLIC PREPARED WITH REACTIVE SINTERING AND SUBSEQUENT POWDER-METALLURGICAL PLASMA-SINTERING COMPACTION

REAKCIJSKO SINTRANJE IN ZGOŠČEVANJE S PLAZEMSKIM SINTRANJEM NiAl INTERMETALNE ZLITINE

Alena Michalcová¹, Dalibor Vojtěch¹, Tomáš František Kubatík², Pavel Novák¹, Petr Dvořák¹, Petra Svobodová¹, Ivo Marek¹

¹University of Chemistry and Technology, Department of Metals and Corrosion Engineering, Prague, Technická 5, 166 28 Prague 6, Czech Republic

²Institute of Plasma Physics AS CR, v. v. i., Za Slovankou 1782/3, 182 00 Prague 8, Czech Republic
michalca@vscht.cz

Prejem rokopisa – received: 2015-04-30; sprejem za objavo – accepted for publication: 2015-06-02

doi:10.17222/mit.2015.089

This paper proposes a novel method for powder-metallurgy preparation of compact NiAl intermetallics. In the first step, the NiAl powder is prepared with the reactive-sintering procedure. The porous NiAl product of the SHS reaction is milled to a fine powder and consequently compacted by SPS processing. The compaction of powder metals and alloys is a very difficult field due to the need of preserving the unique properties of the initial materials. One of the few possible methods of a successful compaction is plasma sintering. To describe detailed structures of powder-metallurgy materials, it is necessary to use advanced microscopy methods such as SEM and TEM. In this study, the structure of a NiAl intermetallic compound is described. The material was first produced, with reactive sintering, from pure elements. Subsequently, the NiAl porous master alloy was milled and compacted with the spark-plasma-sintering (SPS) technique. The particle size of the NiAl powder was comparable to the grain size of the compacted material, which exhibited a low porosity. It was proved that the interconnection of the NiAl particles is made by a thin layer of nanocrystalline oxides.

Keywords: SPS, intermetallics, powder metallurgy

Članek predlaga novo metodo za pripravo kompaktno NiAl intermetalne zlitine s pomočjo metalurgije prahov. V prvem koraku je bil NiAl prah pripravljen s postopkom reakcijskega sintranja. Z SHS reakcijo proizvedeni porozni NiAl je bil zmlet v droben prah in nato kompaktno z SPS postopkom. Kompaktiranje kovinskega prahu je težavno zaradi potrebe po zadržanju enkratnih lastnosti začetnih materialov. Ena od redkih uspešnih metod kompaktiranja je sintranje s plazmo. Za podroben opis mikrostrukture materialov v metalurgiji prahov je potrebno uporabiti napredne mikroskopske metode, kot sta SEM in TEM. V študiji je opisana struktura intermetalne zlitine NiAl. Material je bil najprej izdelan z reakcijskim sintranjem iz čistih elementov. Nato je bila porozna zlitina NiAl zmleta in kompaktno s tehniko iskričnega plazma sintranja (SPS). Velikost delcev prahu NiAl je bila primerljiva z velikostjo zrn v kompaktnem materialu, ki je imel tudi majhno poroznost. Dokazano je bilo, da se povezava delcev NiAl izvede s tanko plastjo nanokristaliničnih oksidov.

Ključne besede: SPS, intermetalne zlitine, metalurgija prahov

1 INTRODUCTION

Like many other transition metal aluminides, nickel aluminide exhibits properties that are very interesting for industrial utilization. These are a high melting point (1638 °C), a low density (5.95 g/cm³), a high thermal conductivity (70 W m⁻¹K⁻¹), an excellent corrosion resistance^{1,2} and a very good wear resistance.³ These properties allow intermetallics to be used in the applications where metallic and ceramic materials fail. In addition, nickel aluminide is easily produced in atmospheric air with a self-propagating high-temperature synthesis (SHS)^{2,4-5} even when pre-pressed into a green body.⁴ This makes the Ni-Al system to be an ideal model for the study of a possible powder preparation using metallurgical methods based on SHS.

The intermetallic materials usually exhibit good mechanical properties at elevated temperatures, but unfortunately, they seem to be quite brittle at room

temperature. When decreasing the grain size of a material, this factor limiting its utilization can be solved. One of the promising ways is to produce fine-grained intermetallics with a two-step powder-metallurgy method: in the first step, an intermetallic is formed with the SHS procedure; then it is milled to a very fine powder and compacted with the spark-plasma-sintering (SPS) procedure. The advantage of the SPS process lies in extremely short sintering times, due to which there is almost no grain coarsening.⁶⁻⁹ The SPS method is well described for ceramics, but for metals and especially for intermetallics, the description of the process is still being formed.⁶⁻⁹

The spark-plasma sintering method has been very popular in the last two decades, mainly in the field of compaction of ceramics. It is an ideal tool for obtaining homogenous nanocrystalline bulk materials with a high density, i.e., fine-grained ceramics, thermo-electric semi-

conductors and biomaterials.⁶ Compared to the other compaction methods (cold and hot isostatic pressing), the SPS is distinguished by a low overall sintering temperature, short sintering times and better properties of the prepared bulk materials.⁷

Using the SPS method, many successes were achieved in the fields of increasing the superplasticity of ceramic materials, improvement of magnetic properties, reduction of the amount of impurities segregated at the grain boundaries, improvement in the binding quality and many others.⁷ From the historical point of view, the first machine comparable to SPS was built in Germany, as reported in reference⁶. In 1933, in the USA, F. Taylor was awarded a patent for the first resistance-sintering method used for sheets.¹⁰

Basically, the SPS method for sintering materials can be divided into four generations: the first SPS was built in Japan (in 1962) and called spark sintering (SS).¹¹ The next generation can be described as plasma-activated sintering (PAS), followed by spark-plasma sintering (SPS), while the fourth and currently the last generation is the one described in¹².

The study of a NiAl alloy prepared with SPS can be used, in future, as a milestone for the preparation of NiAl-based composites.² Preparation conditions can be easily changed by adding reinforcements to the reaction system before the SHS reaction or by adding them to the powder before the SPS compaction.

2 EXPERIMENTAL WORK

The NiAl intermetallic compound was prepared with an SHS synthesis. A high-purity nickel powder with a particle size <100 µm and an aluminium powder with a purity of 99.99 % and a particle size of 200–400 µm were mixed and pressed at room temperature with a pressure of 260 MPa using a LabTest 5.250SP1-VM universal testing machine. Reactive sintering of the pressed powder mixtures was carried out at 900 °C for

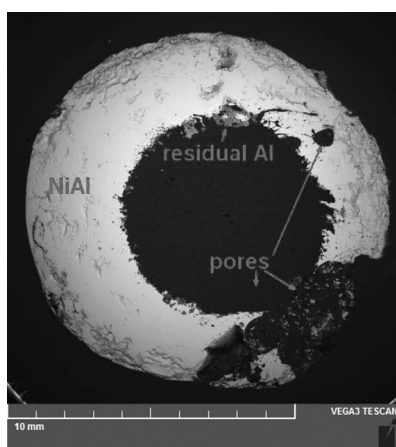


Figure 1: Structure of a NiAl particle prepared with SHS procedure (SEM/BSE)

Slika 1: Struktura delca NiAl, izdelanega z SHS postopkom (SEM/BSE)

15 min in the usual furnace (air) atmosphere. The sintered particles with an approximately cylindrical shape and a size of 1 cm in diameter and 1 cm in height were milled with a laboratory vibration mill VM4. The obtained NiAl powder was leached in a 20 % NaOH solution to dilute any residual Al. The NiAl powder was compacted with the SPS procedure (model SPS 10-4 thermal technology) at a temperature of 1100 °C, for a compaction-process time of 5 min and at a pressure of 80 MPa. The SPS die is made of carbon and its internal diameter is 19.3 mm. To separate the sintered material from the die, a carbon foil with a thickness of 0.15 mm was used. The amount of compacted material was approximately 5 g for each experiment.

The structures of the SHS material, the NiAl powder and the SPS-compacted material were observed with an Olympus PME3 light microscope and a TESCAN VEGA 3 LMU scanning electron microscope equipped with EDS and EBSD detectors (Oxford Instruments). The phase compositions of the materials were determined using X-ray diffraction (PAN analytical X'Pert PRO + High Score Plus, Cu anode). TEM samples were prepared by ion polishing using Gatan PIPS Model 691 and consequently observed with a Jeol JEM 3010 transmission electron microscope. SAED patterns were integrated and phases were identified using Process Diffraction software. The hardness of the materials was measured with a FUTURE-TECH FM700 hardness tester with loads of 10 g and 1 kg.

3 RESULTS AND DISCUSSION

The samples prepared with the SHS procedure had approximately cylindrical shapes. They were mainly composed of the NiAl phase with a low amount of residual Al in the surroundings of the pores. As illustrated in **Figure 1**, the porosity of the SHS samples is extremely high.

The NiAl particles were milled into a powder, whose structure is shown in **Figure 2**. The particles have irregular shapes, as expected after milling a brittle material.

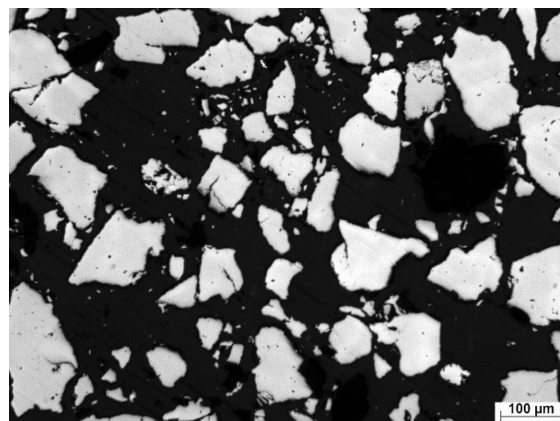


Figure 2: Structure of NiAl powder (LM)

Slika 2: Struktura NiAl prahu (LM)

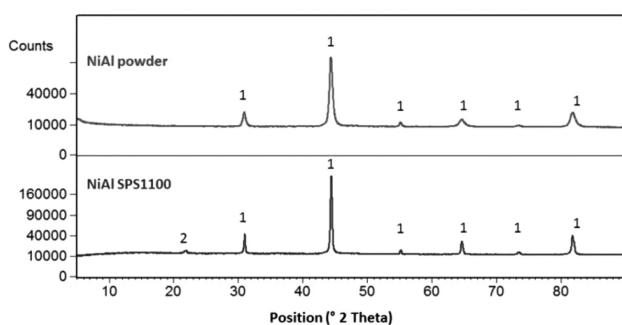


Figure 3: XRD pattern of NiAl powder and compacted material (1 = NiAl, 2 = graphite)

Slika 3: Rentgenogram prahu NiAl in kompaktiranega materiala (1 = NiAl, 2 = grafit)

The size of the majority (96 %) of the particles is less than 140 μm . The phase composition of the powder is given in **Figure 3**. Peaks of residual aluminium are also visible in the milled powder. Although the powder was leached with a 20 % NaOH solution, areas of residual Al are still shown in **Figure 1**.

Subsequently, the powder was compacted with the SPS method at 1100 $^{\circ}\text{C}$ for 5 min. The structure of the SPS-prepared material is given in **Figure 4**. The particles of the initial powder are clearly distinguishable. The dark parts in the structure are pores. The porosity of the SPS-prepared material is 1.9 ± 0.9 %, which is satisfactory for the material prepared by powder-metallurgy processing.

The grains of the compacted material are formed by the particles of the initial powder and no grain coarsening is observed. It can be supposed that the grain size of the compacted material depends only on the particle size of the initial powder. The plot in **Figure 5** shows the particle-size distribution of the initial NiAl powder and the grain-size distribution of the SPS-compacted material. It seems that the powder contains more particles with a size of up to 20 μm . This slight disagreement can be caused by a measurement error. Small particles located

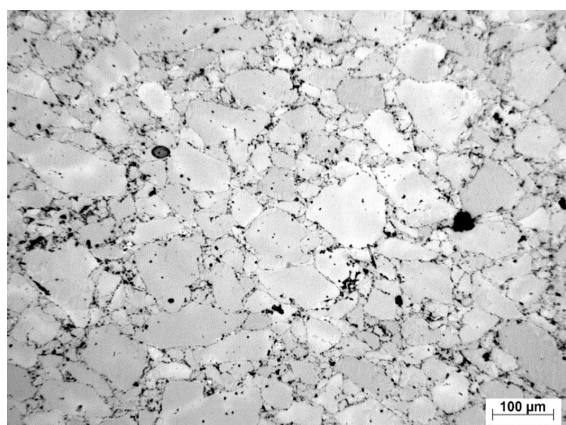


Figure 4: Structure of NiAl material compacted from powder with SPS method (1100 $^{\circ}\text{C}/5$ min) (LM)

Slika 4: Struktura NiAl materiala, kompaktiranega iz prahu po SPS metodi (1100 $^{\circ}\text{C}/5$ min) (LM)

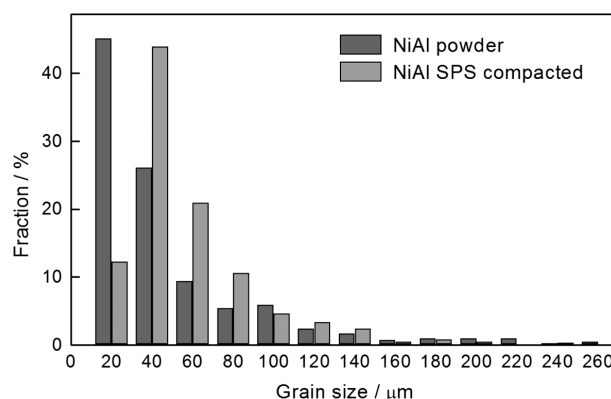


Figure 5: Grain (particle) size distribution of NiAl powder and compacted material

Slika 5: Razporeditev velikosti delcev prahu NiAl in kompaktiranega materiala

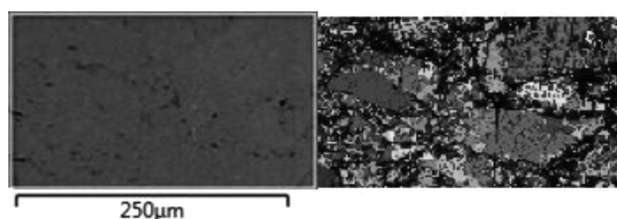


Figure 6: SEM micrograph of NiAl material compacted from powder with SPS method (1100 $^{\circ}\text{C}/5$ min) and EBSD scan of the area

Slika 6: SEM-posnetek NiAl materiala, kompaktiranega iz prahu po SPS metodi (1100 $^{\circ}\text{C}/5$ min) in EBSD posnetek področja

at the grain boundaries cannot be distinguished as easily as the separate particles in the mounting material.

The EBSD analysis (**Figure 6**) of the SPS-compacted material proved that the area of the initial-powder particles is monocrystalline. Between the large, clearly seen particles (grains of the compacted material), there are areas where the crystallographic orientation is not very clear. These areas at the grain boundaries can exhibit a large misorientation or can be oxidised.

The amount of residual Al is lower than a 2–5 % of mass fraction because it is not detectable with XRD, as shown in **Figure 3**. The same is true of the oxide content in the initial powder and also in the SPS-compacted

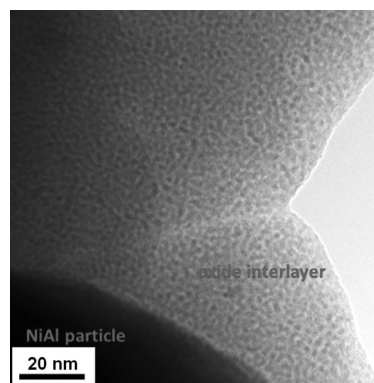


Figure 7: TEM micrograph of NiAl material compacted from powder with SPS method (1100 $^{\circ}\text{C}/5$ min)

Slika 7: TEM-posnetek NiAl kompaktiranega materiala iz prahu po metodi SPS (1100 $^{\circ}\text{C}/5$ min)

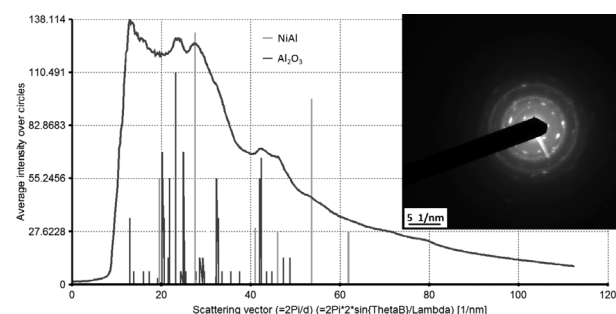


Figure 8: SAED pattern of the grain boundary and diffraction pattern obtained by integrating it in Process Diffraction software. The grain boundary is composed of NiAl and Al₂O₃ phases.

Slika 8: SAED-posnetek meje zrna in posnetek uklona, dobljen z vstavitvijo v programsko opremo Difrakcija procesa. Meja zrna je sestavljena iz faz NiAl in Al₂O₃.

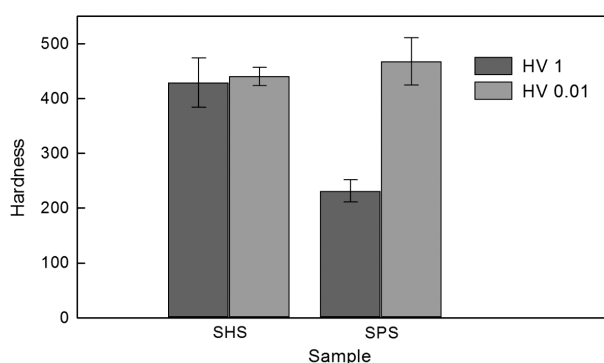


Figure 9: Microhardness and macrohardness of samples after SHS preparation and powder-metallurgy preparation with SPS

Slika 9: Mikrotvrdota in tvrdota vzorcev po SHS pripravi in po metalurški obdelavi z SPS metodo

product. The only excess peak in the XRD pattern of the SPS-compacted material relates to the graphite from the protection graphite foil used in the SPS process.

A detailed material observation made using TEM is given in **Figure 7** and it shows the structure of a grain boundary. In the left bottom part, a dark NiAl particle is located. It can be seen that the particles are connected by a nanocrystalline oxide interlayer. The amount, thickness and crystallinity of the oxide layer are not sufficient to be detected with XRD or EBSD analysis, but they can be distinguished with selected area electron diffraction (SAED), as shown in **Figure 8**.

The fact that the weak parts of the material are the grain boundaries is also proved with the hardness measurement. While the microhardness (inside individual particles) is the same for the SHS material and for the SPS-compacted material, the macrohardness (measured with a load of 1 kg) varies significantly (**Figure 9**). These results indicate that micro-properties stay the same after a consolidation, while macro-properties change significantly due to the formation of an oxide interlayer during a compaction. The question is what would happen if the SHS process was performed in an inert atmosphere.

4 CONCLUSION

The powder-metallurgy preparation of NiAl consisting of the SHS NiAl preparation, the milling and the SPS compaction is a promising method for obtaining bulk intermetallic materials. The grain size of an SPS-compacted material is mainly determined by the grain-size distribution of the initial powder. The grain size was estimated to be less than 40 μm. It was proved that the particles of the initial powder are interconnected by a thin oxide layer, which decreases the macroscopic and also microscopic properties of the material.

Acknowledgement

This research was financially supported by the Czech Science Foundation, project No. P108/12/G043.

5 REFERENCES

- D. Tingaud, L. Stuppfler, S. Paris, D. Vrel, F. Bernard, C. Penot, F. Nardou, Time-Resolved X-ray Diffraction Study of SHS-produced NiAl and NiAl-ZrO₂ Composites, *International Journal of Self-Propagating High-Temperature Synthesis*, 16 (2007) 1, 12–17, doi:10.3103/S1061386207010025
- P. Novák, D. Šotka, M. Novák, A. Michalčová, J. Šerák, D. Vojtěch, Production of NiAl-matrix composites by reactive sintering, *Powder Metallurgy*, 54 (2011) 3, 308–313, doi:10.1179/003258909X12518163
- J. Guo, Z. Wang, L. Sheng, L. Zhou, C. Youya, Z. Chen, L. Song, Wear properties of NiAl based materials, *Progress in Natural Science: Materials International*, 22 (2012) 5, 414–425, doi:10.1016/j.pnsc.2012.10.008
- O. Ozdemir, S. Zeytin, C. Bindal, A study on NiAl produced by pressure-assisted combustion synthesis, *Vacuum*, 84 (2010), 430–437, doi:10.1016/j.vacuum.2009.09.006
- A. Biswas, S. K. Roy, Comparison between the microstructural evolutions of two modes of SHS of NiAl: key to a common reaction mechanism, *Acta Materialia*, 52 (2004), 257–270, doi:10.1016/j.actamat.2003.08.018
- M. Tokita, Spark Plasma Sintering (SPS) Method, Systems, and Applications, *Handbook of Advanced Ceramics*, (2013), 1149–1177, doi:10.1016/B978-0-12-385469-8.00060-5
- Z. A. Munir, U. Anselmi-Tamburini, M. Ohyanagi, The effect of electric field and pressure on the synthesis and consolidation of materials: A review of the spark plasma sintering method, *Journal of Materials Science*, 41 (2006) 3, 763–777, doi:10.1007/s10853-006-6555-2
- D. M. Hulbert, D. Jiang, D. V. Dudina, A. K. Mukherjee, The synthesis and consolidation of hard materials by spark plasma sintering, *International Journal of Refractory Metals and Hard Materials*, 27 (2009), 367–375, doi:10.1016/j.ijrmhm.2008.09.011
- L. Wang, J. Zhang, J. Wan, Recent development in reactive synthesis of nanostructured bulk materials by spark plasma sintering, *International Journal of Refractory Metals and Hard Materials*, 39 (2013), 103–112, doi:10.1016/j.ijrmhm.2013.01.017
- G. F. Taylor, Apparatus for making hard metal compositions, US Patent 1, 896, 854, 1993
- K. Inoue, Electric discharge sintering, US Patent 3, 241, 956, 1966
- M. Tokita, Trends in advanced SPS spark plasma sintering systems and technology, *Journal of the Society of Powder Technology*, 30 (1993) 11, 790–804, doi:10.4164/sptj.30.11_790

MICROSCOPIC CHARACTERIZATION AND PARTICLE DISTRIBUTION IN A CAST STEEL MATRIX COMPOSITE

MIKROSKOPSKA KARAKTERIZACIJA IN RAZPOREDITEV DELCEV V KOMPOZITU Z MATRICO LITEGA JEKLA

Ana Kračun^{1,2}, Matjaž Torkar¹, Jaka Burja¹, Bojan Podgornik¹

¹Institute of Metals and Technology, Lepi pot 11, 1000 Ljubljana, Slovenia

²International postgraduate school Jožef Stefan, 1000 Ljubljana, Slovenia
ana.kracun@imt.si

Prejem rokopisa – received: 2015-10-01; sprejem za objavo – accepted for publication: 2015-12-24

doi:10.17222/mit.2015.310

The purpose of this investigation was to identify the distribution of ultrafine particles in a steel matrix introduced through a conventional melting and casting method, and above all to determine the methodology and analysing techniques suitable for the analysis and identification of ultrafine particles incorporated into the steel matrix. In the frame of this work, steels dispersed with Al₂O₃ ultrafine particles were produced by a conventional casting method and their microstructure investigated with light microscopy (LM), scanning electron microscopy (SEM) and auger electron spectroscopy (AES). Microstructural analyses show that the distribution of the Al₂O₃ ultrafine particles is non-uniform and has a high degree of agglomeration. Furthermore, for a detailed analysis of the nanoparticles a specific preparation and characterization using advanced microscopic techniques is required.

Keywords: particle distribution, microscopic characterization, steel matrix

Namen raziskave je bil ugotoviti porazdelitev ultrafinih delcev v jekleni matrici, ki je bila proizvedena s konvencionalnim postopkom litja, predvsem pa določiti metodologijo in analizne tehnike, primerne za analizo in identifikacijo ultrafinih delcev, ki so bili vključeni v jekleno matrico. Delci Al₂O₃ so bili dodani med procesom konvencionalnega litja in so bili analizirani s pomočjo različnih analiznih tehnik, in sicer: z uporabo optičnega mikroskopa (LM), vrstičnega elektronskega mikroskopa (SEM) in spekroskopije Augerjevih elektronov (AES). Analiza mikrostrukture je pokazala neenakomerno porazdelitev in aglomeracijo Al₂O₃ delcev. Za podrobno analizo je potrebna karakterizacija mikrostrukture s pomočjo naprednih mikroskopskih tehnik.

Ključne besede: porazdelitev delcev, mikroskopska karakterizacija, jeklena matrica

1 INTRODUCTION

The insertion of ceramic reinforcements into metal matrices to produce composite materials with improved properties has been a subject of intensive research during the past three decades.¹⁻³ Ceramic particulates such as borides, carbides, oxides and nitrides are added to metal matrix composites (MMCs) to improve their elastic modulus, wear resistance, creep and strength.⁴⁻⁵

The ductility of MMCs, however, deteriorates at high ceramic particle concentrations⁵. The metal matrix, the so-called metal-matrix nano-composite (MMnCs) is strengthened by nano-sized ceramic particles.⁶ These nanoparticle reinforcements can significantly increase the mechanical strength of the metal matrix, as they promote particle hardening more effectively than micro particles. Moreover, MMnCs improve the performance significantly at elevated temperatures, because the ceramic nanoparticles can maintain their properties at high temperatures.⁶

Steel matrix composites commonly have a combination of hard ceramic (e.g., TiC, TiB₂, WC and Al₂O₃) reinforcements and a ductile metallic matrix, which makes them promising candidates for high-strength and

wear-resistance applications. There are several methods for fabricating particulate-reinforced steel matrix composites, such as powder metallurgy, conventional melting and casting, reactive sintering and self-propagating high-temperature synthesis (SHS). The casting process is simple and more economical than the other available routes for integrating nanoparticles into the microstructure of steel. However, it is extremely difficult to obtain a uniform dispersion of ceramic nanoparticles in liquid metals due to the poor wettability and the difference in the specific gravity between the ceramic particles and the metal matrix.⁷

The microstructure of metals is generally characterized by advanced microscopic techniques (e.g., LM, SEM and TEM) which probe and map the surface and sub-surface structure of a material. These techniques can use photons, electrons, ions or physical cantilever probes to gather data about a sample's structure on a wide range of length scales.⁸ Auger electron spectroscopy (AES) also provides quantitative elemental information from the surfaces of solid materials.⁹

The current work aims at contributing to the knowledge and understanding of the conventional casting route for ultrafine particle inoculation in a steel matrix. This

production route seems to show potential and offers more cost efficiency in achieving the dispersion of second-phase ultrafine particles compared to the powder and metallurgical techniques used until now. The aim of the work was therefore to study the influence of Al_2O_3 ultrafine particles on the microstructure of a steel matrix using a conventional casting method. The additional aim is to determine the methodology and analysing techniques suitable for analysing and necessary to identify the ultrafine particles incorporated in the steel matrix.

2 EXPERIMENTAL WORK

2.1 Material

Austenitic stainless steel was used for the work, mainly due to the distinctive two-phase microstructure of austenite and ferrite. The chemical composition of this alloy is given in **Table 1**. These are the most used group of stainless steels. They are paramagnetic, have a face-centred cubic lattice and excel with a good combination of hot and cold workability, mechanical properties and corrosion resistance.

Table 1: Chemical composition of austenitic stainless steel in mass fractions, (w/%)

Tabela 1: Kemijska sestava avstenitnega nerjavnega jekla v masnih deležih, (w/%)

Elements	w/%
C	0.02
Si	0.33
Mn	1.24
Cr	17.4
Ni	10.1
Cu	0.36
Mo	1.29
V	0.08

As the reinforcement particles, commercial ultrafine Al_2O_3 powder with a mean particle size of 500 nm was used, as shown in **Figure 1**. The Al_2O_3 ultrafine particles were selected due to their high chemical stability to Fe and high specific gravity. In particular, it was reported that the wetting angle θ between Al_2O_3 and molten iron alloy is less than 50° , even at high temperatures and in many different types of atmospheres.¹⁰

2.2 Specimens preparation

A weighed quantity (10 kg) of the austenitic stainless steel was melted in an induction furnace. In the first experiment 20 g of the ultrafine Al_2O_3 particles were wrapped in an Al foil and put into the ingot and the molten metal was poured over it into the same ingot. In the second experiment a mixture of 24 g of Al_2O_3 and 2.4 g of dry glue was prepared. The mixture was then filled in the steel tube and flooded with paraffin. The tube was inserted into the molten metal and when melted, the molten metal was poured into the ingot.

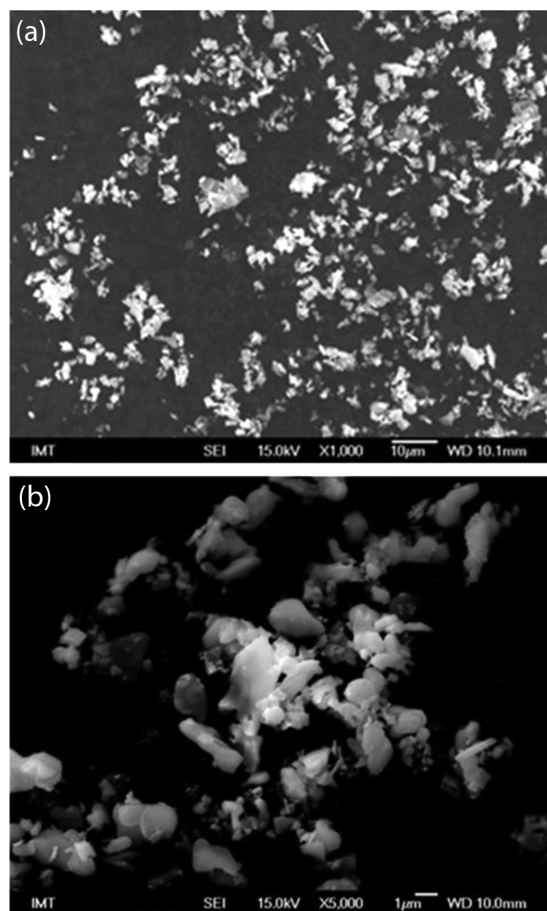


Figure 1: SEM image of Al_2O_3 ultrafine particles at various magnifications

Slika 1: SEM-posnetek ultrafinih delcev Al_2O_3 pri različnih povečavah

2.3 Characterization

The microstructural changes and the dispersion of the ceramic particles in the steel matrix were observed and analysed using light microscopy (LM), scanning electron microscopy (SEM) and auger electron spectroscopy (AES). Samples for the microstructure analysis were taken from the bottom, middle and top portions of the cast piece. Metallographic samples were prepared by grinding, polishing, followed by chemical etching and analysed to reveal the particle distribution. Samples for Auger electron spectroscopy were prepared by grinding and polishing the surface. These samples were attached to the bracket, placed in an experimental container-airlock, pumped to UHV and transferred into an analytical container. The surface of the sample was ion etched and analysed to determine the elemental composition in the surface region of the sample.

3 RESULTS AND DISCUSSION

Figure 2 shows a LM micrograph of the microstructure of pure austenitic stainless steel with a distinctive

two-phase microstructure of austenite and δ -ferrites. A LM micrograph of the microstructure and ultrafine particles' distribution of the sample produced by the casting process of the austenitic stainless steel poured over the Al_2O_3 ultrafine particles is shown in **Figure 3**.

As shown in **Figure 3**, the microstructure of the austenitic stainless steel is modified after the addition of Al_2O_3 ultrafine particles, being incorporated into the metal matrix. However, the distribution of Al_2O_3 particles is non-homogeneous and concentrated in a certain area.

In **Figure 4** the particle distribution of the sample taken from the second experiment, where the steel tube filled with Al_2O_3 particles was inserted into the melt is shown. As in the case of the first experiment, with the molten steel being poured over the Al_2O_3 ultrafine particles, the distribution of the particles is non-uniform and has a high degree of agglomeration (**Figure 4**). However, the degree of particles is lower when inserting the particles-filled steel tube into the molten metal.

From the SEM elemental analysis, shown in **Figure 5**, it was confirmed that the bright, small, spot-like feat-

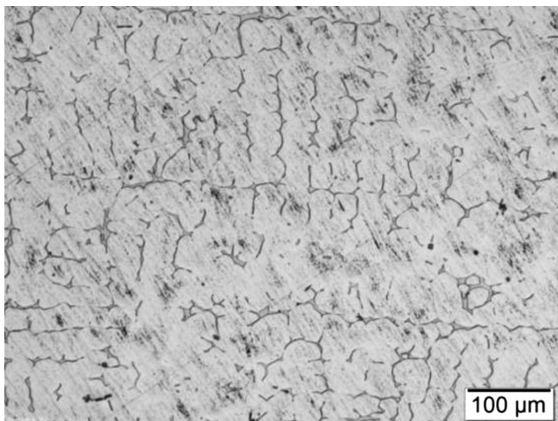


Figure 2: Cast microstructure of austenitic stainless steel with 6 % of δ -ferrite

Slika 2: Lita mikrostruktura avstenitnega nerjavnega jekla s 6 % δ -ferrita

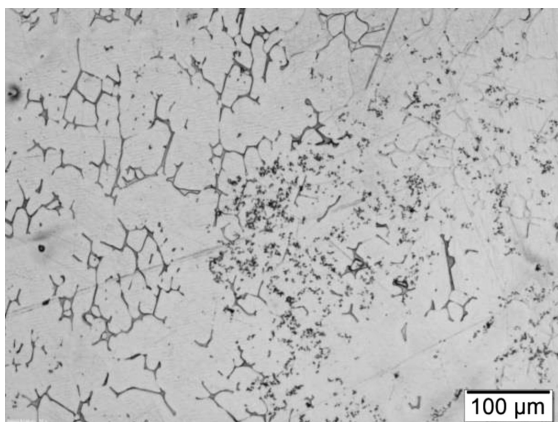


Figure 3: Cast microstructure of austenitic stainless steel with 6 % of δ -ferrite and Al_2O_3 ultrafine particles

Slika 3: Lita mikrostruktura avstenitnega nerjavnega jekla s 6 % δ -ferrita in Al_2O_3 ultrafinimi delci

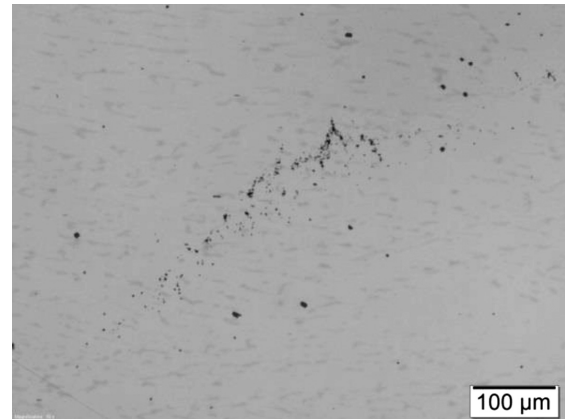


Figure 4: Cast microstructure of austenitic stainless steel with Al_2O_3 ultrafine particles inserted into the melt (experiment 2)

Slika 4: Lita mikrostruktura avstenitnega nerjavnega jekla z Al_2O_3 ultrafinimi delci, vstavljenimi v talino (preizkus 2)

ures represent the Al_2O_3 ultrafine particles that are non-uniformly distributed in the steel matrix.

In **Figure 6** the AES spectrum of the Al_2O_3 ultrafine particles in the cast microstructure of austenitic stainless steel is shown. The spectra of particles (P1 and P2) showing only O and Al peaks confirm the successful introduction of Al_2O_3 ultrafine particles into the steel matrix (P3) without any intermetallic reaction taking place.

4 CONCLUSIONS

Steel matrix composites with non-uniformly dispersed Al_2O_3 ultrafine particles were produced by a conventional melting and casting method. The purpose of this investigation was to determine the methodology and analysing techniques suitable for the analysis and identi-

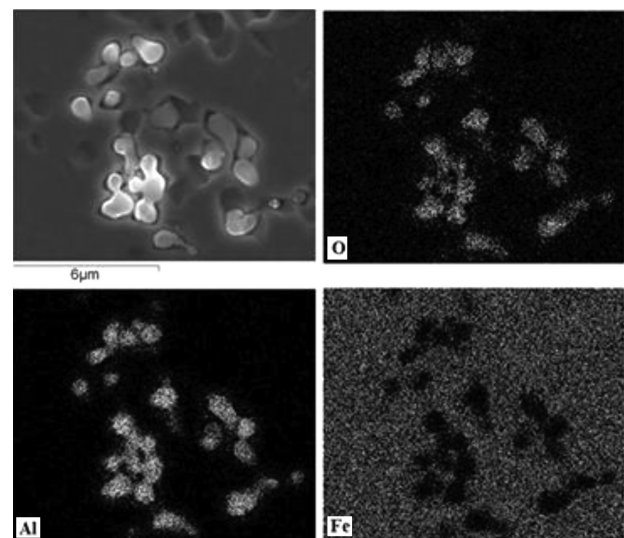


Figure 5: SEM elemental analysis of Al_2O_3 ultrafine particles in the cast microstructure of austenitic stainless steel

Slika 5: SEM-posnetek elementne analize Al_2O_3 ultrafinih delcev v liti mikrostrukturi avstenitnega nerjavnega jekla

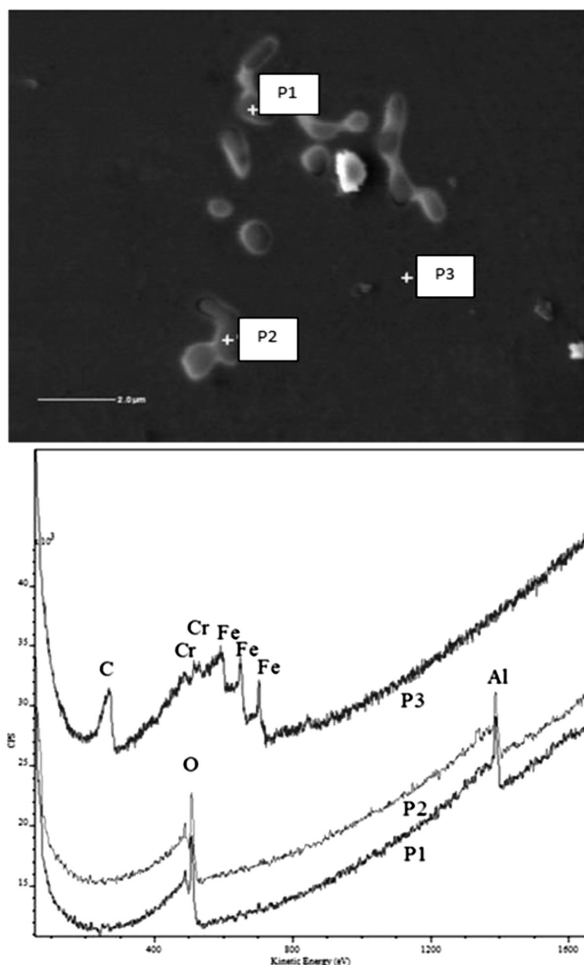


Figure 6: AES spectrum of the Al_2O_3 ultrafine particles in the cast microstructure of austenitic stainless steel

Slika 6: AES-spekter analize Al_2O_3 ultrafinih delcev v liti mikrostrukturi avstenitnega nerjavnega jekla

fication of ultrafine particles incorporated in the steel matrix.

The microstructural changes and the dispersion of the Al_2O_3 ultrafine particles in the steel matrix were observed and analysed by light microscopy (LM), scanning electron microscopy (SEM) and auger electron spectroscopy (AES). This work clearly shows that for a proper analysis and identification of the successful nano-particles' incorporation, different analysing techniques need to be used and combined.

Based on the experimental results the dispersion of the Al_2O_3 ultrafine particles in the steel matrix is non-homogeneous and concentrated in certain areas.

In order to be able to obtain a homogeneous distribution of reinforcements in the metal matrices the following factors need to be understood and taken into consideration for future work:

- particle density, size, shape and volume fraction will influence the reinforcement settling rate,
- surface properties of the particles will affect the wetting with molten metal,
- rheological behaviour is influenced by the reaction of the particles with the melt and each other,
- in general, the reinforcement particles occupy interdendritic or between secondary dendrite arm spacings, while the particle distribution is also metal-matrix dependent.

5 REFERENCES

- ¹ Y. Q. Liu, H. T. Cong, W. Wang, C. H. Sun, H. M. Cheng, AlN nanoparticle-reinforced nanocrystalline Al matrix composites: Fabrication and mechanical properties. *Met.Sic.Eng.A*, 505 (2009), 151–156, doi:10.1016/j.msea.2008.12.045
- ² C. S. Goh, J. Wei, L. C. Lee, M. Gupta, Ductility improvement and fatigue studies in Mg-CNT nanocomposites. *Compos. Sci. Tech.* 68 (2008), 1432–1439, doi:10.1016/j.compscitech.2007.10.057
- ³ Z. Razavi Hesabi, A. Simchi, S. M. Seyed Reihani, Structural evolution during mechanical milling of nanometric and micrometric Al_2O_3 reinforced Al matrix composites. *Mater. Sci. Eng. A*, 428, (2006), 159–168, doi: 10.1016/j.msea.2006.04.116
- ⁴ J. Llorca, Fatigue of particle-and whisker reinforced metal-matrix composites. *Prog.Mater.Sci.*, 47 (2002), 283–353, doi:10.1016/S0079-6425(00)00006-2
- ⁵ B. N. Chawla, Y. Shen, Mechanical Behavior of Particle Reinforced Metal Matrix Composites, *Adv.Eng.Mater.*, 3 (2001) 6, 357–370, doi:10.1002/1527-2648(200106)3:6<357::AID-ADEM357>3.3.CO;2-9
- ⁶ R. Casati, M. Vedani, Metal Matrix Composites Reinforced by Nano-Particles – A Review, *Metals (Basel)*, 4 (2014) 1, 65–83, doi:10.3390/met4010065
- ⁷ S. H. Lee, J. J. Park, S. M. Hong, B. S. Han, M. K. Lee, C. K. Rhee, Fabrication of cast carbon steel with ultrafine TiC particles. *Trans Nonferrous Met. Soc. China (English Ed.)*, 21 (2011), 54–57, doi:10.1016/S1003-6326(11)61060-1
- ⁸ R. Konwar, A. B. Ahmed, Nanoparticle: an Overview of Preparation, Characterization and Application. *Int. Res. J. Pharm.*, 4 (2013) 4, 47–57, doi:10.7897/2230-8407.04408
- ⁹ C. Linsmeier, Auger electron spectroscopy. *Vacuum*, 45 (1994) 6–7, 673–690, doi:10.1016/0042-207X(94)90108-2
- ¹⁰ S. Y. Cho, J. H. Lee, Anisotropy of wetting of molten Fe on Al_2O_3 single crystal. *Korean J. Mater. Res.*, 18 (2008) 1, 18–21, doi:10.3740/MRSK.2008.18.1.018

A COMPARISON OF AS-WELDED AND SIMULATED HEAT AFFECTED ZONE (HAZ) MICROSTRUCTURES

PRIMERJAVA MIKROSTRUKTURE TOPLOTNO VPLIVANEGA PODROČJA VARJENEGA IN SIMULIRANIH VZORCEV

Roman Celin¹, Jaka Burja¹, Gorazd Kosec²

¹Institute of Metals and Technology, Lepi pot 11, 1000 Ljubljana, Slovenia

²Acroni d.o.o., Cesta Borisa Kidriča 44, 4270 Jesenice, Slovenia
roman.celin@imt.si

Prejem rokopisa – received: 2016-01-05; sprejem za objavo – accepted for publication: 2016-01-29

doi:10.17222/mit.2016.006

The high-strength steel grade S690QL and a filler welding wire Mn3Ni1CrMo were the materials chosen for welding a V-shaped butt weld. In order to prevent the weld's cold cracking, a multi-pass welding technique was applied. A metallographic investigation revealed microstructure variations in different areas of the weld's heat-affected zone. A reverse-engineering approach was used to test a dilatometer's capabilities to simulate different HAZ microstructures. Hollow steel-cylinder specimens were subjected to several weld thermal cycles in order to generate similar microstructures as in the real weld's HAZ. The microstructures of the as-welded and simulated heat-affected zone specimens were investigated. Good agreement was found between the dilatometer-simulated HAZ microstructures and those in a real HAZ weld.

Keywords: welded joint, microstructure, high-strength low-alloy steel, simulation, dilatometer, heat-affected zone

Visokotrdno jeklo S690QL in varilna žica Mn3Ni1CrMo kot dodatni material, sta bila uporabljena pri varjenju sočelnega V-spoja. Za preprečitev pokanja v hladnem je bila uporabljena tehnika večvarkovnega varjenja. Metalografska preiskava je odkrila različne mikrostrukture v različnih predelih toplotno vplivanega področja zvara. Za preizkus delovanja dilatometra je bil, za simulacijo mikrostruktur različnih področij toplotno vplivanega področja, uporabljen princip povratnega inženirstva. Različna mikrostruktura toplotno vplivanega področja je bila simulirana z izpostavitvijo votlih cilindričnih vzorcev različnim toplotnim ciklom. Opravljena je bila metalografska preiskava realnega zvarjenega spoja in simuliranih vzorcev. Primerjava rezultatov je pokazala dobro ujemanje simuliranih in realnih mikrostruktur.

Ključne besede: zavarjen spoj, mikrostruktura, visokotrdno jeklo, simulacija, dilatometer, toplotno vplivano področje

1 INTRODUCTION

The decision to use high-strength steel depends on a number of application requirements, such as thickness reduction, corrosion resistance, formability and weldability. The quenched and tempered low-alloy (QTLA) steels, usually containing less than 0.25 % carbon and less than 5 % alloying elements, are strengthened primarily by quenching and tempering to produce microstructures containing martensite and bainite.¹ S690QL is such a steel grade with high strength and toughness.²

Any common welding procedure can be used to join QTLA steels.³ For any given steel, the welded joint's microstructures and the mechanical properties in the weld metal (WM) and the heat-affected zone (HAZ) are influenced mainly by the welding thermal cycle.

Due to the welding thermal cycle and the associated peak temperature, a change of the parent metal's microstructure and the mechanical properties happens in the HAZ. With increasing distance from the fusion line the peak temperature decreases, thus forming different microstructures. The width of the HAZ depends on the welding procedure, the thermal conditions and the physical properties of the parent metal.

Figure 1 shows a simplified presentation of different HAZ regions of a multi-pass welded joint. Weld pass 2 has a portion of HAZ that can be treated as a single weld pass and can be divided into four regions. These regions are defined by the peak temperature to which the region was exposed during the weld thermal cycle:^{4,5}

- Coarse-grain region (CG HAZ) – material adjacent to the fusion line that reaches a peak temperature T_P above 1300 °C,
- Fine-grain region (FG HAZ) – T_P is lower, but still above A_{C3} ,
- Inter-critical region (IC HAZ) – T_P is between $A_{C1} < T_P < A_{C3}$,
- Sub-critical region (SC HAZ) – T_P is lower than A_{C1} .

However, the welding of thick steel components usually requires the application of a multi-pass welding procedure. In this case, the first pass (weld pass 1) HAZ regions are reheated to different peak temperatures during the second weld pass thermal cycle (weld pass 2).

Figure 1 also shows a simplified presentation of the different reheated first weld pass HAZ regions:^{4,5}

- region 1: Super-critically reheated coarse-grain HAZ – SCR CG HAZ,

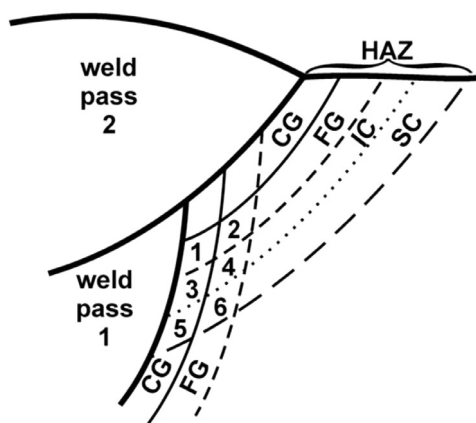


Figure 1: Simplified representation of the different regions of the HAZ

Slika 1: Poenostavljena predstavitev različnih območij toplotno vplivanega področja

- region 2: Inter-critically reheated coarse-grain HAZ – IR CG HAZ,
- region 3: Sub-critically reheated coarse-grain HAZ – SC CG HAZ,
- region 4: Super-critically reheated fine-grain HAZ – SCR FG HAZ,
- region 5: Inter-critically reheated fine-grain HAZ – IR FG HAZ,
- region 6: Sub-critically reheated fine-grain HAZ – SC FG HAZ.

In a real weld the HAZ regions are narrow in relation to the weld. To achieve regions of uniform microstructure suitable for investigations, weld simulators are used.⁶⁻¹² Usually, these weld thermal simulations are made in conjunction with weldability investigations to determine the proper welding parameters.

In the presented investigation a dilatometer with a controlled heating and cooling fixture was used to simulate the weld thermal cycles. The goal of the investigation was to test the dilatometer’s capability to simulate the microstructures that correspond to the real weld’s HAZ microstructures using a reverse-engineering approach.

2 EXPERIMENTAL PART

The chemical analysis of the Micral 690 sample with an ICP spectrometer was made prior to any further investigations. The determination of the welding parameters for the Micral 690 welding procedure was carried out by considering the EN 1011-2 recommendations, the steel manufacturer’s specifications and the data from several papers.¹³⁻¹⁶

The two plates, with a thickness of 15 mm, a length of 500 mm, a width of 150 mm and a V-groove joint geometry, were welded with 8 passes using the sequence shown in **Figure 2**. A manual MAG welding procedure in a flat (PA) position was used. The filler material was grade Mn3Ni1CrMo welding wire with a diameter of

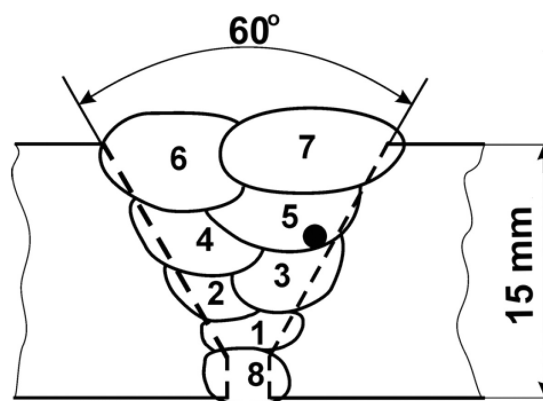


Figure 2: Sketch of the welded joint
Slika 2: Skica zavarjenega spoja

ϕ 1.2 mm, according to SIST EN ISO 16834¹⁷. The shielding gas used was a mixture M21 (82 % Ar + 18 % CO₂). The welding was carried by a skilled, certified welder and without preheating.

The welding current, voltage and time were recorded during the procedure. The weld pass 5 thermal cycle was recorded by dipping a type-S thermocouple (Pt Rh–Pt) directly into the weld’s molten bead. The approximate position of the thermocouple is marked with a dot. Standard¹⁸ non-destructive examinations and mechanical tests of the weld joint were also carried out and are described in a previous paper.¹⁹

Seven hollow, 10-mm-long cylinders with a 4-mm outer diameter and 1.5-mm inner diameter were machined from the weld’s parent material (base metal) plate. Holes were bored in order to obtain a uniform heating and cooling of the sample during the thermal simulation.

The simulations were carried out with a TA instruments DIL805A/D quenching dilatometer in a vacuum atmosphere, with argon used as a coolant. Control of the thermal cycle was maintained via a type-S thermocouple that was spot welded directly onto the hollow cylinder sample.

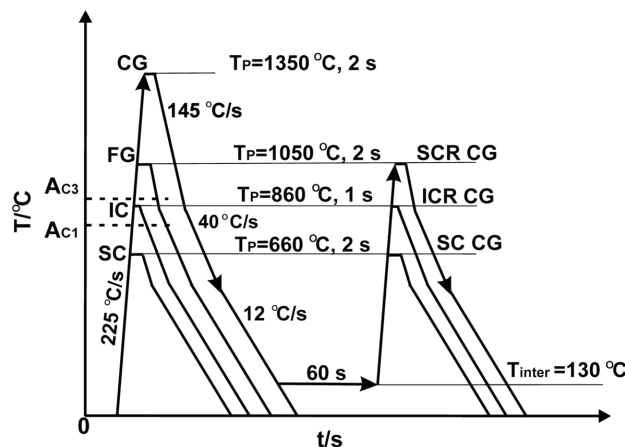


Figure 3: Schematic diagrams for the thermal cycle simulations
Slika 3: Diagrami za potek simulacij termičnih ciklov

Figure 3 shows schematic diagrams with the parameters for seven thermal cycle simulations used to generate the corresponding microstructure:

- single weld pass CG, FG, IC and SC regions of the HAZ,
- reheated weld pass SCR CG, IC CG, SC CG regions of the HAZ, as in **Figure 1**.

For the reheated simulated thermal cycles the same parameters were used as for the single-cycle simulation. The time–temperature dependence (**Figure 4**) recorded during weld pass 5 was used to determine the simulation heating rate, the peak temperatures, the holding times and the cooling rates.

During a single coarse-grain (CG) thermal cycle simulation the specimens' phase-transition temperatures A_{C1} and A_{C3} were recorded as well as the dilatation and temperature data from each simulation. The specimen was prepared by grinding and polishing with diamond paste, followed by a chemical etching with 5 % Nital.

Macro- and microscopic examinations^{20–22} were performed using a light microscope (LM) to characterize the microstructures of the deposited weld metal, the heat-affected zone, the parent metal and the dilatometer-simulated hollow cylinder specimens of the parent metal.

A comparison between the as-welded and the dilatometer-simulated microstructures was carried out.

3 RESULTS AND DISCUSSION

The results of the parent metal's quantitative chemical analysis are presented in **Table 1**. The steel contains strong carbide-forming elements such as Nb, Mo, Cr and Ti, which ensure high strengths, even at elevated temperatures.

Table 1: Chemical composition of parent metal in mass fractions, w/%

Tabela 1: Kemična sestava jekla v masnih deležih, w/%

C	Si	Mn	P	S	Cr	Ni
0.164	0.29	0.72	0.006	0.001	0.54	0.20
Cu	Mo	Ti	Nb	Al	B	N
0.25	0.263	0.02	0.028	0.028	0.001	0.011

The applied welding parameters and the calculated welding speed and heat input were:

- weld length, 500 mm
- welding time, 132–422 s
- voltage, 21–22 V
- current, 100–165 A
- weld inter-pass temperature, 130 °C
- welding speed, 1.8–2.89 mm/s
- heat input, 1.03–1.63 kJ/mm

Lower-value welding parameters were applied for the root pass welding.

After the temperature–time data acquisition from the temperature-measurement instrument's memory card and data analysis for the welding pass 5, a cooling time $t_{8/5}$ of

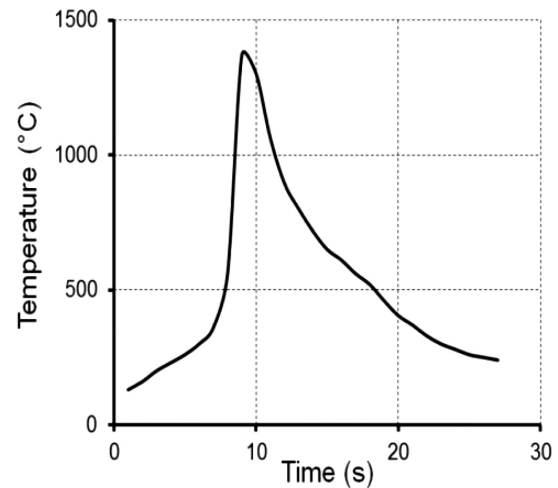


Figure 4: Weld pass 5 – recorded temperature – time dependence
Slika 4: Polnilni varek 5 – zabeležena odvisnost temperatura – čas

7.6 s was determined and the peak temperature T_P was 1370 °C (**Figure 4**).

The shape of the cooling curve (**Figure 4**) is affected by the inter-pass temperature. Also, the weld's cooling time is prolonged due to the reduced temperature difference between the weld material and the surrounding parent metal.

Figure 5 shows the ICR CG HAZ recorded thermal cycle simulation with the temperature and the dilatation curve. From the dilatation data analysis of the phase transformation during the CG thermal cycle simulation the transition temperatures A_{C1} and A_{C3} were found to be 830 °C and 885 °C, respectively. During the rapid heating of steel, as in the case of welding, the phase-transformation temperatures are increased, the observed transformation temperatures A_{C1} and A_{C3} are well above equilibrium, i.e., about 710 °C and 785 °C respectively. The increase of the transformation temperatures is attributed to the diffusion process of the transformation from ferrite to austenite, which is time and temperature dependent. The dilatation curve in **Figure 5** clearly indicates that a transformation took place below 500 °C,

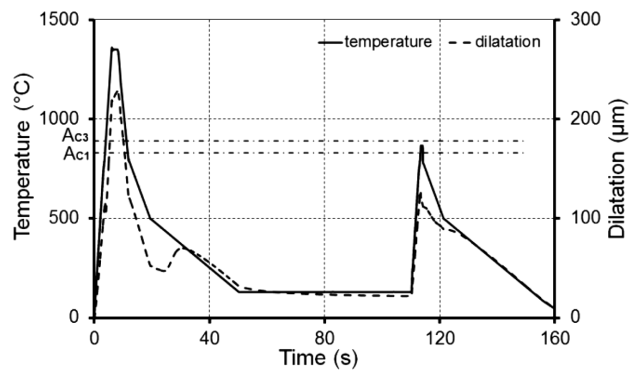


Figure 5: ICR CG HAZ thermal simulation with temperature-time and dilatation-time dependence

Slika 5: Potek temperature in raztezka v odvisnosti od časa pri simulaciji interkrtičnega grobozrnatega TVP

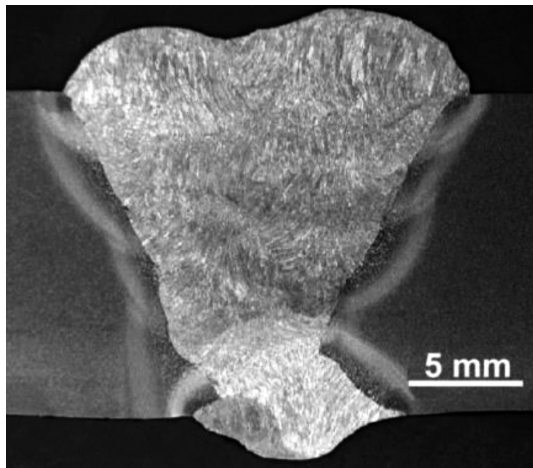


Figure 6: Welded joint macro section
Slika 6: Makroposnetek zavarjenega spoja

during the first cooling, and that another transformation took place during the second cooling, but it was not as intense as the first one, thus proving that the inter-critical temperature was indeed reached.

A good fit was found between the theoretical (**Figure 3**) and dilatometer-simulated thermal IR CG HAZ cycle (**Figure 5**). The heating rates, cooling rates, and holding times were very close to those programmed, with minor deviations due to the response of the dilatometer control and the regulation system. The first thermal cycle peak temperature was 1360 °C, with an inter-critical peak temperature of 866 °C.

Figure 6 shows the welded joint's macro section with each weld pass and the corresponding HAZ. Between subsequent weld passes an unaffected region of the coarse-grain HAZ microstructure can be distinguished. The reheated pockets of the CG HAZ regions are small and discontinuous, which makes their microstructure difficult to identify and investigate. During metallographic investigations the dimensions of the IR CG HAZ microstructure region were estimated to be 0.8 mm long and 0.3 mm wide.

Figure 7 shows the weld pass 5 HAZ area not affected by a subsequent weld pass thermal cycle. It is an area with a longitudinal microstructure transition from the weld metal (WM) through the heat-affected zone (HAZ) microstructures to the parent metal (PM).

The weld metal (WM) consists of columnar dendrites with a bainite microstructure. Some individual martensitic grains are also present in the middle of the deposi-

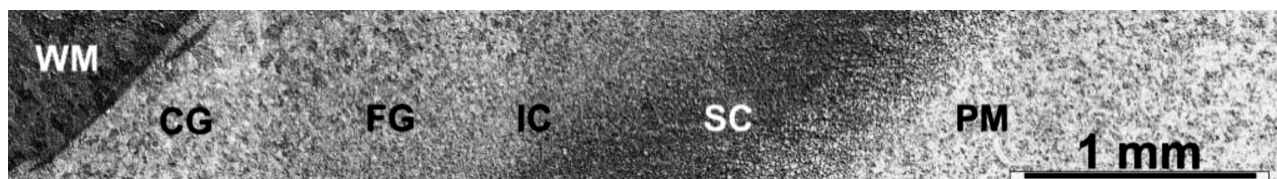


Figure 7: Transition from weld metal (WM) to parent metal (PM)
Slika 7: Prehod iz vara (WM) v osnovni material (PM)

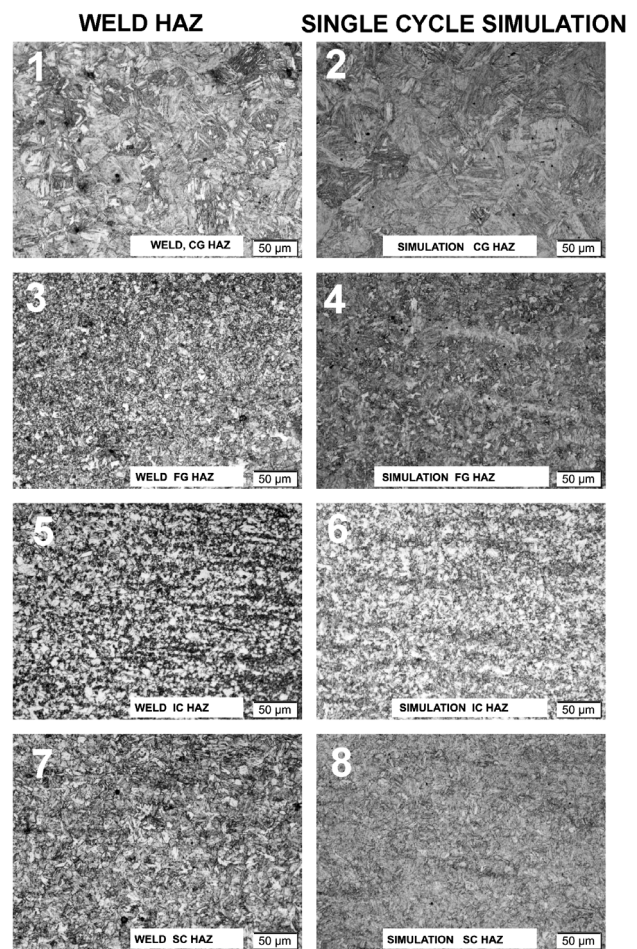


Figure 8: Real and simulated HAZ microstructures
Slika 8: Realne in simulirane mikrostrukture TVP

ted weld metal. The microstructure of the HAZ consists of martensite and bainite with a transition to the unaffected tempered martensitic microstructure of the parent metal (PM) (**Figures 8** and **9**).

Figure 8.1 shows the coarse grains (CGs) that are present in the HAZ adjacent to the fusion boundary of the weld. The fine-grain (FG, **Figure 8.3**) region follows due to the peak temperature above A_{C3} but lower than in the CG region, the temperature and time were not sufficient to cause severe grain growth. With increasing distance from the fusion boundary there are inter-critical (IC, **Figure 8.5**) and subcritical (SC, **Figure 8.7**) regions of the HAZ.

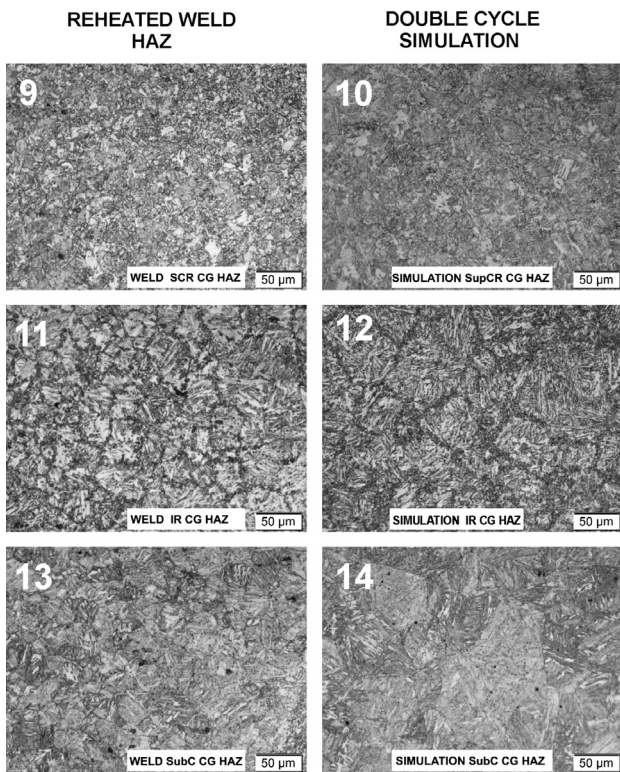


Figure 9: Real and simulated HAZ microstructures; reheated regions
Slika 9: Realne in simulirane mikrostrukture TVP; ponovno pregreta področja

The reheated inter-critical region (**Figure 9.11** and **9.12**) is very susceptible to failure, due to the fact that the phase transformation into austenite began on the grain boundaries; these small areas were then quickly cooled and are in turn hard and brittle. The subcritical regions are mainly tempered bainite and martensite with precipitated carbides and therefore represent no danger to the structural integrity of the weld. The simulated microstructures in **Figure 8** and **Figure 9** are labelled with even numbers. Although the grain size of the simulated specimen is slightly larger than that of the real welded joint when comparing the identical thermal cycle, we can distinguish a similarity between the welded HAZ and the dilatometer-simulated microstructures. The reason for the larger grains is that the thermal pinning is not considered in the thermal cycle simulation process.⁶

4 CONCLUSIONS

Normally, a dilatometer is used to observe a specimen's dimensional changes under a controlled heating or cooling rate. It can also be used to construct a continuous-cooling- transformation (CCT) diagram or an isothermal time-temperature-transformation (TTT) diagram. The TA DIL805A/D dilatometer with controlled heating and cooling fixtures was tested to simulate a real weld's HAZ microstructure. Based on the investigation the following can be concluded:

- The use of a simulated HAZ microstructure is a convenient way to study the weldability of a given steel.
- The presented investigation was limited to microstructure, due to the specimen's size and geometry.
- The simulation of a weld's HAZ microstructure is possible within the limits of the dilatometer's capabilities and the specimen's size.
- Hollow cylinder samples had a better response to the heating and cooling rate change than a solid cylinder.
- The inter-critical temperature during welding of S690QL is between 830 °C and 885 °C.

Acknowledgment

The authors are thankful to the Acroni d.o.o. and Elektrode Jesenice for the technical support related to work presented in this paper.

5 REFERENCES

- ¹ F. J. Winsor, ASM Handbook, Vol. 6: Welding, Brazing and Soldering, ASM, International, Materials Park, OH 1993, 662
- ² SIST EN 10025-6:2005+A1:2009, Hot rolled products of structural steels – Part 6: Technical delivery conditions for flat products of high yield strength structural steels in the quenched and tempered condition
- ³ S. Kou, Welding metallurgy, 2nd ed., Wiley Interscience, Hoboken 2003, 406
- ⁴ M. Hamada, Control of strength and toughness at the heat affected zone, Welding International, 17 (2003) 4, 265-270
- ⁵ T. Lolla, S. S. Babu, S. Lalam, M. Manohar: Understanding the Role of Initial Microstructure on Intercritically Reheated Heat-Affected Zone Microstructures and Properties of Microalloyed Steels, Proc. of the 9th Inter. Conf., June 4–8, 2012 Chicago, 34-42
- ⁶ Y. Shi, Z. Han, Effect of weld thermal cycle on microstructure and fracture toughness of simulated heat-affected zone for a 800 MPa grade high strength low alloy steel, Journal of Materials Processing Technology, 207 (2008), 30–39, doi: 10.1016/j.jmatprotec.2007.12.049
- ⁷ G. R. Goodall, J. Gianetto, J. Bowker, M. Brochu, Thermal simulation of HAZ regions in modern high strength steel, Canadian Metallurgical Quarterly, 51 (2012), 1, 58–66, doi:10.1179/1879139511Y.0000000023
- ⁸ I. Samardžić, A. Stoić, D. Kozak, I. Kladaric, M. Dunder, Application of Weld Thermal Cycle Simulator in Manufacturing Engineering, Journal of Manufacturing and Industrial Engineering, Journal of Manufacturing and Industrial Engineering, 12 (2013), 1–2, 7–11, doi: http://dx.doi.org/10.12776/mie.v12i1-2.177
- ⁹ G. L. Liang, S.W. Yang, H. B. Wu, X. L. Liu, Microstructure and mechanical performances of CGHAZ for oil tank steel during high heat input welding, Rare Metals 32 (2013) 2, 129–133, doi:10.1007/s12598-013-0036-y
- ¹⁰ Y. Adonyi, Heat-Affected Zone Characterization by Physical Simulations, Welding Journal, 10 (2006), 42-47
- ¹¹ J. Wang, S. Lu, L. Rong, D. Li, Thermal cycling, microstructure and mechanical properties of 9Cr2WVTa steel welds, Journal of Materials Processing Technology, 222 (2015) 8, 434–443, doi:10.1016/j.jmatprotec.2015.03.017
- ¹² M. Dunder, I. Samardžić, T. Vuherer, Dependence of hardness and impact energy on cooling time $\Delta t_{8/5}$ and temperature for S960QL, Metalurgija, 54 (2015) 3, 539–542, doi:10.12776/mie.v12i1-2.177
- ¹³ Welding – Recommendations for welding of metallic materials – EN 1011-2 Part 2: Arc welding of ferritic steels

- ¹⁴ I. Hajro, O. Pašić, Z. Burzić, Karakterizacija zavarenih spojeva na visokočvrstom konstrukcionom čeliku S690QL, Zavarivanje i zavarene konstrukcije, 58 (2010) 4, 123–129
- ¹⁵ M. Shome, Effect of heat-input on austenite grain size in the heat affected zone of HSLA-100 steel, Materials Science and Engineering A, 39 (2007) 13, 454–460, doi:10.1016/j.msea.2006.09.085
- ¹⁶ Acroni Micral 690 Datasheet, <https://www.metalandsteel.com/documentserver/store/17606/2b66fa1b-adaa-4b42-9700-1ab07d115e60.pdf>
- ¹⁷ SIST EN ISO 16834: – Welding consumables – Wire electrodes, wires, rods and deposits for gas shielded metal arc welding of high strength steels – Classification
- ¹⁸ SIST EN ISO 15614-1: Specification and Qualification of Welding Procedures for Metallic Materials – Welding Procedure Test – Part 1: Arc and Gas Welding of Steels and Arc Welding of Nickel and Nickel Alloys
- ¹⁹ R. Celin, J. Bernetič, D. A. Skobir Balantič, Welding of the steel grade S890QL, Mater. Tehnol., 48 (2014) 6, 931–935
- ²⁰ S. Kožuh, M. Gojčić, I. Ivanić, B. Kosec, Microstructure of welded austenitic stainless steel after annealing at 900 °C, Zavarivanje i zavarene konstrukcije, 61 (2013) 4, 149–156
- ²¹ F. Tehovnik, B. Arzenšek, B. Arh, D. Skobir, B. Pirnar, B. Žužek, Microstructure evolution in SAF 2507 super duplex stainless steel, Mater. Tehnol., 45 (2011) 4, 339–345
- ²² M. Pournavari, S. P. H. Marashi, H. L. Jaber, DP780 dual-phase-steel spot welds: critical fusion-zone size ensuring the pull-out failure mode, Mater. Tehnol., 49 (2015) 4, 579–585, doi:10.17222/mit.2014.184

DEGRADATION OF AN AISI 304 STAINLESS-STEEL TANK

DEGRADACIJA REZERVOARJA IZ AISI 304 NERJAVNEGA JEKLA

Matjaž Torkar, Irena Paulin, Bojan Podgornik

Institute of Metals and Technology, Lepi pot 11, 1000 Ljubljana, Slovenia
matjaz.torkar@imt.si

Prejem rokopisa – received: 2016-01-28; sprejem za objavo – accepted for publication: 2016-02-10

doi:10.17222/mit.2016.027

Some austenitic stainless steels are sensitive to the stress corrosion cracking (SCC) that appears only localized and with the specific combination of a relatively high internal tensile stress and the presence of corrosion media with chloride ions. The presented results are from an investigation of the leakage from a tank containing medical disinfection liquids. Due to a crevice below the insulation and the presence of condensed moisture, the corrosion pits started to grow on the surface of the tank. These crevice corrosion pits led to the appearance of SCC, which was responsible for the leakage from the AISI 304 stainless-steel tank.

Keywords: tank, AISI 304, leakage, crevice corrosion, stress corrosion cracking, brittle fracture

Nekatera avstenitna nerjavna jekla so občutljiva na napetostno korozijsko pokanje (SCC), ki se pojavi samo lokalno pri specifični kombinaciji relativno velikih notranjih nateznih napetosti in prisotnosti korozijskega medija s kloridnimi ioni. Predstavljeni so rezultati raziskave puščanja rezervoarja z medicinskimi dezinfekcijskimi tekočinami. Zaradi špranje pod izolacijo in prisotnosti kondenzirane vlage, so pričele rasti korozijske jamice na površini rezervoarja. Jamice, nastale pri špranjski koroziji, so omogočile pojav SCC, ki je odgovoren za puščanje rezervoarja iz AISI 304 nerjavnega jekla.

Ključne besede: rezervoar, AISI 304, puščanje, špranjska korozija, napetostno korozijsko pokanje, krhek prelom

1 INTRODUCTION

Stress corrosion cracking (SCC) is a localized form of corrosion that occurs under the simultaneous action of a tensile stress and a corrosive environment such as a chloride. SCC is characterized by fine cracks that can propagate extremely rapidly, leading to failure of the component and, potentially, of the associated structure.^{1,2}

Typical for SCC is the conjoint action of stress and a corrosive environment, which leads to the formation of a crack that would not have developed from the action of the stress or environment alone.³

Extensive research studies indicate that SCC appears only localized and under a specific combination of three conditions:

- the use of susceptible grades of material,
- a relatively high tensile stress relative to the yield strength (0.2 % proof strength), either from structural loading or present as residual stresses from forming or welding operations during manufacture and installation,
- the presence of a specific aggressive environment with chlorine-containing compounds (for instance by-products of disinfection) that can produce a highly corrosive film, which can lead to SCC.

Some grades of stainless steel, including 1.4301 (AISI 304) and 1.4401 (AISI 316), have long been recognised as susceptible to SCC, but generally only above 55 °C. However, failures in swimming pools in recent years occurred at around 30 °C, in highly stressed components

that had not been washed by pool water or frequently cleaned.³ Suitable steels for safety-critical and load-bearing components in a pool hall atmosphere³ are the grades 1.4547, 1.4529 and 1.4565. All three types of austenitic stainless steels have a high content of molybdenum and nickel, which provide good resistance to chloride SCC.

Several studies were made on the influence of the surface condition of austenitic stainless steel on SCC.⁴⁻⁶ It was also revealed how highly cold-worked material showed a higher crack propagation rate.^{4,5}

A model was proposed for the crack propagation based on brittle fracture, localized oxidation and shearing near the crack tip.⁶ In all cases the cracks were initiated at the pitting sites.⁷

The mechanical fracture model of SCC assumes that the crack essentially propagates by dissolution, and then the remaining ligaments fail as a result of mechanical fracture (ductile or brittle). There are several proposed models described by the mechanical fracture model: the film-induced cleavage model, the tarnish rupture model, the tunnel model, the adsorption model and the hydrogen models.

The dissolution mechanism of SCC assumes that the crack propagation is due to active dissolution at the crack tip. The different models under this mechanism are the slip-dissolution model or the film-rupture model and intergranular SCC.⁸

SCC causes a rapid, brittle failure of the steel without any prior indication, and for this reason it is considered to be catastrophic. Several major disasters have been

attributed to the SCC of steel equipment, including the rupture of high-pressure gas-transmission pipes, boiler explosions and severe damage to power stations and oil refineries.⁸⁻¹⁰

The SCC propagation mechanisms can be divided into two groups: those which involve embrittlement of the metal due to corrosive reactions (mechanical fracture models) and those in which the cracks grow due to a localized dissolution process.⁸

The disinfection liquid storage tank was part of an industrial washer-disinfector assembly used for cleaning medical equipment and was made of 1.8-mm-thick cold-rolled AISI 304 stainless steel. The whole assembly was in operation for 2 years. Two kinds of liquids were stored in the tank: 1 % of volume fractions of solution of cleaning liquid in demineralized water with pH = 11.3, and 1 % of volume fractions of solution of neutralizing liquid in demineralized water with pH = 2.6.

The aim of this paper is to present a corrosion degradation investigation and the reasons for the leakage from the storage tank.

2 EXPERIMENTAL PART

The samples for the investigation were cut from the wall of the tank, in the corrosion-damaged area where the wall leaks. Metallographic samples of the cross-section of the wall were prepared by a standard metallographic procedure. The samples were observed with a Nikon Microphot FXA light microscope with a video camera and analySIS software. The surface and the cracks were observed using a JSM-6500F FE SEM scanning electron microscope and analysed by EDS (Energy-Dis-



Figure 1: Corroded outer surface below the insulation
Slika 1: Korodirana zunanja površina rezervoarja pod izolacijo



Figure 2: Local corrosion damage inside the tank
Slika 2: Lokalne korozijske poškodbe znotraj rezervoarja

persive Spectroscopy). The EDS analyses were performed on the corroded internal surface and on the fractures. The base material was analysed using the X-ray Fluorescence (XRF) method.

3 RESULTS AND DISCUSSION

3.1 Visual examination

The corroded areas inside and outside the tank under the insulation are shown in **Figure 1** and **Figure 2**. Inside the tank the corrosion damage is limited to the area shown in **Figure 2**, while the corroded area on the outside surface below the insulation is spread much wider (**Figure 1**) and looks more uniform. In addition, the place where the sample material was cut from the tank wall is presented in **Figure 1**.

Inner surface of the tank, shown in **Figure 3**, looks like a general pitting-corrosion attack with some pits joining together to form interconnected pits.

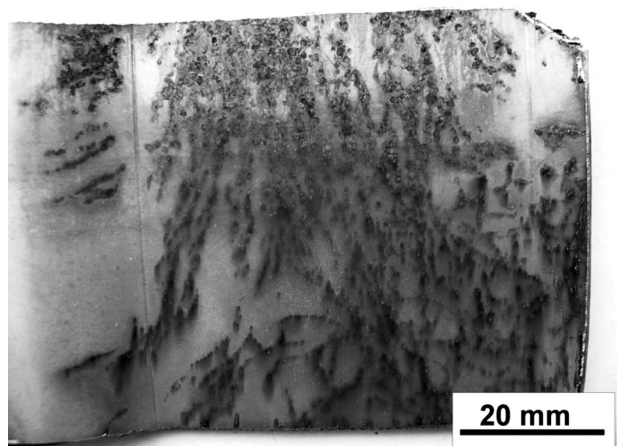


Figure 3: Corrosion damage on the inner surface of the tank
Slika 3: Korozijske poškodbe na notranji površini rezervoarja

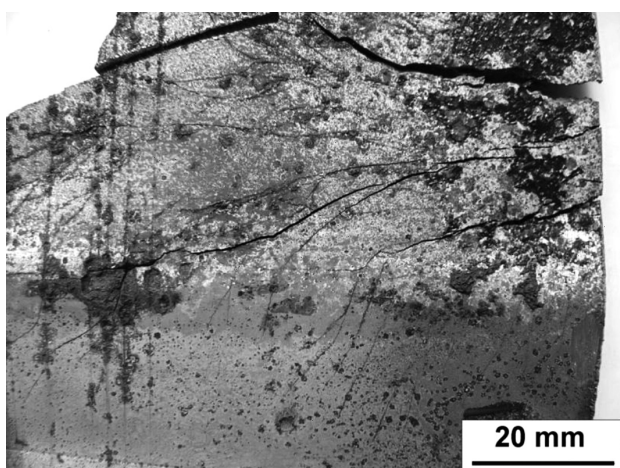


Figure 4: Corroded external surface of the tank with corrosion pits and cracks

Slika 4: Zunanja površina rezervoarja s korozivskimi jamicami in razpokami

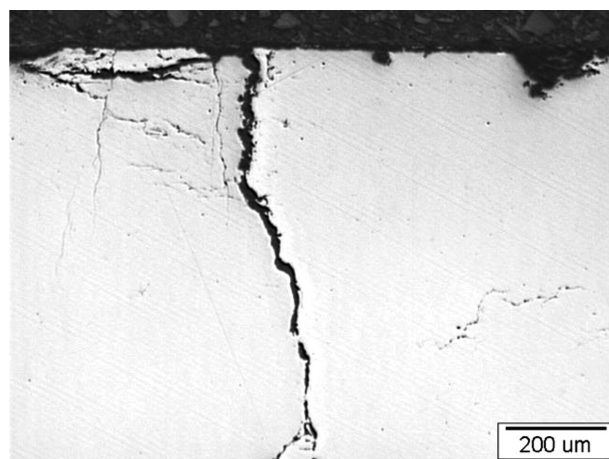


Figure 6: Cross-section of the tank wall

Slika 6: Presek stene rezervoarja

Figure 4 depicts the sample material cut from the tank wall. Corrosion pits due to crevice corrosion and cracks due to stress corrosion are present on the outer surface of the tank.

3.2 Chemical analysis

An XRF analysis was performed on the sample material from the tank. The results of the analysis are shown in **Table 1**.

The sample chemical composition analysis results are in accordance with the AISI 304 grade stainless steel's specification requirements.

3.3 Metallographic examination

During the cutting of the samples for metallography it was evident that the material is brittle in the region of the corrosion and did not resist even a small bending force. In contrast, out of the region of corrosion the

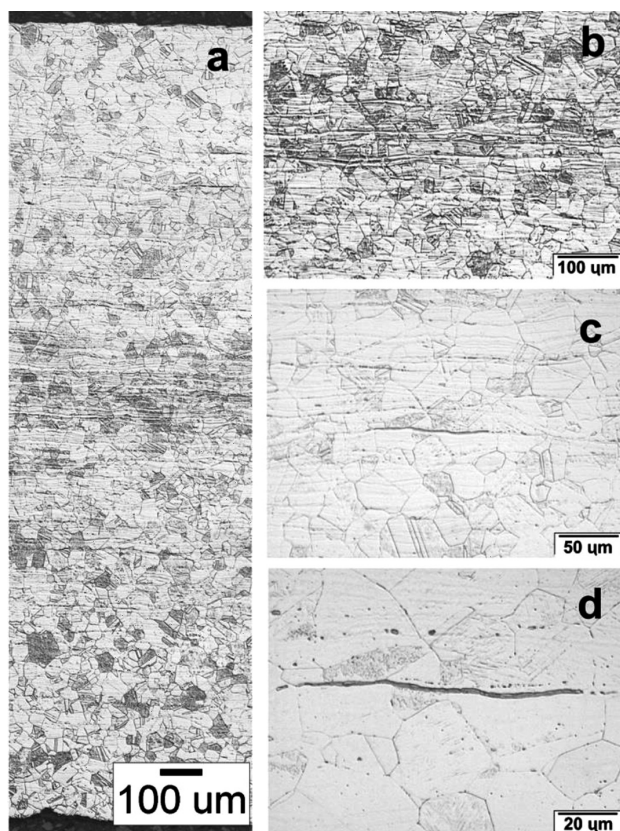


Figure 5: Microstructure of the cross-section of the wall

Slika 5: Mikrostruktura preseka stene

Table 1: Chemical composition of the tank sample in mass fractions (w/%)

Tabela 1: Kemijske sestave vzorca rezervoarja v masnih deležih (w/%)

	C	Si	Mn	Cr	Ni	Mo	Fe
tank sample	0.07	0.68	1.2	19.2	9.1	–	69.75
AISI 304	Max 0.08	Max. 1.00	Max. 2.0	18–20	8–10.5	–	

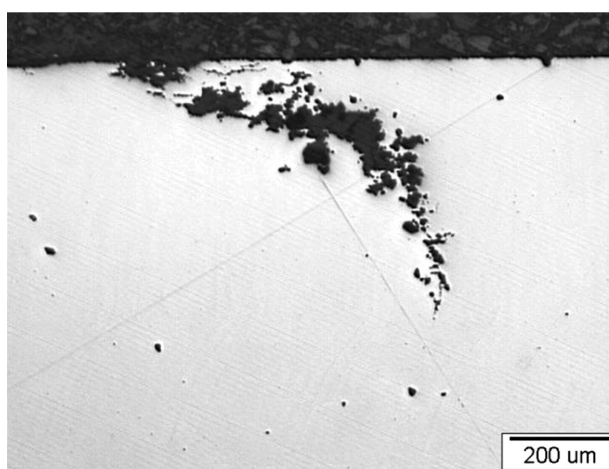


Figure 7: Crevice-corrosion pit

Slika 7: Špranjska korozija

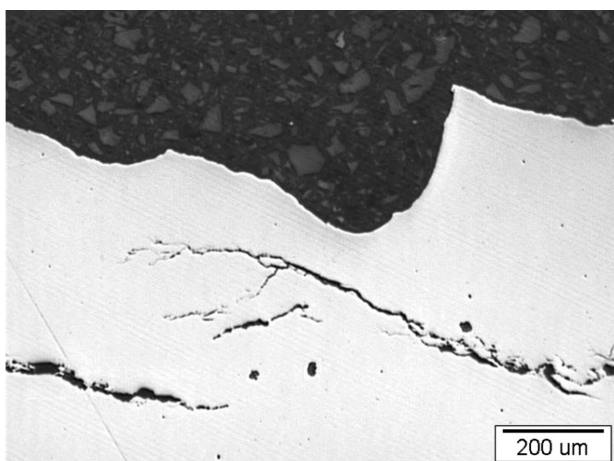


Figure 8: Internal surface pitting corrosion stress corrosion cracks
Slika 8: Jamičasta korozija na notranji površini rezervoarja in napetostne korozijske razpoke

material behaved normally and was bent at an angle of 180° without any damage.

The microstructure of the cross-section in the sound part of the material is presented in **Figure 5a**. In the central part (**Figure 5b**) are the elongated grains. The elongated inclusions of MnS are shown in **Figures 5c** and **5d**, both oriented in the cold-rolling direction.

The cross-section of the degradation area, below the tank insulation, is presented in **Figure 6**. The crack originates from the crevice corrosion on the external surface of the tank.

The presence of condensed moisture in the gap between the insulation and the tank's external surface caused the development of a crevice-corrosion pit shown in **Figure 7**.

The cracks (**Figures 6** and **8**) are typical for SCC and spread through the wall, mostly across the grains (trans-crystalline). Through the wall the cracks caused the leakage of the liquid stored in the tank. The cracks are connected with the pits and the pits act as initiation

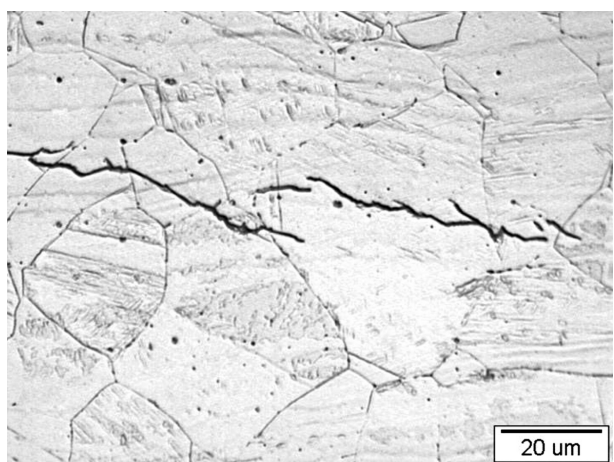


Figure 9: Trans-crystalline crack formed during SCC
Slika 9: Transkristalna razpoka, nastala pri napetostnem korozijskem pokanju

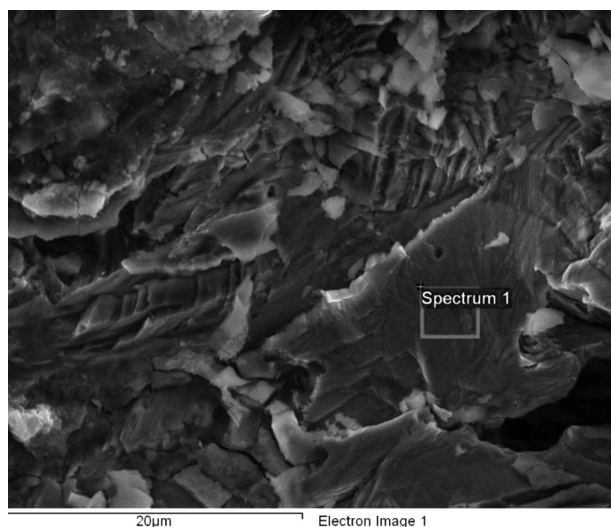


Figure 10: Brittle fracture of the wall
Slika 10: Krhek prelom stene

places for the cracks' formation. We can conclude that the corrosion processes started as crevice corrosion on the external surface below the insulation.

The internal surface of the tank is shown in **Figure 9**. Wide corrosion pits can be seen (**Figure 9**). These pits can be classified as pitting corrosion. Branched stress corrosion cracks are also present.

3.4 Scanning electron microscopy

The brittleness of the material was observed only in the areas damaged by corrosion. The fracture of the wall is brittle (**Figure 10**) and typical for the SCC of stainless steel. The region of the EDS analysis (SEM) is marked as Spectrum 1.

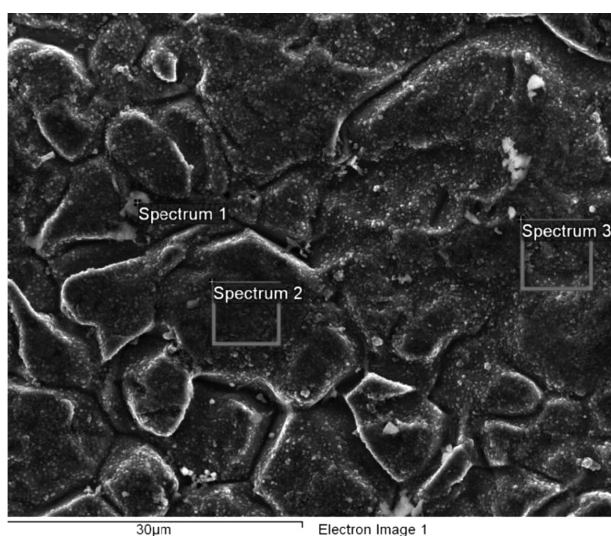


Figure 11: Surface with deep-etched grain boundaries and corrosion products with marked areas of EDS analysis (SEM)
Slika 11: Površina z globoko jedkanimi mejami med zrn in korozijski produkti z označenimi področji EDS-analize (SEM)

The EDS analysis of the fracture surface (**Table 2**) detected the presence of chlorine, which is a regular companion in the corrosion of stainless steels and acts as the main accelerator of the pitting corrosion.

The deep-etched grain boundaries presented in **Figure 11** are due to the pickling of the sheet's surface. The surface is partially covered with corrosion products. The EDS analysis (**Table 3**) of the grain (Spectrum 1) revealed an increased content of oxygen, silicon, chlorine, manganese and nickel. On the other two areas analysed (Spectrum 2 and 3) traces of rust prevailed with contents of iron, chromium, nickel and oxygen. The origin of the chlorine is not known. This chlorine was detected on the corroded external surface as well as on the surfaces of the brittle cracks.

Table 2: EDS analysis of a brittle fracture surface, in mass fractions (w/%)

Tabela 2: EDS-analiza površine krhkega preloma, v masnih odstotkih (w/%)

Spectrum	Cr	Ni	Si	Mn	Fe	Cl
1	19.24	8.99	0.68	1.14	69.56	0.40

Table 3: EDS analysis of corroded surface (w/%)

Tabela 3: EDS analiza korodirane površine (w/%)

Spectrum	O	Si	Cl	Mn	Cr	Ni	Fe
1	35.62	0.61	5.78	4.37	5.76	23.14	24.71
2	14.51	0.49		1.08	13.83	6.41	63.69
3	12.92	0.54		1.14	14.46	6.78	64.15

The cracks were formed due to the internal or external stresses or a combination of both in the presence of the corrosion media. It is typical for the cracks to form at relatively low stresses. The crack spreads through the material, either in a trans-crystalline or inter-crystalline direction, depending on the material, the stress and the corrosion environment.

The real mechanism of SSC is not quite understood, despite there being several explanations for it. In general, the mechanism of SSC can be divided into two main parts: the mechanism of anodic dissolving and the cathode mechanism that causes hydrogen embrittlement of the material.²

For some types of austenitic stainless steels, like AISI 304 and AISI 316, it has been known for a long time that they are sensitive to SCC, but mostly at temperatures above 55 °C.

The performed investigations revealed that the local damage and leaks are a result of SCC phenomena. The SCC in austenitic stainless steel appears locally in the form of thin branched cracks that can grow very quickly and can cause failure of the structure.

One possible reason for SCC of the tank is the longitudinal orientation of the crystal grains due to cold rolling of the sheet (**Figure 5**). The directed microstructure is evidence that the material was not properly recrystallization annealed after the cold rolling, and thus

the internal stresses remained in the material. This was also confirmed with cracks in the longitudinal direction following the longitudinally deformed crystal grains.

Additional possible sources of stresses are the cold forming and the welding of the tank.

The elimination of internal stresses and the stabilization of austenite is possible in austenitic stainless steel with annealing to a temperature of 1050 °C, followed by rapid cooling in water. Such measures also prevent the formation of brittle phases in the steel, typical for a slow cooling process.

In general, SCC can be prevented by the:

- selection of a more resistant material,
- elimination of internal stresses with material annealing,
- elimination of chloride ions in the storage liquid.

The corrosion pits were observed on the external surface of the tank due to crevice corrosion in the gap between the insulation and the tank surface. Crevice corrosion is typical for narrow crevices with a lack of oxygen. At such places the formation of a new protective layer of chromium oxide (re-passivation) on the steel surface is not possible and crevice corrosion proceeds. The corrosion process is also accelerated by the presence of chloride ions. Crevice corrosion led to the formation of pits where the initiated cracks and SCC started. The brittle cracks due to SCC that spread from the surface through the tank wall are probably a consequence of hydrogen embrittlement.

Both stored media in the tank have a pH from 2.6 to 11.3. The content of the tank was either acid or alkaline, both of which accelerate the corrosion processes on the internal surface of the tank.

For the investigated tank the corrosion process could be prevented by good contact between the insulation and the wall. This would prevent the formation of condensed water on the surface of the tank from the trapped moisture in the gap.

4 CONCLUSIONS

Our investigations confirmed that the leakage of the tank, made of AISI 304 austenitic stainless steel, is a consequence of the interaction of several localized corrosion processes and the presence of internal stresses in the material. The SCC originates in the crevice corrosion pits on the external surface of the tank. The moisture captured in the gap below the insulation condensed during the cooling of the tank and together with the presence of chloride ions enabled the start of crevice corrosion.

All the necessary factors were met for the appearance of SCC: sensitive material, internal stresses in the material and corrosion media. With the proper combination of all three, the crevice corrosion pits start to grow and later the SCC developed. Cracks, as a result of SCC, are responsible for the leakage of the tank.

5 REFERENCES

- ¹ C. L. Page, R. D. Anchor, Stress corrosion cracking of stainless steels in swimming pools, *The Structural Engineer*, 66 (1988) 24, 418
- ² S.P. Lynch, Mechanistic and fractographic aspects of stress-corrosion cracking (SCC), *Stress Corrosion Cracking, Theory and Practice*, A volume in Woodhead Publishing Series in Metals and Surface Engineering, 2011, 3–89, doi:10.1533/9780857093769.1.3
- ³ N. Baddoo, P. Cutler, Stainless steel in indoor swimming pool buildings, *The Structural Engineer*, 82 (2004) 9, 24–26
- ⁴ M. Tsubota, Y. Katayama, Y. Saito, Stress Corrosion Crack Growth Behavior of Cold Worked Austenitic Stainless Steel in High Temperature Water, *Environmental Degradation of Materials in Nuclear Systems XII, Proc. 12th International Conference on Environmental Degradation of Materials in Nuclear Power Systems – Water Reactors*, ed. by T.R. Allen, P.J. King and L. Nelson, TMS, Warrendale, PA 2005, 109–115
- ⁵ A. Turnbull, K. Mingard, J.D. Lord, B. Roebuck, D. Tice, K. Motterhead, N. Fairweather, A. Bradbury, Sensitivity of stress corrosion cracking of stainless steel to surface machining and grinding procedure, *Corros. Sci.*, 53 (2011) 10, 3398–3415, DOI: 10.1016/j.corsci. 2011.06.020
- ⁶ S. Lozano-Perez, T. Yamada, T. Terachi, M. Schroder, C.A. English, G.D.W. Smith, C.R.M. Grovenor, B.L. Eyre, Multi-scale characterization of stress corrosion cracking of cold-worked stainless steels and the influence of Cr content, *Acta Mat.*, 57 (2009) 18, 5361–5381, doi:10.1016/j.actamat.2009.07.040
- ⁷ G. Hinds, L. Wickström, K. Mingard, A. Turnbull, Impact of surface condition on sulphide stress corrosion cracking of 316L stainless steel, *Corrosion Science*, 71 (2013) 43–52, doi:10.1016/j.corsci. 2013.02.002
- ⁸ A. Bhattacharya, *Stress Corrosion Cracking of Duplex Stainless Steels in Caustic Solutions*, Georgia Institute of Technology, Atlanta, GA 2008, 8
- ⁹ J. Orlikowski, S. Krakowiak, Pitting corrosion and stress corrosion cracking of buffer tanks in a brewery, *Engineering Failure Analysis*, 29 (2013) 75–82, doi:10.1016/j.engfailanal.2012.10.013
- ¹⁰ J. Woodtli, R. Kieselbach, Damage due to hydrogen embrittlement and stress corrosion cracking, *Engineering Failure Analysis*, 7 (2000) 6, 427–450